Available to DOE and DOE Contractors from the
Office of Scientific and Technical Information
P.O. Box 62, Oak Ridge, TN 37831
Prices available from (615) 576-8401, FTS 626-8401

Available to the public from
National Technical Information Service
U.S. Department of Commerce
5285 Port Royal Road, Springfield, VA 22161
Price: Printed Copy A09, Microfiche A01

LBL--27913

DE91 004657

Joint Seismic, Hydrogeological, and Geomechanical Investigations of a Fracture Zone in the Grimsel Rock Laboratory, Switzerland

Ernest L. Majer, Larry R. Myer, John E. Peterson Jr.,
Kenzi Karasaki, Jane C. S. Long, and Stephen J. Martel

Earth Sciences Division
Lawrence Berkeley Laboratory
University of California
Berkeley, California 94720

Peter Blümling and Stratis Vomvoris

Swiss National Cooperative for the Storage of Nuclear Waste
Baden, Switzerland

June 1990

This work was supported by the Manager, Chicago Operations, Repository Technology Program, Repository Technology and Transportation Division, of the U.S. Department of Energy under Contract No. DE-AC03-76SF00098 and by the Swiss National Cooperative for the Storage of Nuclear Waste (NAGRA).

Preface

This report is one of a series documenting the results of the Nagra-DOE Cooperative (NDC-I) research program in which the cooperating scientists explore the geological, geophysical, hydrological, geochemical, and structural effects anticipated from the use of a rock mass as a geologic repository for nuclear waste. This program was sponsored by the U. S. Department of Energy (DOE) through the Lawrence Berkeley Laboratory (LBL) and the Swiss Nationale Genossenschaft für die Lagerung radioaktiver Abfälla (Nagra) and concluded in September 1989. The principal investigators are Jane C. S. Long, Ernest L. Majer, Karsten Pruess, Kenzi Karasaki, Chalon Carnahan and Chin-Fu Tsang for LBL and Piet Zuidema, Peter Blümling, Peter Hufschmied and Stratis Vomvoris for Nagra. Other participants will appear as authors of the individual reports. Technical reports in this series are listed below.

1. Determination of Fracture Inflow Parameters with a Borehole Fluid Conductivity Logging Method by Chin-Fu Tsang, Peter Hufschmied, and Frank V. Hale (NDC-1, LBL-24752).
2. A Code to Compute Borehole Fluid Conductivity Profiles with Multiple Feed Points by Frank V. Hale and Chin-Fu Tsang (NDC-2, LBL-24928; also NTB 88-21).
3. Numerical Simulation of Alteration of Sodium Bentonite by Diffusion of Ionic Groundwater Components by Janet S. Jacobsen and Chalon L. Carnahan (NDC-3, LBL-24494).
4. P-Wave Imaging of the FRI and BK Zones at the Grimsel Rock Laboratory by Ernest L. Majer, John E. Peterson Jr., Peter Blümling, and Gerd Sattel (NDC-4, LBL-28807).
5. Numerical Modeling of Gas Migration at a Proposed Repository for Low and Intermediate Level Nuclear Wastes at Oberbauenstock, Switzerland by Karsten Pruess (NDC-5, LBL-25413).
6. Analysis of Well Test Data from Selected Intervals in Leuggern Deep Borehole — Verification and Application of PTST Method by Kenzi Karasaki (NDC-6, LBL-27914).
7. Shear Wave Experiments at the U. S. Site at the Grimsel Laboratory by Ernest L. Majer, John E. Peterson Jr., Peter Blümling, and Gerd Sattel (NDC-7 LBL-28808).
8. The Application of Moment Methods to the Analysis of Fluid Electrical Conductivity Logs in Boreholes by Simon Loew, Chin-Fu Tsang, Frank V. Hale, and Peter Hufschmied (NDC-8, LBL-28809).
9. Numerical Simulation of Cesium and Strontium Migration through Sodium Bentonite Altered by Cation Exchange with Groundwater Components by Janet S. Jacobsen and Chalon L. Carnahan (NDC-9, LBL-26395).
10. Theory and Calculation of Water Distribution in Bentonite in a Thermal Field by Chalon L. Carnahan (NDC-10, LBL-26058).
11. Prematurely Terminated Slug Tests by Kenzi Karasaki (NDC-11, LBL-27528).
12. Hydrologic Characterization of Fractured Rocks — An Interdisciplinary Methodology by Jane C. S. Long, Ernest L. Majer, Stephen J. Martel, Kenzi Karasaki, John E. Peterson Jr., Amy Davey, and Kevin Hestir, (NDC-12, LBL-27863).
13. Exploratory Simulations of Multiphase Effects in Gas Injection and Ventilation Tests in an Underground Rock Laboratory by Stefan Finsterle, Erika Schlueter, and Karsten Pruess (NDC-13, LBL-28810).
14. Joint Seismic, Hydrogeological, and Geomechanical Investigations of a Fracture Zone in the Grimsel Rock Laboratory, Switzerland by Ernest L. Majer, Larry R. Myer, John E. Peterson Jr., Kenzi Karasaki, Jane C. S. Long, Stephen J. Martel, Peter Blümling, and Stratis Vomvoris (NDC-14, LBL-27913).
15. Analysis of Hydraulic Data from the MI Fracture Zone at the Grimsel Rock Laboratory, Switzerland by Amy Davey, Kenzi Karasaki, Jane C.S. Long, Martin Landsfeld, Antoine Mensch, and Stephen J. Martel (NDC-15, LBL-27864).
16. Use of Integrated Geologic and Geophysical Information for Characterizing the Structure of Fracture Systems at the US/BK Site, Grimsel Laboratory, Switzerland by Stephen J. Martel and John E. Peterson Jr. (NDC-16, LBL-27912).

Table of Contents

List of Figures

List of Tables

Abstract

From 1987 to 1989 The United States Department of Energy (DOE) and the Swiss Cooperative for the Storage of Nuclear Waste (Nagra) participated in an agreement to carryout experiments for understanding the effect of fractures in the storage and disposal of nuclear waste. As part of this joint work field and laboratory experiments were conducted at a controlled site in the Nagra underground Grimsel test site in Switzerland. The primary goal of these experiments in this fractured granite was to determine the fundamental nature of the propagation of seismic waves in fractured media, and to relate the seismological parameters to the hydrological parameters. The work is ultimately aimed at the characterization and monitoring of subsurface sites for the storage of nuclear waste. The seismic experiments utilized high frequency (1000 to 10000 Hz.) signals in a cross-hole configuration at scales of several tens of meters. Two-, three-, and four-sided tomographic images of the fractures and geologic structure were produced from over 60,000 raypaths through a 10 by 21 meter region bounded by two nearly horizontal boreholes and two tunnels. Intersecting this region was a dominant fracture zone which was the target of the investigations. In addition to these controlled seismic imaging experiments, laboratory work using core from this region were studied for the relation between fracture content, saturation, and seismic velocity and attenuation. In-situ geomechanical and hydrologic tests were carried out to determine the mechanical stiffness and conductivity of the fractures. The results indicate that both P-waves and S-waves can be used to map the location of fractures, both natural and induced from mining activities. In addition, it appears that at frequencies approaching several kilohertz, attenuation measurements are more useful than velocity measurements. At lower frequencies the opposite seems to be true. In addition, fractures that are open and hydrologically conductive are much more visible to seismic waves than non-conductive fractures.

Acknowledgements

This work was supported through U.S. Department of Energy Contract No. DE-AC03-76SF00098 by the DOE Office of Civilian Radioactive Waste Management, Office of Geologic Repositories. We also want to thank the personnel at NAGRA and the Grimsel Rock Laboratory for their help and support, in particular Piet Zuidema and Gerdt Sattel, as well as Eric Wyss of SOLEXPERTS AG.

1.0. INTRODUCTION

The Swiss National Cooperative for the Storage of Radioactive Waste (Nagra) has hosted and carried out a variety of experiments at the underground Grimsel Rock Laboratory near the Grimsel Pass in the Swiss Alps (Figures 1.1, 1.2, and 1.3). From 1987 through 1989 the U. S. Department of Energy (DOE) has participated in an agreement with Nagra to perform joint research on various topics related to geologic storage of nuclear waste. As part of this Nagra-DOE Cooperative (NDC-I) project Lawrence Berkeley Laboratory (LBL) has participated in several projects at Grimsel which are directed towards improving the understanding of the role of fractures in the storage of nuclear waste. This report describes a series of experiments at Grimsel called the Fracture Research Investigation (FRI). The FRI project has been designed to address the effects of fractures on the propagation of seismic waves and the relationship of these effects to the hydrologic behavior.

It is necessary to locate and characterize fractures to accurately model the hydrological and geomechanical behavior of geologic repositories. Although fracture properties can be observed directly at the surface, in underground openings, and from boreholes, a vast majority of the rock can not be examined directly. Because almost all rock is heterogeneous, one can not rely on the simple interpolation or extrapolation of structural information for adequate fracture characterization. Unobserved features within a rock body may play a dominant role in its geomechanical or hydrologic behavior. Therefore, there is a crucial need to have techniques for fracture detection and characterization between boreholes and underground openings.

The FRI work was aimed at developing practical borehole seismic and hydrological methods for use during the characterization and monitoring of underground nuclear waste facilities. The fundamental design of the project was to find a simple, well defined, accessible fracture zone surrounded by relatively unfractured rock and use this zone as a point of comparison for

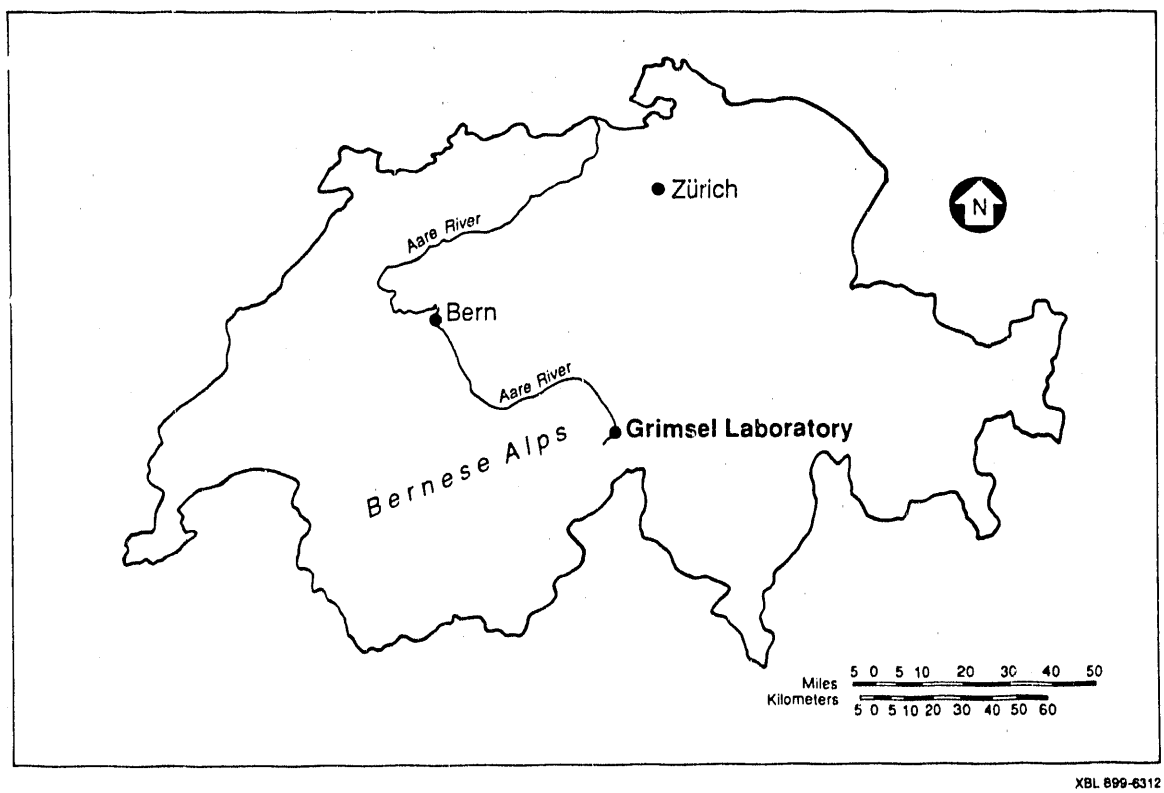

Figure 1.1. Regional setting of the Grimsel Rock Laboratory.

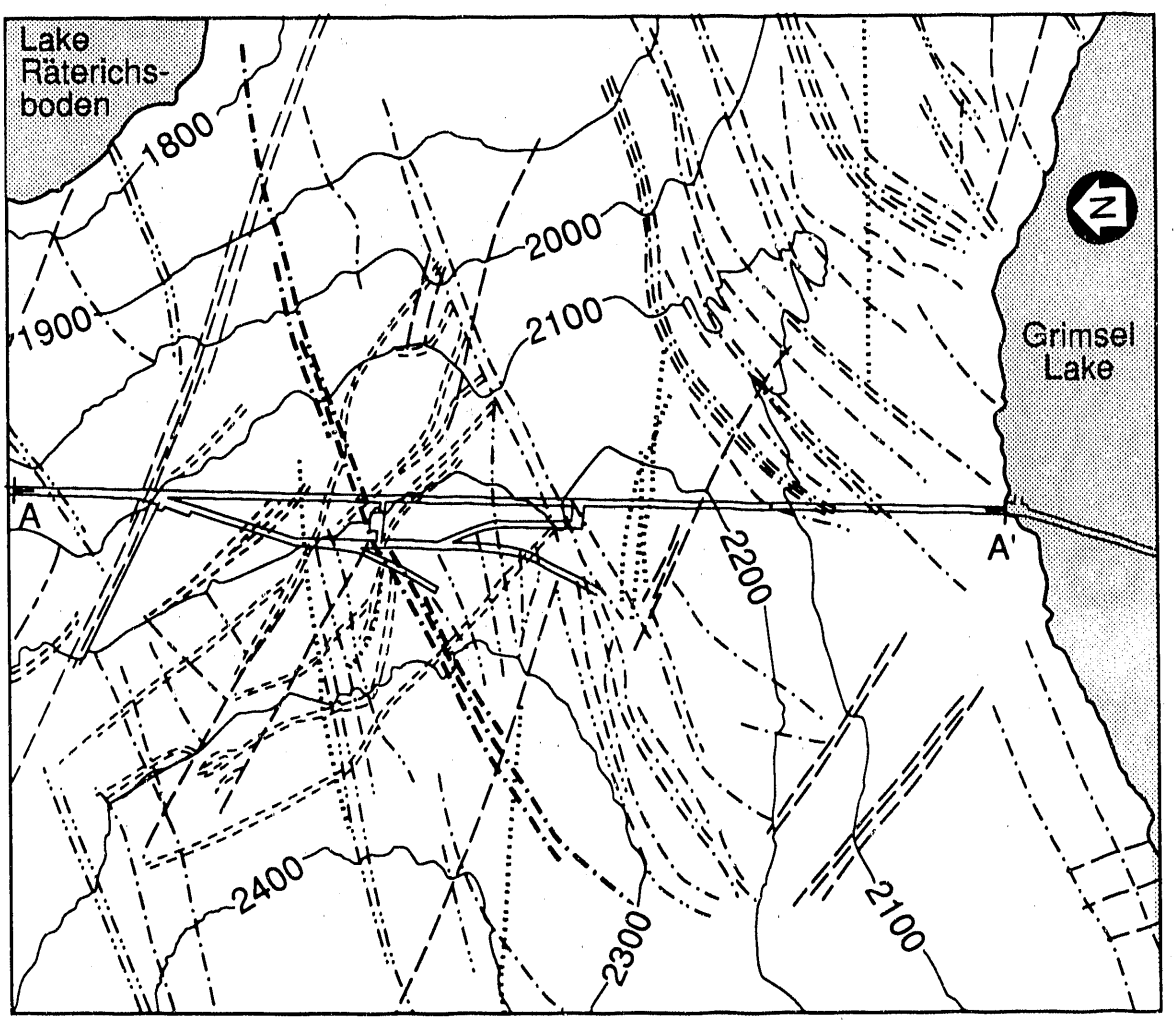

Figure 1.2. Geologic map showing the major structures at the surface above the Grimsel laboratory (from NTB 87-14). The S1 zones shown in heavy lines project down to the vicinity of the FRI site.

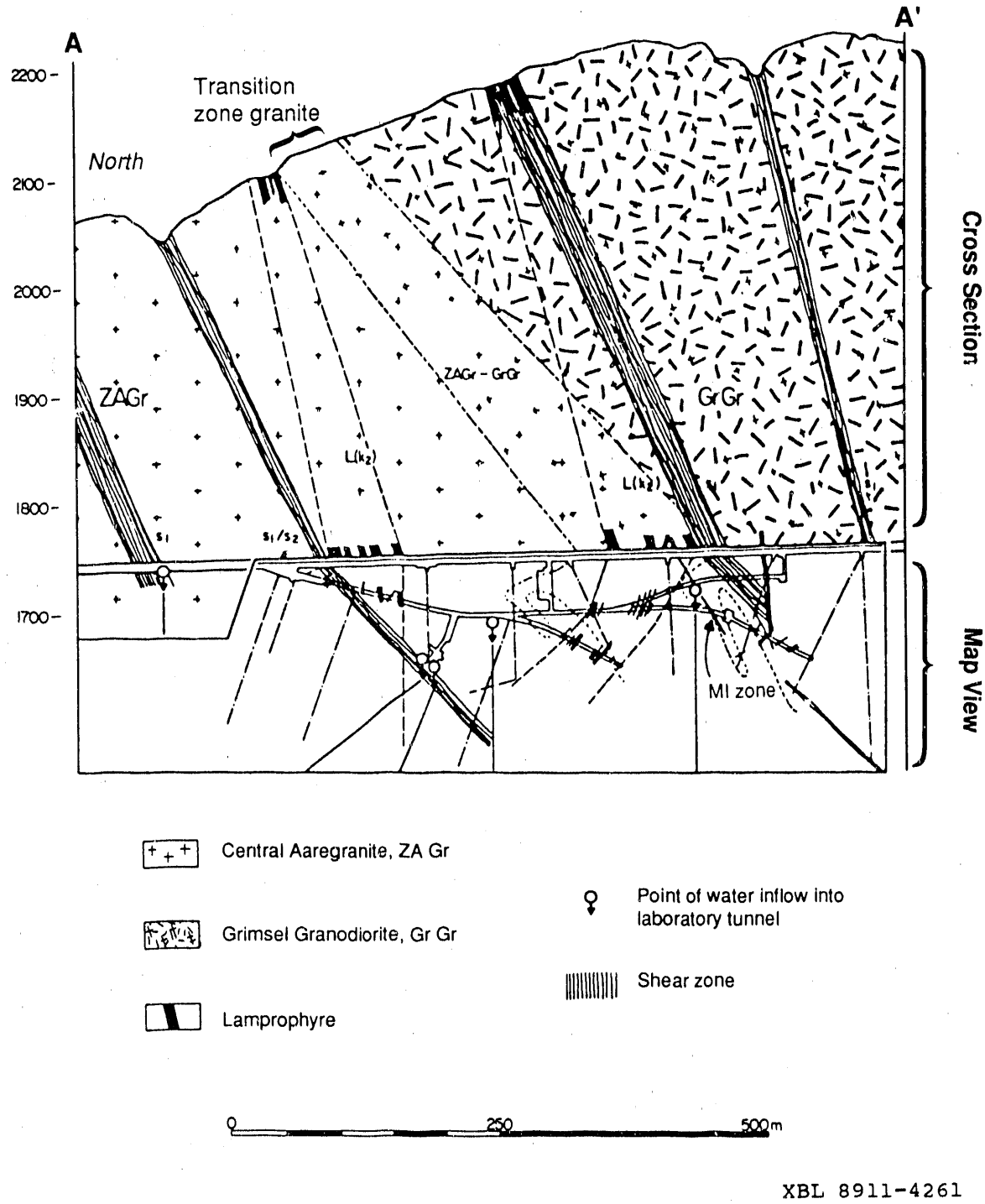

Figure 1.3. Geologic cross section along the main access tunnel and generalized map showing major geologic structures at Grimsel (from NTB 87-14). Line of this cross section is shown on Figure 1.2.

seismic, hydrologic and mechanical behavior. The FRI site was designated in the Grimsel Rock Laboratory for this purpose and field work was carried out during each year of the three year NDC-I project (1987-1989). The FRI project has involved separate and simultaneous, detailed geologic studies, field measurements of seismic wave propagation, geomechanical measurements of fracture properties, and the hydrologic response of the fractured rock. Laboratory measurements of core have also been carried out to address the fundamental nature of seismic wave propagation in fractured rock. Because all these studies were focussed on the same fracture zone, the study provided insight into

- New theories of seismic wave propagation through fractures,
- How changes in the fracture properties affect seismic wave propagation,
- Interpretation of seismic tomography to identify hydrologic features, and
- Integration of seismic data into a hydrologic testing plan.

The FRI work was interdisciplinary with the strongest emphasis on seismic imaging. Compared to other efforts the seismic measurements were most extensive and comprehensive. The hydrologic measurements were not as complete and although the laboratory studies of the seismic properties of cores was reasonably comprehensive, the *in situ* mechanical measurements were only prototypes. This scheme was appropriate for the FRI site, because the fracture zone is well exposed in the two parallel drifts which intersect it, therefore it seemed clear that the hydrology of the site would be mainly confined to the fracture zone Because of this the number one focus of the work was to evaluate and develop seismic methods to provide information about hydrologic properties in a fractured rock environment.

As the work progressed, it followed the course of most projects in the earth sciences in that as our understanding of the rock increased, the "simple" fracture zone became more complex. It is natural in such cases to plan for a follow up validation exercise where new holes would be drilled to obtain direct observations of features predicted by the geophysical interpretation and more extensive hydrologic testing would be conducted to determine the hydrologic role of these features. Although this effort could not be accommodated withing the NDC-I project, the authors feel that such efforts would be elucidating. This is an unnecessary page for all but the computer.

Overall the project is a unique effort in combining several different disciplines to define a complex problem.

2.0. GEOLOGIC OVERVIEW OF THE FRI SITE

2.1. Introduction

The FRI site is located in the southern part of the Grimsel Rock Laboratory (Figure 2.1) and is bounded on the west by the AU laboratory tunnel, on the east by the main access tunnel, and on the north and south by boreholes BOFR 87.001 and BOFR 87.002 respectively (Figure 2.2). The FRI site lies within the Grimsel Granodiorite, close to a very irregular contact with the lighter-colored Central Aaregranite. The eastern parts of the cores from the two boreholes bounding the site are distinctly lighter in color than the western parts of the cores. This color change may reflect differences in hydrothermal alteration across the site, variation in the original mineralogy of the grandiorite, or the presence of lenses of Central Aare granite. Both the Grimsel Grandiorite and the Central Aareganite are foliated. The foliation strikes northeast, and dips steeply to the southeast. It is defined by aligned grains of biotite and bands of mylonite. A steeply-plunging linear fabric element within the foliation is defined by aligned and elongated feldspar grains.

Of the many different rock structures at Grimsel, four are hydrologically dominant: S-zones, K-zones, lamprophyres, and tension fissures (NTB 85-46). The S-zones are fracture-bearing shear zones that generally dip steeply to the southeast, parallel to the foliation in the host rock. Within the S-zones, both the fractures and the grain-scale mineral fabric of the rock dip steeply to the southeast. The K-zones are fracture zones that generally strike west or northwest; they cut the host rock fabric at a high angle. The lamprophyres are mafic igneous dikes. They dip steeply and generally strike west or northwest. These have been metamorphosed and contain abundant biotite. The lamprophyres are highly discontinuous and are widely distributed at Grimsel. Tension fissures are subhorizontal and usually filled with quartz crystals and chlorite. S-zones, lamprophyres, and tension fissures are exposed in the tunnels bounding the FRI site (Figures 2.3 and 2.4).

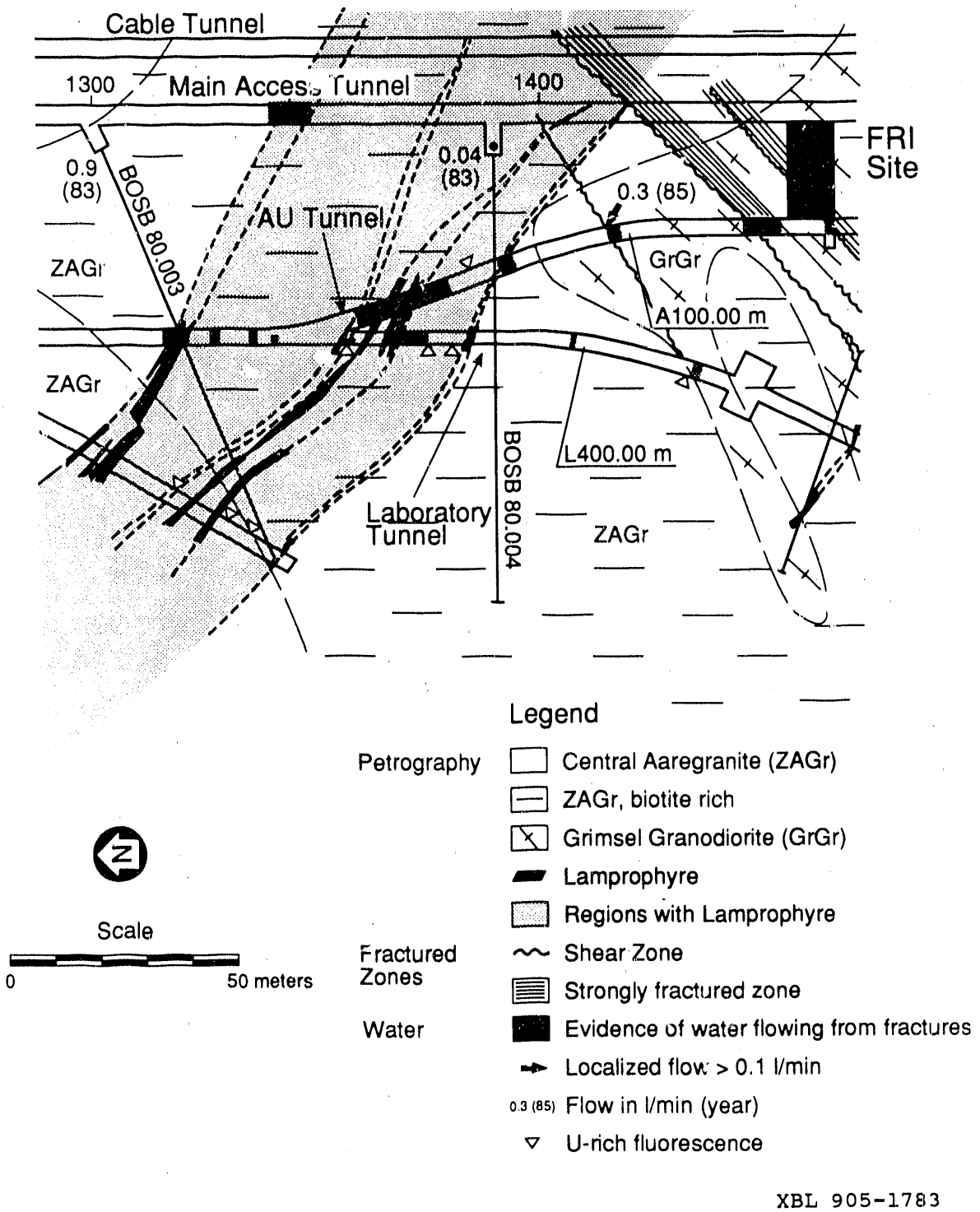

Figure 2.1. Map of the southern part of the Grimsel laboratory showing key geologic features and the location of the FRI site. From Nagra Technical Report 87-14.

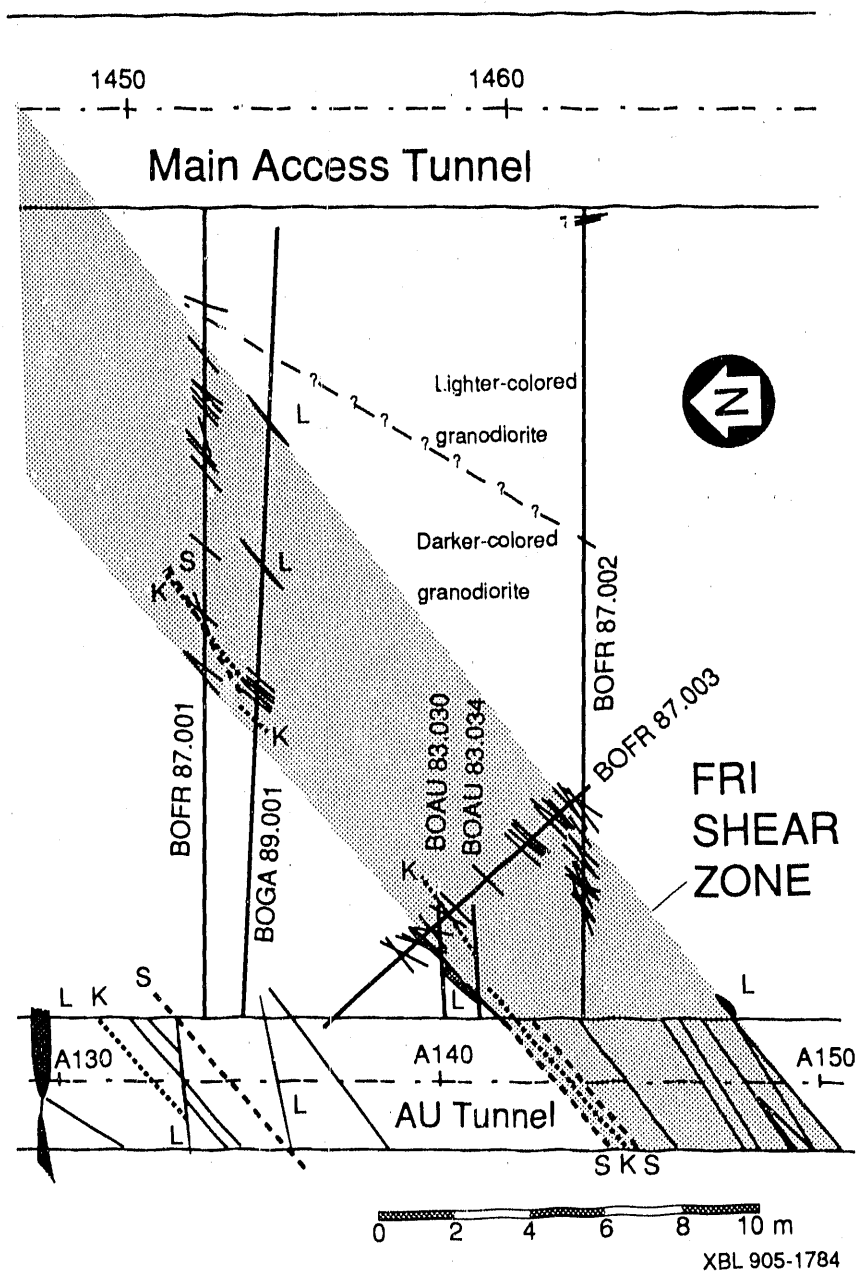

Figure 2.2. Geologic map of the FRI site in the plane of boreholes BOFR 87.001 and 87.002. Unmatched lines are fractures. Lamprophyres are marked L. kakirite (cataclasite) zones K, and thin shear bands S, modified from Geotest Report 87048A.

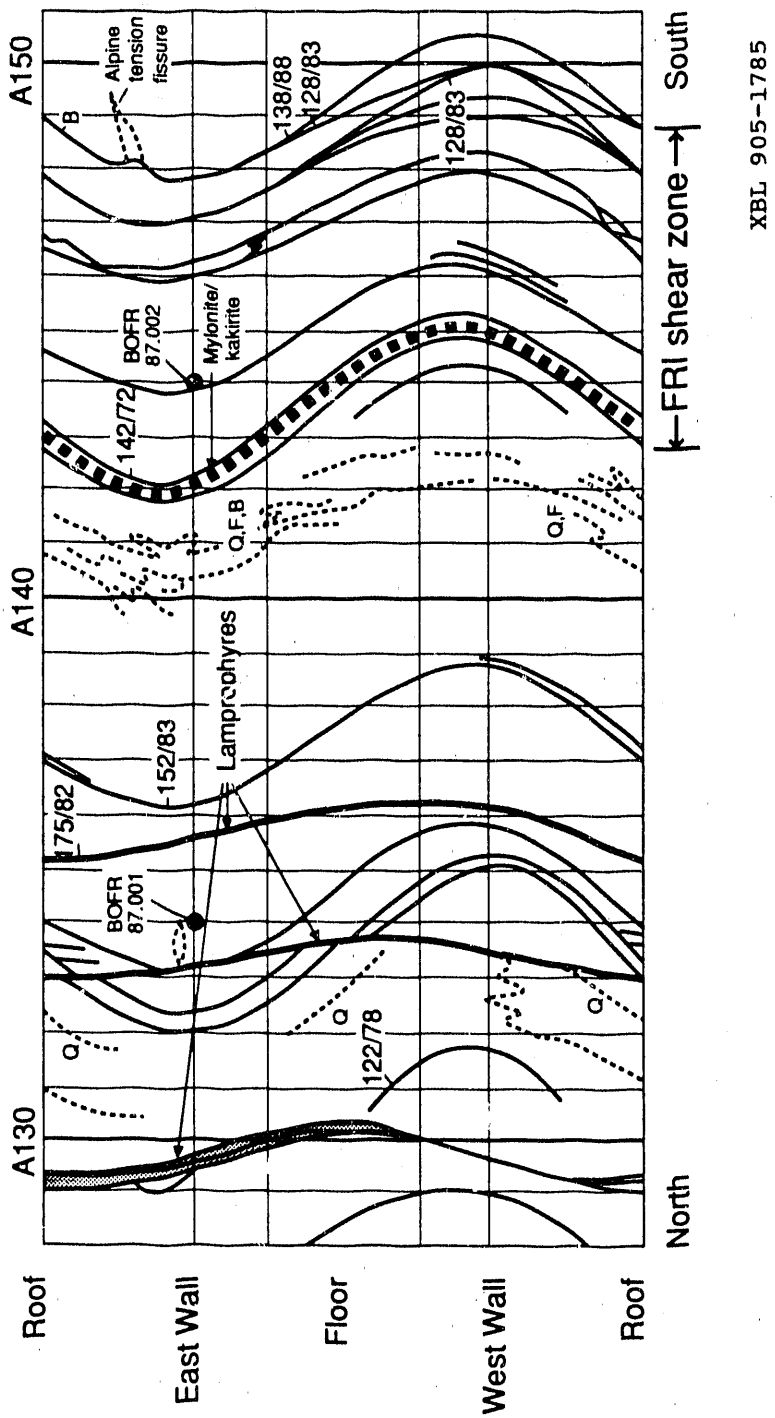

Figure 2.3. Log of the AU tunnel showing traces of fractures (solid lines), mineralized veins (dashed lines), and other geologic structures exposed in the AU tunnel near the FRI site. Pairs of numbers separated by a slash indicate fracture dip direction and dip. The NE strike of the features is revealed by the orientation of the traces on the tunnel floor. Mineralization key: Q = quartz, F = feldspar, and B = biotite. From preliminary draft of NTB 87-14.

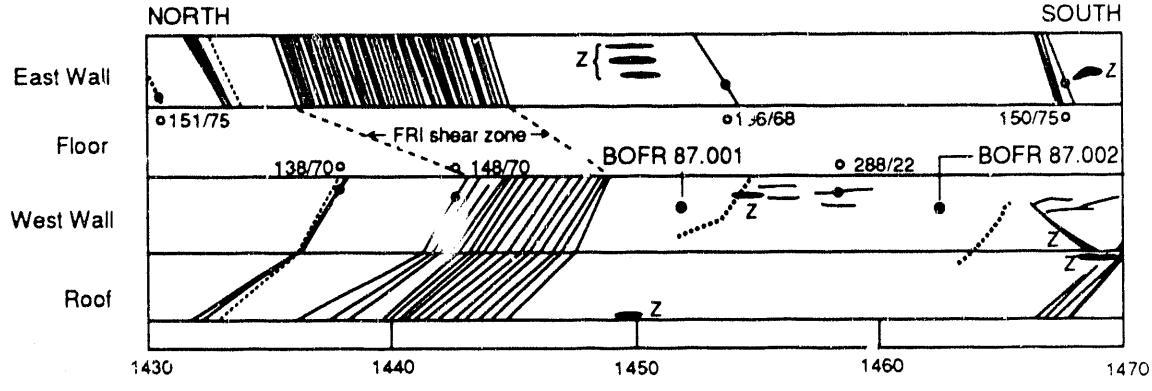

XBL 905-1786

Figure 2.4. Log of the main access tunnel showing fractures (solid line), zones of concentrated biotite (dashed line), and Alpine tension fissures (marked by a z) on the east side of the FRI site. Pairs of numbers separated by a slash indicate fracture dip direction and dip. Numbers at bottom of figure show distance (in meters) from north entrance to the main access tunnel. The floor was covered by concrete when the tunnel was logged. From preliminary draft of Nagra Technical Report 87-14.

Table 2.1. Description of core from BOGA 89.001

Depth (m)	Description
0.00 – 4.50	Grimsel Granodiorite, moderately dark, medium- to coarse-grained, nonuniform grains, distinct foliation
4.50 – 4.85	Zone with sealed quartz-filled fractures; quartz filling shows distinct cracks
4.85 – 8.56	Grimsel Granodiorite, moderately dark, medium- to coarse-grained, nonuniform grains, distinct foliation
	At 7.73 m is a kakiiite zone 5–10 cm thick
8.56 – 9.00	Zone of numerous fractures in part filled with fault gouge
9.00 – 11.43	Grimsel Granodiorite, moderately dark, medium- to coarse-grained, nonuniform grains, distinct foliation
11.43 – 11.76	Grimsel Granodiorite, moderately dark, medium- to coarse-grained, nonuniform grains, intensive mylonitization
11.76 – 11.84	Grimsel Granodiorite, moderately dark, medium- to coarse-grained, nonuniform grains, distinct foliation
11.84 – 11.95	Lamprophyre, biotite-rich, foliated, fractured along foliation
11.95 – 15.73	Grimsel Granodiorite, moderately dark, medium- to coarse-grained, nonuniform grains, distinct foliation, feldspars are saussuritized (chemically altered)
15.73 – 15.80	Lamprophyre, biotite-rich, foliated, fractured along foliation
15.80 – 20.54	Grimsel Granodiorite, moderately dark, medium- to coarse-grained, nonuniform grains, distinct foliation, feldspars are distinctly saussuritized, quartz-rich

Seven main boreholes (Table 2.1 and Figure 2.5) have been drilled and logged at the FRI site to investigate the zone. Two parallel boreholes (BOFR 87.001 and 87.002) connect the two tunnels and bracket a section of the FRI shear zone. Borehole BOFR 87.003 was drilled across the shear zone and borehole BOFR 87.004 was drilled along the northwest edge of the shear zone. Borehole BOGA 89.001 was drilled after the field investigations reported here were completed. In addition to the main boreholes, a series of small holes were drilled 25 cm apart in the AU tunnel and in the main access tunnel between BOFR 87.001 and 87.002 for emplacing instruments for the seismic tomography experiments at the site.

2.2. The FRI S-Zone

This site was chosen for testing because it intersects a prominent S-zone (Figure 2.2). This S-zone is 5 meters thick and is the most prominent structure at the FRI site. It strikes northeast and dips steeply to the southeast. The FRI tests were sited at this S-zone because it was considered to have a relatively simple and predictable structure, characteristics which would be an asset in conducting the various tests planned for the project. The leakage of water from the shear zone indicates that it is hydrologically active.

Fractures in the FRI borehole cores are most numerous where the foliation in the S-zone is best developed. In some places where the rock contains fractures it is schistose. Many of the fractures in the borehole cores occur at edges of mylonite bands which help define the ductile fabric of the shear zone. The planar anisotropy of the rock in the shear zone thus strongly controls the position and orientation of the fractures in the zone.

The S-zone does not consist of parallel fractures, but rather a network of fractures that form a braided pattern (Figure 2.6). Thus, the zone as a whole strikes ~N49°E, but internal fractures range in strike from N38°E to N52°E. Fracture dip measurements range from 65° to 88° to the southeast. Most of the fractures have similar appearances, similar orientations, and may be noticeably nonplanar. Although in general it is difficult to correlate individual fractures from borehole to borehole, narrow interconnected networks of fractures appear to extend between boreholes.

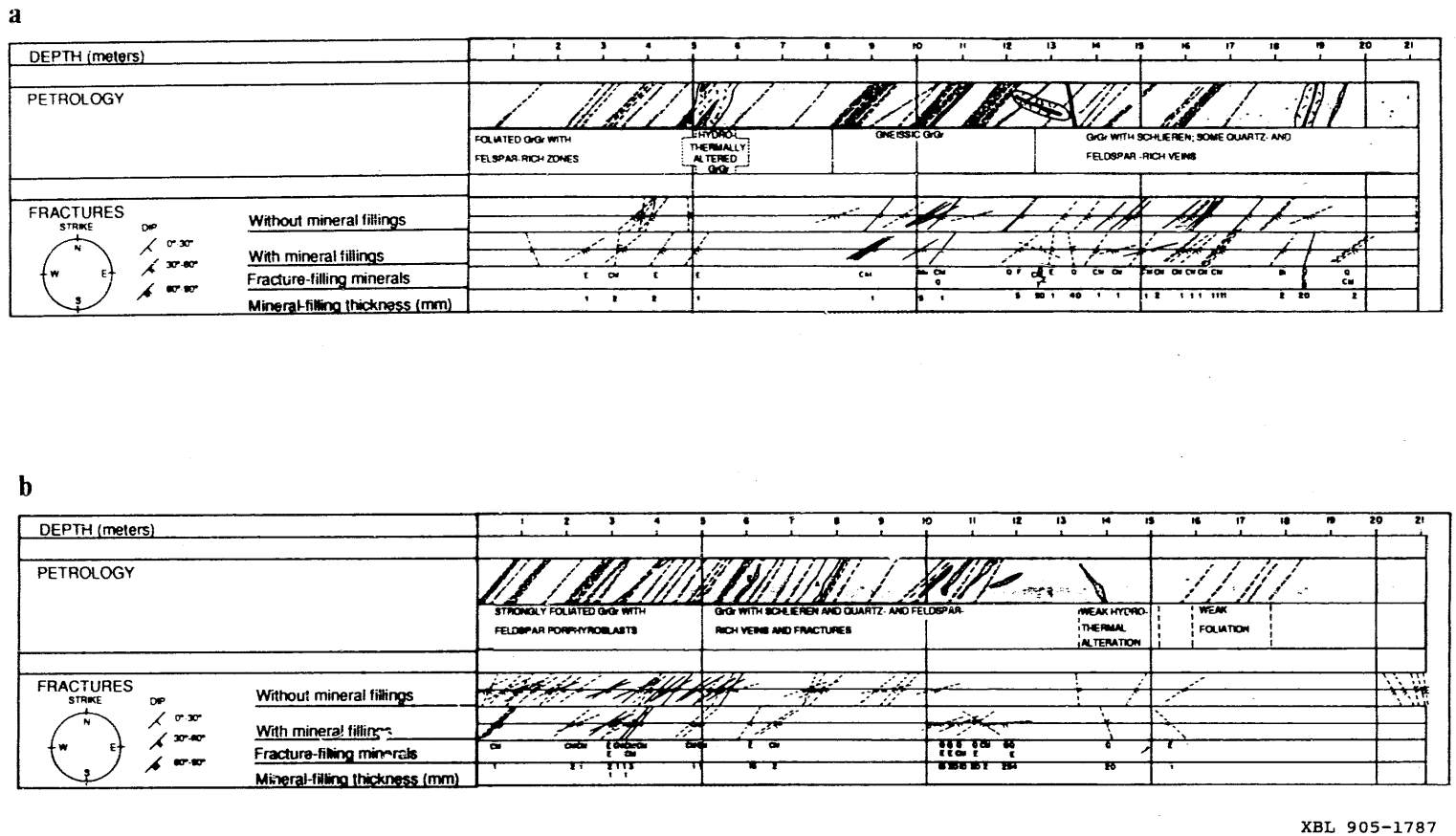

Figure 2.5a,b. Logs of core from six boreholes (a) BOFR 87.001 and (b) BOFR 87.002 at the FRI site. Logs are from Geotest Report 87048A. Explanation for fracture minerals: Q = quartz, E = epidote, Chl = chlorite, B = biotite.

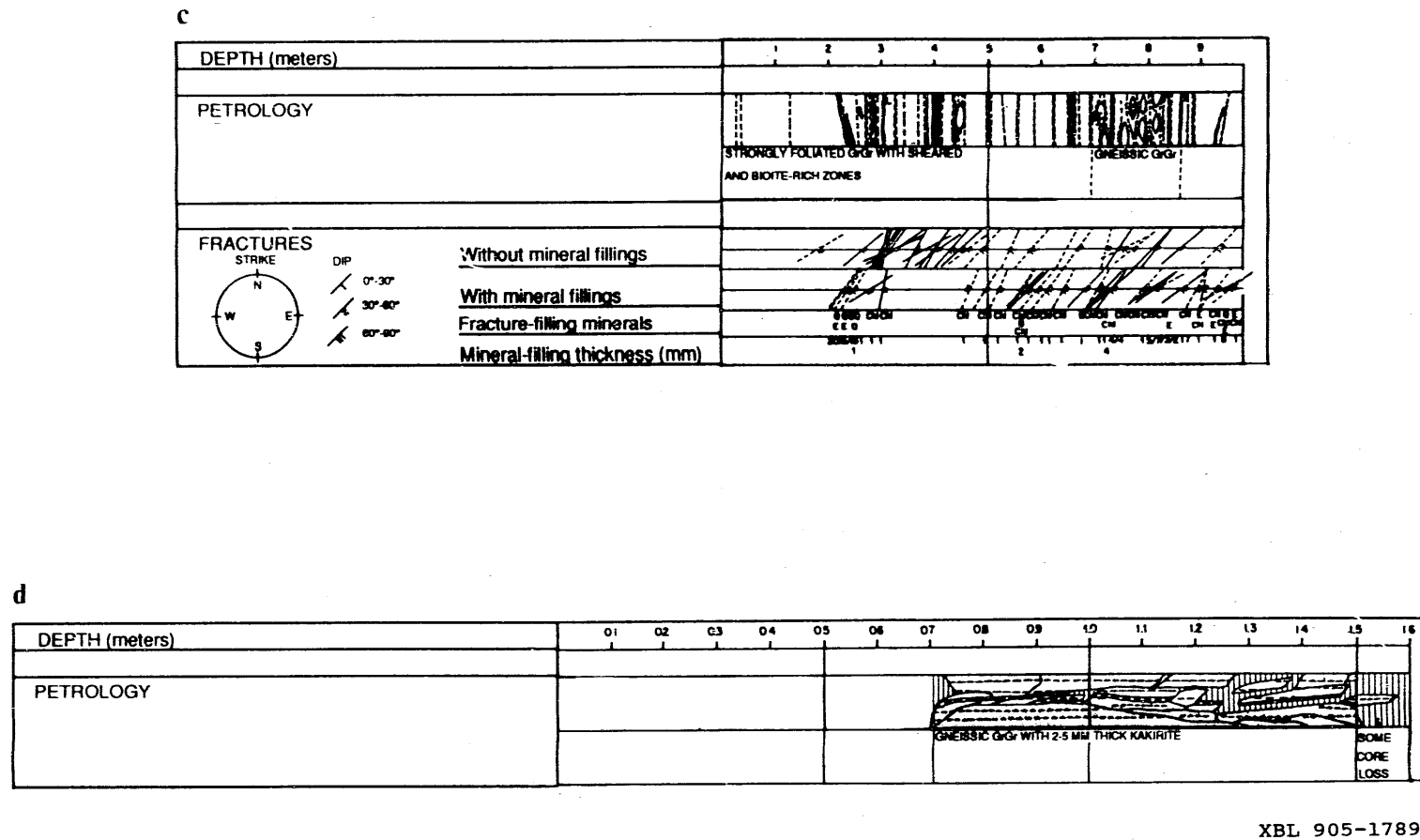

Figure 2.5c,d. Logs of core from six boreholes (c) BOFR 87.003 and (d) BOFR 87.007 at the FRI site. Logs are from Geotest Report 87048A. Explanation for fracture minerals: Q = quartz, E = epidote, Chl = chlorite, B = biotite.

e

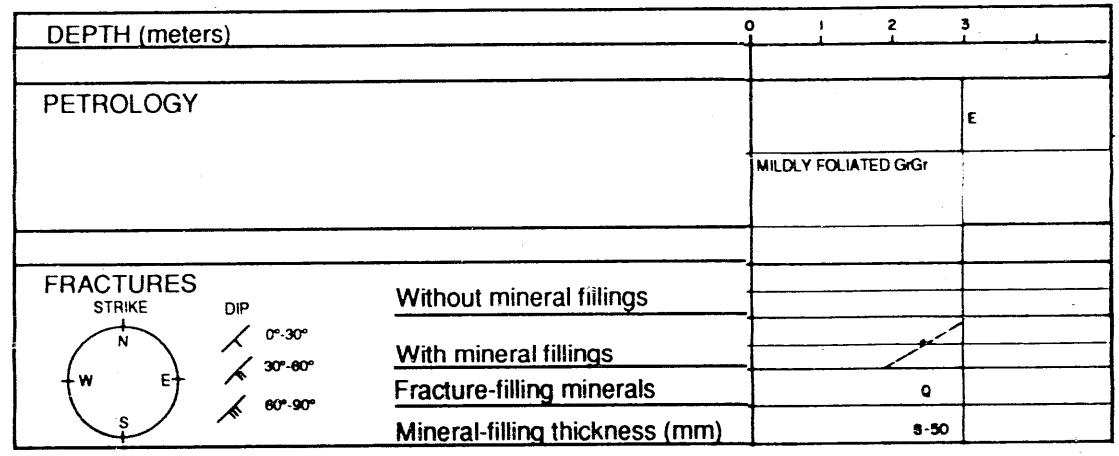

f

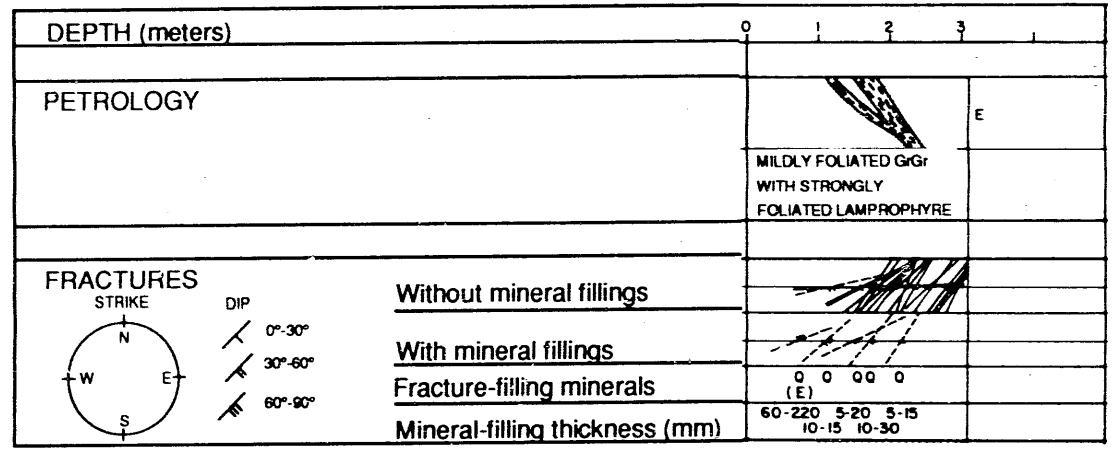

XBL 905-1788

Figure 2.5e,f. Logs of core from boreholes (e) BOAU 83.030 and (f) BOAU 83.034 at the FRI site. Logs are from a preliminary volume of Nagra Technical Report 87.14. Explanation for fracture minerals: Q = quartz, E = epidote, Chl = chlorite, B = biotite.

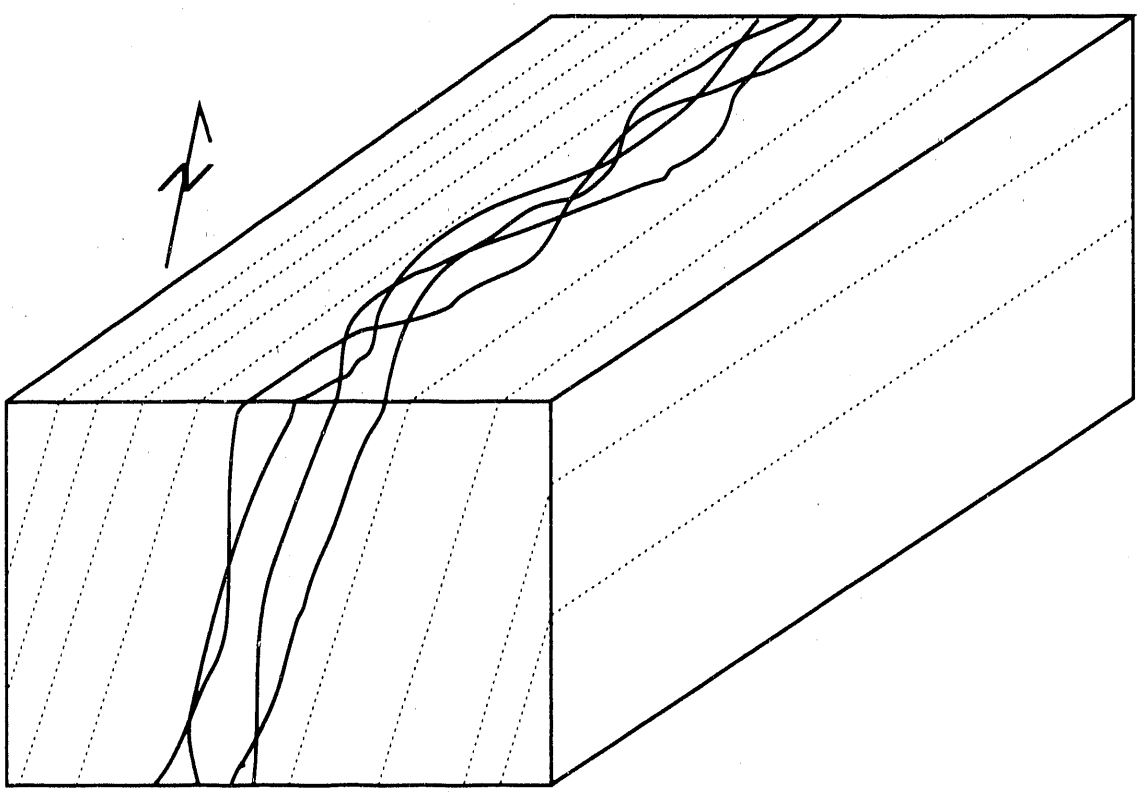

XBL 903-782

Figure 2.6. Schematic diagram showing the braided fracture pattern within northeast-striking shear zones near the Grimsel Rock Laboratory. The heavy dashed line is a kakirite-bearing fracture. The light dashed lines mark the foliation in the rock.

Some fractures that do have a distinctive appearance are those that contain kakirite. These are the main focus of this study. Kakirite is a fine-grained breccia or gouge and is considered diagnostic of fractures that are faults (i.e. fractures that accommodate significant shear displacement). Most of the water that leaks into the laboratory AU tunnel from the FRI shear zone comes from a kakirite-bearing fracture near the northwest edge of the shear zone (Figure 2.2). Boreholes BOFR 87.001, BOGA 89.001, and BOFR 87.003 also intersect kakirite-bearing fractures in a narrow band within a meter of the northwest edge of the FRI shear zone. It is entirely possible that these four kakirite occurrences are along a single kakirite-bearing fracture. If these kakirites do mark a continuous fracture, then it would have a nearly linear trace between the laboratory AU tunnel and BOGA 89.001, and would curve between BOGA 89.001 and BOFR 87.001. The FRI project site was designed to focus on this distinctive kakirite-bearing fracture because it appeared to be a dominant hydrologic and mechanical feature.

2.3. Lamprophyres

Although lamprophyres in the vicinity of the FRI site generally strike west or northwest, (Figures 2.1 and 2.2), strongly-foliated lamprophyres that strike northeast (parallel to the FRI shear zone) were intersected by boreholes at three points within the FRI shear zone. Each lamprophyre is several centimeters thick. Two of the lamprophyres occur in BOGA 89.001, with one coinciding with the southeast edge of the FRI shear zone. Neither of these lamprophyres were logged in borehole BOFR 87.001, which is less than two meters away from BOGA 89.001, or in BOFR 87.003. These lamprophyres are thus constrained to extend along the strike of the FRI zone for less than 15 meters. Borehole BOAU 83.034 intersects the third lamprophyre at a depth of 1.0-2.5 meters. This lamprophyre is along the northwest edge of the FRI zone. Surprisingly, no lamprophyres are logged where this lamprophyre would project into the AU tunnel or BOFR 87.003. Instead, the AU tunnel log shows a thin shear band and the log of BOFR 87.003 shows a series of biotite-rich zones that parallel the foliation in the rock.

Taken together, the borehole observations indicate that lamprophyres cannot be projected far along strike within the FRI zone and that they may pass into features identified as shear bands

or biotite-rich zones. The northeast strikes of these lamprophyres are anomalous; most of the lamprophyres exposed in the AU tunnel and at the surface strike west or northwest. These findings are consistent with the northeast-striking lamprophyres having been stretched out along the FRI zone during shear deformation in the geologic past. Stretching could account for the apparently discontinuous nature of FRI lamprophyres, their strong foliation, and their zone-parallel strikes. Interestingly, the FRI lamprophyres seem most common where the foliation and fracturing within the zone is most extensively developed, near the edges of the FRI shear zone.

West-striking lamprophyres at the FRI site are logged in the AU tunnel but none have been logged in the main access tunnel. Some might intersect the main access tunnel and yet not be logged, for the blocky nature of the main access tunnel makes logging difficult. However, the lamprophyres might also pinch out within the FRI site or be offset across the FRI shear zone. As an example, the lamprophyre exposed in the AU tunnel near the mouth of borehole BOGA 89.001 apparently pinches out before reaching the hole.

2.4. Tension Fissures

Many gently-dipping Alpine tension fissures (*Zerrklüfte*) occur in the southern part of the laboratory. Most of the exposed fissures have apertures of several centimeters, but some fissures that are several meters long have apertures that locally exceed a meter. The fissures commonly occur near lamprophyres. A fissure exposed in the AU tunnel at A148 (Figure 2.3) may extend from a lamprophyre along the SE margin of the FRI shear zone (Figure 2.2). A cluster of gently-dipping fissures near the 1450-meter mark of the main access tunnel occur near a biotite-rich area that may be associated with a lamprophyre (Figure 2.4). Borehole BOFR 87.001 encounted a gently-dipping, quartz-filled fracture within the FRI site, approximately 12.8 meters from the laboratory AU tunnel. This fracture is not far from the more westerly lamprophyre encountered in BOGA 89.001. In addition to the fissures that are associated with the lamprophyres, several gently-dipping fractures that appear to be distant from lamprophyres have been logged in the AU tunnel at the west side of the FRI site. Given the number of gently-dipping fissures encountered near the FRI site, it would not be surprising if more occurred within it.

2.5. Summary

The FRI project was designed to test the coupled seismic, mechanical, and hydrologic behavior of a prominent, yet relatively simple fracture. Key goals of the project were to evaluate and improve our ability to use seismic methods as part of a hydrologic characterization of a fractured rock mass. The kakirite-bearing fracture in the shear zone at the FRI site was the principal target of the FRI tests. The distinctive appearance, water-bearing capacity, and general setting of this fracture indicated that it would be appropriate for our purposes.

Some additional aspects of the geology at the FRI site are expected to bear on the seismic, mechanical, and hydrologic tests. First, the rock mass at the site is decidedly heterogeneous. The granitic rock within the site is compositionally nonuniform and contains lamprophyres. Two objectives of the seismic experiments were to determine whether the lithologic heterogeneity within the site can be imaged and whether this heterogeneity prevented the kakirite-bearing fracture from being imaged. A second important aspect of the rock at the site is its anisotropy, which locally is quite pronounced. Both the grain-scale fabric of the rock and most of the macroscopic fractures are preferentially aligned subparallel to planes that dip steeply to the southwest. The rock also possesses a linear fabric element in which the rock grains are elongated in the direction of the foliation dip. Fluid flow may occur most readily in the direction of the foliation dip because potential fracture flow paths are least tortuous (Figure 2.6). A final set of important points regards the structure of the FRI shear zone. Many individual features within the shear zone are either discontinuous or do not extend far along strike. Because of the braided fracture pattern with shear zones at Grimsel, the kakirite-bearing fracture on which we focus may not be hydrologically isolated. The presence of lamprophyres and gently-dipping fissures, features that are hydrologically important at many points in the laboratory, may also complicate the hydrology of the FRI site.

3.0. LABORATORY SEISMIC MEASUREMENTS

3.1. Introduction

The FRI geomechanical experiments were designed to sort out the effects rock properties on the propagation of seismic waves under controlled laboratory conditions. This information was in turn used to help interpret the tomographic data discussed in Chapter 4. The goals of the laboratory work were to determine the effects of

- Saturation
- Stress
- Scale
- Fracturing

on transmitted compressional and shear waves. The geomechanical tests for FRI encompassed laboratory seismic testing of intact and fractured core specimens to measure P- and S-wave velocities and amplitudes for a range of loads and saturation conditions bracketing the in-situ conditions. These data were important for the interpretation of the in-situ seismic measurements.

We were able to complete a fairly extensive study of the first two goals. For the last two goals, we were able to gain useful insight despite the problems that were encountered. To study scale effects one core sample was drilled so that the kakirite fracture was oriented along the core axis. This core was essentially rubble and could not be tested. Had testing been possible, laboratory hydromechanical and seismic measurements could have been compared with field measurements on the same fracture at a much larger scale. Quantitative interpretation of the effects of fractures on wave propagation was hampered by a high degree of heterogeneity in the rock. Even though fractured and intact samples were adjacent to one another in the core, the rock matrix in the intact core was different than the rock matrix of the fractured core. In order to overcome this problem, one fractured sample was injected with Wood's metal to "erase" the effect of

the fracture. Seismic measurements were then performed before and after the fracture had been filled with Wood's metal, a low temperature melting point metal. Tests were also conducted on an aluminum specimen of identical geometry and dimensions to serve as reference standard.

Using two sets of transducers with different center frequencies, tests were also conducted on two specimens which contained natural fractures whose planes were approximately perpendicular to the axis of the specimens, and on an intact specimen prepared from a portion of core directly adjacent to one of the fractured specimens.

3.2. Theory

The traditional approach to modelling seismic wave propagation in fractured rock has been one that treats the medium in terms of equivalent bulk properties (Crampin, 1978, 1981, 1984a,b 1985). These theories have been used to interpert the behavior of bulk P- and S- wave propagation and explain such phenomena as shear wave splitting. Recently, theoretical, (Schoenberg, 1980, 1983) and laboratory work, (Pyrak-Nolte et al., 1990) has been done to explain shear wave anisotropy by a theory which explicitly incorporates the stiffness of individual fractures. The fracture stiffness, defined as the ratio of applied stress to fracture deformation, is the only physical property of the fracture needed in the model. The fracture stiffness theory differs from effective property models such as those of Crampin in that at a fracture, or a non-welded interface, the displacement across the surface is not required to be continuous as a seismic wave passes. Stress must however remain continuous across an interface. The displacement discontinuity is taken to be linearly related to the stress through the stiffness of the discontinuity. Using this model one can describe the effect of single fractures on both the velocity and amplitude of a transmitted wave based on a single set of assumptions.

The implication of the fracture stiffness theory is that very thin discontinuities, for example fractures, can significantly affect the propagation of a wave. Seismic resolution is usually defined in terms of a ratio of the thickness of a bed or other feature to wavelength. In the stiffness theory, if the fracture stiffness is small enough, the thickness of the feature can be much less than the seismic wavelength and still be detected. The effect should be even more pronounced in an

unsaturated environment, such as at the DOE site at Yucca Mountain, Nevada, because the stiffness of an unsaturated fracture is less than that of a saturated fracture. Thus for any given size of fracture the lower limit of fracture detectability in an unsaturated fracture will be smaller than if the fracture is saturated. Alternatively, if the fracture stiffnesses are fairly uniform, it may be possible to map isolated saturated zones or perched water.

This stiffness theory is also attractive from several other points of view. Schoenberg (1980, 1983) shows that the ratio of the velocity of a seismic wave perpendicular and parallel to a set of discontinuities is a function of the spacing of the discontinuities as well as their stiffness. Thus, given the velocity anisotropy and fracture stiffness, one could determine the average fracture spacing or density. Or, alternatively, given independent information on fracture density, one could determine the fracture stiffness and hopefully relate this stiffness to fracture properties such as the extent of fracture infilling or hydraulic conductivity.

Figure 3.1a summarizes effects of a single fracture on a propagating wave as predicted by the model. To the left of the fracture in Figure 3.1a is shown the incident waveform. To the right is the transmitted waveform shown for various values of specific stiffness of the fracture. Note, the numerical values are in terms of specific stiffness divided by the acoustic impedance of the intact rock. The corresponding frequency spectra for these waveforms is shown in Figure 3.1b. As seen in the figure the effect of decreasing stiffness is to slow and attenuate the wave. The attenuation is characterized by both decreasing amplitude and filtering of the high frequency components of the waveform.

The approach to testing the fractured specimens was motivated by this stiffness model. Seismic measurements on intact and fractured specimens were therefore planned in order to obtain quantitative estimates of the properties of the fractures at the FRI test site. Since the presence of fluid affects the fracture stiffness (particularly for P-waves), saturated as well as dry tests were performed. Transducers of different center frequencies were used because of the theoretical prediction that, for a given fracture stiffness, high frequencies are attenuated more than low frequencies.

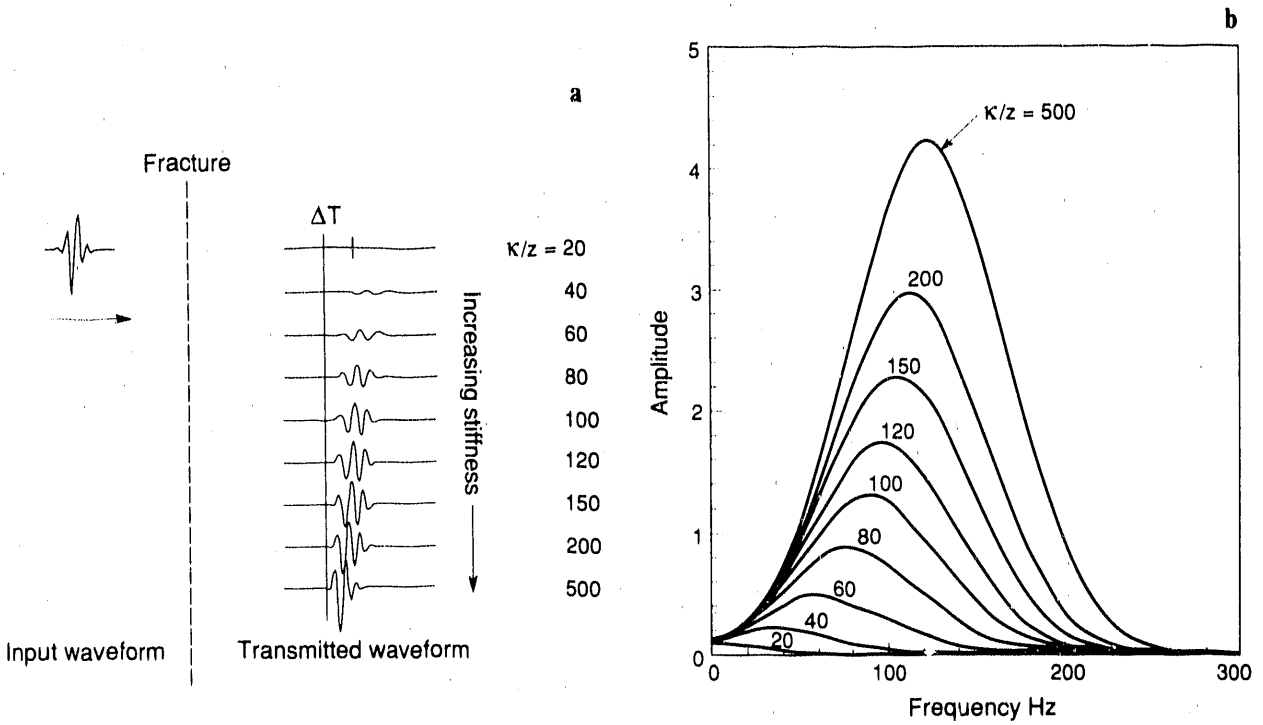

Figure 3.1. Theoretical prediction of effect of a fracture on velocity and amplitude of transmitted wave; (a) change in pulse for a range of fracture stiffness; (b) corresponding frequency spectra.

3.3. Specimen Description, Preparation

Specimens were selected from core from BOFR 87.003, which was drilled at an angle nearly perpendicular to the FRI shear zone. Three specimens were prepared: two incorporating natural fractures (specimens #1, #2 and one intact specimen #3). The locations of the centers of these specimens with respect to the borehole collar were (Figure 3.2) about 3.58 m for the intact specimen, 4.28 m for fractured specimen #1 and 4.48 m for fractured specimen #2. The pressurization interval in the FRI inflation test (see Chapter 6) was from 2.7 m to 4.2 m, but the core in this interval was broken up and no specimens containing a natural fracture suitable for laboratory testing could be obtained from the core over this interval. The specimens were 130 mm long and 116 mm in diameter, and the ends were finished so as to be parallel with a deviation of less than 0.01 mm. The fractures in specimens #1 and #2 were nearly perpendicular to the axis of the core, and were located midlength in the prepared specimens. The fractures were parallel to the foliation of the rock. Core was also provided by NAGRA from BOFR 87.004, drilled along the kakirite fracture. As discussed above, the original intention was to use specimens of the fracture from this core in a laboratory study of scale effects. Unfortunately the altered condition of the rock in, and adjacent to the kakirite fracture made it unsuitable for preparation of specimens which could be tested in the laboratory.

3.4. Experimental Equipment and Procedures

Specimens were tested under ambient conditions, oven-dried and saturated conditions. Specimens to be tested dried were first placed in an oven and were dried at a temperature of 120°C for 24 hours. This was followed by placement in a vacuum jar for a further period of 24 hours. The specimen was kept under vacuum until testing was ready to commence. Specimens to be injected with Wood's metal were also dried prior to injection. Saturation also took place in the vacuum jar, which was filled with water, and evacuated for 24 hours.

Initial tests on Specimen #1 and Specimen #3 were performed under ambient conditions as preliminary scoping tests. Before tests under more controlled conditions could be performed on Specimen #1, however, the sample was inadvertently crushed in the loading frame. Specimens

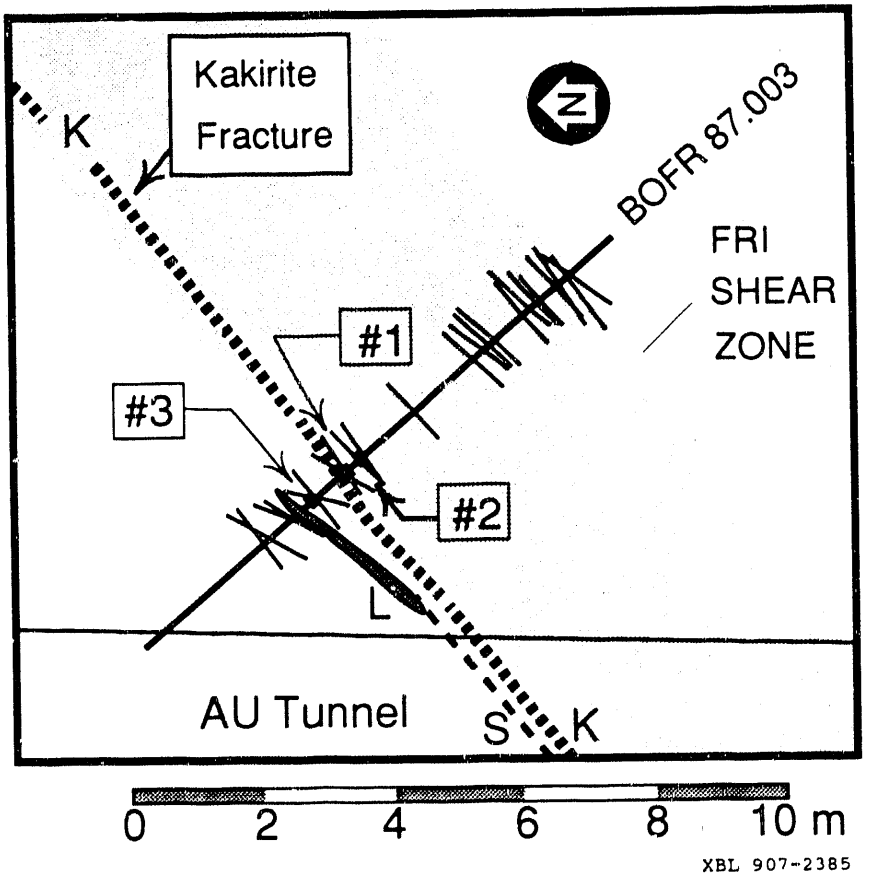

Figure 3.2. Plan view showing the location of specimens tested in the laboratory.

#2 and #3 were tested under both saturated and dry conditions; Table 3.1 lists the times and the preparation each was subjected to during the period 3/23/88 to 2/21/89.

Table 3.1. Chronology of sample conditions for laboratory seismic testing of Specimens 2 and 3.

Specimen #2 (Fractured)		Specimen #3 (Intact)	
Dried	06/28/88	Saturated	08/04/88
Saturated	07/17/88	Dried	08/07/88
Saturated	08/11-21/88	Saturated	09/21/88
Saturated	08/29-09/05/88		
Dried	09/21/88		
Saturated	09/26/88		
Heated-first	10/16/88		
Wood's metal injection			
Saturated	12/15/89		
Dried	12/27/89		
Saturated	01/05/89		
Dried	01/17/89		
Heated-second	01/18/89		
Wood's metal injection			
Dried	02/21/89		
Heated-third	02/21/89		
Wood's metal injection			

Two different sets of transducers were used: one high frequency and the other low frequency. A cross section of a low frequency transducer is shown in Figure 3.3. The two-component transducer was constructed of aluminum with a main body 114 mm in diameter. In each transducer the S-wave piezoelectric element is in direct contact with the end plate, followed by a cast iron electrode, the P-wave piezoelectric element and its electrode, a teflon spacer and finally by a rubber spacer. The entire stack is insulated from the body of the transducer by a teflon sleeve. The electrodes are accessed through the body of the transducer by an insulated banana plug connection to insure good transmission between the piezoelectric element and the endplate. The rubber spacer is compressed during assembly leading to a compressive stress in the stack of about 25 MPa. To allow injection of fluid, the design of the low frequency transducers was altered following the first Wood's metal injection test by increasing the endplate thickness from 19.0 mm (0.75 in) to 38.1 mm (1.5 in). The resonate frequency of the piezoelectric elements

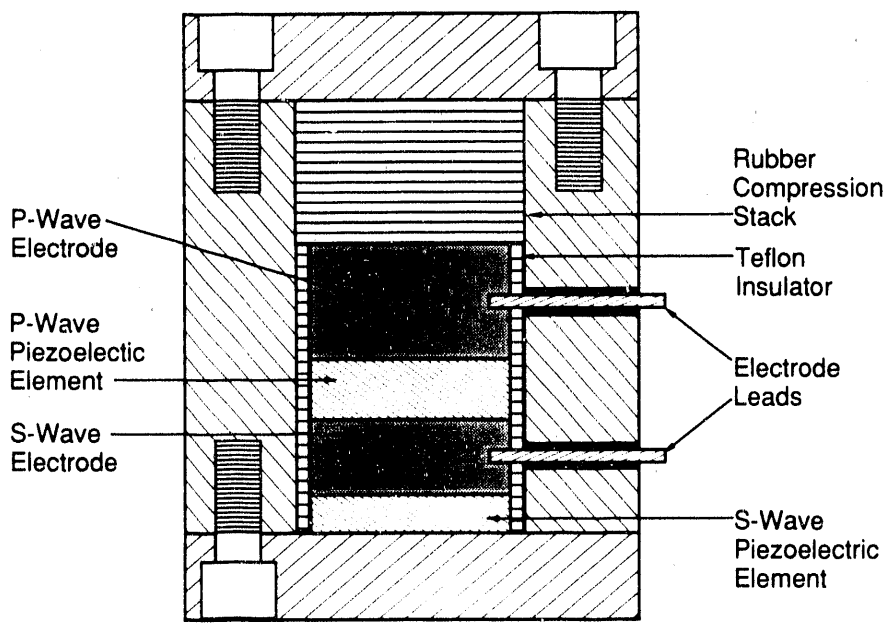

Figure 3.3. Schematic cross section of low frequency transducers used in experiments.

used in the low frequency transducers was about 150 kHz.

The high frequency transducers were constructed of steel, and are 76.2 mm in length by 50.8 mm in diameter. The resonant frequency of the piezoelectric elements is approximately 1 MHz. The crystals and the electrodes are assembled in a stack and insulated in the same manner as for the low frequency transducers.

The frequency content of the pulse generated by the transducers is affected by the construction of the transducer body, and the nature of the pulse used to excite the piezoelectric elements, as well as the resonate characteristics of the elements. The output of the transducers used in these experiments was characterized by comparing pulses from measurements on the aluminum standard using both sets of transducers. Spectra were obtained from an Fast Fourier Transform of the tapered pulses. Figures 3.4a and 3.4b show the P- and S-wave spectra for the low frequency transducers, respectively, while Figures 3.5a and 3.5b show the spectra for the high frequency transducers, respectively. It can be seen that the frequencies of the peak spectral amplitudes for the low frequency transducers is about 475 kHz for P-waves and 400 kHz for S-waves while for the high frequency transducers, they are about 900 kHz for P-waves and 750 kHz for S-waves.

Seismic measurements were made over a range of axial stresses for all specimens. For some tests, as discussed below, a manifold was placed around the specimen. Otherwise the experimental set-up was as schematically illustrated in Figure 3.6. Specimens were placed in the load frame with the axis oriented vertically, the transmitting transducer above the receiving transducer below the specimen. Contact surfaces between the transducers and the specimen were cleaned with isopropyl alcohol, and a lead foil disk (0.05 mm thick) was placed between them to reduce transmission losses due to poor contact. An axial stress of 1.9 MPa was applied prior to initiation of measurements to produce good contact between transmission surfaces. The axial stress was then increased to a target level and P- and S-wave pulses digitized. This sequence was repeated until the maximum stress level was achieved, and again, during unloading.

The energy for the transmitted signal is provided by a Velonex 350 High Power Pulse Generator. A broad band pulse with a peak voltage of 1 KV and a pulse width of 3 μs was used for

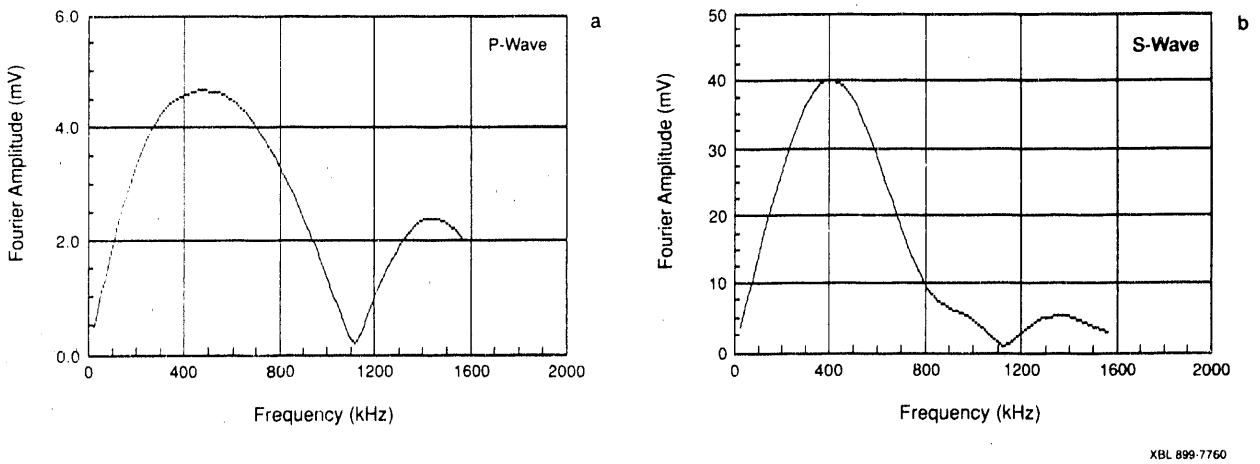

Figure 3.4. Spectra for a test on the aluminum standard using low frequency transducers; (a) P-wave spectrum; (b) S-wave spectrum.

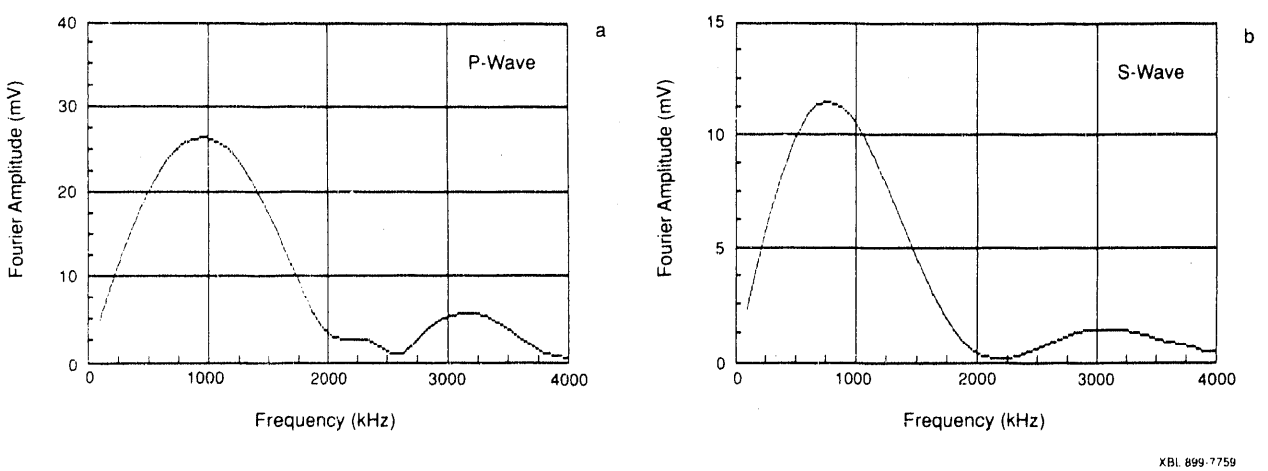

Figure 3.5. Spectra for a test on the aluminum standard using high frequency transducers; (a) P-wave spectrum (b) S-wave spectrum.

both the low frequency and the high frequency transducers. Data acquisition was performed with a LeCroy 8013A mainframe with an installed TR8818 Transient Recorder system. The TR8818 is a digitizer designed for high speed, long record waveform recording, which converts an analog input signal into 8-bit digital words at sampling frequencies from 0.01–100 MHz. The TR8818 was used with Waveform-Catalyst, a multichannel digital oscilloscope software package intended for use on IBM personal computers. The Waveform-Catalyst program allows acquisition, averaging, and analysis of waveforms and was used for all experiments.

The sampling frequency for tests using the low frequency transducers was 6.25 MHz, yielding a Nyquist frequency of 3.125 MHz. When the high frequency transducers were used, the sampling frequency was 25 MHz, yielding a Nyquist frequency of 12.5 MHz. Typically 20 waveforms were averaged at each stress level.

The apparatus shown schematically in Figure 3.7 was used for the Wood's metal injection tests. The specimen was first dried, and then was placed in the pressure vessel. The main body of the vessel was centered on the fracture, and the fracture was sealed off with Viton O-rings retained by aluminum compression rings. The specimen was then placed in the load frame as previously described, and a set of waveforms was sampled at a set of prescribed loads. The specimen was then placed under an axial stress of 5.72 MPa (60 kN axial load). Strip heaters were placed around the body of the pressure vessel and the transducers, and the body of the vessel was heated. The vessel was heated to a temperature of 120°C, and the transducers to 90°C to prevent loss of the heat through the ends of the specimen. These conditions were maintained for at least two hours to insure uniform heating of the specimen. At the time of injection, liquid Wood's metal was pressurized to 2 MPa, and injected into the fracture. Once flow was detected through the valve on the opposite site of the vessel, both the injection and the outlet valve were closed. The heaters were turned off, and the specimen was allowed to cool for 24 hours with the axial pressure remaining at 5.72 MPa. Waveforms were then taken as the load on the specimen was cycled. The pressure vessel was installed on all specimens to be injected with Wood's metal, or whose waveforms were to be compared with those specimens to be injected with Wood's metal.

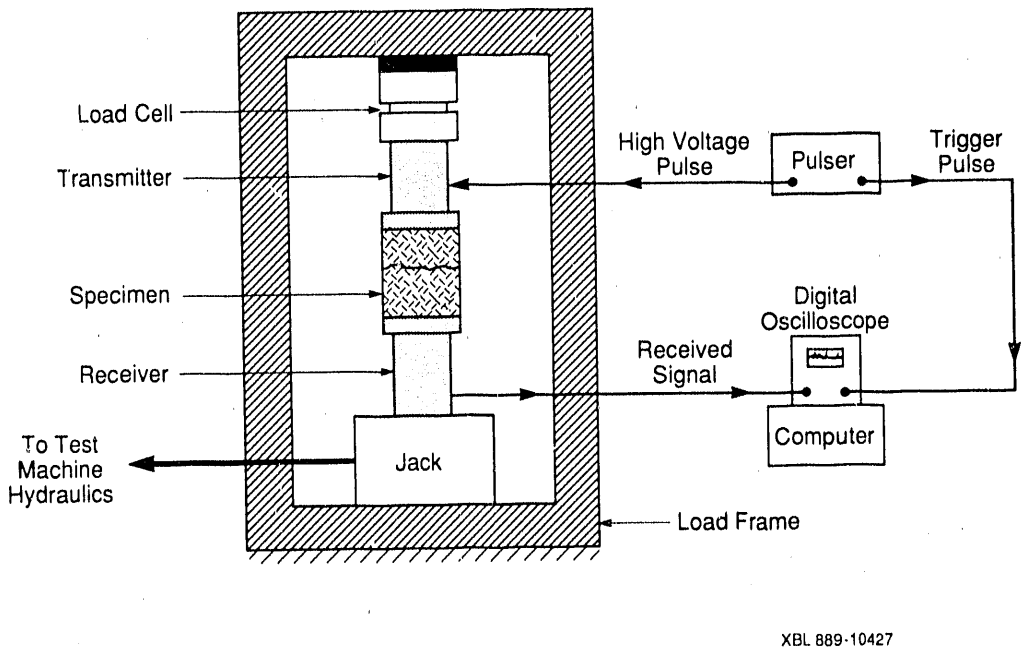

Figure 3.6. Schematic illustration of experimental setup for seismic measurements.

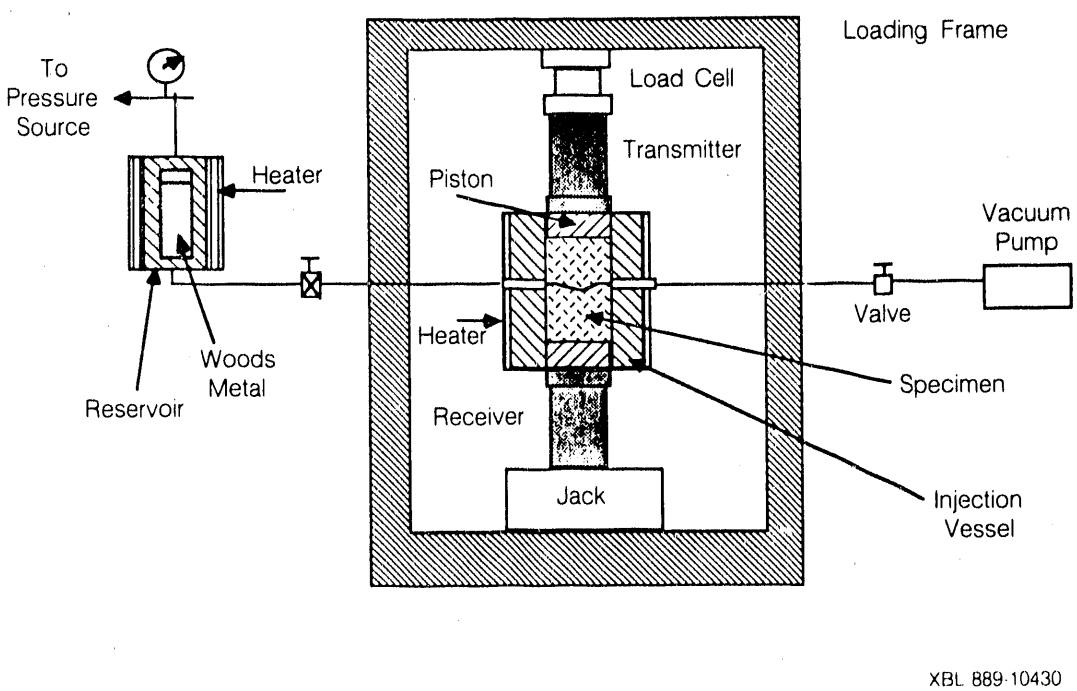

Figure 3.7. Schematic illustration of apparatus for measurements with Wood's metal injection.

A manifold similar to that illustrated in Figure 3.7 was placed around the specimen for tests on the fractured specimens under saturated and dry conditions using the low frequency transducers. All tests using the high frequency transducers were performed without a manifold, as shown in Figure 3.6. In this case, to prevent fluid loss, the saturated samples were wrapped with foil.

3.5. Results of Laboratory Measurements

Examples of typical P- and S-wave waveforms for each of the various test conditions are given in Figures 3.8 – 3.15. For each figure the first arrival pick and the corresponding travel time through the sample is shown. Some of the waveforms are quite disturbed, due to their low amplitudes, making it difficult to accurately determine the first arrival. This data was included, however, because it demonstrated the effect on attenuation of changing conditions in the same rock. It was important to show that changing some conditions resulted in increased attenuation even though the poor data made the change difficult to quantify. For tests yielding disturbed waveforms, picks were made by visually comparing all the waveforms from the test to identify features which were consistent from one measurement to the next.

Velocities were calculated, and peak-to-peak amplitudes of the first arrivals were recorded for waveforms taken during the experiments. These were plotted with respect to the axial load (1 kN corresponds to 9.5×10^{-2} MPa). Peak to peak amplitudes were used to describe attenuation because they were the most readily obtainable data. Experience has shown that peak to peak amplitudes show, to a first order, the same trends as more sophisticated spectral analysis. Also, the quality of some of the data did not warrant the additional time needed to perform spectral analysis. The amplitude of only the first arriving pulse was used to minimize effects of contamination of the waveform by reflections arising from the sample geometry. Dotted lines have been added by hand to help delineate trends in the data.

The results are organized first (Section 3.5.1) to illustrate the effects of saturation on velocities and amplitudes from tests using both the low and high frequency transducers. Amplitudes of tests employing different transducers could not be compared. In Section 3.5.2 data is replotted in order to illustrate the effects of a single fracture on velocities and amplitudes under the various

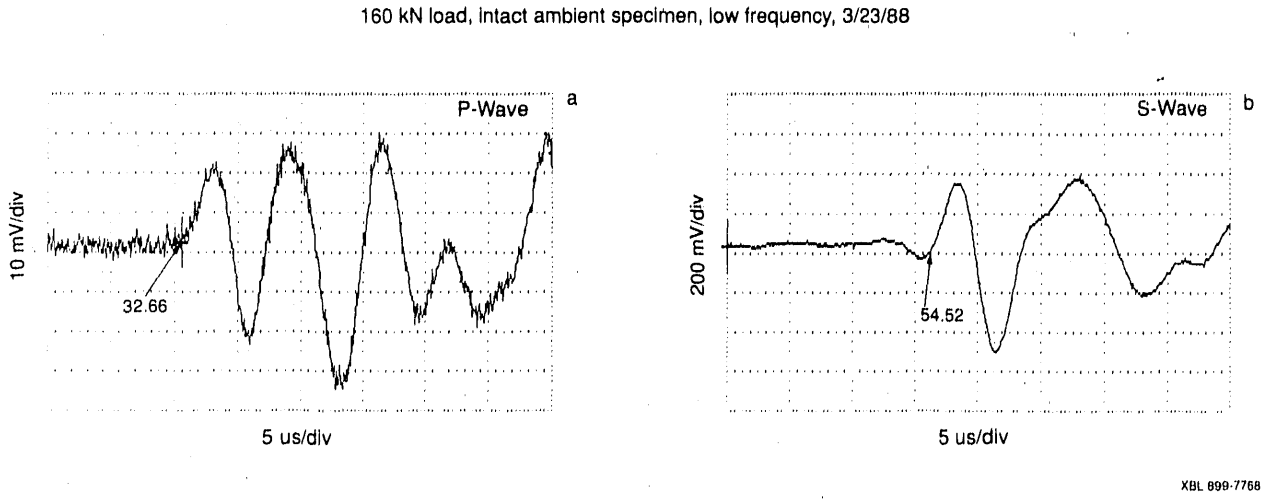

Figure 3.8. Example waveforms for intact specimen, ambient conditions, low frequency transducers, 160 kN load level, total travel time of first arrival in μs; (a) P-wave (b) S-wave.

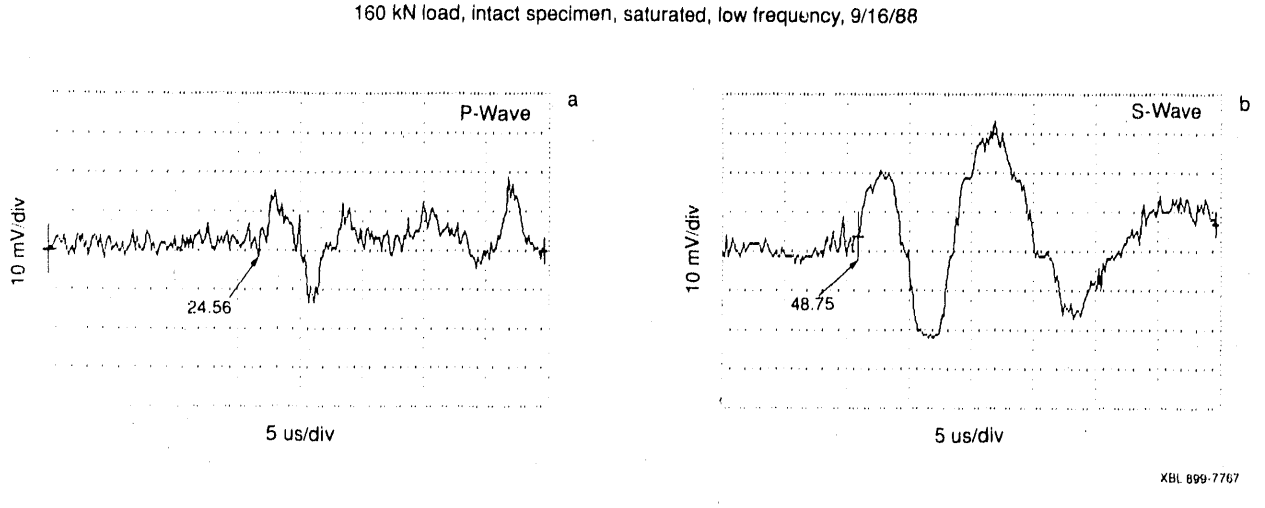

Figure 3.9. Example waveforms for intact specimen, saturated conditions, low frequency transducers, 160 kN load level, total travel time of first arrival in μs; (a) P-wave (b) S-wave.

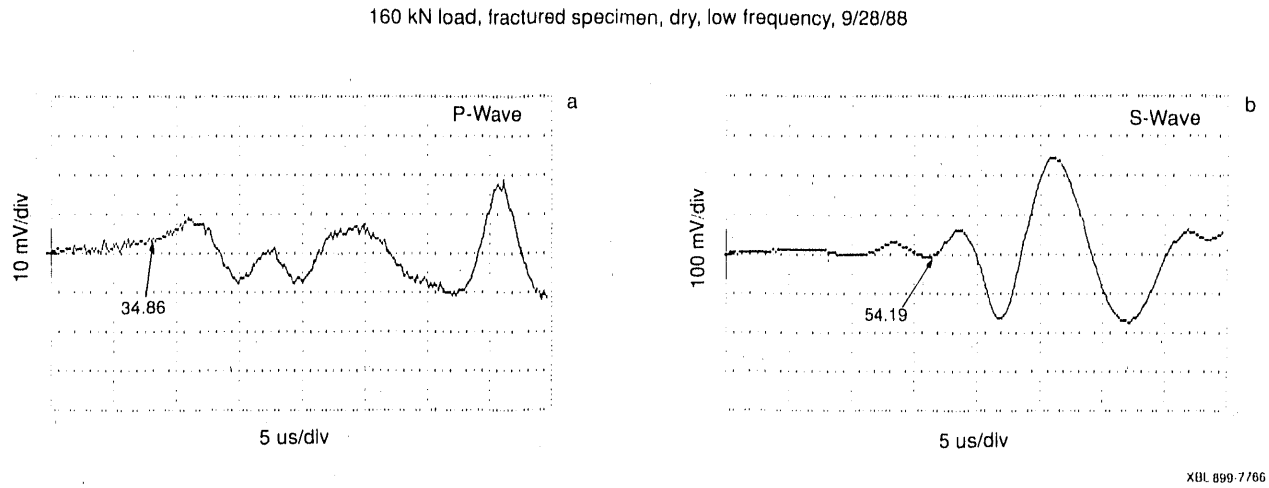

Figure 3.10. Example waveforms for fractured specimen, dry conditions, low frequency transducers, 160 kN load level, total travel time of first arrival in μs; (a) P-wave (b) S-wave.

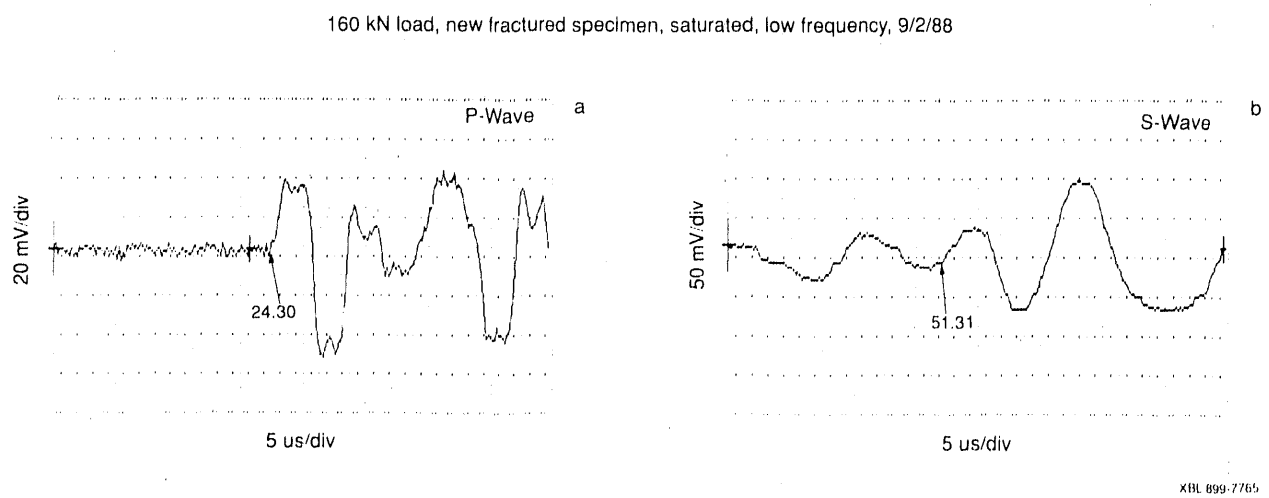

Figure 3.11. Example waveforms for fractured specimen, saturated conditions, low frequency transducers, 160 kN load level, total travel time of first arrival in μs; (a) P-wave (b) S-wave.

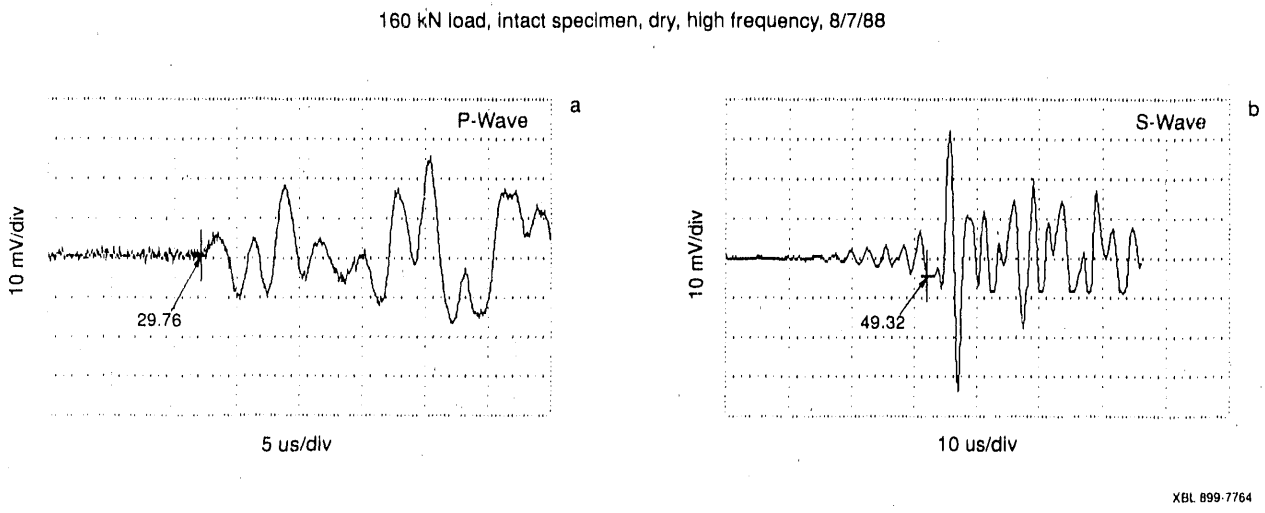

Figure 3.12. Example waveforms for intact specimen, dry conditions, high frequency transducers, 160 kN load level, total travel time of first arrival in μs; (a) P-wave (b) S-wave.

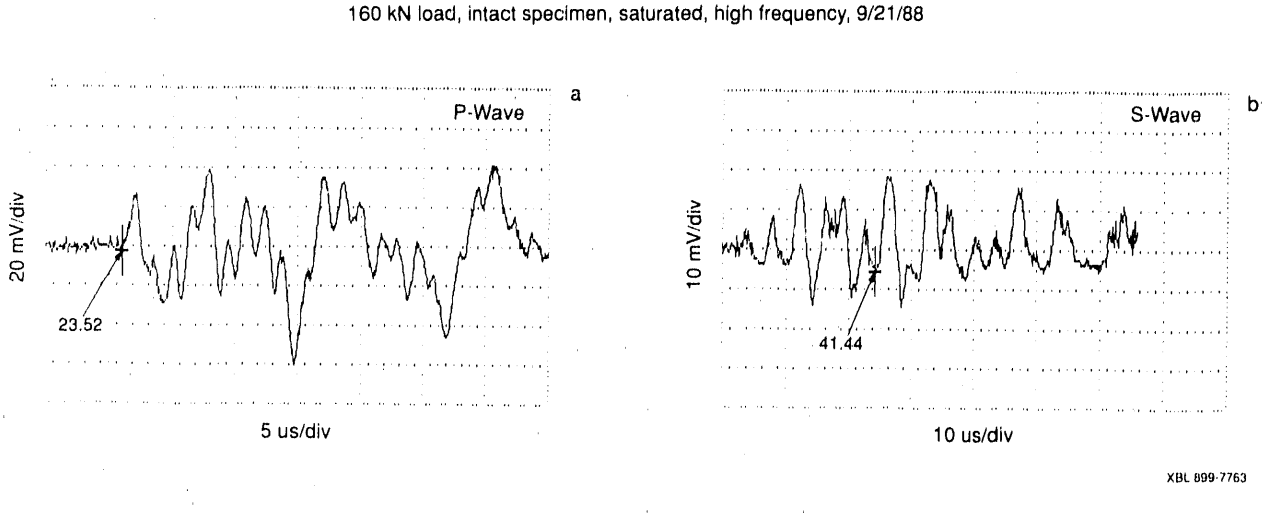

Figure 3.13. Example waveforms for intact specimen, saturated conditions, high frequency transducers, 160 kN load level, total travel time of first arrival in μs; (a) P-wave (b) S-wave.

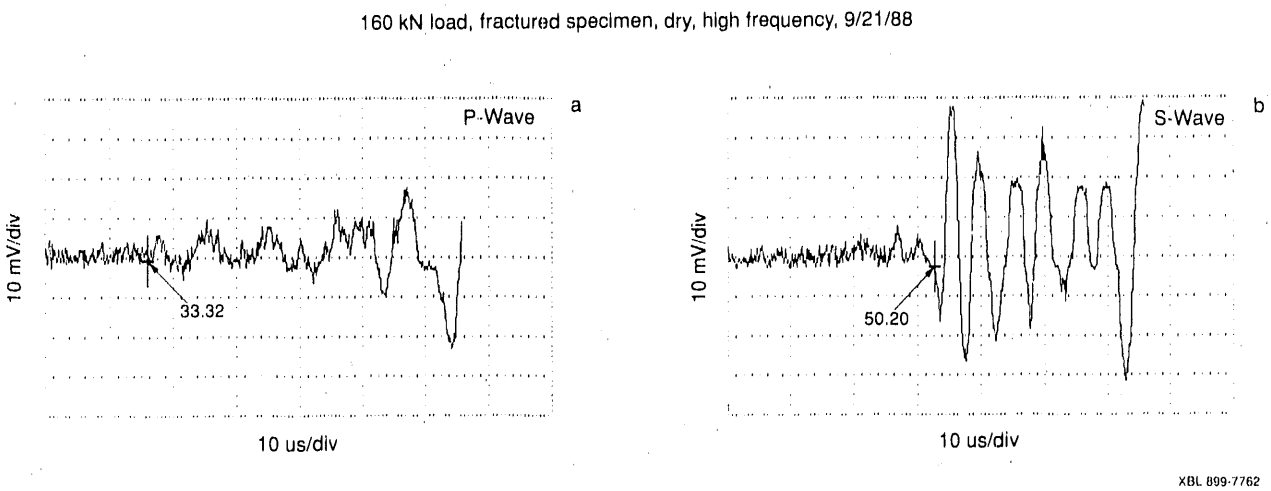

Figure 3.14. Example waveforms for fractured specimen, dry conditions, high frequency transducers, 160 kN load level, total travel time of first arrival in μs; (a) P-wave (b) S-wave.

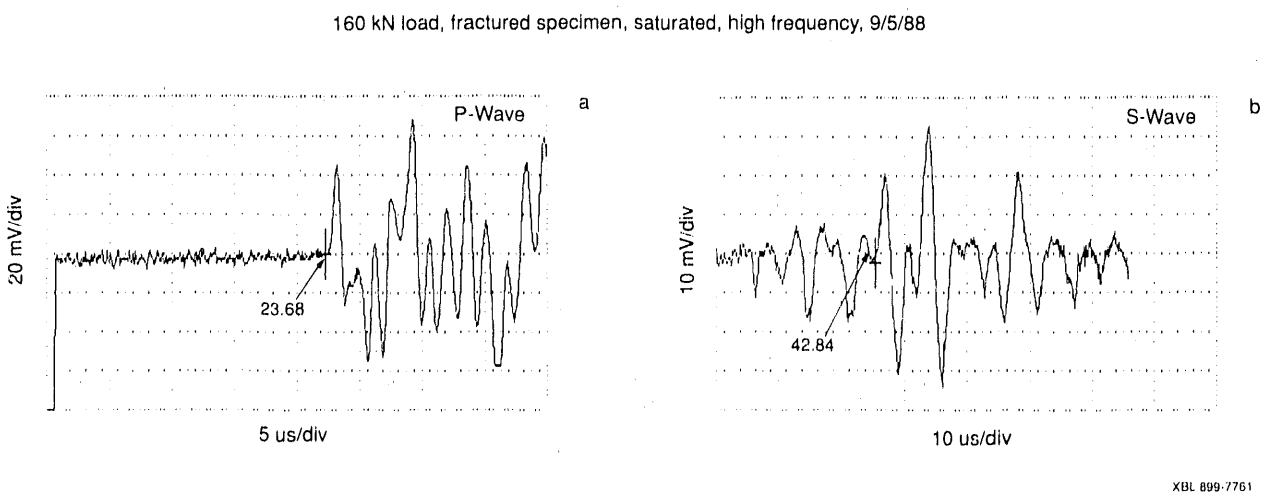

Figure 3.15. Example waveforms for fractured specimen, saturated conditions, high frequency transducers, 160 kN load level, total travel time of first arrival in μs; (a) P-wave (b) S-wave.

test conditions. Heterogeneity in the rock introduced ambiguity in the comparison of results from fractured and intact specimens, so a test was performed in which one of the specimens was injected with Wood's metal. Comparison of seismic attenuation before and after Wood's metal injection are presented in Section 3.5.3.

3.5.1. Effects of Saturation

Velocity Data. P- and S-wave velocities at low frequency for intact specimen #3 under ambient and saturated conditions are shown in Figures 3.16a and 3.16b, respectively. The velocities increased with increasing load for both ambient and saturated conditions, reflecting the closure of cracks in the matrix of the rock. The effect is pronounced, particularly for ambient conditions, probably because the foliation of the sample is perpendicular to the direction of the loading.

Though the ambient condition specimen was not vacuum or oven dried, a difference in both the P- and S-wave velocities for ambient and saturated conditions is apparent. This difference between the ambient and saturated velocities is particularly pronounced for the P-wave. Under saturated conditions the P-wave velocities under 40 kN load was 5100 m/s, approximately 1500 m/s higher than for dry conditions. At 150 kN load the difference is approximately 1000 m/s. The saturated P-wave velocity appears to asymptote in the region of 5700 m/s. The ambient P-wave velocity, beginning at 3000 m/s at 25 kN load, rises to 4500 m/s at 150 kN load. At a load where all cracks are fully closed, the velocities should asymptote towards the same value. The S-wave velocities display the same behavior; velocities increase with increasing axial load for both ambient and saturated conditions. Saturated S-wave velocities begin at 2400 m/s at 10 kN, increasing to 2700 m/s at 150 kN, and asymptoting to approximately 2800 m/s. The ambient S-wave velocity begins at 2250 m/s at 20 kN load, increasing to 2650 m/s at 150 kN load.

The fractured specimen, specimen #2, exhibited similar behavior. Velocities increased with increasing load, with the P-wave velocity behavior corresponding particularly well with the behavior in the intact specimen. Figure 3.17a shows the velocities for the P-wave for two experiments with specimen #2 oven dried and saturated. The data is remarkably similar considering the

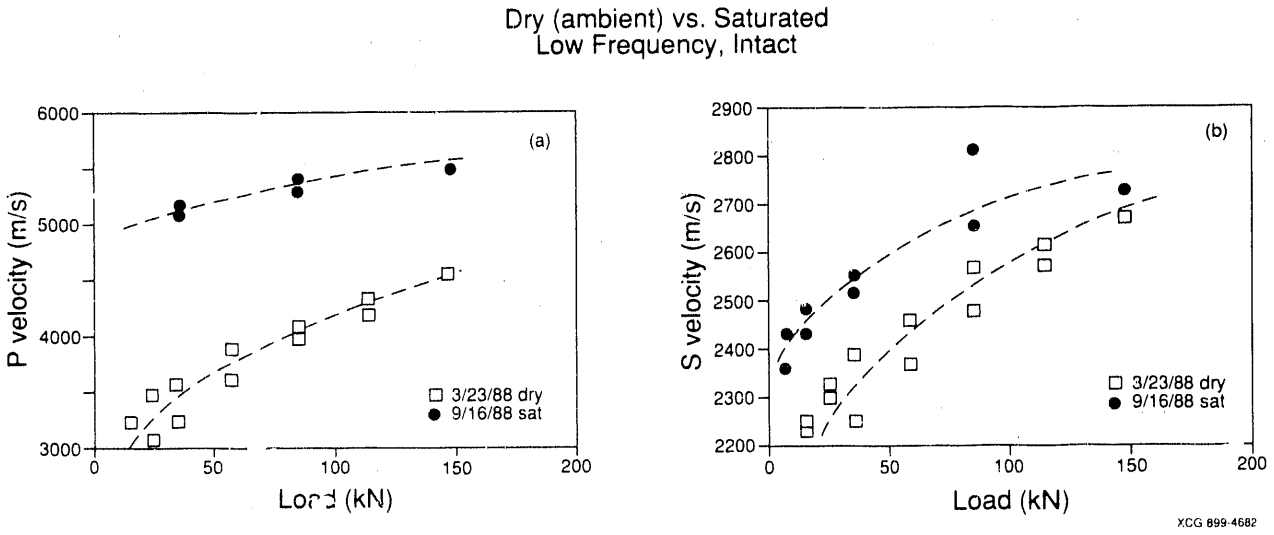

Figure 3.16. Comparison of velocities for ambient and saturated conditions, intact specimens, low frequency transducers; (a) P-wave; (b) S-wave.

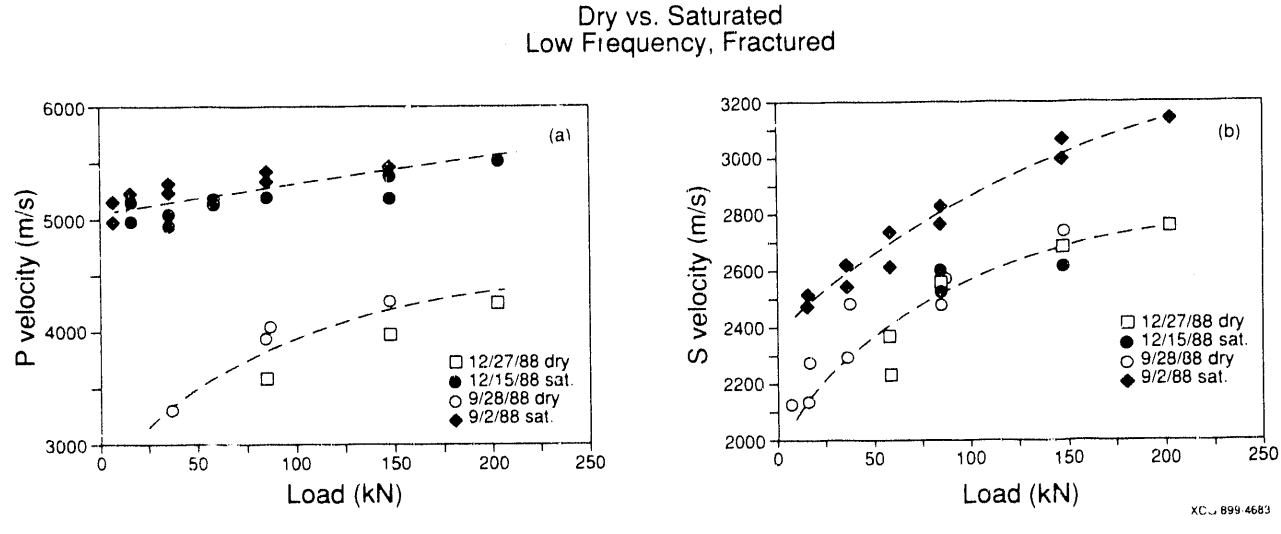

Figure 3.17. Comparison of velocities for dry and saturated conditions, fractured specimens, low frequency transducers; (a) P-wave; (b) S wave.

length of time between tests and that the transducers were modified in the interval between 9/28/88 and 12/15/88. S-wave velocities were not as easily interpreted, in part due to the difficulty of determining the first arrival of the wave in many cases. This may account for the anomalous nature of the 12/15/88 saturated velocity data in Figure 3.17b. Except for this, Figure 3.17 shows that both P- and S-wave velocities were higher under saturated conditions.

The general trend shown by the results from velocity measurements using the low frequency transducers is that saturation has an effect on both P- and S-wave velocities, yielding higher values for both types of wave, although the effect on the P-wave is the largest. The difference diminishes with increasing axial stress. For P-waves this behavior can be ascribed to the effects of microcracks on the modulus of the rock; the modulus would be expected to increase with both saturation and or increased axial stress. For S-waves, increasing velocity would also result from microcrack closure as axial stress increased. However, saturation, by conventional models, should not affect the shear modulus. The results also show that the effect of the single fracture on velocities for these specimens under either the intact or saturated conditions did not dominate in this rock type.

P- and S-wave velocities for the intact specimen under dried and saturated conditions using the high frequency transducers are plotted in Figures 3.18a and 3.18.b, respectively. The P-wave velocities for the dry condition are considerably less than for the saturated condition. For dry conditions, the velocities begin at 3500 m/s at 50 kN and increase with load to 4700 m/s at 150 kN, while for the saturated condition, values range from 4900 m/s to 5600 m/s, respectively. For the range of loads used in the test, velocities for the dry and saturated conditions asymptote to 5100 m/s and 5800 m/s, respectively. S-wave velocities behave similarly; the dry velocities beginning at 2250 m/s at 20 kN load and increase to 2800 m/s at 150 kN; the values for the saturated condition 2650 m/s to 3100 m/s, respectively. The saturated velocity asymptotes to 3200 m/s, and the dry velocity to about 3000 m/s. These values are uniformly higher than those obtained using the low frequency transducers. It is also interesting to note that the difference between day and saturated are larger for the high frequency S-waves than for low frequency S-

waves, especially at higher loads.

Figures 3.19a and 3.19b are high frequency P- and S-wave velocities, respectively, for the fractured specimen under dry and saturated conditions. Velocities for the dry fractured specimen appear to be a linear function of load for both the P- and S-waves. Saturation results in a pronounced increase in both P- and S-wave velocities. P-wave velocities for the fractured specimen under saturated conditions are similar to those for low frequencies (see Figure 3.16a), but S-wave velocities are 400 m/s higher at 20 kN load, and 100 m/s higher at 150 kN load.

Results of tests using high frequency transducers were similar to those of the low frequency transducer in that velocities under saturated conditions are typically higher than those for the dried condition.

Amplitude Data. Peak-to-peak amplitude data for measurements made using low frequency transducers are shown in Figures 3.20–3.21. Figures 3.20a,b and 3.21a,b compare amplitudes for the fractured specimen in dry and saturated conditions. Figures 3.20a and 3.20b present data prior to modifications on the low frequency transducers (Section 3.4) while Figures 3.21a and 3.21b present data after modifications. The figures show that amplitudes increase as axial load increases, which is a reflection of the influence of the microcracks. As the microcracks are closed at higher stresses, less attenuation is expected. Figure 3.20a shows that saturating the specimen resulted in increases in P-wave amplitudes of 2-4 times. Comparison with Figures 3.20a and 3.21a show that the P-wave data obtained at a later date exhibited the same trend but there was less difference between amplitudes for dry and saturated conditions in the later tests.

The effect of saturation on S-wave amplitudes for the fractured specimen is shown in Figures 3.20b and 3.21b. The behavior of the S-wave amplitudes is quite different from that of the P-wave amplitudes. The S-wave amplitudes under dry conditions increase with axial stress much more rapidly than those under saturated conditions. Thus, at low loads, the S-wave amplitudes under dry conditions were equal or less than those under saturated conditions, but under high loads they were much greater than the amplitudes under saturated conditions. Note the similarity in the S-wave amplitude trends shown in Figures 3.20b and 3.21b even though the tests were

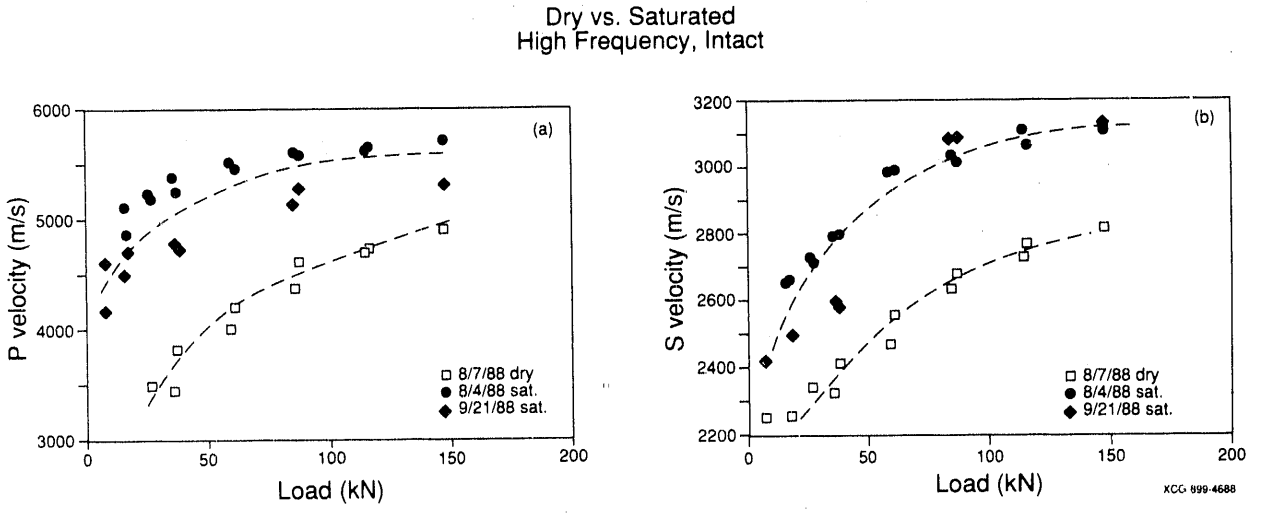

Figure 3.18. Comparison of velocities for dry and saturated conditions, intact specimens, high frequency transducers; (a) P-wave; (b) S-wave.

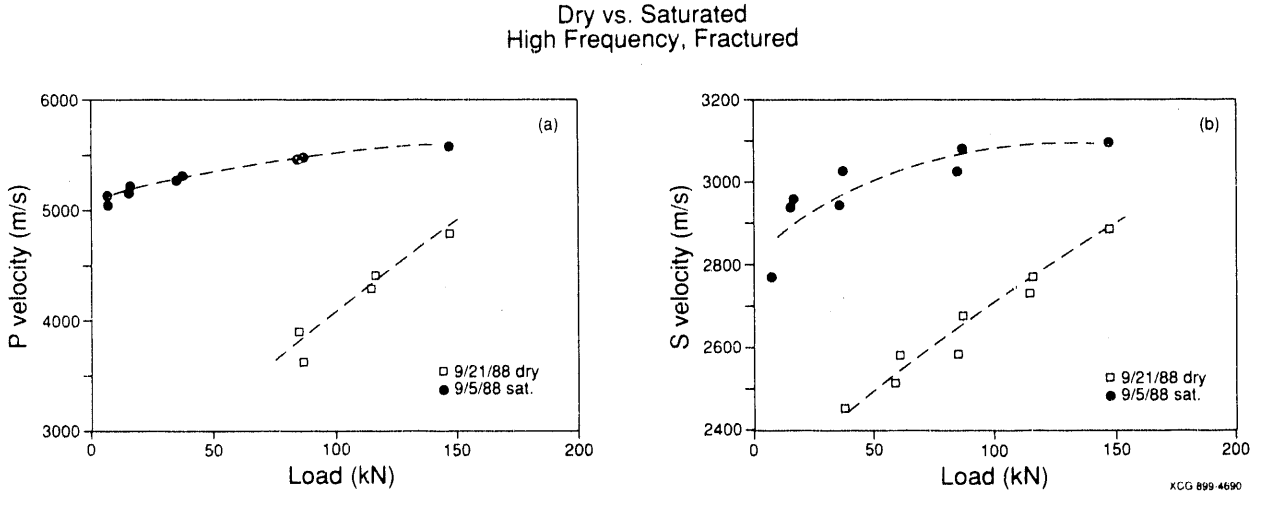

Figure 3.19. Comparison of velocities for dry and saturated conditions, fractured specimens, high frequency transducers; (a) P-wave (b) S-wave.

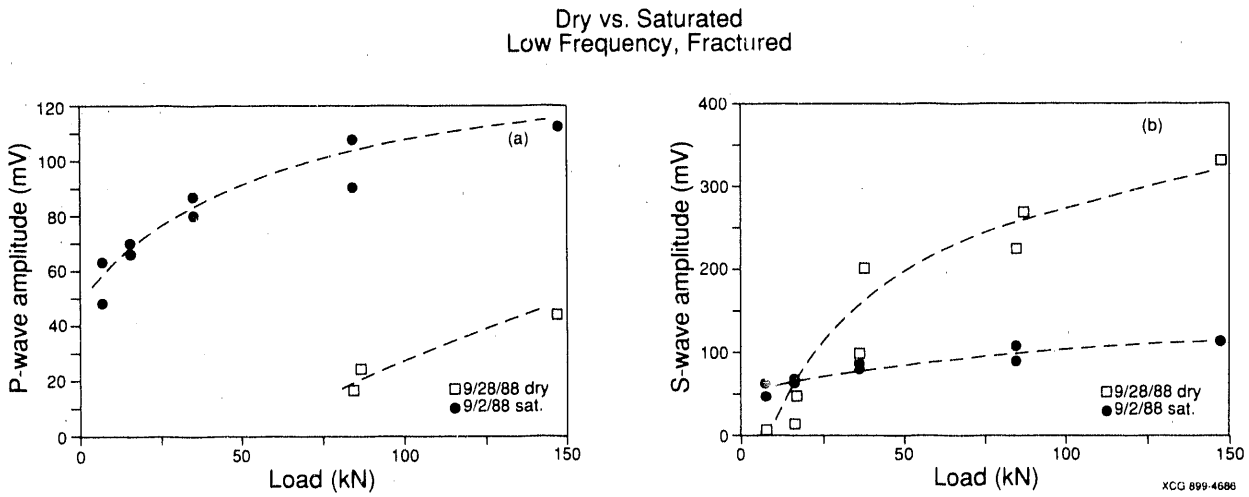

Figure 3.20. Comparison of peak to peak amplitudes for dry and saturated conditions, fractured specimen, low frequency transducers; (a) P-wave (b) S-wave.

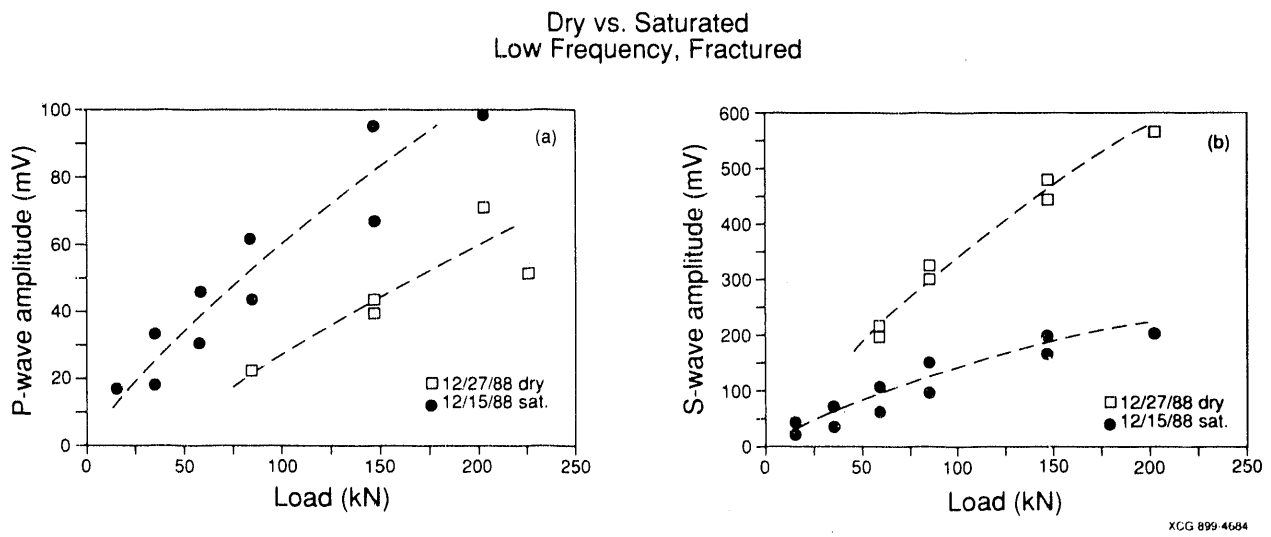

Figure 3.21. Comparison of peak to peak amplitudes for dry and saturated conditions, fractured specimen, low frequency transducers after modifications; (a) P-wave (b) S-wave.

separated in time by a considerable amount and the transducers had also been rebuilt.

Peak to peak amplitude data for measurements made using high frequency transducers are shown in Figure 3.22 and 3.23. Figures 3.22a and 3.22b compare P- and S-wave amplitudes for the fractured specimen under dry and saturated conditions. The observed trends are very similar to those obtained using the low frequency transducer. Figures 3.23a and 3.23b compare P- and S-wave amplitudes for the intact specimen under dry and saturated conditions. Here, again it is seen that the P- wave amplitudes obtained under saturated conditions are larger than those for the dry conditions, and in both cases amplitudes increase roughly linearly with increasing load. For S-waves, however, while the amplitudes of the dry test increase nearly linearly with load, the amplitudes from the saturated test tend to asymptote toward a constant level, lower than that of the dry test, at higher loads. These trends are very similar to those observed for the fractured sample.

3.5.2. Comparison of the Fractured and Intact Samples

Both the velocity data and peak to peak amplitude data collected under the various test conditions were replotted to compare results from fractured and intact specimens. This technique had previously been used successfully (Pyrak-Nolte et al. 1990) to demonstrate the effect of a single fracture on wave propagation. Based on this previous work it was anticipated that velocities in the fractured specimens would be slightly less than or nearly equal to those in intact specimens. Significant differences between amplitudes, however, were expected. In particular, the previous work indicated that amplitudes of both P- and S-waves in the fractured specimens should be less than those in the intact specimens. This difference should diminish as load is increased for both P- and S-waves and, for P-waves, the difference should also diminish under saturated conditions.

Results from comparisons of data for fractured and intact specimens of the FRI core were ambiguous. For several tests there was very little difference between velocities for the fractured and intact specimens, while, for other tests the velocity in the intact specimen was higher. Similarly, the amplitude of waves transmitted through the fractured sample were actually larger than

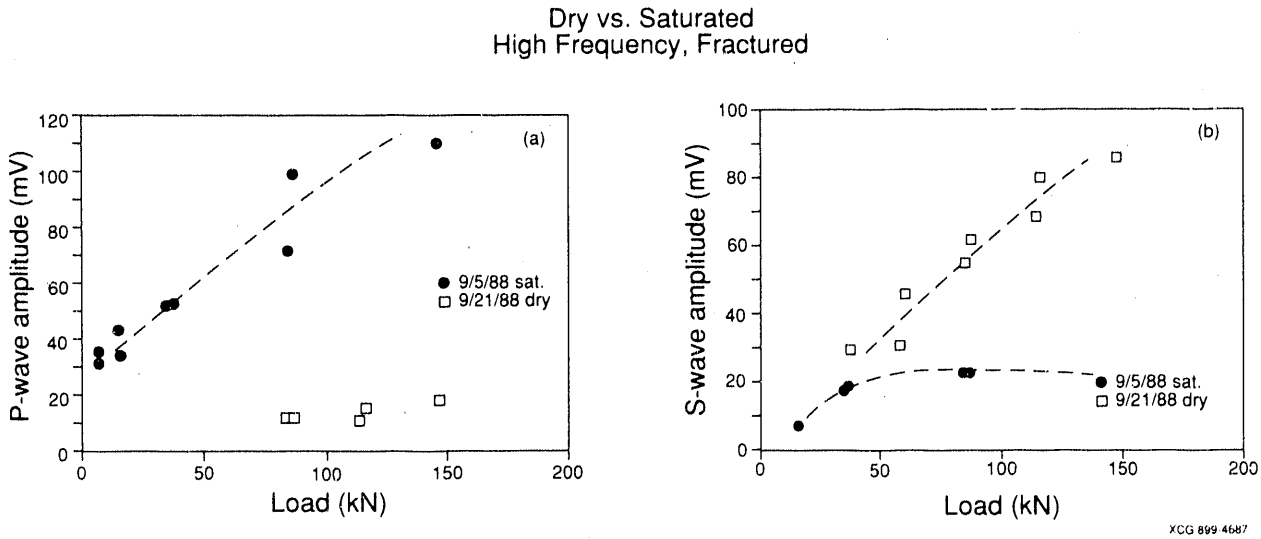

Figure 3.22. Comparison of peak to peak amplitudes for dry and saturated conditions, fractured specimen, high frequency transducers; (a) P-wave (b) S-wave.

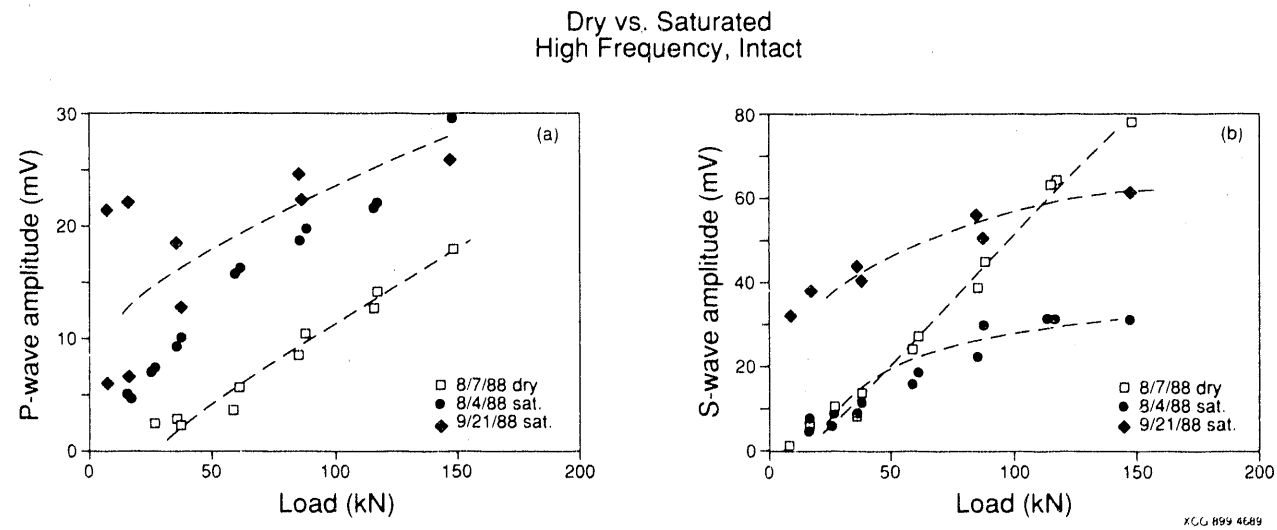

Figure 3.23. Comparison of peak to peak amplitudes for dry and saturated conditions, intact specimen, high frequency transducers; (a) P-wave (b) S-wave.

those transmitted through the intact specimens, in some tests, while in others the peak to peak amplitudes for this intact specimen were higher.

It is believed the main cause for the ambiguity may have been the bands of strong foliation which were present to varying degrees in each specimen. Adjacent to the fracture these bands of foliation were schistose in character. A comparison between a fractured and an intact specimen is only meaningful if the properties of each specimen are identical except for the presence of the fracture. The small scale of the heterogeneity in the rock and the presence of schistosity close to the fractures made it very difficult to meet these conditions.

The Wood's metal test, described in the next section was performed to evaluate the effects of fractures from tests on only one sample, thereby eliminating ambiguity due to differences in intact rock properties between samples.

3.5.3. Spectral Analysis of the Fractured Specimen before and after Wood's Metal Injection

Records of P- and S-wave pulses were taken for fractured specimen #2 prior to, and after injection of Wood's metal as the load was cycled. In addition, waveforms of an aluminum specimen of identical dimensions were also taken to be used in a spectral ratio analysis. The spectral ratio analysis was made necessary because heating the transducers altered the spectral content of the source pulse. Had this not occurred a direct comparison between results before and after Wood's metal injection would have been possible.

P-and S-wave pulses for both the fractured and aluminum specimen were first tapered. After trying several different tapers, boxcar tapers were selected for both P- and S-waves. Though boxcar tapers can introduce spurious spectral content, particularly in the high frequencies, for this data the boxcar taper resulted in improved spectra than tapers of other shapes. A window length of 3.04 μs was used for P-waves and 7.20 μs was used for S-waves. Spectra were then obtained by performing an FFT.

A spectral ratio analysis was performed to evaluate the attenuation in the fractured specimen before and after Wood's metal inspection. In this method, the amplitudes of the transmitted

waves are assumed to take the form

$$A_i(f) = G_i(x)\, e^{-\alpha_i(f)} e^{i(2\pi ft - kx)} \tag{3.1}$$

where x is the length of the wave path, G(x) is a factor incorporating the effects of the geometry of the specimen (such as spreading of the wave and reflections), f is the frequency of interest, k is the wavenumber, t is the time and $\alpha(f)$ is the attenuation coefficient. If the same test is run on a second specimen (which could be a reference aluminum specimen), the ratio of amplitudes from the two measurements is given by:

$$\frac{A_i}{A_j} = \frac{G_i}{G_j}\, e^{-(\gamma_i - \gamma_j)fx} \tag{3.2}$$

in which it is assumed that $\alpha(f) = \gamma f$. If the natural logarithm of both sides of (3.2) is taken, the resulting equation is

$$\ln \frac{A_i}{A_j} = (\gamma_j - \gamma_i)\, fx + \ln\left(\frac{G_i}{G_j}\right) \tag{3.3}$$

where $\gamma = \frac{\pi}{Qc}$ and c is the phase velocity of the medium. For a high Q reference material γ_i is very small, and can, to the first order, be neglected. In addition for specimens of identical geometry, G(x) are identical, and their ratio is unity. Under such assumptions Equation (3.3) can be used to determine the attenuation coefficient of the material of unknown properties, since $\frac{1}{Q}$ is the slope of the graph of the log amplitude ratio vs. frequency. In the special case where α is not a function of frequency, the slope of the line is constant.

Plots comparing spectral ratios at different axial load levels before and after Wood's metal injection are shown in Figures 3.24a,b,c and 3.25a,b,c, for P- and S-waves, respectively. The load levels refer to the load applied to the rock. The aluminum reference spectrum for the plot labeled 120 kN consisted of the average of two spectra obtained at loads of 80 kN and 160 kN. For the plot labeled 320 kN, the aluminum reference spectrum was obtained at 300 kN load.

The first characteristic of these curves to be noted is that, typically, for the results before injection, there is a discontinuity in slope, in the range of about 450 kHz to 650 kHz for P-waves,

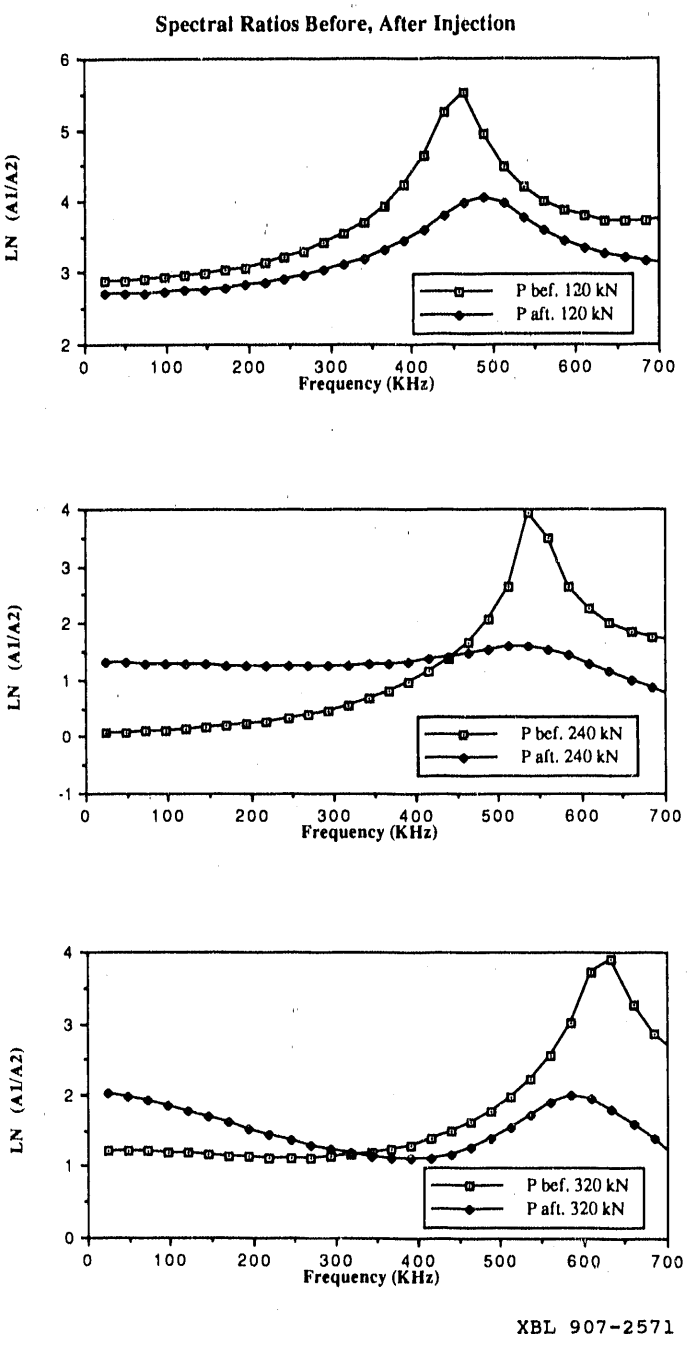

Figure 3.24. Comparison of log spectral ratios for P-waves before and after Wood's metal injection at axial loads of (a) 120 kN, (b) 240 kN, and (c) 320 kN.

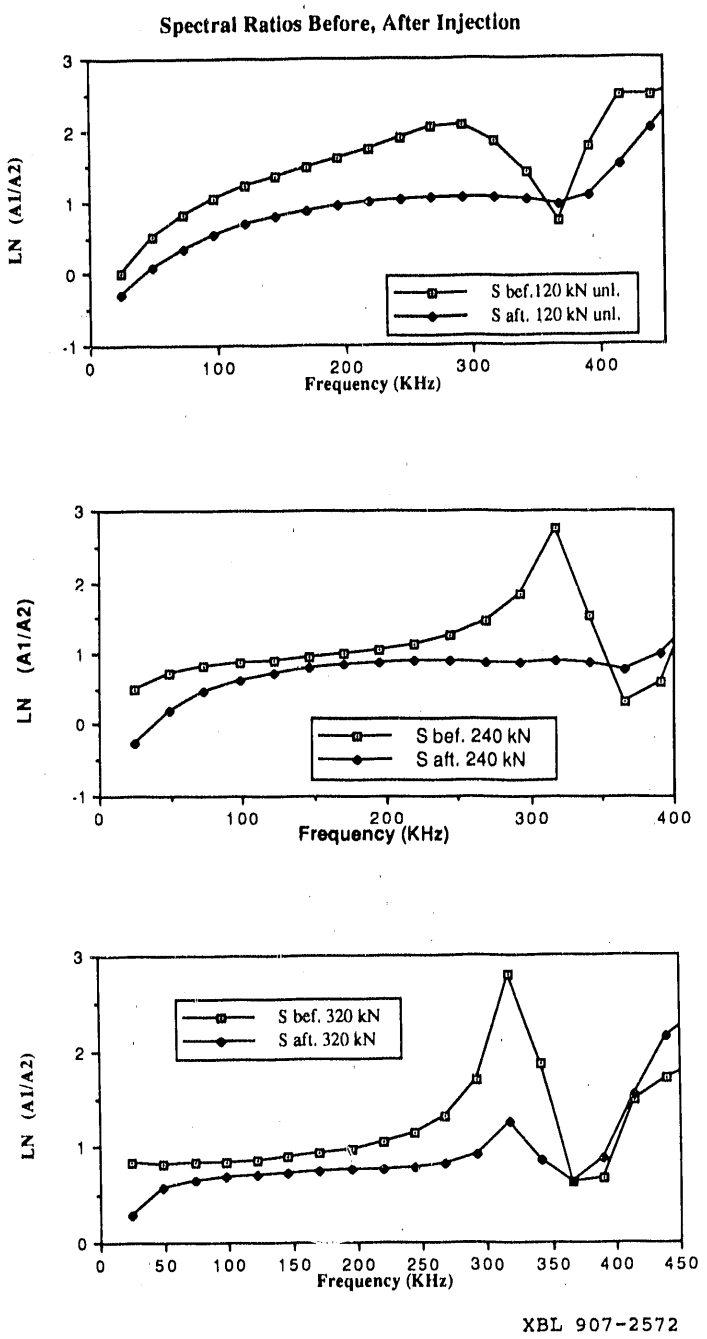

Figure 3.25. Comparison of log spectral ratios for S-waves before and after Wood's metal injection at axial loads of (a) 120 kN, (b) 240 kN, and (c) 320 kN.

and about 250 kHz to 350 kHz for S-waves. The frequency content of the first arrival is represented by the region to the left of this slope change; to the right of the change there is very little energy in the spectrum, so values of spectral ratio are not considered to be physically meaningful.

The second general characteristic is that the curves are non-linear. This means that the Q of the rock, represented by the inverse of the slope of the curves, is a function of frequency. Comparison of curves before and after Wood's metal injection at any of the loads shows that slope of the curves is less after Wood's metal injection, corresponding to less attenuation. The effect is particularly pronounced in the range of 450 kHz to 650 kHz for P-waves and 250 kHz to 350 kHz for S-waves. While there was little energy in these frequency ranges before injection, there was substantial energy present after Wood's metal injection. This means that the transmission of the high frequencies was improved more by the presence of the Wood's metal than transmission of the low frequencies. The negative slope of the spectral ratio curve over the range of 0-400 kHz for P-waves at 320 kN after injection (Figure 3.24c) indicates the reverse trend of more attenuation at higher frequencies. This results remains unexplained.

The advantage of comparing results before and after Wood's metal injection as opposed to comparing results from intact and fractured samples is that ambiguities due to compositional and textural differences between samples are precluded. Thus the observed differences between results before and after injection represent the effect of the voids, in and adjacent to the fracture, on wave propagation. (The seismic impedance of Wood's metal is similar to that of granite). Since the Wood's metal was injected into the fracture plane, if the rock adjacent to the fracture were impermeable the differences in measurements before and after injection would be due only to the void space in the fracture. After disassembly it was noted, however that Wood's metal had intruded into the shistose layers adjacent to the fracture, and it is believed that the observed behavior was primarily due to the effects of this intrusion.

The intrusion provides further evidence to support the hypothesis that water intrusion into these same layers resulted in the higher velocities and larger than expected P-wave amplitudes in

the saturated fracture tests. For P-waves the effect of either Wood's metal or water in the voids would be to stiffen the rock.

3.6. Summary and Discussion

Compressional and shear wave velocities and amplitudes were measured as a function of axial stress on an intact specimen and a specimen containing a single natural fracture. Measurements were performed on both specimens under dry and saturated conditions using two sets of transducers of different frequencies. Measurements were also made before and after Wood's metal was injected into the fracture.

Results showed that saturation had a dominant affect on velocities and amplitudes. For P-waves a pronounced increase in both velocity and amplitude resulted from saturating either the intact or fractured specimen. An increase in P-wave amplitudes in response to saturation is contrary to what is commonly observed in porous rocks at low saturation (<90%). It is, however, consistent, with measurements made on single fractures (Pyrak-Nolte, 1990). For S-waves the effect of saturation was more complicated. S-wave velocities for the saturated intact and fractured specimens increased relative to the dry condition. S-wave amplitudes, however, at the high axial loads, were higher for the dry condition than the saturated condition. Understanding the S-wave behavior should be addressed in further work. Of particular interest would be the effect of the foliation (anisotropy) on S-wave velocities and attenuation.

Results of comparing velocities and amplitude for fractured and intact specimens were ambiguous due, probably, to the foliation in the rock, which changed over short distances. To eliminate the effects of sample to sample variations in foliation seismic measurements were performed on a fractured specimen before and after Wood's metal had been injected into the fracture. Results showed that the transmitted wave was less attenuated after the Wood's metal was injected. Inspection of the specimen showed that Wood's metal not only filled the void space in the fracture but also invaded the shistose layers adjacent to the fracture. The structure at a microscale produced by the shistosity of the rock is, in many ways, analogous to the macroscopic structure produced by fractures. Therefore it seems reasonable that the fracture stiffness theory

may be applicable to describing effects of the shistosity on both P- and S-wave behavior. In this respect, work is currently underway to apply the theory to describing the effects of thin liquid layers in fractures on S-wave transmissions.

4.0. SEISMIC IMAGING EXPERIMENTS

4.1. Introduction

Borehole seismic methods offer promise on a variety of scales for characterizing the significant mechanical and hydrologic features in an underground waste repository. As applied on a repository-wide scale, the most likely borehole seismic method would be multi-offset/multi-source Vertical Seismic Profiling (VSP). On a smaller scale, the crosshole and VSP techniques would be used for detailed characterization of the rock surrounding the mine working, canister areas, and for "looking ahead" of the tunneling activities. By performing a tomographic analysis of the VSP and crosshole data from multiple offsets and azimuths, it may also be possible to map the fracture structure in greater detail than with conventional techniques. This data could then be used in hydrologic or geomechanical models of fracture networks to study the behavior of the rock mass. Before these methods can be applied in a routine fashion, many fundamental questions remain regarding the propagation of seismic energy in fractured anisotropic rock which must be addressed. This project was designed to address several of these issues by performing controlled seismic, geomechanical, and hydrologic experiments in a well calibrated environment.

The goal of the seismic experiments was to identify the factors that control the propagation of seismic energy in a fractured anisotropic rock. When these factors are identified, it will be easier to extrapolate fracture characteristics observable at the borehole walls and underground workings to the entire repository block, thus providing a more complete set of data to characterize the overall hydrologic and geologic parameters.

Three experiments were performed in the FRI site, one each in the summers of 1987, 1988, and 1989. Presented here are the results of the 1987 and 1988 field studies in saturated conditions. The 1989 investigations repeated some of the previous measurements after air had been injected into the fracture. These results are not reported here.

The FRI experiment offered an excellent opportunity to perform calibrated experiments in a rock mass where the fracture locations and characteristics are relatively well known. An advantage of the FRI site is that there is access to the fracture zone from all four sides which allows a comparison of techniques between two-, three-, and four-sided tomography. The greatest attraction, however, is the opportunity to evaluate theories of wave propagation in fractured media and to evaluate these theories at several different scales. For example, Pyrak et al. (1990) have performed laboratory experiments which have confirmed the effect of fracture stiffness at small scales. The scaling of this phenomenon to larger distances is yet unknown. Therefore, one of the main objectives of the FRI experiments was to observe the effect of individual fractures as well as a fracture zone on the propagation of seismic waves. A second objective was to relate the seismic response to the hydrologic behavior of the fractures, i.e., do all fractures effect the seismic wave, or do just fluid filled, or partially saturated fractures effect the seismic waves in a measurable amount. The final objective of the study was to assess the amount of seismic data necessary to provide useful information, and how one would process data for the maximum information in a routine fashion. These are important questions when one progresses to the point of applying these techniques on larger scales in an actual nuclear waste repository.

4.2. FRI Zone Experimental Procedure

Shown in Figure 2.2 is a map showing the FRI zone in the plane of boreholes BOFR 87.001 and BOFR 87.002. As stated in the geologic overview, there is a common shear feature crossing the FRI zone. The boreholes were drilled to intersect this fracture zone as shown in Figure 2.2. Three long boreholes were drilled through the FRI zone for seismic investigations. Boreholes BOFR 87.001 and BOFR 87.002 are 86 mm diameter, 21.5 m long holes that were drilled from the AU tunnel to the access tunnel to provide a means of performing crosshole seismic work, core of the fracture zone, and for carrying out hydrologic experiments. Borehole BOFR 87.003 is a 127 mm diameter, 9 m long hole drilled through the fracture zone for obtaining large core for laboratory analysis and also for hydrologic testing. In addition to these holes, 76, 74 mm diameter, 50 cm long holes were drilled into the AU and access tunnel walls between boreholes BOFR

87.001 and BOFR 87.002 at 0.25 meter spacing to allow the placement of the seismic sources and receivers.

For the collection of the data seismic sources were placed in the holes (boreholes BOFR 87.001, BOFR 87.002, and the shallow holes in the sides of the tunnel) and activated. The data from a clamped three component accelerometer package was recorded at 0.5 meter spacing in boreholes BOFR 87.001 and BOFR 87.002. The receiver package was also placed in the shallow (.25 m spacing) holes to give complete four sided coverage. In the 1987 studies the source and three component receiver package were clamped to the bore hole wall to provide good seismic coupling. For the acquisition of 1987 cross well data, the source was in a dry hole and the receiver was in a fluid filled hole. In the 1988 studies, both boreholes were filled with fluid. Thus, the fluid in the borehole provided improved coupling between the source and the rock. We found that fluid coupling was more efficient than mechanical coupling and also allowed for faster data acquisition. The data were recorded on an in-field PC-based acquisition system. The description and details of the equipment used are described in Appendix A. Four channels of data were acquired, the x, y, and z receivers and the "trigger" signal. The sample rate was 50,000 samples/sec on each channel with 20 milliseconds of data being recorded for each channel in the 1987 experiments and 250,000 samples/second in the 1988 data. Typical travel times were less than 5 milliseconds for the P-wave and 10 milliseconds for the shear wave. Seismograms were acquired from nearly 60,000 ray paths (X, Y, and Z components) in the FRI zone, at distances from 1/2 meter to nearly 23 m. The peak energy transmitted in the rock was at frequencies from 5,000 to 10,000 Hz, yielding a wavelength of approximately $\frac{1}{4}$ to 0.5 meter in the 5.0 km/sec velocity rock.

4.3. Data Processing Sequence

Simple processing was carried out on the field tapes to transform the data into a usable format. The data was first demultiplexed using software which allows us to quickly demultiplex the entire data set at one time. The computer requirements remain large in terms of space, but the process can now be done in batch mode with the requirements similar to that of a reflection

survey. The data are formatted such that the three components of each sweep of a stationary source position are put into a file. Therefore, the number of files is equal to the number of sweeps, or stationary source locations.

During acquisition, multiple signals were sometimes produced with the same source-receiver pairs in order to stack the data for improved signal quality. After the data were demultiplexed, the traces were stacked so that a single trace exists for each component of each source-receiver pair.

4.3.1. Picking the Travel Times

The travel times were picked manually using an interactive picking routine developed at LBL. The times were picked on the radial component (component 3), which is in the direction of strongest P-wave motion. This was confirmed by rotating the data into the P-, SV- and SH-directions. Due to field equipment modifications the data quality was improved from 1987 to 1988. The source electronics used in 1988 was improved in power and rise time from the 1987 electronics so that the signal to noise ratio improved at higher frequencies. The repeatability of this system resulted in more accurate travel time picks from the more consistent waveforms. This can be seen by comparing Figures 4.1 (1987) and 4.2 (1988), a sample crosshole sweep from the two data sets. The travel time picks are marked on each of the traces.

After the travel times have been picked, they were initially checked by plotting a time-distance curve (Figure 4.3a), a velocity-distance curve (Figure 4.3b) and a velocity vs. incidence angle curve (Figure 4.3c). Any large variation from the general trend would indicate picking errors or acquisition problems. Figures 4.4a through 4.4c show the corresponding 1988 plots, respectively. As can be seen, the bulk of the 1988 travel time values (Figure 4.4) form a tighter line than the 1987 values (Figure 4.4). The 1988 values which deviate from the tight line are those which travel from the middle of BOFR 87.001 to the access tunnel, almost to BOFR 87.002. These values will be discussed later in the context of the interpretation. Compared to the 1988 data, the bulk of the 1987 travel time picks form a broader line of values indicating a greater deviation in times. This is primarily due to the relatively large deviation in the picking of

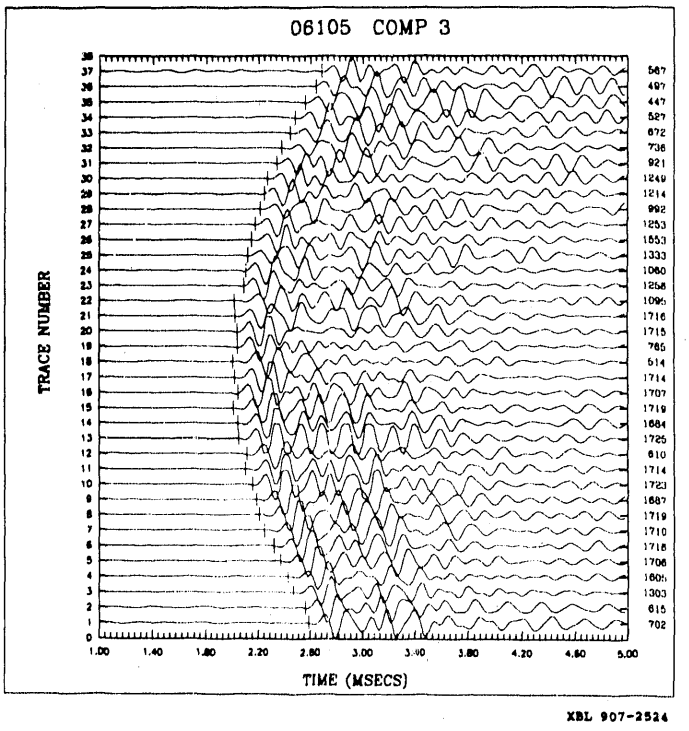

Figure 4.1. Typical example of the crosshole 1987 P-wave data acquired at the FRI zone.

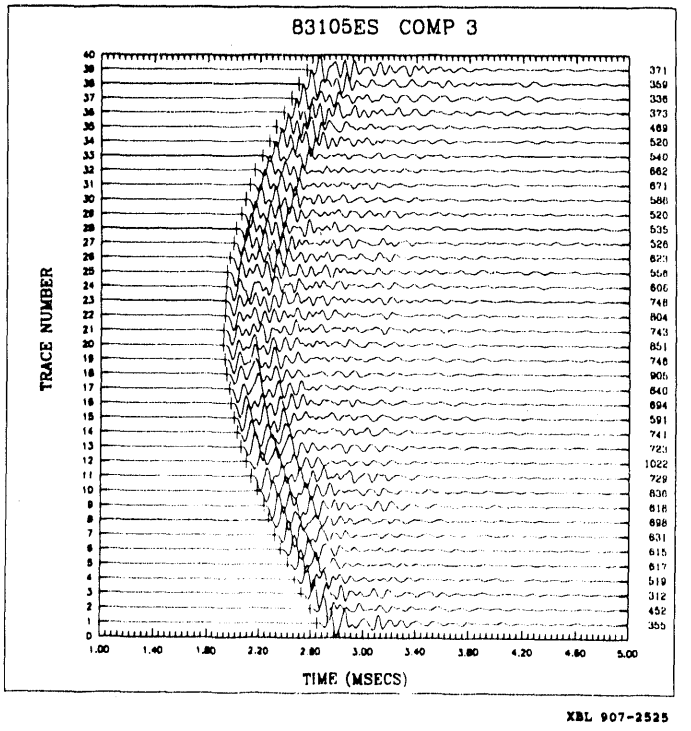

Figure 4.2. Typical example of the crosshole 1988 P-wave data acquired at the FRI zone. Shown on both figures are the picked arrival times.

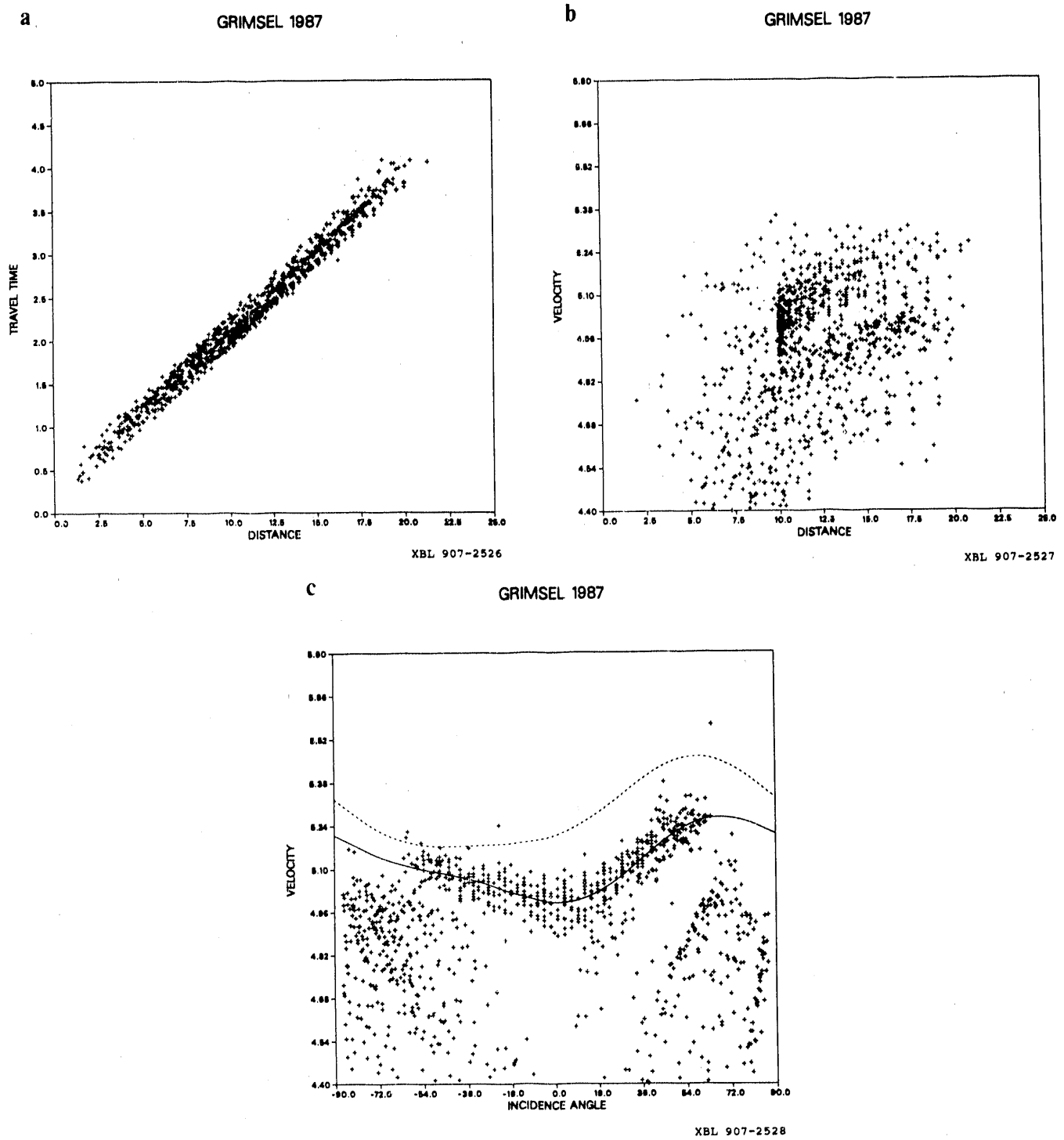

Figure 4.3. (a) 1987 travel time versus distance data; (b) 1987 velocity versus distance data; and (c) 1987 velocity versus incidence angles. The dashed and solid lines are the least square fit of the data for the 1988 and 1987 data respectively, compare to Figure 4.4 for 1988 data.

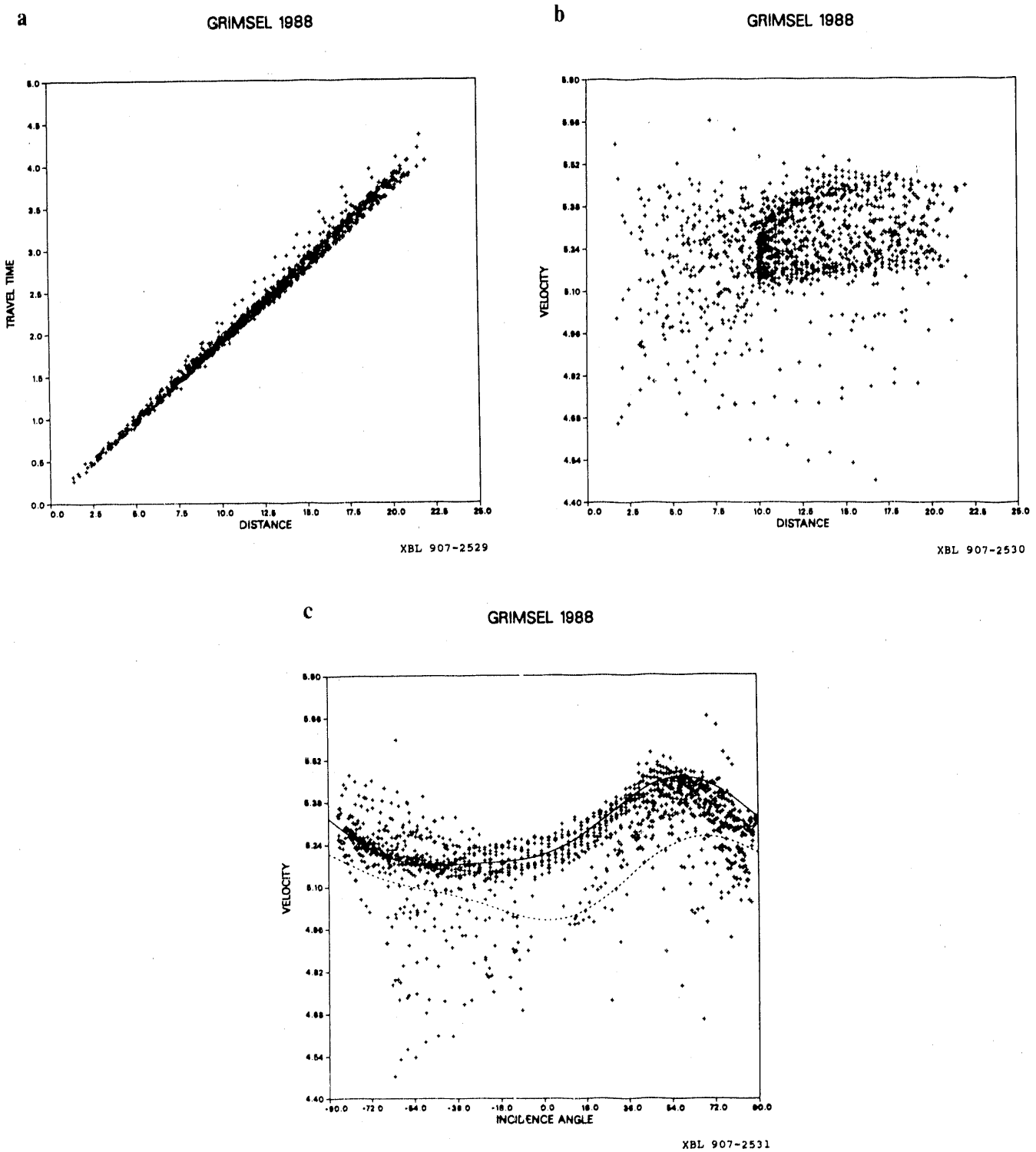

Figure 4.4. (a) 1988 travel time versus distance data; (b) 1988 velocity versus distance data; and (c) 1988 velocity versus incidence angles. The dashed line is the least square fit of the data for the 1987 data, the solid line is the fit for the 1988 data, compare to Figure 4.3 for 1987 data.

the data created from the weaker source used in 1987 producing lower amplitudes. This presents a problem in picking the correct first arrival, since the initial impulse has a low amplitude, especially for the rays passing through the damaged zones bordering the tunnels. Another source of error was that the trigger signal component was not working constantly. This caused errors of up to 1 or 2 samples (0.02 to 0.04 msec) in the origin time, although this was taken into account.

Another check on the quality of the travel time picks was done by plotting the travel times of each sweep versus the station number. Since the distance between measurement points in each sweep was a constant 0.5 m, the values plotted in this manner should form smooth curves in the form of the wavefront. Consistent or sharp deviations in these curves warrant further investigation and are probably due to improper station locations or poor travel time picks. Small deviations in the plotted values should be present, however, due to variations in the rock velocities. Plotting the travel time versus the station number for the crosshole sweeps again indicates the difference in quality between the 1987 (Figure 4.5) and the 1988 data (Figure 4.6a). The difference is entirely due to the travel time picks, the station locations remained the same, and the same geometry was used for both cases. As can be seen in Figure 4.6c and 4.6e, erratic deviations between some sweeps still remain in the 1988 data, especially between the access tunnel and borehole BOFR 87.001 (Figure 4.6e). We believe that most of these deviations were caused by some physical property or anomaly of the rock itself. However, some of the "unusual rays" may be due to errors in the collection process. Figure 4.7 shows examples of these "unusual" rays that pass through a highly attenuating zone. The most obvious deviating sweeps were removed entirely from the data used to perform the inversion. The removal of these data had little effect on the major features in resultant image. No additional travel time corrections were necessary in either the 1987 or 1988 data, and few of the signals were too noisy or did not have sufficient amplitude to pick times accurately.

4.3.2. Inversion

The travel times were inverted using an algebraic reconstruction technique (ART) (Peterson, 1986). A 44 x 88 array of pixels was chosen for the tomographic inversion. This produces a

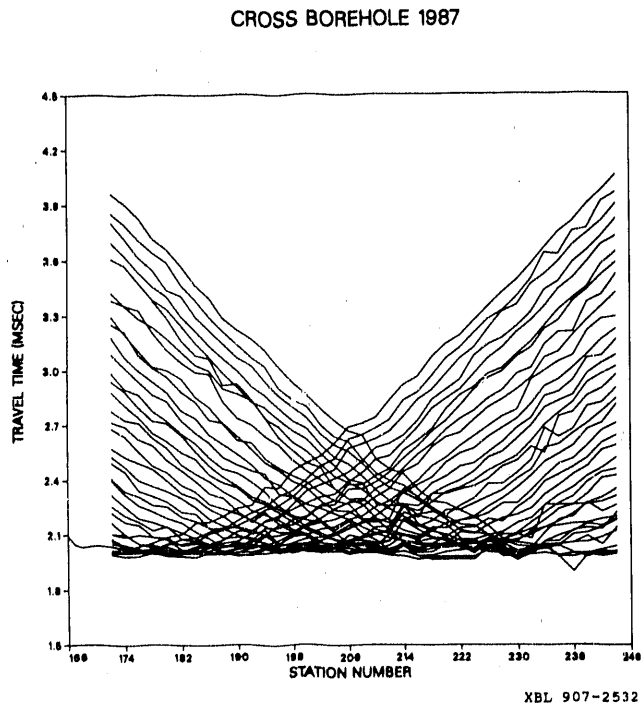

Figure 4.5. The travel time versus station number for the 1987 crosshole data, compare to Figure 4.6a.

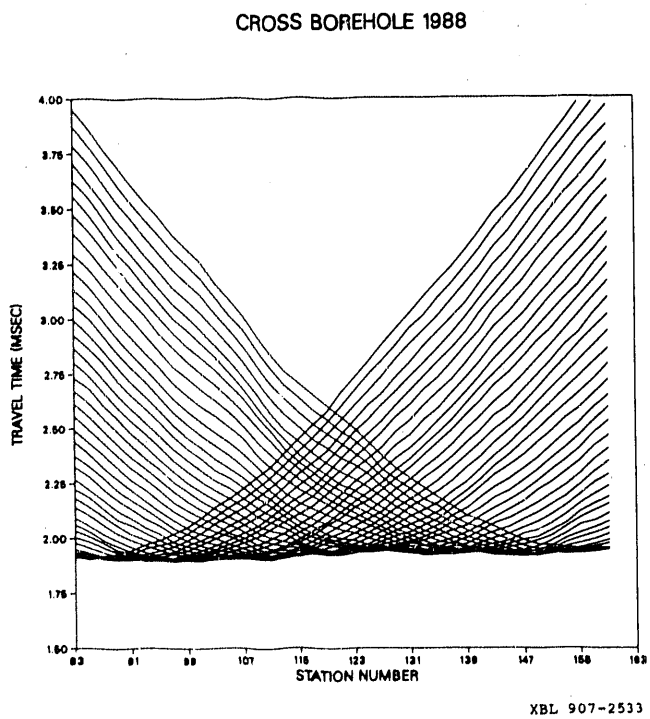

Figure 4.6a. Travel time versus station number from the 1988 crosshole paths for rays actually used in the final inversion.

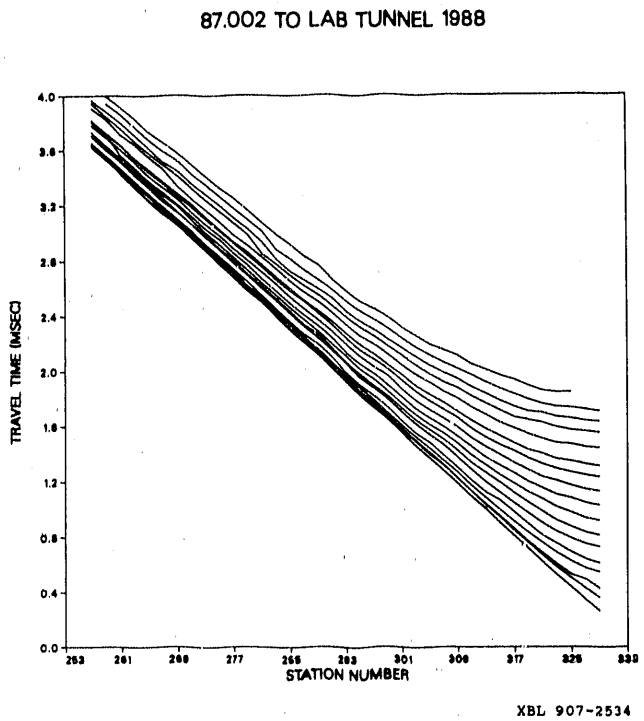

Figure 4.6b. The travel time versus stations number for rays from BOFR 87.002 to the laboratory tunnel.

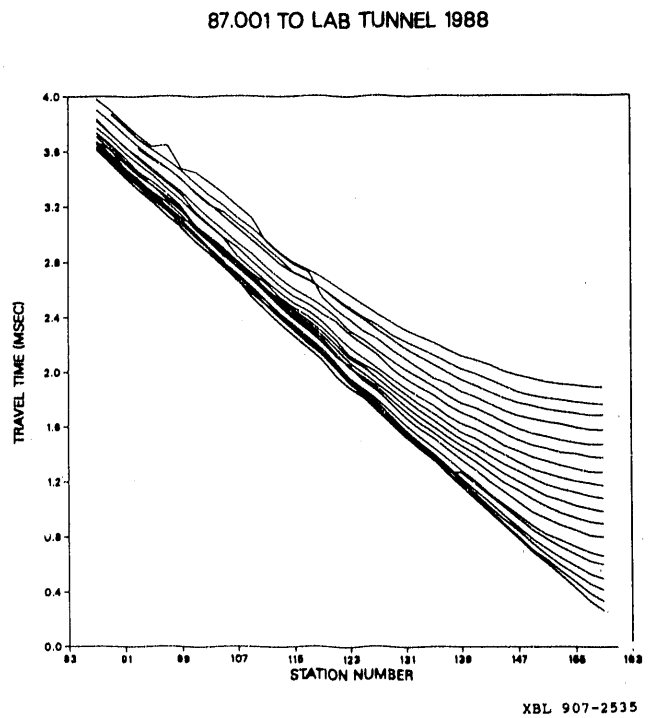

Figure 4.6c. The travel time versus station number for rays from BOFR 87.001 to the laboratory tunnel.

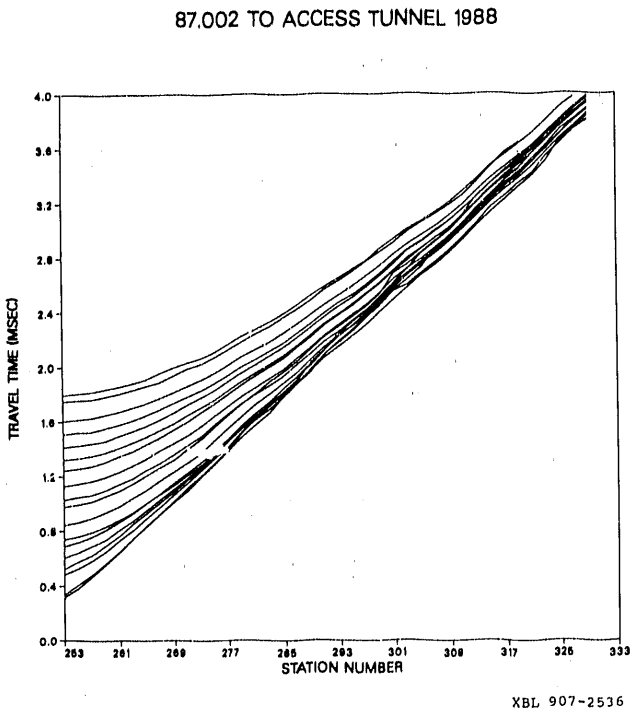

Figure 4.6d. The travel time versus station number for rays from BOFR 87.002 to the access tunnel.

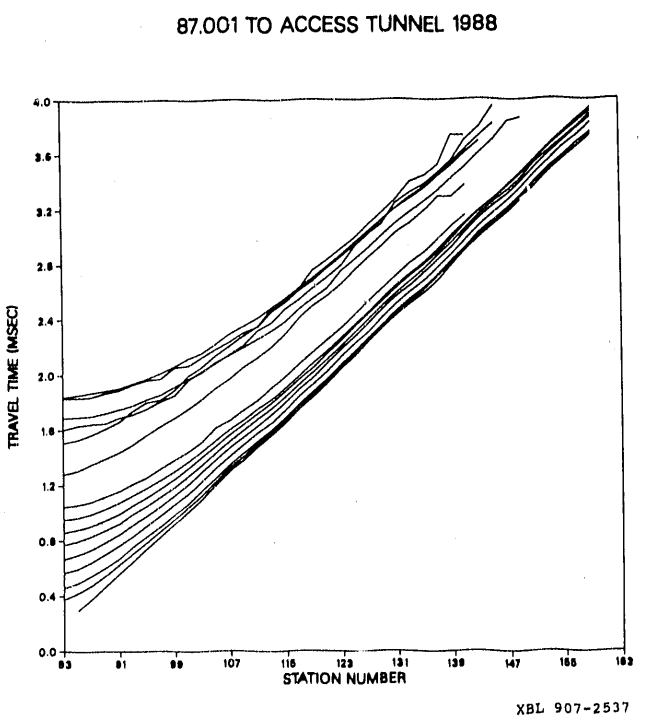

Figure.4.6e. The travel time versus station number for rays from BOFR 87.001 to the access tunnel.

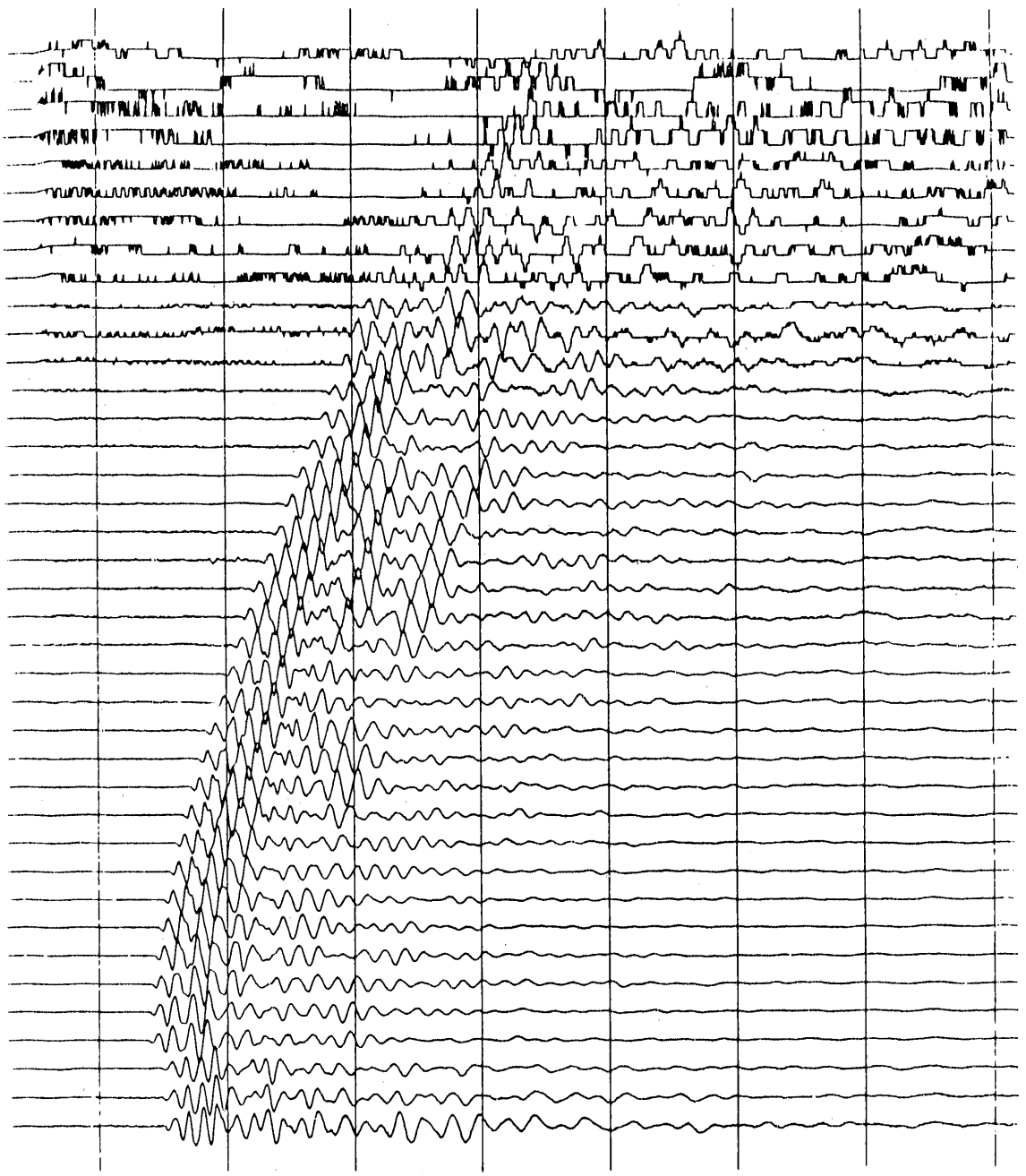

Figure 4.7a. Waveform data from ray paths BOFR 87.001 to the access tunnel. These are unusual rays that were not used in the final inversion. Note the shift in the data at the top and bottom of the figure. Total time shown is 8.2 milliseconds with each time line 1.0 milliseconds. The traces are for station 329 (top) through 253 (bottom) at 0.5 meter intervals.

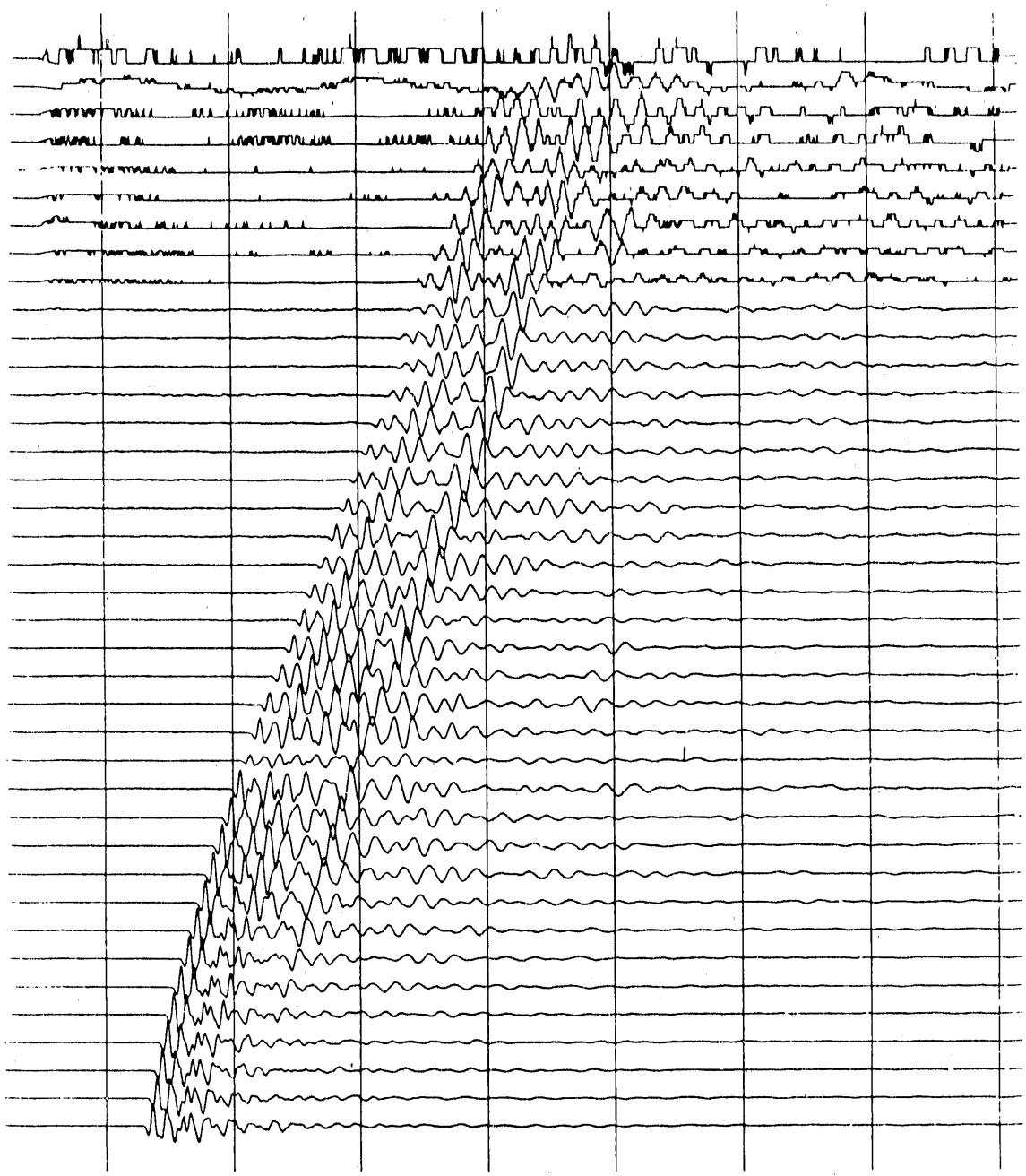

Figure 4.7b. Waveform data from ray paths BOFR 87.001 to the access tunnel. These were not deleted from the final version of the tomogram.

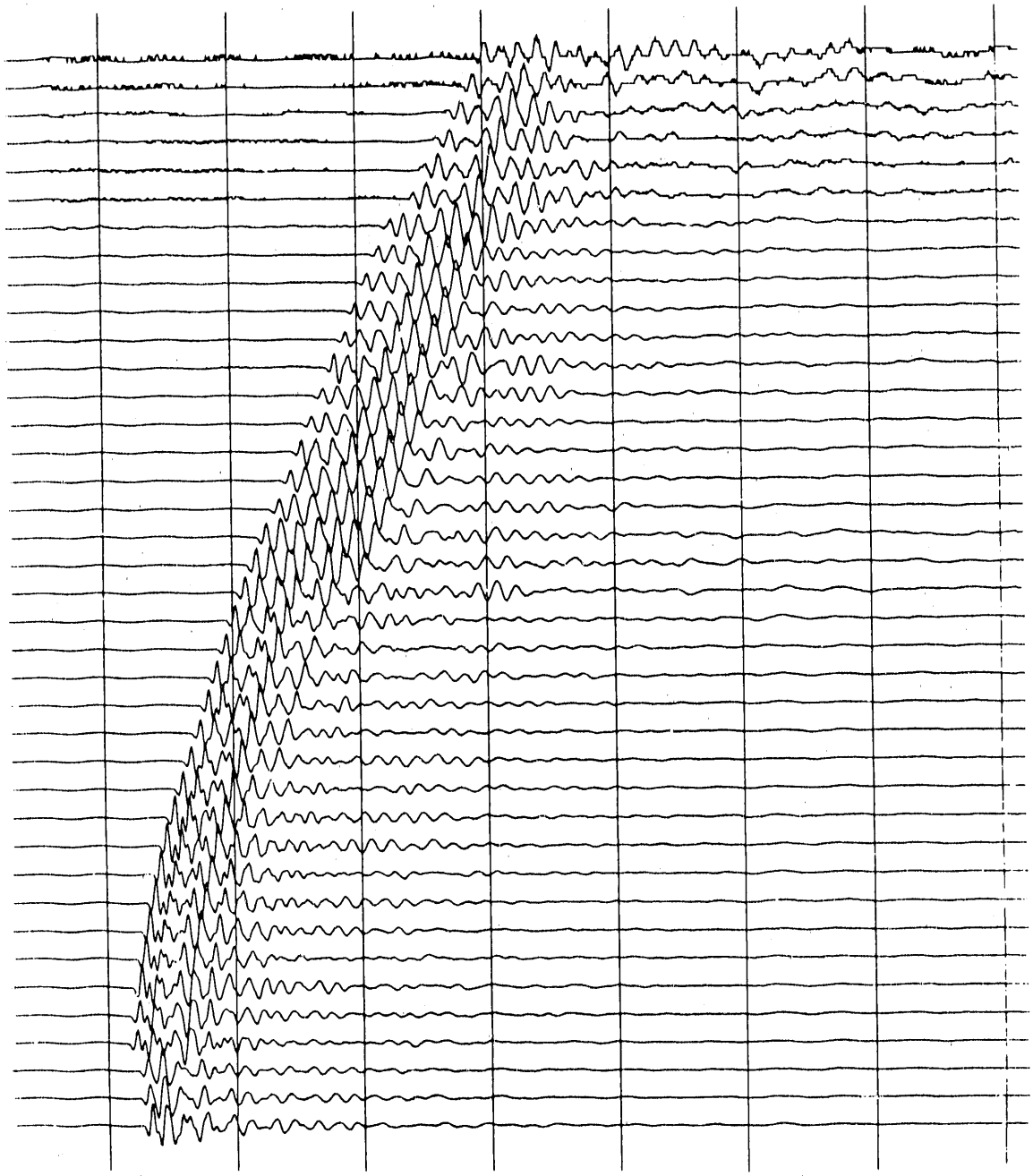

Figure 4.7c. Waveform data from ray paths BOFR 87.002 to the access tunnel. These were the unusual rays that were not used in the final inversion. Note the shift in the data at the top and bottom of the figure.

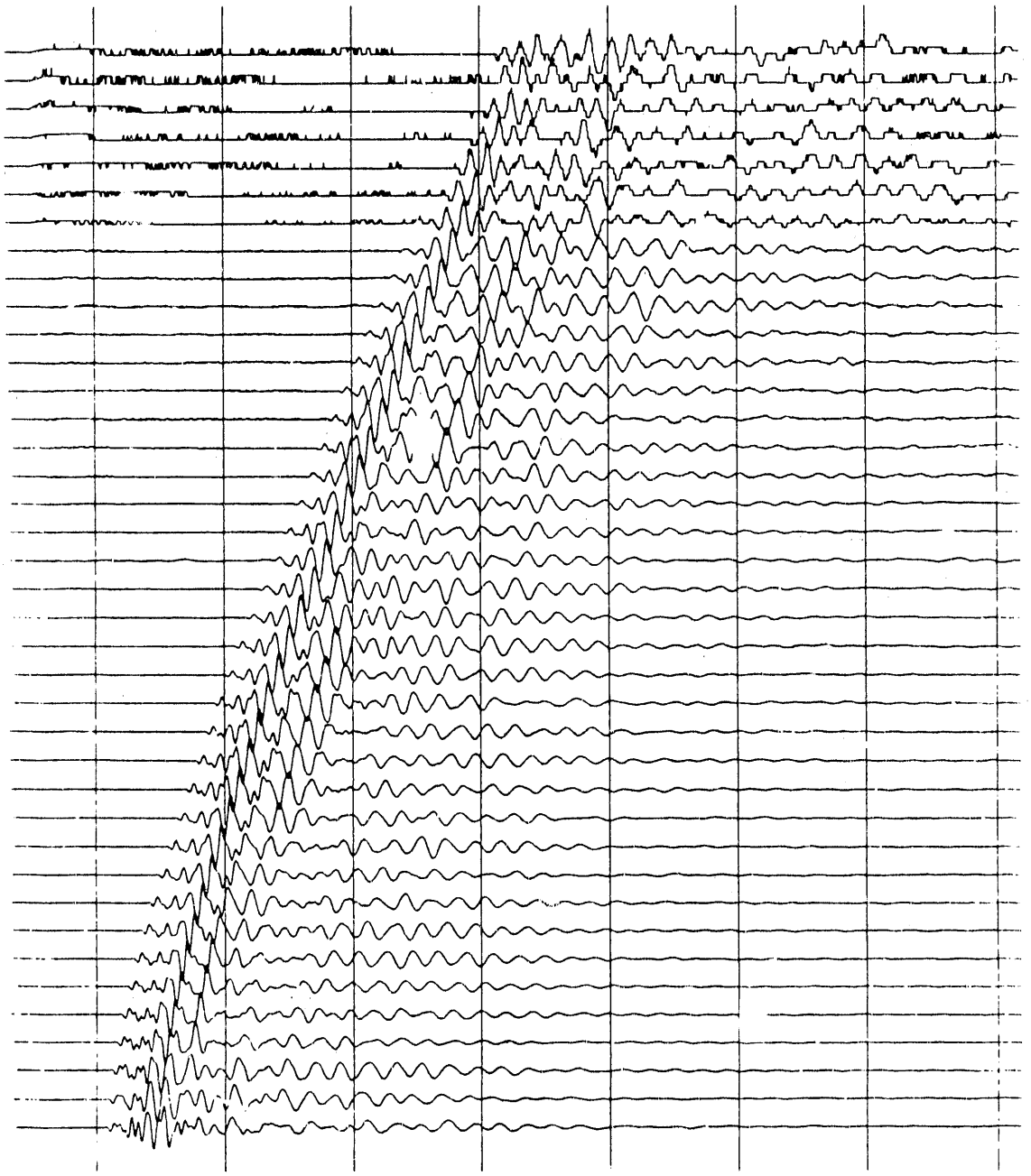

Figure 4.7d. Waveform data from ray paths BOFR 87.002 to the access tunnel. These were not deleted from the final version.

pixel size of 0.25 m which is the size of the smallest anomaly we can expect to see given the wavelength of 0.7 m and station spacing of 0.5 m. Our previous experience has shown that for this geometry a pixel size of half the station spacing gives the optimal combination of resolution and inversion stability.

An image was produced using the entire 1987 data set (Figure 4.8). This image can be compared to the 1988 results (Figure 4.9) using the same velocity intervals and same number of rays (4.9 km/s to 5.4 km/s). As stated previously the sweeps that contained the "unusual rays" were not used in the 1988 inversions. The main features identified in the 1987 results (Figure 4.8) are the low velocity zones adjacent to the tunnels, assumed to be damaged zones, and a low velocity zone (Feature A) extending from the middle of borehole BOFR 87.001 to the AU tunnel/borehole BOFR 87.002 intersection, and two other low velocity zones (B and C in Figure 4.8).

The 1988 image has many differences from the 1987 results. The main differences are:

1. There is little evidence of the extensive 1987 damaged zones near the tunnels in the 1988 results. Also, the average velocity values in the entire 1988 field (5.2 km/s) are higher than the average velocities in the 1987 field (4.9 km/s).

2. The prominent feature (Feature A, Figure 4.8) is observed in 1987 results as a single strong low velocity zone about 2 m wide. The corresponding zone in the 1988 results, Figure 4.9, consists of two or three very thin (< 0.5 m thick) zones which become discontinuous at about 4 or 5 m from the laboratory tunnel and are located in a different orientation and place. Also, Feature C is not as pronounced in the 1988 results as in the 1987 results.

3. There appears to be an additional structure, Feature B, in the 1988 image which was masked by the low velocity zone on the center-north edges of the 1987 result. This feature in the 1988 results extends from near the access tunnel/BOFR 87.002 intersection, to the middle of BOFR 87.001, and is, in fact, the dominant feature of the 1988 results. Evidence of this feature exists in the 1987 data, but is obscured by a low

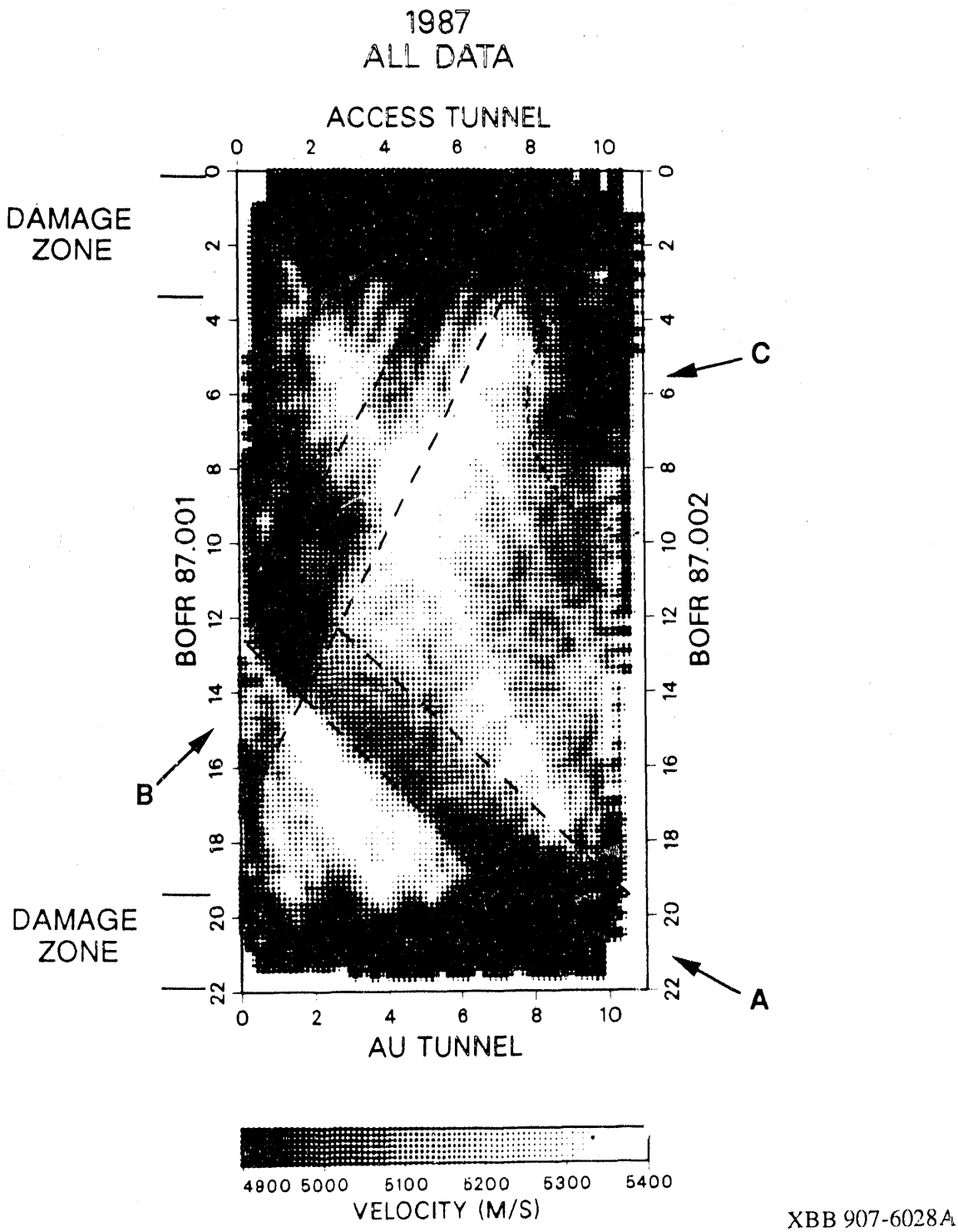

Figure 4.8. The final result of inverting all the good data from the 1987 tests.

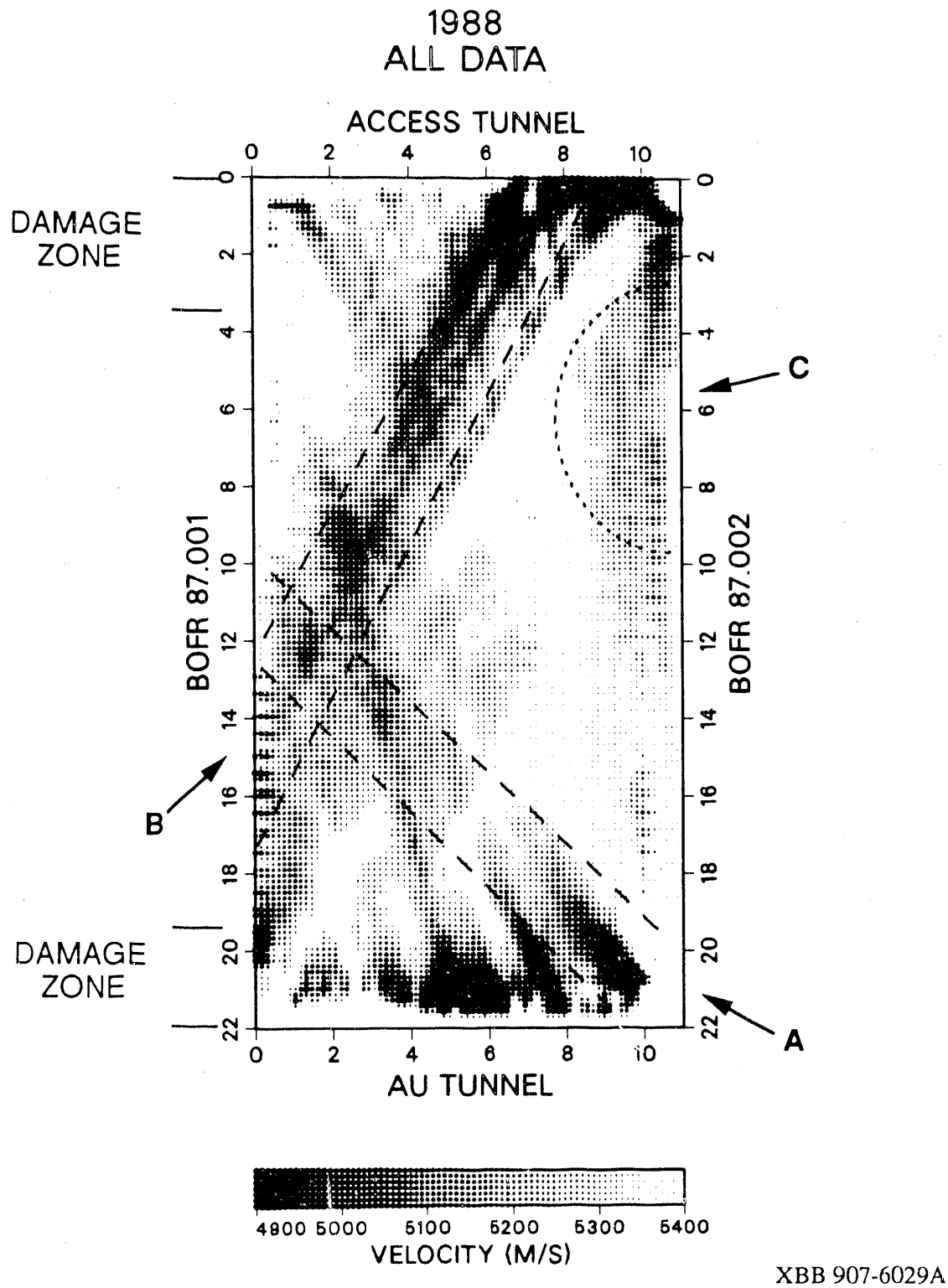

Figure 4.9. The final result of inverting all of the good data from the 1988 tests. No anisotropic corrections, "unusual" ray paths deleted.

velocity feature on the east side of the tomogram.

The discrepancies between the two images seem severe and will be discussed in detail later in the report. These differences between 1987 and 1988 results were very significant. The 1988 hydrologic testing program was based on the results of the 1987 tomogram. Features A and and C were the target of these tests and Feature B had not yet been identified as a major feature. Therefore we were very interested in the appearance of Feature B and its hydrologic significance.

4.3.3. Anisotropy Corrections

As discussed in the geology section, the strong foliation in the Grimsel granodiorite suggests that the rock may be highly anisotropic with respect to wave propagation. An obvious step was to correct for this anisotropy in order to improve the image. Previous work has shown us that image improvement may be achieved by removing the background anisotropy from the travel times (Johnson and Peterson, 1986).

In general, the P wave anisotropy may be approximately represented as

$$V_p^2 = A + B\sin(2\phi) + C\cos(2\phi) + D\sin(4\phi) + E\cos(4\phi) \qquad (4.1)$$

where ϕ is the angle of direction of propagation. A function of this form is fitted to the data. The coefficients A, B, C, D and E represent the strength of the anisotropy. These values may be determined in the laboratory or in the field. The laboratory values are difficult to determine and may not adequately represent the in-situ anisotropy. In the field, the same travel times gathered for the tomographic survey may be used to determine the coefficients or a separate test may be set up in a more homogeneous (though not differing in anisotropy) area.

At Grimsel the tomographic travel time data was initially used for this calculation, but a problem develops when the entire data set is used. Because of their relatively large size, the existence of the low velocity zones associated with the tunnels will distort the estimate of anisotropy. The damaged zones associated with the tunnels at FRI are such that the rays with high incidence angles will always pass through this zone, whereas the shallow angled rays will primarily travel cross borehole, through less fractured rock. This creates a false anisotropy centered

with maximum value north-south (parallel to the tunnels). Therefore, removing the anisotropy in this way would not be meaningful.

We attempted to overcome this problem by using only the cross well data between BOFR 87.001 and BOFR 87.002 to determine the anisotropy coefficients. Although this removes the effect of the damage zone near the tunnels, the shear zone (Feature A) may also create artifacts in the anisotropy correction. Because the shear zone has the same orientation as the anisotropy it may enhance the anisotropy, and thus produce an over correction which would result in fading the image of the shear zone. We do not know the magnitude of this over correction, if any, so we did not attempt to remove it.

The anisotropy coefficients calculated from the 1987 and 1988 cross well data show rock matrix anisotropy in the direction of the foliation. Table 4.1 shows these values are slightly different.

Table 4.1. Anisotropy coefficients

coef	A	B	C	D	E
1987	26.211	0.544	-1.122	-0.331	-0.185
1988	27.942	1.375	-0.633	-0.309	-0.196

The fit of these anisotropy corrections to the data is shown in the velocity vs. incidence angle plots (Figures 4.3c and 4.4c). The apparent change in the anisotropy correction from 1987 to 1988 may be caused by several factors: 1) A systematic error in the data collection or measurements may have occurred. 2) In 1987 the receiver borehole was not water filled, while in 1988 both the source and receiver boreholes were water filled. This may have produced some effect on the travel times picked to produce an apparent anisotropy. 3) In 1988, hydrologic experiments were conducted during the week previous to the tomographic data collection (see following Sections). This may have increased the saturation of the rock which would explain the increase in average velocity in 1988, since the velocity increases with saturation as discussed in Chapter 3.0.

Although it is not likely that the background anisotropy changed from 1987 to 1988, the anisotropy was removed from each data set using their respective correction coefficients. In each case the contribution of the anisotropy was calculated and removed from the observed travel times. This was done by calculating the difference between the travel times calculated with coefficients A-E and the travel time calculated with only coefficient A, and then subtracting this value from the measured travel time.

The travel times corrected for anisotropy were inverted in the same fashion as the uncorrected data. The effect of the anisotropy corrections on the 1987 results (Figure 4.10) change the magnitude of the anomaly corresponding to the shear zone. The corrections also cause the amplitude of the anomaly to vary along the strike of the main fracture zone. Also, smaller zones within the large low velocity feature adjacent to borehole BOFR 87.001 are more resolved and coincide with similar features in the 1988 result.

The result of applying the correction to the 1988 data is shown in Figure 4.11. The uncorrected image has been smoothed with the low velocity zones more distinct. The inversion also appears to remove some artifacts that are produced in the original inversion. The smearing seen to the upper left of Figure 4.9 is reduced, as is the effect of a strong, thin low velocity feature extending from the middle of the laboratory tunnel to the center of BOFR 87.001. The "secondary" features which parallel the main low velocity zone (Feature A) in Figure 4.9 are also greatly reduced leaving a single zone whose intersection with the laboratory tunnel coincides with the large fracture observed on the wall of the AU tunnel.

4.4. Cross Well Studies

In many field cases only the cross well ray paths can be obtained. This maybe due to the damaged or weathered zone preventing adequate surface to borehole arrivals or simply lack of access. At FRI we see a damaged zone associated with the tunnel which strongly affects the wave amplitudes, thus affecting the quality of the travel time picks. In order to determine the effectiveness of cross well data to image the region between the boreholes we inverted only the cross well travel times. Because the 1987 and 1988 differences are greatest in the regions of the

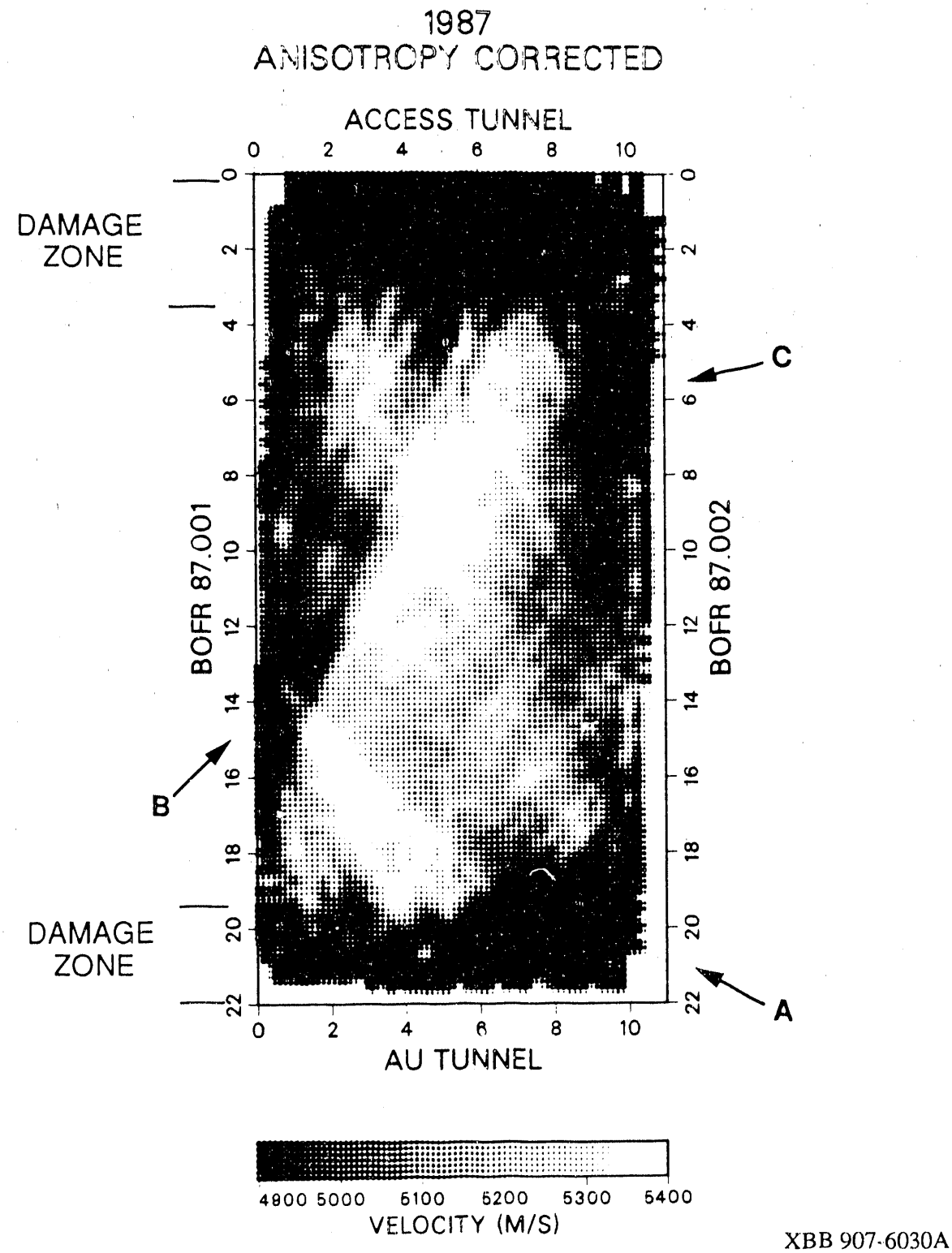

Figure 4.10. The final 1987 inversion after correcting for anisotropy.

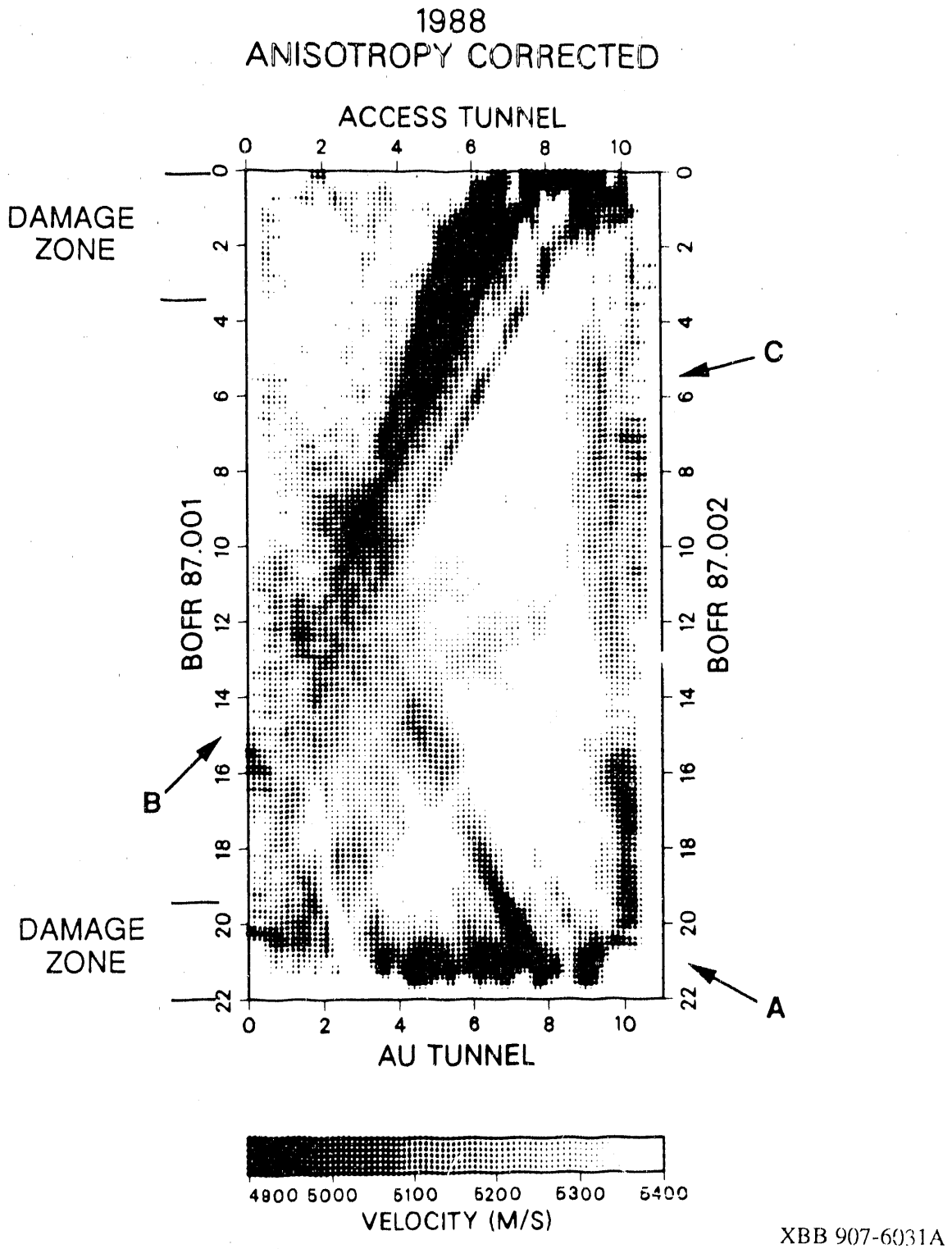

Figure 4.11. The final 1988 inversion after correcting for anisotropy. The "unusual" rays have been deleted.

tunnel, we expected the cross well images to be more similar when the rays sampling areas adjacent to the tunnel are removed.

Initially the 1987, and 1988 cross well travel times were inverted without removing the anisotropy (Figures 4.12 and 4.13, respectively). Compared to the 1987 cross hole results, the 1988 cross hole image is much "smoother" and has a higher average velocity, 5.26, than the 1987 image, 5.09. These images also show that the inversion is strongly affected by the background anisotropy. In this crosshole geometry, the rays traveling from the upper part of BOFR 87.001 to the lower part of BOFR 87.002 are in the high velocity direction of the anisotropy, with the other rays perpendicular to this direction being in the "slow direction." This creates a pattern of velocity values symmetric about an axis in the direction of the anisotropy. The result is an excellent example of what happens when the anisotropy of the background medium is ignored.

We removed the background anisotropy as before and performed an inversion of the corrected crosshole values for the 1987 (Figure 4.14) and 1988 (Figure 4.15) data. Note that Features A and B seen in the four-sided images (see Figures 4.8 and 4.9) are not imaged in the cross well results. These anomalies are unresolvable because they occur near the tunnel walls where only horizontal rays sample them in a cross hole configuration. The images do show a low velocity zone corresponding to a fractured area seen in the core logs at about 7 and 15 m down from the access tunnel in borehole BOFR 87.001 and 15 m down borehole BOFR 87.007. The orientations of the imaged zone agrees with the general orientation of the fractures.

The only real difference in the two crosshole results is that the velocities in 1988 are much higher than in 1987. We feel that these differences may be attributed to the saturation of the rock, coupling of the sources and receivers to the borehole walls, the different sources, and/or the quality of data. Note that in Figure 4.2 (1988) the initial arrival is taken to be a small downward pulse. In Figure 4.1 (1987) the downward pulse exists for only a few of the traces, so that the initial arrival was often taken at the second zero crossing, thus resulting in later picks. In effect we see a combined amplitude-velocity effect on the 1987 data, and mainly a velocity variation in the 1988 data.

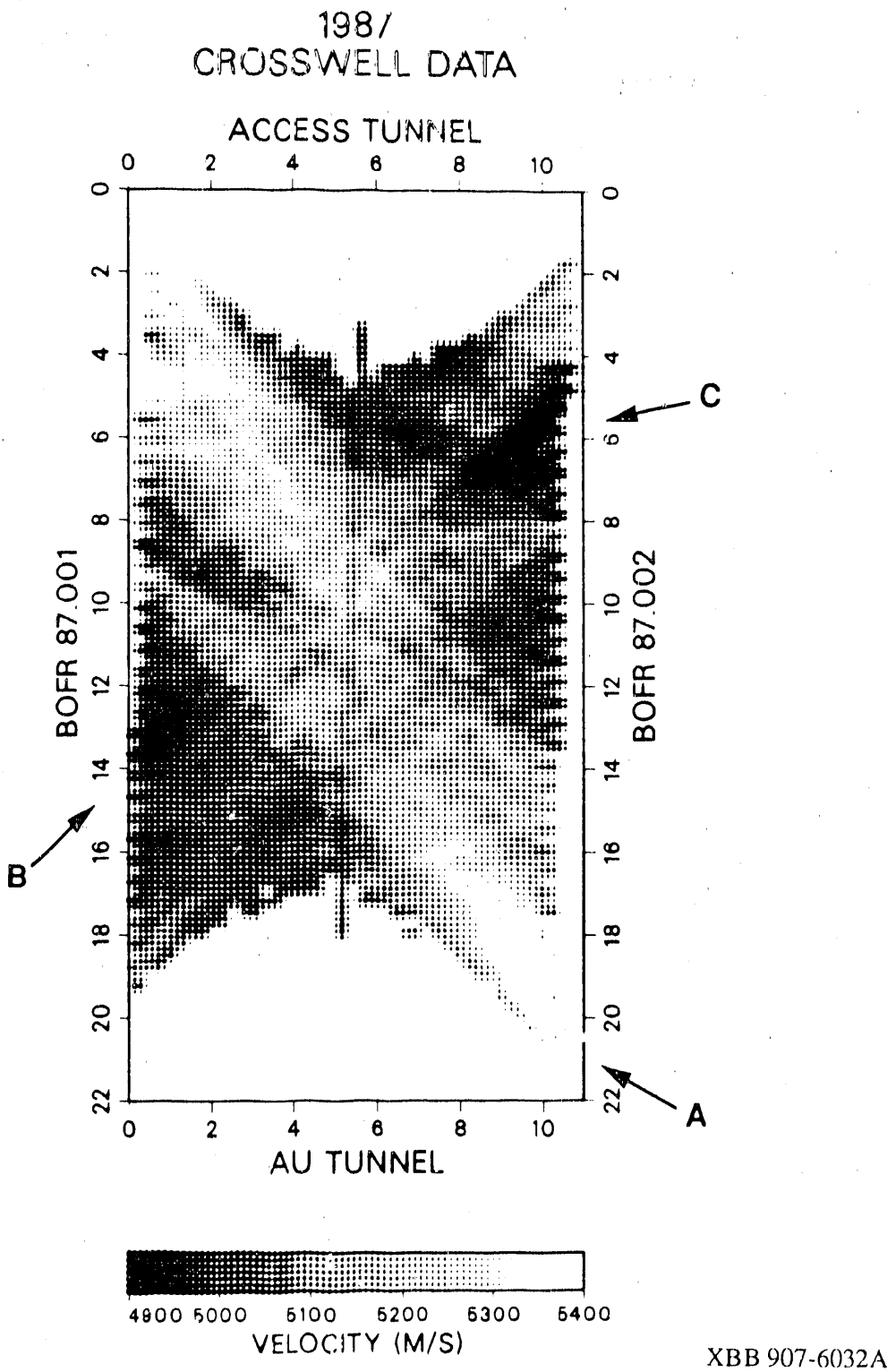

Figure 4.12. Cross borehole data inversion of 1987 data, no anisotropy correction.

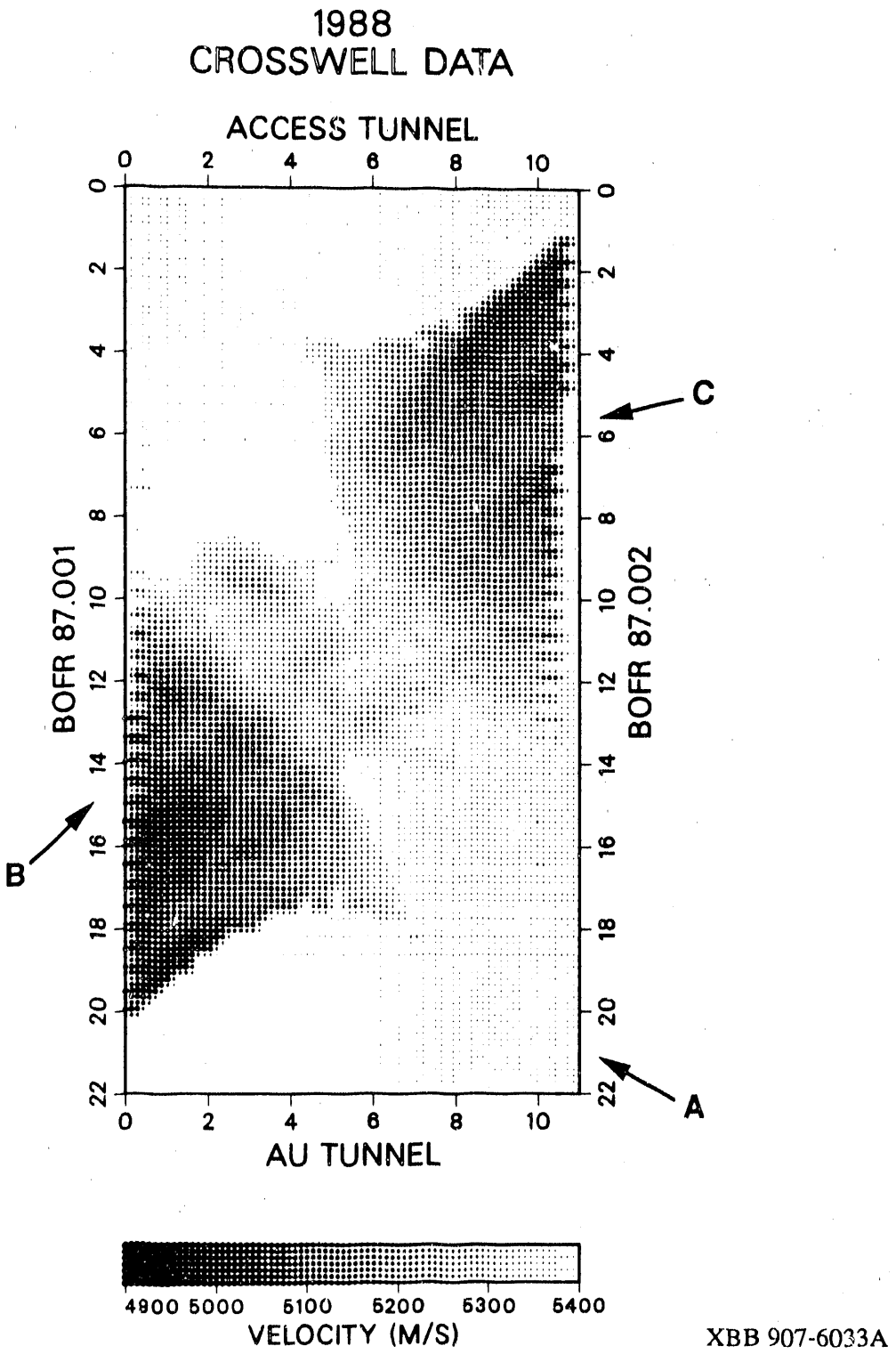

Figure 4.13. Cross borehole data inversion of 1988 data, no anisotropy correction.

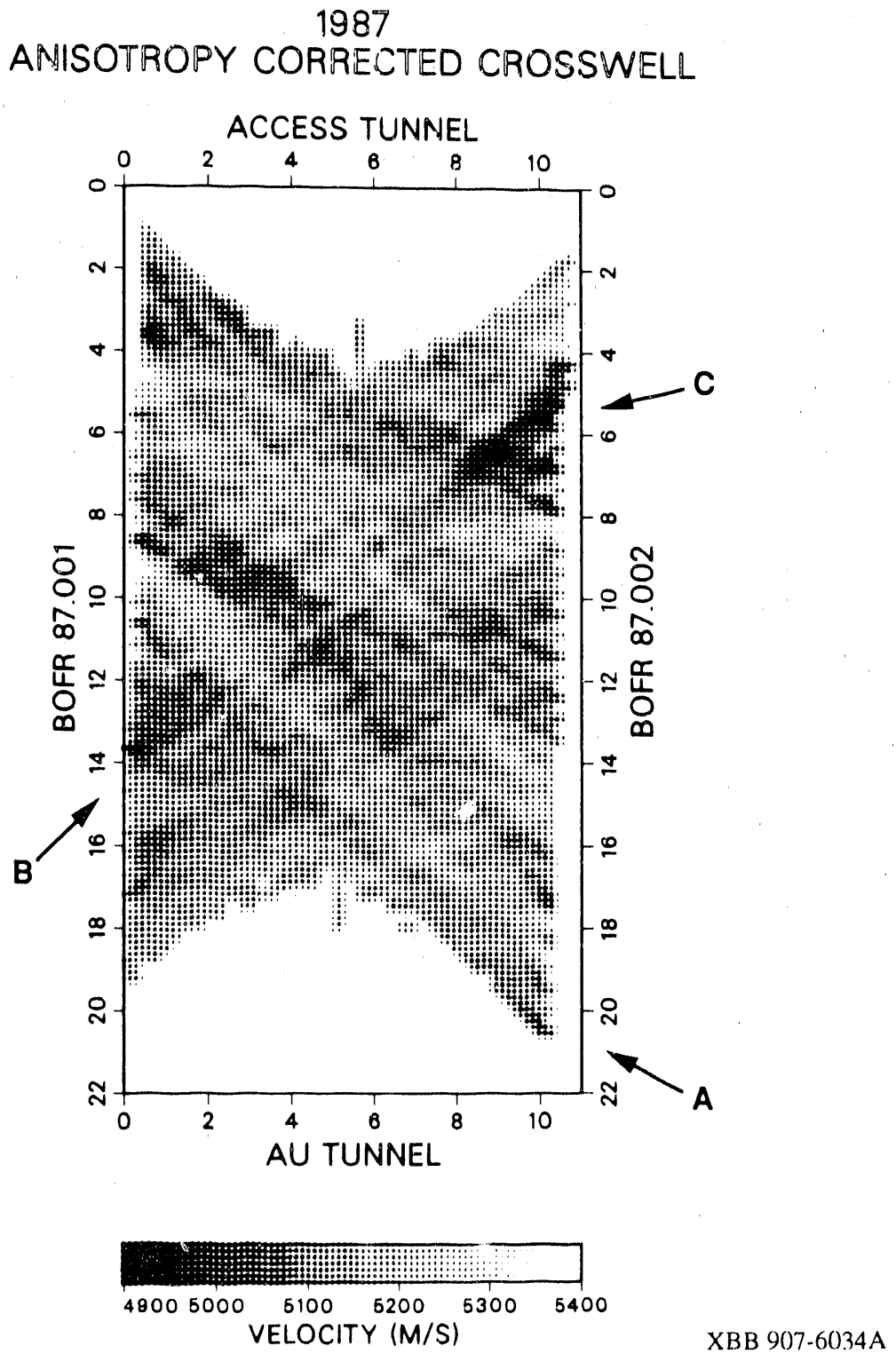

Figure 4.14. Cross borehole data from 1987 which was corrected for anisotropy and inverted.

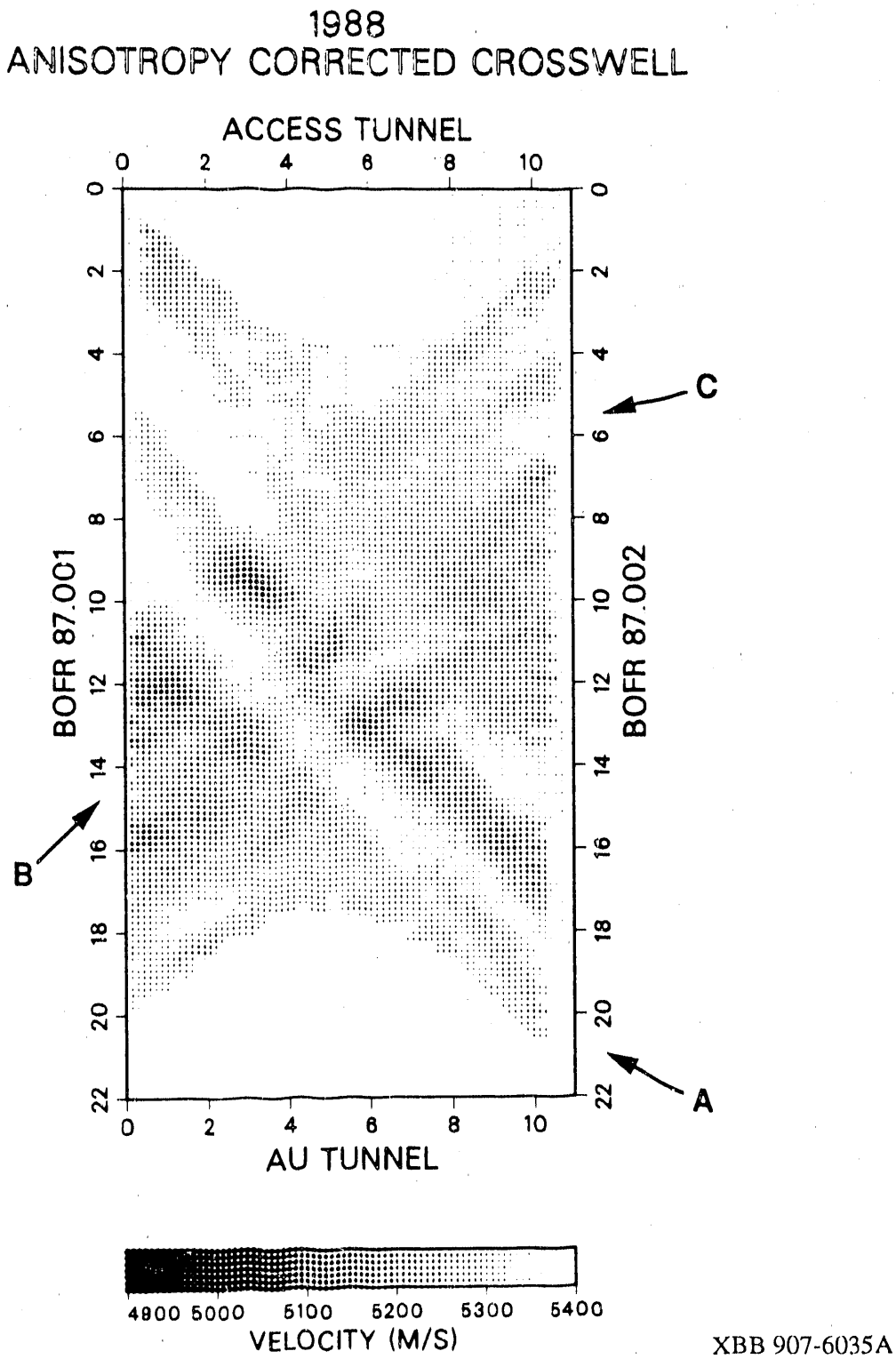

Figure 4.15. Cross borehole data from 1988 which was corrected for anisotropy and inverted.

4.5. Amplitude Tomography

In order to investigate the utility of using amplitudes for imaging the FRI zone we decided to use the 1988 data to invert for attenuation information. We felt that because no mechanical clamping was used for the source, and only fluid coupling was used in the 1988 data, source and receiver effects would be minimized.

The first arrival wave amplitudes may be inverted for the attenuation field using the same inversion process used for the travel times through the equation

$$P_k = -\ln\frac{A_k}{A_0} = \int_{R_k} \alpha(x,y)ds \tag{4.2}$$

where P_k is the "projection" of the ray, A_k is the measured amplitude, A_0 is the source amplitude, R_k is the ray path, and $\alpha(x,y)$ is the attenuation at the x,y coordinate. Additional data processing must be performed to properly determine the amplitudes, and assumptions are made for the cause of the dissipative mechanisms of medium. It is assumed that the measured amplitude is a sufficient measure of the initial energy received and that the data can be corrected for the geometric spreading and the source radiation pattern with the remaining energy dissipation due to the intrinsic attenuation of the medium.

The wave amplitude, A_k, is considered to be a measure of the received energy and is usually measured from the peak-to-peak or zero-to-peak amplitude of the initial arrival. A comparable value is the square root of the power, which is a more stable parameter. The power is determined by the formula

$$P = \sum_{i=1}^{N} \Delta t \, |A(i)| / N \tag{4.3}$$

where Δt is the sample rate, A(i) is the amplitude at time i, and N is the number of samples in the specified window. We took a window of 66 samples, or 0.264 msec, i.e., the initial arrival to about one and a half cycles. The total energy from all three components were added to determine the total energy.

The amplitude values must be corrected for geometric spreading and the radiation pattern.

The geometric spreading correction simply multiplies the amplitude value by the distance traveled. The radiation pattern is assumed to be a cosine function with θ measured from the horizontal. The actual radiation pattern was checked by performing measurements in boreholes BOAU 83.002 and BOAU 83.003 to the south of the FRI site. The geologic logs of these boreholes show no fractures or anomalous zones between 5.0 and 10.0 m down each hole from the access tunnel. In order to accurately determine the radiation pattern of the source, the attenuation, α, of the rock must be known. A simplistic method of determining α is to take two measurements at two different source-receiver offsets and apply the formula:

$$\alpha = \frac{1}{x_2 - x_1} \ln \left[\frac{A(x_1)}{A(x_2)} \right] \tag{4.4}$$

where x_1 and x_2 are the two offsets and A_1 and A_2 their respective amplitudes. We again calculate the amplitude from the power formula. For the source-receiver offset, we used the path directly across boreholes BOAU 83.002 and BOAU 83.003, a distance of 1.0 m at $\theta = 0°$. For this offset, A_1 = 15402 and x_1 = 1.0. Source-receiver offset A_2 was taken from across boreholes BOFR 87.001 and BOFR 87.002, a distance of 10.0 m at $\theta = 0°$. Although there were a total of 40 direct crosshole measurements taken between these boreholes, most of the ray paths intersect at the fracture zone. Because only the background attenuation is wanted, the values for the five largest amplitudes were calculated and averaged. In this case, A_2 = 1300 and x_1 = 10.0. Applying Equation (4.2), α becomes 0.3 m^{-1}. We calculated the Q of the medium by using the equation

$$Q = \frac{\pi f}{\alpha v} \tag{4.5}$$

assuming a velocity of v = 5200 m/s and frequency f = 6000 Hz, a value of about 12 was obtained for Q. Because the ray paths were not common, Q becomes relative.

The radiation pattern for the source was obtained by plotting the observed amplitudes $A(x,\theta)$ with the calculated amplitudes $A_o(x,\theta) = e^{-\alpha x}$ for several angles, and fitting the resulting curve with an angular function. The values used are from the tests carried out between boreholes BOAU 83.002 and BOAU 83.003. The amplitudes are plotted in Figure 4.16 along with the values for a cosine function. As expected, the values fit closely to the cosine function. The

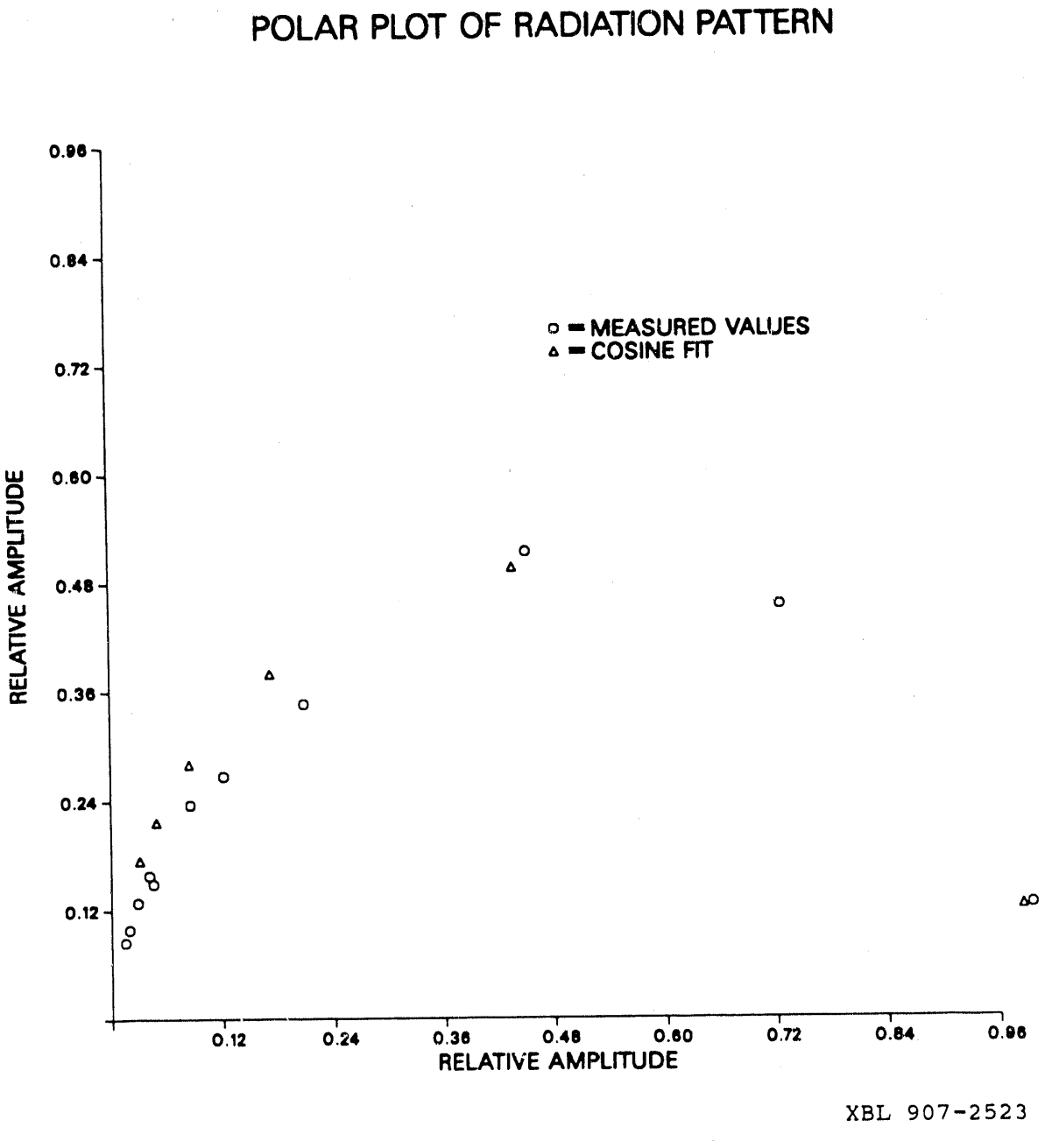

Figure 4.16. Measured radiation pattern of the 1988 source.

difference may be due to a slightly erratic value for α and the attenuation anisotropy of the medium. The amplitudes were then corrected for the radiation pattern by dividing each value by $\cos\theta$.

The source amplitude, A_0, is a difficult parameter to determine. The effect of having a poor value is the same as neglecting a constant time correction when inverting travel time values. This usually results in excessive smearing and false anomalous zones. One method of estimating the source amplitude is to solve Equation (4.2) for A(x=0) given α:

$$A(x=0) = A(x_2)e^{\alpha x_2} \tag{4.6}$$

Using x_2 = 1.0 m, $A(x_2)$ = 15402 and α = 0.3 m^{-1} the source amplitude becomes 21000. This value was used for A_0 in Equation (4.1).

The same inversion routine was used to invert amplitude data as was used to invert travel time data. The amplitudes were calculated and corrected for each source-receiver offset, producing the same number of data points as for the travel time inversion.

The inversion was first performed on a 33 x 66 pixel map (Figure 4.17). The shading ranges from 0.31 m^{-1} (dark) to 0.28 m^{-1} (light) agrees with our calculated value of 0.31 m^{-1} for the background anisotropy. The values obtained in the inversion range from about 0.22 m^{-1} in the central region to about 0.65 m–1 in the damaged zone near the tunnel walls. As can be seen from Figure 4.17, this damaged zone dominates the image so that smaller anomalies are not evident. The only additional anomaly that is observed is located near the 10 meter point of borehole BOFR 87.001. This position coincides with a large velocity anomaly, the intersection of feature A and B, seen in the velocity tomogram (Figure 4.11).

An inversion was done with only the cross borehole rays to eliminate the contribution of the damaged zones to the result. This image (Figure 4.18) produces other anomalies, but the limited angular coverage and the large reduction of data seems to lead to some smearing. Using the crosshole data, the anomalous zone near the 10 m point of borehole BOFR 87.001 is more distinct. Other zones near the boreholes also coincide with highly fractured areas or with the velocity results. However, the large zone extending from the intersection of BOFR 87.002 and the

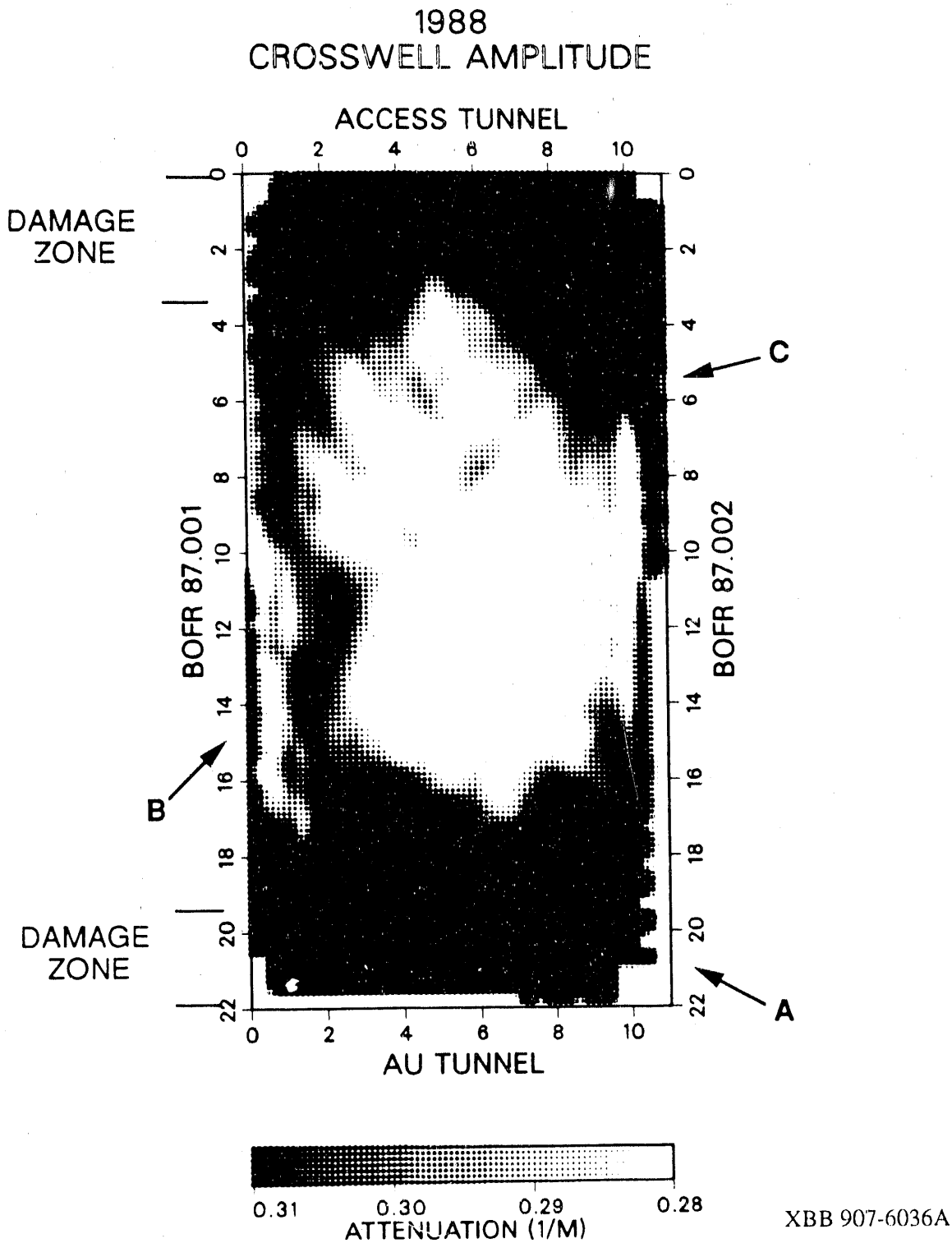

Figure 4.17. Result of inverting the 1988 amplitude data.

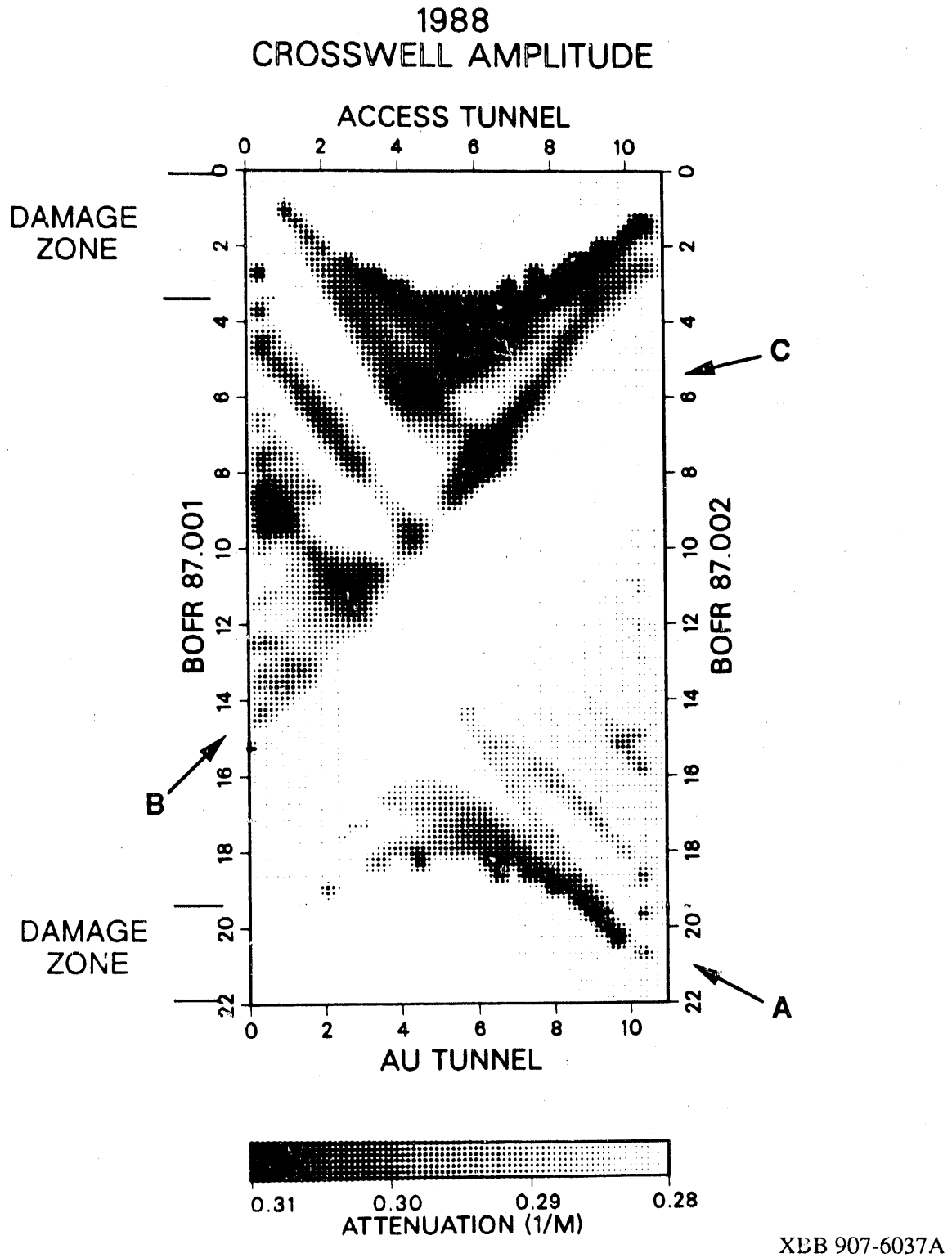

Figure 4.18. Result of inverting the 1988 cross borehole amplitude data.

access tunnel does not coincide with any other velocity or geologic feature except at the intersection itself. This anomaly seems to be due to a smearing, i.e. low ray coverage, of this known fracture zone toward the main anomaly, Feature A.

The attenuation results do not substantially improve our knowledge of the FRI region. They suggest that the most important feature besides the damaged zones is the low velocity/high attenuation anomaly near the middle of borehole BOFR 87.001. This zone is strongly identified in all the images. The cause of the feature is probably some intersection of fractures and/or lamprophyres.

However, the results do support the stiffness theory at these frequencies. The time delay produced by a large number stiff fractures would be negligible at these frequencies, but the attenuation effects would be significant. This is dependent on the number of fractures and the stiffness value. These parameters are unknown, but the damaged zone probably contains a large number of microcracks. The attenuation results also support the theory that the 1987 velocity tomogram is an effective combination of velocity and attenuation effects. The attenuation measurement would have yielded much more information if we had used a data collection system with more dynamic range. Our system was a 12 bit system. A 16 bit system would have provided 16 times more contrast in amplitudes, thus providing a wider range of amplitudes to analyze.

4.6. Discussion of Results

Although not immediately obvious, after anisotropy corrections, the 1987 and the 1988 results show essentially the same features. We will first discuss how the two results compare, then analyze the best image in terms of what is known of the geology in the FRI site.

An obvious difference between the two results is the disappearance of the low velocity features near the tunnels in 1988 results (Figures 4.10 and 4.11). Because these features were the most dominant anomalies in 1987, a satisfactory reason must be found to explain its disappearance. As previously stated, the data quality was much better in 1988 than 1987 for several reasons. The source was more powerful and its repeatability improved. Also, when the source and/or

receiver were in BOFR 87.001 and BOFR 87.002 the coupling was improved over 1988 because both holes were water filled. We also stacked from 2 to 9 traces for each source receiver pair. These improvements increased the signal to noise ratio providing much more accurate travel time picks on higher frequency first arrivals. In effect, the reduced data quality in 1987 prevented the "proper" first arrival travel times to be picked in 1987. In some cases the value picked was a pulse or two later than the time picked in 1988. This is especially true where the attenuation is greater, e.g., the damaged zones adjacent to the tunnel and in the main shear zone. The entire 1987 travel time data for sources or receivers along the tunnels are probably picked consistently late, producing a velocity reconstruction which shows consistently lower velocities near the tunnels and resulting in a lower average velocity. This means that the 1987 tomogram was essentially a mixed velocity-attenuation tomogram.

Another difference in the results is that the shear zone (Feature A, Figures 4.10 and 4.11) becomes discontinuous and less dominant in 1988. This result is of great interest because this is the zone that we were initially trying to image. Also, Feature C is less obvious in the 1988 results, again a target of the hydrologic tests. In 1987, we had assumed that we had imaged Feature A satisfactorily as a several meter wide low velocity zone. However, the 1988 inversion does not show such an extensive feature, but a thinner zone which extends to about 4 m from the laboratory tunnel. The zone dies out for a meter, then reoccurs as a more massive feature with variable velocity. To show the actual difference in the results, the 1988 image is subtracted from the 1987 image pixel by pixel (Figure 4.19). (An inversion using the differences in travel times could not be performed because slightly different stations were used for a few of the sweeps). As can be seen from Figure 4.19, there is little difference between the two images except at the tunnels, suggesting that the 1987 low velocity zone in the region of the shear zone and Feature C exists in the 1988 result, but has a slightly different form and magnitude.

Both 1987 and 1988 images show a lower velocity near the intersection of the AU tunnel and the shear zone where the excavation of the tunnel may have "loosened" the fractures. The large low velocity features toward borehole BOFR 87.001 on strike with the shear zone are also

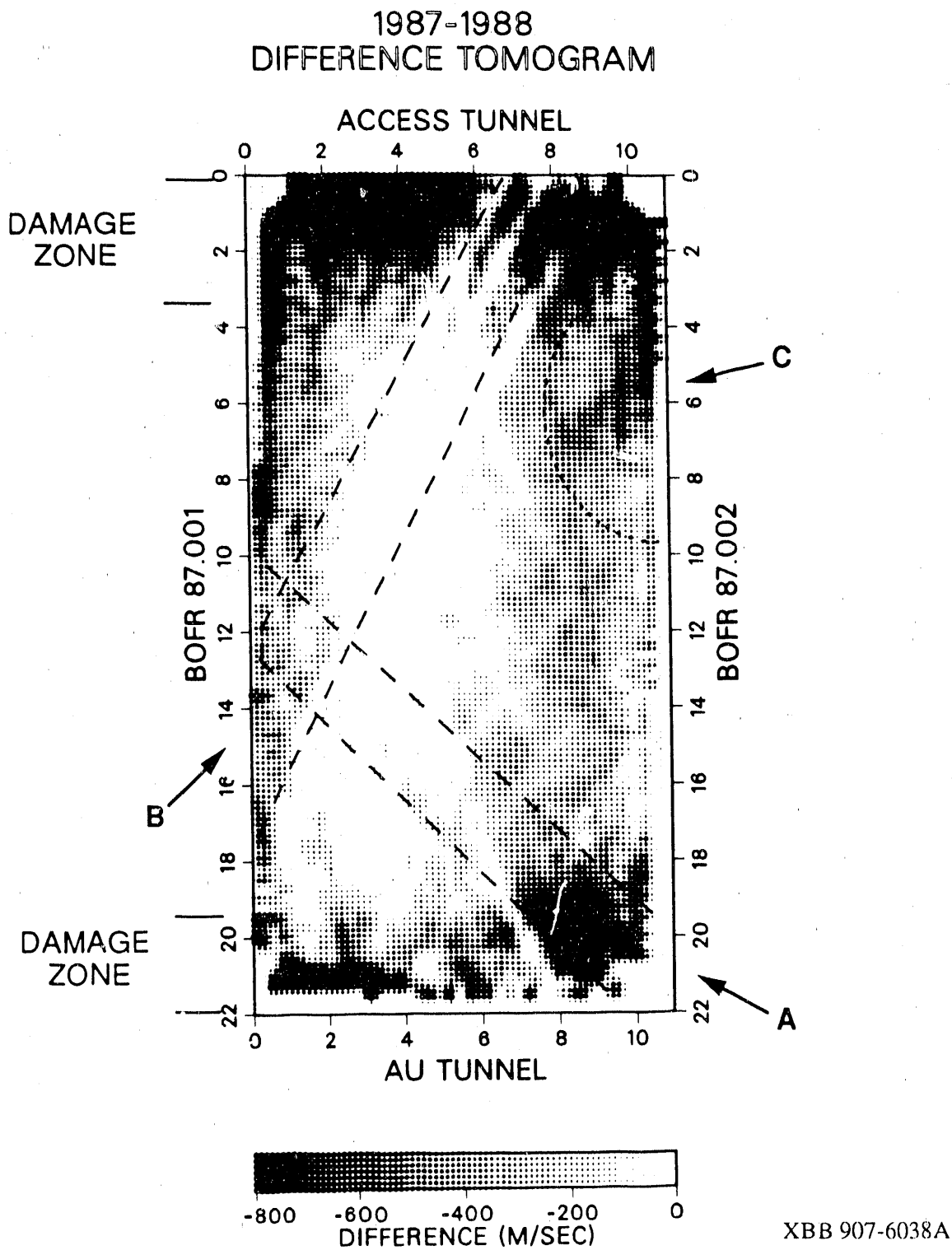

Figure 4.19. Difference between the 1988 and 1987 tomograms after anisotropy corrections.

comparably imaged in the 1987 and 1988 results.

The most unexpected result from the 1988 inversion is the dominance of the low velocity feature (Feature B), which extends from the intersection of the access tunnel and BOFR 87.002 intersection to the large low velocity feature near BOFR 87.001. As mentioned earlier extensive efforts through careful examination of the data were made to determine whether this is an actual zone of low velocity material or an artifact of the inversion process or some kind of error. The 1987 result does show a hint of this feature protruding from the large low velocity zone adjacent to the access tunnel. However, in the 1987 results it is not a dominant continuous feature and is obscured by the extensive damaged zone. Checking the plots of the difference between the 1987 and 1988 data, Figure 4.19, we see again that the difference is not significant. This indicates that the anomaly actually exists in the 1987 results, but it is overshadowed by the effect of the damaged zones. There is always the possibility that errors occurred in both years for several of the sweeps whose source was in this region, but this is unlikely. However, if these sweeps were removed from the data, the region of interest would not be fully sampled and the anomaly would not be adequately resolved.

The cross well results (Figure 4.14 and 4.15) are interesting in that they show that large velocity anomalies can be missed without adequate ray coverage. Feature A, B, and C are not seen in the resulting images because their proximity to the tunnels make them unresolvable. Without the tunnel-to-borehole paths, the sampling of the area near the tunnel is low, and the angular coverage is poor. The area of poor resolution extends at least 5 or 6 m from the tunnels. The crosshole results also show that the 1987 data produces a lower average velocity even when the tunnel rays are removed suggesting that there may be other reasons for this than poor travel time picks. Except for the different average velocities, the 1987 and 1988 images are quite similar. They both show an anomalous zone extending from about 7 m down borehole BOFR 87.001 to about 15 m down borehole BOFR 87.002 in the orientation of the shear zone. The magnitude of the anomaly is quite small which is why it is obscured in the results using the entire data sets (Figures 4.10 and 4.11).

4.7. Geologic Interpretation of the Results

The geologic map of the structures at FRI is shown next to the "final" 1988 tomographic image to assist in the interpretation (Figure 4.20). To be useful the interpretation of the tomographic images must include the geologic structure that is associated with each of the main features that are imaged and an explanation for the differences between the results of the 1987 and 1988 experiments. These include:

1. The large low velocity anomalies observed along the tunnels in the 1987 image which do not exist in the 1988 result.
2. The shear zone (Feature A) is observed in 1987 as a single large low velocity zone about two meters wide. The corresponding zone in the 1988 results consists of a very thin (< 0.5 m thick) zone which become discontinuous.
3. Feature B, which extends from near the access tunnel BOFR 87.002 intersection, to the middle of BOFR 87.001, and is, in fact, the dominant feature of the 1988 results.
4. Two strong low velocity features at the intersection of Feature B and the shear zone.

We have already mentioned that the low velocity zones associated with the tunnels in the 1987 results may be due to the initial P-wave pulse being highly attenuated. This was primarily due to a weaker source being used in the 1987 experiment. However, this does not explain why the 1988 velocity data did not resolve the damage zones, i.e., if there are damage zones with high fracture content, why did we not detect them in the 1988 velocity data. It is true that one explanation may be that the 1987 result only detected the damage zone by picking later arrivals because the initial pulse was attenuated, not slowed, and thus an artificially low velocity result was obtained. The attenuation data from 1988, however, did detect the damage zones near the tunnels. This suggests that at the frequencies we used, 5 to 10 Khz, the effect of these thin fractures on the velocity was much less than that on attenuation. This is in fact what the "stiffness" theory predicts. As frequency increases, for a constant stiffness, the velocity or delay becomes less relative to the attenuation effect. Apparently we were at frequencies where for the stiffnesses involved, attenuation is important and delay is less important.

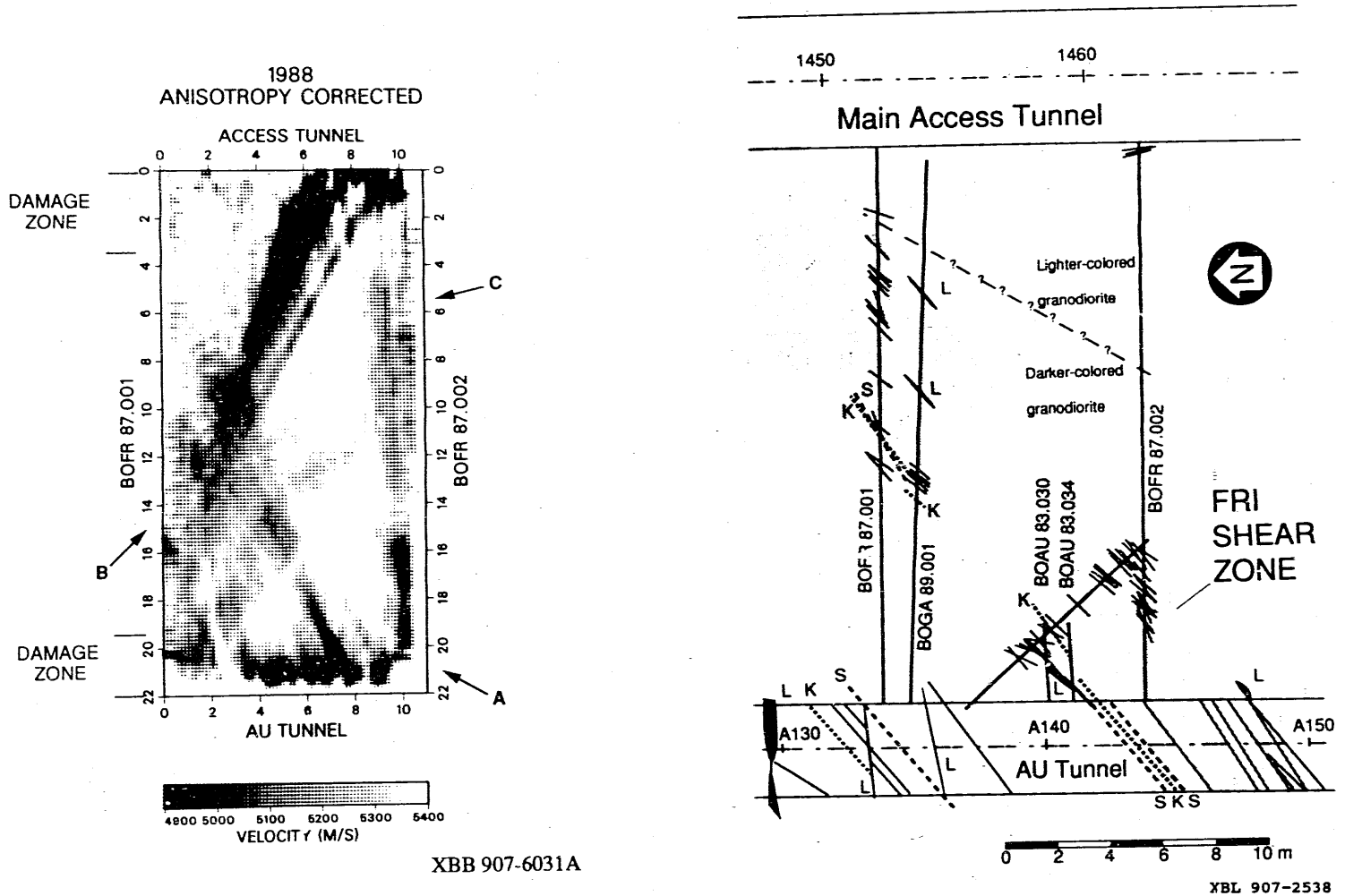

Figure 4.20. (a) The velocity tomogram for 1988 compared to (b) the geologic map of the FRI site.

In the final 1988 tomogram, the shear zone appears to produce a relatively weak velocity anomaly. The zone appears as expected from the 1987 results, but its form is altered in 1988. Although there is a visual difference, the actual differences are not great and may be due to the better resolution obtained in 1988. The 1988 results indicate that it is likely that the zone is not a simple single planar feature and thus the permeability along the zone may also be variable rather than being a single well connected feature. Figure 4.20 indicates that the shear zone produces a large velocity anomaly near the AU tunnel wall, until the point where this anomaly intersects a lamprophyre at about 4 m from the AU tunnel wall along the strike of the shear zone. The intersections of lamprophyres and shear zones are areas of more intense fracturing, probably causing larger velocity anomalies. This lamprophyre is probably discontinuous, being stretched along the shear zone during deformation. After this velocity anomaly dies out, another small low velocity anomaly is encountered at about 2 m further along strike of the shear zone. This anomaly may be another piece of lamprophyre or a region of high fracturing.

The most dominant feature in Figure 4.20 is Feature B, which extends from a highly fractured area in the access tunnel to the shear zone. It is unlikely that the anomaly is totally an artifact of the inversion or due to data errors since it occurs in the results from both years. The anomaly may not actually extend to the shear zone, but may be smeared somewhat in this direction. The visible fractured area at the access tunnel where the anomaly begins consists of subhorizontal fractures and a tension fissure. From geologic considerations, it is most likely that this feature is associated with a lamprophyre or an especially large tension fissure. The strike is different from the lamprophyres in the immediate area, but as noted in the geology section, lamprophyres are not consistent in their behavior, especially when associated with shear zones. Since the geologic information about this feature is sparse, the only way to validate its presence is to drill into it. A subsequent borehole (BOGA 89.001) was drilled parallel to BOFR 87.001, but unfortunately it was several meters away from the anomaly and could not validate the prediction.

Where Feature B intersects the shear zone, Feature A, two large anomalies are also

observed. These anomalies may be areas of intense fracturing, most likely due to lamprophyres intersecting the shear zone. A small lamprophyre was logged in borehole BOGA 89.001 (Table 2.1) which coincides exactly with one of these anomalies. The other anomaly coincides with a kakirite zone which also indicates a region of increased fracturing. These anomalies also suggest that there may be hydrologic communication across the shear zone in this region.

Except for Feature B, all the anomalous velocity zones are coincident with geologic structures. Feature C is still not verified, but the core suggests a different rock type, lighter colored granite, rather than fracturing may be the cause of this feature. Although the core from this region were not tested, the testing of the other core from the FRI zone suggested that the lighter colored granite has lower velocity than the more altered darker colored granite (Chapter 3). The two low velocity anomalies near borehole BOFR 87.001 were interpreted as zones of intense fracturing likely due to the presence of lamprophyres. Borehole BOGA 89.001 was drilled, and validated this interpretation. Though the geologic information determined the possibility of such fractured regions, these anomalies could not be located by geologic data alone. It is always possible that feature B could be an artifact caused by some data error. However, there is no basis on which to reject its existence since it is observed in both the 1987 and 1988 results. Direct examination leaves little doubt that there is some anomalous zone that exists near the tunnel wall, probably a tension fissure.

Overall, the tomographic inversions seem to successfully image the major structures in the test region. At the frequencies used, the tomograms do not successfully image the minor structures such as individual fractures. The main conclusions from these tests are:

1. The velocity anomalies observed associated with fracturing were not due to single fractures but groups of fractures.

2. The seismically important features associated with fracturing were fracture intersections and fracture-lamprophyre intersections. These are also the structures that should be hydrologically important.

3. An interpretation of the results can not be done adequately without knowledge of the geology.

4. Structures were resolved that could not be anticipated from the borehole and tunnel data.

5. Although shear wave data were sparse, it is obvious that given the proper source, S-wave data would greatly aid in the interpretation of the geologic features.

6. The seismic visibility of the features from the amplitude and velocity tomograms seem to support the stiffness theory.

5.0. HYDROLOGIC ANALYSIS OF FRI EXPERIMENT

5.1. Introduction

Geophysical methods can be used to obtain useful information for characterization of underground geologic systems. The next step is to assess the hydrologic significance of the features identified by the geophysical methods. Geophysically significant features are not always hydraulically important and vice versa. In seismic methods, attenuation and velocity are measured as a seismic wave travels through a rock. In other words, it is a point to point measurement of the mechanical properties of the rock. On the other hand, hydraulic behavior is not entirely governed by the mechanical properties of a rock, although it is closely related. It is the connectivity of the void spaces that controls the overall hydraulic properties.

At the Grimsel test site, LBL and Nagra designed hydraulic tests in conjunction with the seismic tests described in the previous chapter. The tests were conducted by the company SOLEXPERTS AG under the supervision of Nagra. In this chapter, we will describe how the information obtained by geophysical investigations was used to design hydrologic investigations. We will then discuss the hydraulic results and analysis of the hydraulic tests. In particular we will focus on the anomalous interference data and attempt to find an explanation for it. We will also try to relate the analysis to seismic and geomechanic test results.

5.2. Background

5.2.1. Constant Pressure vs. Constant Rate Test

As a background we will briefly describe constant pressure tests, which were the type of tests conducted at FRI site. In a constant pressure test, the hydraulic head in an isolated interval is kept constant and the transient flow rate at the interval as well as pressure reaction in adjacent intervals are monitored. In most groundwater applications, however, constant flux tests are more

commonly used because in moderate to highly permeable rocks, it is generally easier to achieve and maintain a constant flux, q, than a constant pressure from the onset of the test. Therefore, analytical solutions are more readily available for constant flux tests. The majority of the published papers in the literature are based on constant flow rate tests. Constant flow tests are also easier to analyze because the type curves have somewhat more distinct shapes compared to constant pressure tests. In the latter, the type curve matching of q| vs. time data from the pumping well is less difficult because the curves are more or less flat. In analyzing constant pressure crosshole tests, pressure vs. time type curves have to be developed for each observation well at different radial distances. This is because the constant pressure solution is not similar in $Kt/S_s r^2$. The constant rate boundary condition is in general mathematically easier to work with to develop a new analytical model.

However, constant pressure tests do have advantages. In very low permeability rocks, like the one at Grimsel test site, constant pressure is generally easier to achieve than a constant rate. It is also easier to minimize the wellbore storage effect in a constant pressure case. Moreover, because the rock near the wellbore is subjected to a constant pressure throughout the test, there is less concern about the permeability changing as a function of time (pressure). However, the permeability may change in the location away from the well as the pressure front propagates into the rock.

Whichever method is used, when conducting well tests in a tight fractured rock, it is important to measure early time data as accurately as possible. Transient data reflects the change of permeability in space as a function of time. In this regard, transient data is more descriptive of the rock heterogeneity than steady state data, which is influenced by the spatial arrangement of heterogeneity in an unknown way. Especially when there is a skin zone near the well, one should be able to evaluate the properties of the zone if there is good transient data for both the flow period and the shut-in period.

5.2.2. Constant Pressure Solution

The dimensionless pressure in Laplace space for a constant pressure test with skin in an infinite homogeneous two-dimensional system can be written as:

$$\bar{h}_D(r_D,p) = \frac{K_0(p^{1/2} \cdot r_D)}{p[K_0(p^{1/2}) + s(p^{1/2}) \cdot K_1(p^{1/2})]} \quad , \tag{5.1}$$

and for dimensionless flow, the solution is:

$$\bar{q}_D(p) = \frac{K_1(p^{1/2} \cdot r_D)}{p^{1/2}[K_0(p^{1/2}) + s(p^{1/2}) \cdot K_1(p^{1/2})]} \quad , \tag{5.2}$$

where p is the Laplace space variable, s is the skin factor, r_D is the dimensionless radius, and K_0 and K_1 are the modified bessel functions of the second kind of zero-th and first order, respectively. The solutions in real space, h_D and q_D, can be obtained by inverting Equations (5.5) and (5.5) numerically (Figures 5.1 and 5.2). For references readers may consult Carslaw and Jaeger (1945), Van Everdingen and Hurst (1949), and Ehlig-Echnomides (1979).

5.3. Test Configuration

The hydraulic tests were planned based on the 1987 tomography results (Figure 4.8). Packer locations are shown on Figure 5.3. Each test consisted of pumping water in the interval at a constant pressure and monitoring in all the other intervals. Objectives of each test were

1. to find hydraulic connection with other zones,
2. to characterize the properties of zones that are hydrologically active, and
3. existence of zones about which we have only inconclusive evidence.

The purpose of Test 1 was to provide a hydrologic characterization of a feature which is clearly evidenced by geophysics. The packers for Interval I1.2 were placed such that they confine the main fracture zone (corresponding to Feature A on Figure 4.8) as tightly as possible in order to minimize wellbore storage and isolate the hydrology of the feature. Interval I1.2 was used as the inflow interval and pressure was monitored in all the other intervals.

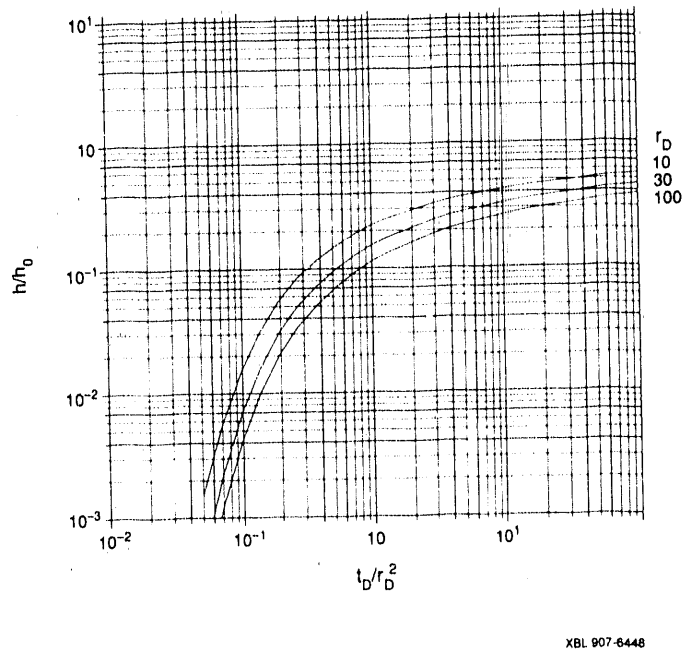

Figure 5.1. Dimensionless head at r_D = 10, 30, and 100.

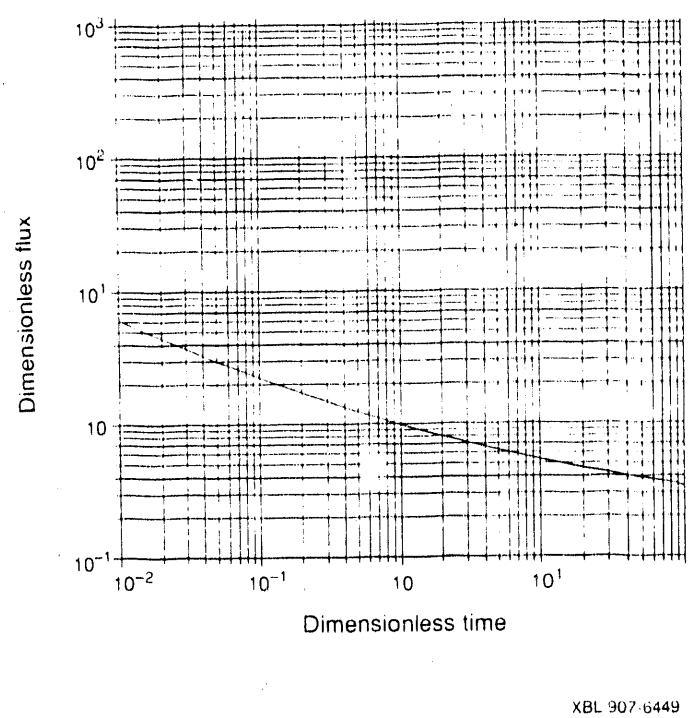

Figure 5.2. Dimensionless flow at the well.

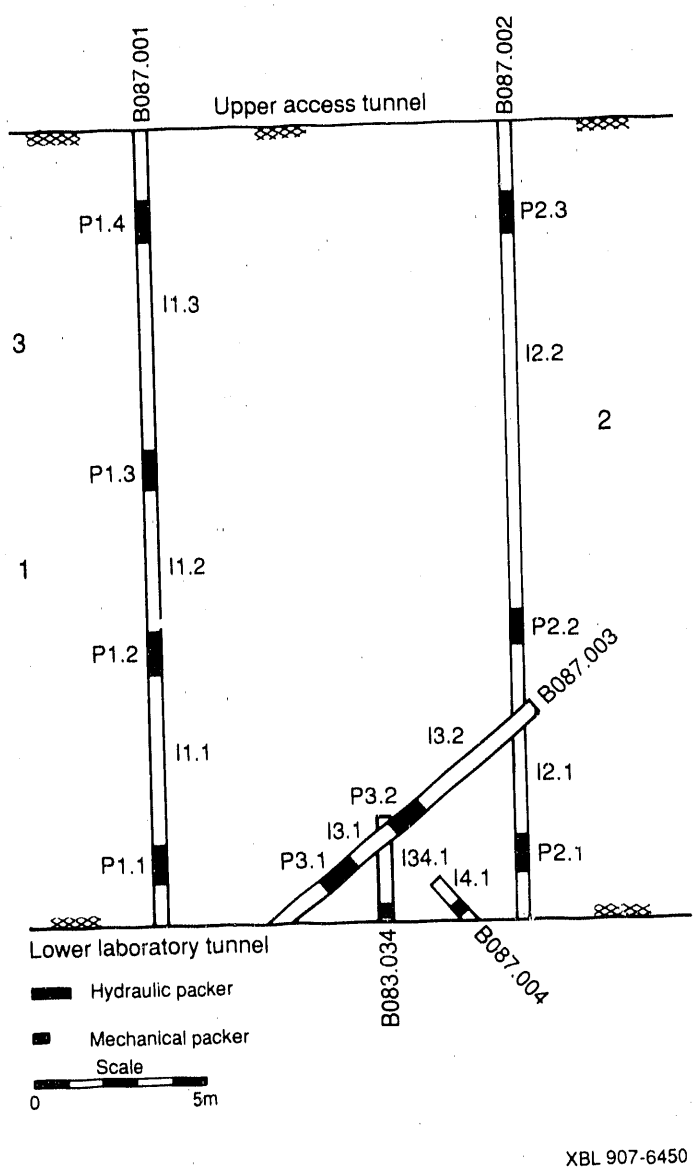

Figure 5.3. Packer locations used in Tests 1, 2 and 3 as of August 1988.

The purpose of Test 2 was to determine if the region to the north of I2.2 is hydrologically significant. This test would only have been conclusive if the result were positive. The tomogram of Figure 4.8 showed this area to be a low velocity zones (Feature C). A negative result would have meant that we did not find any connection between the low velocity region and any area being monitored. A positive test result would have been very significant because this feature had only been located with geophysics.

Test 3 was designed to understand the south-eastern part of the shear zone. Feature A appeared clearly in the tomogram as extending across the tomographic plane. A parallel feature to the south-east appeared in BOFR87.001 and in the BOFR87.002 core and nearby in the tomogram. However, the tomogram did not indicate that this part of the shear zone is continuous. The test was designed to determine if there is continuity or if there is a cross-cutting fracture connecting this part of the shear zone to I2.2 or I1.1.

5.4 Test Results and Analysis

In the present report, we will focus on the results of Test 1. Comparison with the results of Test 2 and 3 indicated that Feature A is clearly the most significant hydrologic feature at the FRI site as expected. In Test 2, a coherent analysis is difficult because although I2.1 did take up some water and a weak interference was observed in some intervals, some intervals were still recovering from Test 1. Therefore, there is no evidence that the low velocity zone to the north of I2.2 is hydrologically significant. A similar conclusion can be drawn for Test 3 results. A weak but definite hydrologic connection between Interval I1.2 and I2.2 was observed. Although the existence of a cross-cutting feature cannot be completely denied, one can postulate that the hydrologic significance is quite weak even if it does exist. Readers interested in the details of the test results are referred to Wyss (1988).

Figure 5.4 shows the pressure transient of interference data at various observation points in Test 1. Note that the interval I3.1 responds most markedly. The response data at I3.1 is compared to the theoretical response obtained by evaluating Equation (5.5) at r = 10.2 m, or r_D = 10.2 m/43 mm = 237 for s = 0 (Figure 5.5). As can be seen from the figure, the pressure observed at

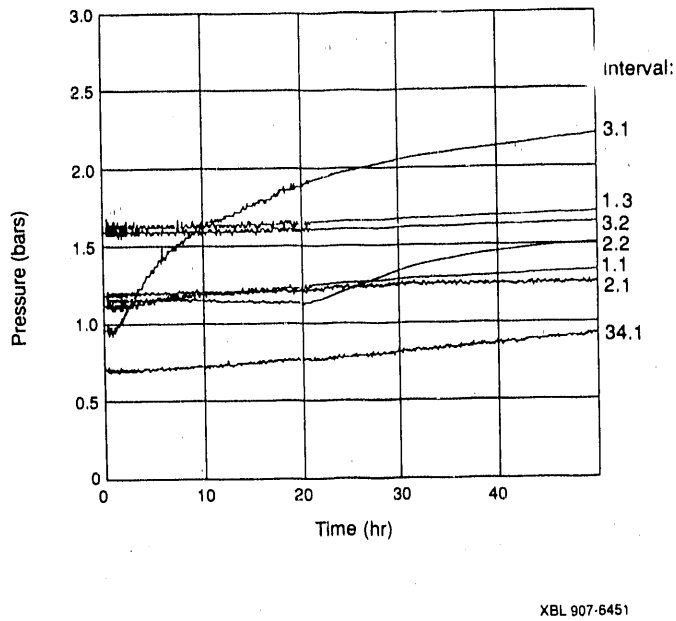

Figure 5.4. Interference buildup data for Test 1 at various observation points.

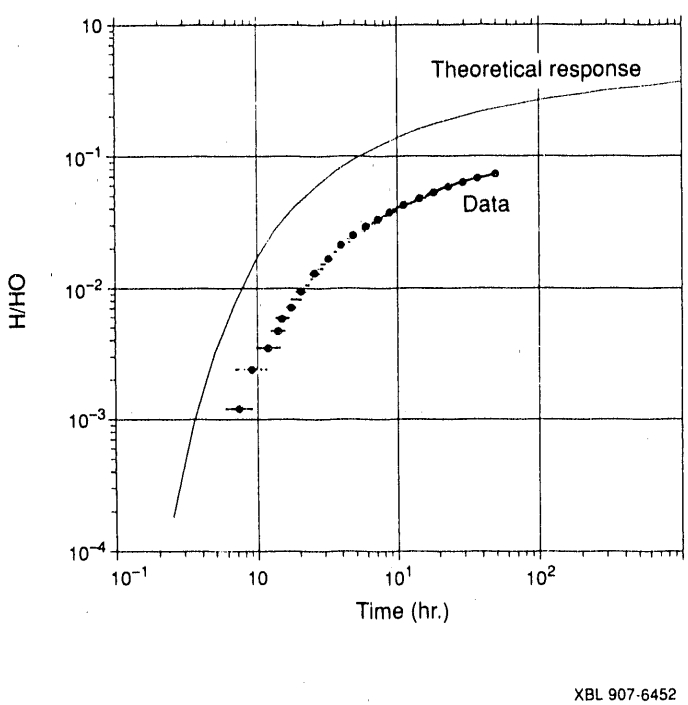

Figure 5.5. Comparison between data and the theoretical response curve.

I3.1 is significantly lower than that predicted by the analytical solution, although the shapes of the curves are almost identical. The analytical solution assumes that the fracture is infinite, isotropic and homogeneous. Therefore, conditions must exist where one or more of the above assumptions are not appropriate. The plausible scenarios are:

1. Skin: There is a low permeability zone around the injection well, i.e., a skin that causes the effective pressure at I1.2 to be lower.
2. Anisotropy: The fracture is anisotropic where the maximum permeability direction is oriented vertically.
3. Leakage: There is leakage from the fracture to the adjacent rock so that the pressure is more dispersed.
4. Boundary Effect: The boundary effect of the laboratory tunnel is keeping the pressure low at I3.1.

In the following sections, more detailed discussions will be given for each case, although in reality all of the above conditions may coexist. As is the case with any field experiment, the possibility of an erroneous measurement should not be completely discounted. For example, the pressure loss through the tubing may not be negligible. However, we will limit our discussions to the effects of the hydrologic features in the rock only.

5.4.1. Skin

Skin effect is usually suspected when anomalous results are obtained. Equation (5.5) can be used to obtain pressure response curves at I3.1 for various values of skin factor, s. Figure 5.6 shows that the curve for s = 13 yields a relatively good match with the data except for the late time portion. However, an almost perfect match can be obtained if the pressure in I1.2 is assumed to be 6.6 bars, which is much lower than 19 bars (Figure 5.7). This is equivalent to assuming that there is a constant pressure loss of more than 12 bars at the borehole wall. However, this assumption contradicts the conventional skin concept where the pressure loss is assumed to be proportional to the flow rate. Because the test was a constant pressure test, the

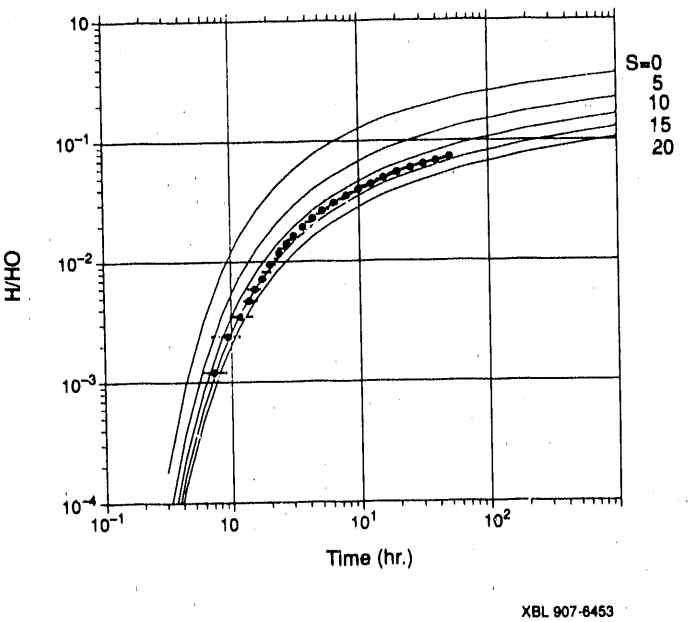

Figure 5.6. Type curve match with the skin curves.

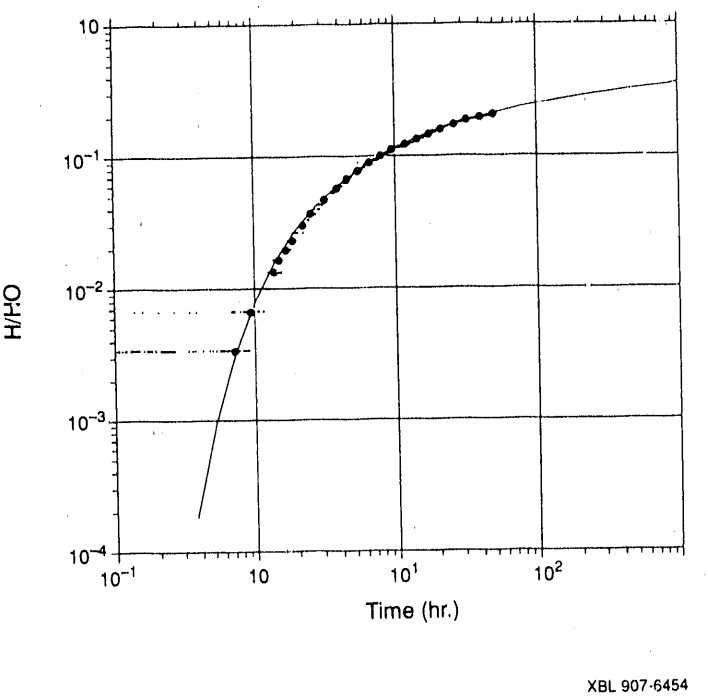

Figure 5.7. Type curve match assuming the lower injection head of 6.6 bars.

flow rate in I1.2 varied with time as shown in Figure 5.8. As can be seen in the figure, there is an inflection point in the curve at around 0.18 hours, which cannot be explained by assuming an ideal homogeneous medium. Figure 5.8 also shows the dimensionless flow rate for various values of s. The curves are obtained by evaluating Equation (5.5). As can be seen from the figure, the flow rate curve does not match any of the skin curves. When considered in combination with the fact that the match for I3.1 is not very good, it seems that the conventional skin concept cannot explain the observed behaviors. If a constant pressure drop is assumed at the borehole wall independent of the flow rate, the flow rate curve would look identical to that of no skin. Although the no-skin curve is closer to the observed curve, it still does not explain the inflection in the flow rate curve.

5.4.2. Anisotropy

Geologic observations (Chapter 2) indicate that the fracture zone may be highly anisotropic with the highest permeability in the vertical direction. Thus the injected water may flow preferentially in the vertical direction. As a result, observed pressure head in the horizontal direction at I3.1 may become lower than that in the isotropic case. In this section, the effect of anisotropy on the interference pressure is investigated.

Analytical solutions for flow to a well in an anisotropic medium can be obtained through a transformation of coordinates. The transformation of a coordinate is equal to the square root of the ratio of the permeability in its direction to the geometric mean permeability. In the transformed coordinates, the governing equation for flow becomes identical to that in an isotropic medium. However, the shape of the well becomes elliptical. Kucuk and Brigham (1979) solved the flow equation in the elliptical coordinate system. The dimensionless pressure outside the well producing at a constant pressure in the Laplace space can be written as:

$$\bar{h}_D = \sum_{n=0}^{\infty} (-1)^n \frac{1}{2\lambda} \frac{A_0^{(2n)} Fek_{2n}(\xi,-\lambda)}{Fek_{2n}(\xi_w,-\lambda)} \cdot ce_{2n}(\eta,-\lambda) \quad , \tag{5.3}$$

where $\lambda = p/4$, $A_0^{(2n)}$ is Fourier coefficient, ξ, and η are space coordinates in elliptical coordinate system, and $Fek_{2n}(\xi,-\lambda)$, and $ce_{2n}(\eta,-\lambda)$ are Mathieu functions. To obtain the exact value of the

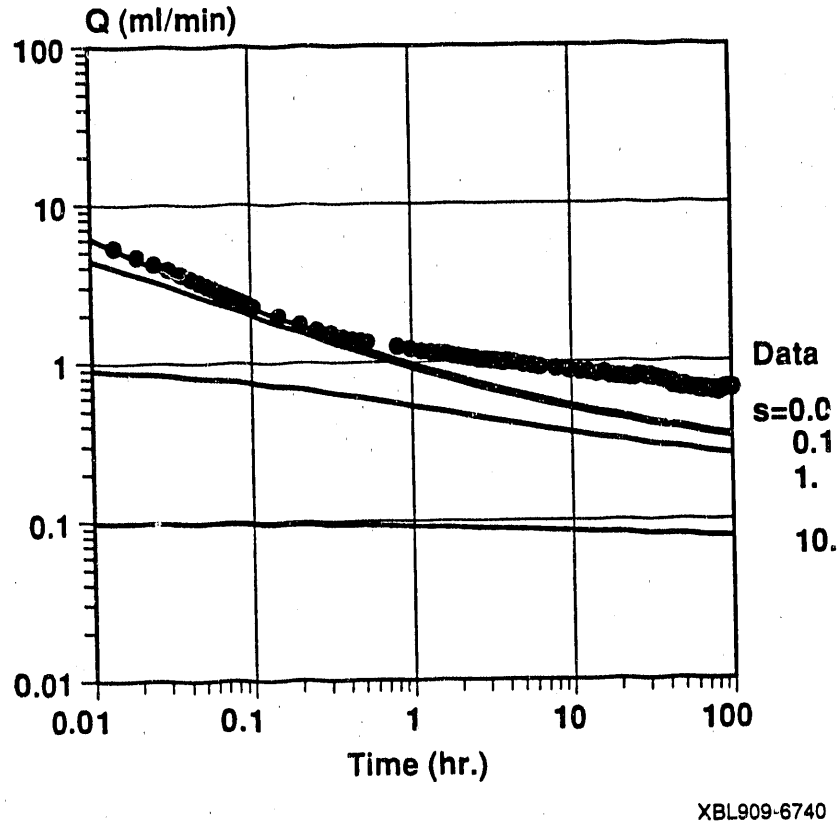

Figure 5.8. Flow rate decline curve. Also shown are the decline curves for various values of s observed at I1.2.

dimensionless pressure at I3.1, Equation (5.3) can be evaluated and transformed back to the Cartesian coordinate systems in the real space. Alternatively, an effective well radius can be used to approximate the elliptical well and Equations (5.5) and (5.5) can be used in the transformed coordinates. This approximation should be adequate because the dimensionless distance from I1.2 to I3.1 is large enough (r_D = 247) so that the elliptical shape of the well does not have much effect. Thus, a lower pressure than the theoretical pressure can be translated as a longer distance from the pumping well in the transformed coordinates. Figure 5.9 shows the dimensionless pressure at various r_D and the equivalent anisotropy ratio normalized to r_D = 247. As can be seen from the figure, an unreasonably large anisotropy ratio (2×10^9) is necessary to explain the pressure drop. Therefore, it is unlikely that anisotropy is the cause for the low pressure measurement. However, this does not preclude the existence of anisotropy itself.

5.4.3. Leakage

So far, it was assumed that the flow is confined within the fracture zone. However, as can be seen from Figure 5.5, interference responses, although small, were observed at various intervals that are not in the plane of the fracture zone. This implies that there was a leakage from the fracture zone into the adjacent rocks, which may explain why the interference response at I3.1 was low. The solution for pressure under a constant pressure test in a leaky aquifer is not readily available in the literature. However, if the thickness of the rock that leakage occurs into is assumed to be a finite size and that the leakage is at quasi steady-state, the solution presented by Da Prat et al. (1981) for a double porosity medium can be used. Figures 5.10 and 5.11 show the matches to the flow rate and the observed pressure at I3.1, respectively. As can be seen from the figures, although the flow rate match is very good, the match with the observed pressure at I3.1 is not good at all. The theoretical pressure is too high compared to the data. This is because the rock is assumed to be a finite size.

Let us now consider leakage into an infinite size rock. The Laplace space solution for the normalized pressure in the fracture zone at a nondimensional distance, r_D under a constant pressure test with leakage into an infinite size rock can be written as:

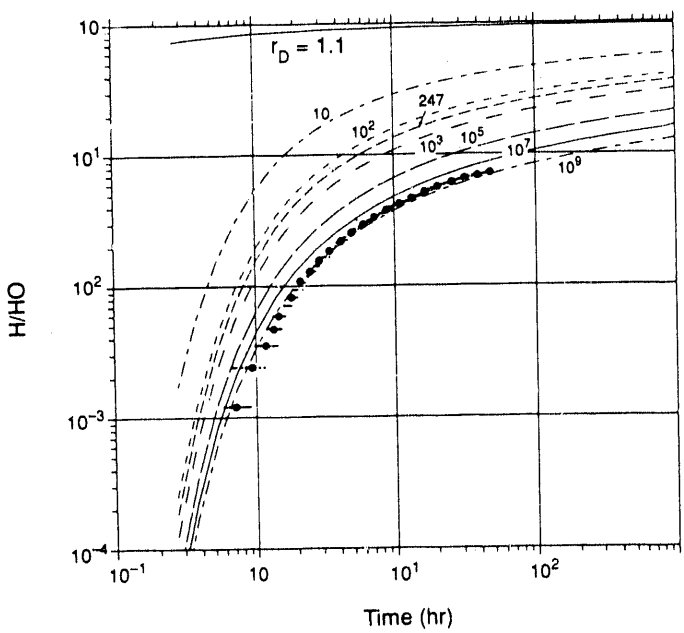

Figure 5.9. Dimensionless pressure at various r_D and the equivalent anisotropy ratio.

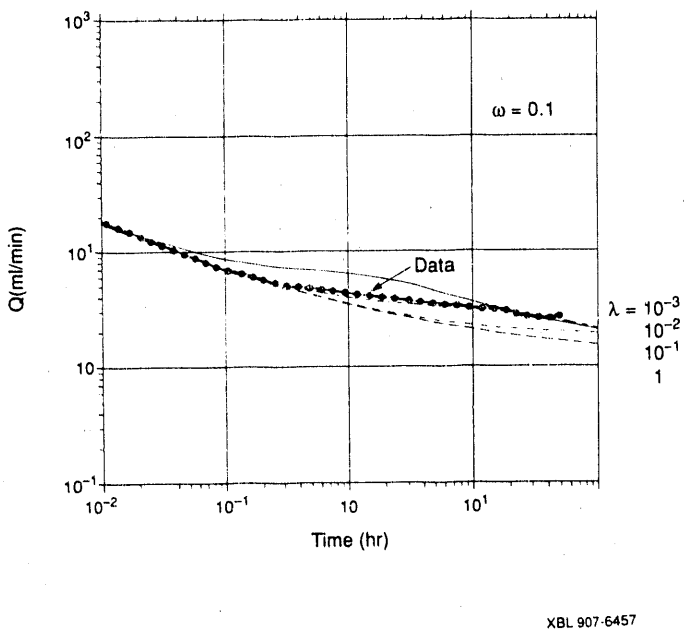

Figure 5.10. Type curve match of the flow rate with Da Prat et al. solution.

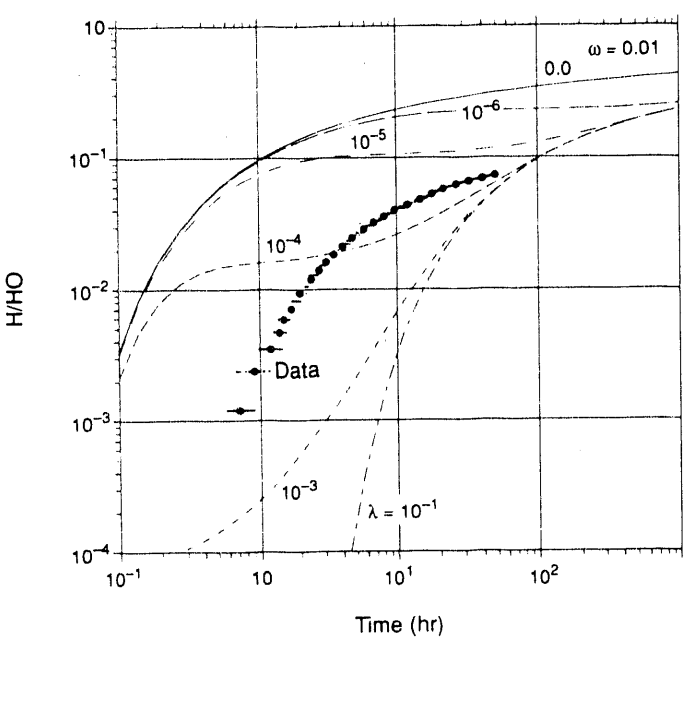

Figure 5.11. Type curve match of the pressure at I3.1 with Da Prat et al. solution.

$$\bar{h} = \frac{K_0\left[(S_{sD}\delta p)^{1/2} + p\right]^{1/2} \cdot r\right]}{pK_0\left[(S_{sD}\delta p)^{1/2} + p\right]^{1/2}\right]} \tag{5.4}$$

and the dimensionless flow rate at the well is simply:

$$\bar{q}_D = \frac{[(S_{sD}\delta p)^{1/2} + p]^{1/2} \cdot K_1\left[(S_{sD}\delta p)^{1/2} + p\right]^{1/2}\right]}{pK_0\left[(S_{sD}\delta p)^{1/2} + p\right]^{1/2}\right]} , \tag{5.5}$$

where S_{sD} is the ratio of the fracture specific storage to that of the matrix, K_D is the ratio of the hydraulic conductivity of the same, and $\delta = K_D/b_D^2$, where b_D is the ratio of fracture thickness to the well radius. Equations (5.4) and (5.5) are evaluated for various values of δ and plotted in Figures 5.12 and 5.13. Also plotted are the observed data. As can be seen in Figure 5.12, the match with the interference data at I3.1 is now much better compared to the case of Da Prat's solution. However, the late time data of I3.1 is still not matched very well. Also, the observed flow rate curve is much flatter in the late time than the theoretical curves (Figure 5.13).

Nonetheless, the concept of leakage seems to explain the trend of the data: low interference pressure, and the flattening of the flow rate curve. The weak hydrologic connection between Interval I1.2 and I2.2 may be through this low permeability rock matrix. It is worth noting that the 1988 seismic tomography results indicate the existence of a feature (B) that extends diagonally from the access tunnel toward BO87.001 (Figure 4.9). This may be the actual conduit of the leaking water. Although a localized leakage cannot be handled with an analytical solution, this will also explain the low pressure at I3.1 and the flattening of the flow rate curve.

5.4.4. Boundary Effect

In the previous analyses the boundary effects of the tunnels were neglected. However, during the injection test it was observed that water was seeping out thorough the shot-crete along the zone where the FRI fracture intersects the access drift (Peterson, personal communication 1989). In this section the effects of the drifts on the measured pressure is investigated. Because of the complexity of the geometry and the boundary conditions, a numerical model was used, where the FRI fracture is assumed to consist of a two-dimensional interconnected channel network (Figure

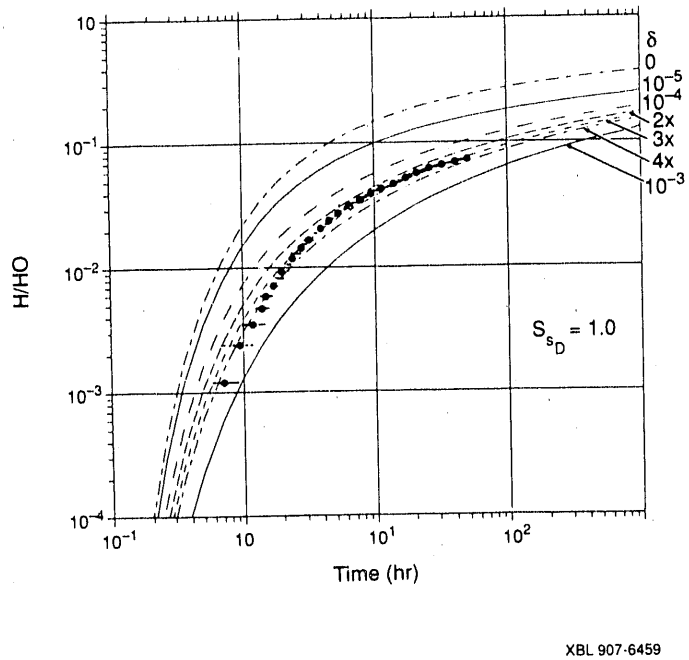

Figure 5.12. Type curve match at I3.1 with a leaky fracture zone solution.

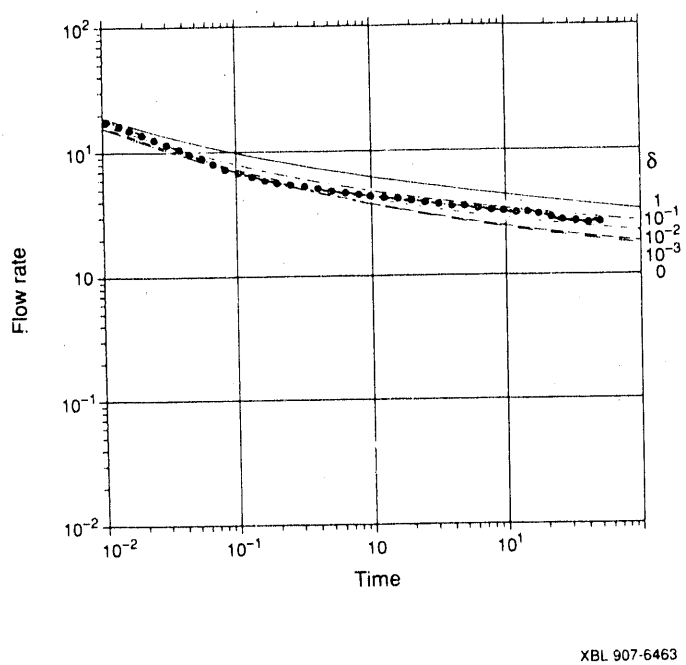

Figure 5.13. Type curve match at I1.2 with a leaky fracture zone solution.

5.14). Both models were assumed to be initially at steady-state subjected to the same hydrostatic head. Then the node that corresponds to the location where the interval I1.2 intersects the fracture was opened to simulate the field test. Results of the simulated well test are compared using the cases with and without tunnels. Figure 5.15 shows the comparison of the pressures at I3.1. As can be seen from the figure, the effect of the tunnels is felt at time equals 10. The curve for the case with the tunnels flattens and deviates compared to the case without the tunnels, as the pressure in I3.1 responds to the atmospheric pressure in the laboratory tunnel. However, the actual data shows no sign of flattening as can also be seen in the figure. The effect of the laboratory tunnel on the interference data at I3.1 seems to have been minimal. This indicates that the permeability of the fracture around the laboratory tunnel is low. This agrees with the observation (Peterson, personal communication 1989) that no apparent increase of water seepage was noted in the vicinity where the FRI fracture intersects the laboratory tunnel.

Figure 5.16 shows the comparisons between the flowrates at I1.2 for the two cases. The figure shows that the effect of the tunnels would be seen as a flattening of the flowrate decline curve. However, it is not as significant as the previous case. The inflection in the actual data cannot be explained by the effect of the tunnels alone.

5.5. Conclusions

The hydraulic tests have confirmed the hydrologic significance of the fracture zone which was previously identified by the seismic tomography. It appears that the majority of the flow occurred within the relatively thin fracture zone which connects Interval I1.2 and I3.1. A weak but definite hydrologic connection between Interval I1.2 and I2.2 was also observed. Feature B identified by the seismic tomography that extends diagonally from the access tunnel to BOFR87.001 may partially explain this hydrologic connection.

Because of the anomalous interference and flow-rate data, four different scenarios that differ from the ideal conditions were examined. They are 1) skin, 2) anisotropy, 3) leakage, and 4) boundary effects. Although it is possible for all of the four conditions to coexist, the most plausible scenario seems to be the leakage effect outside of the fracture plane.

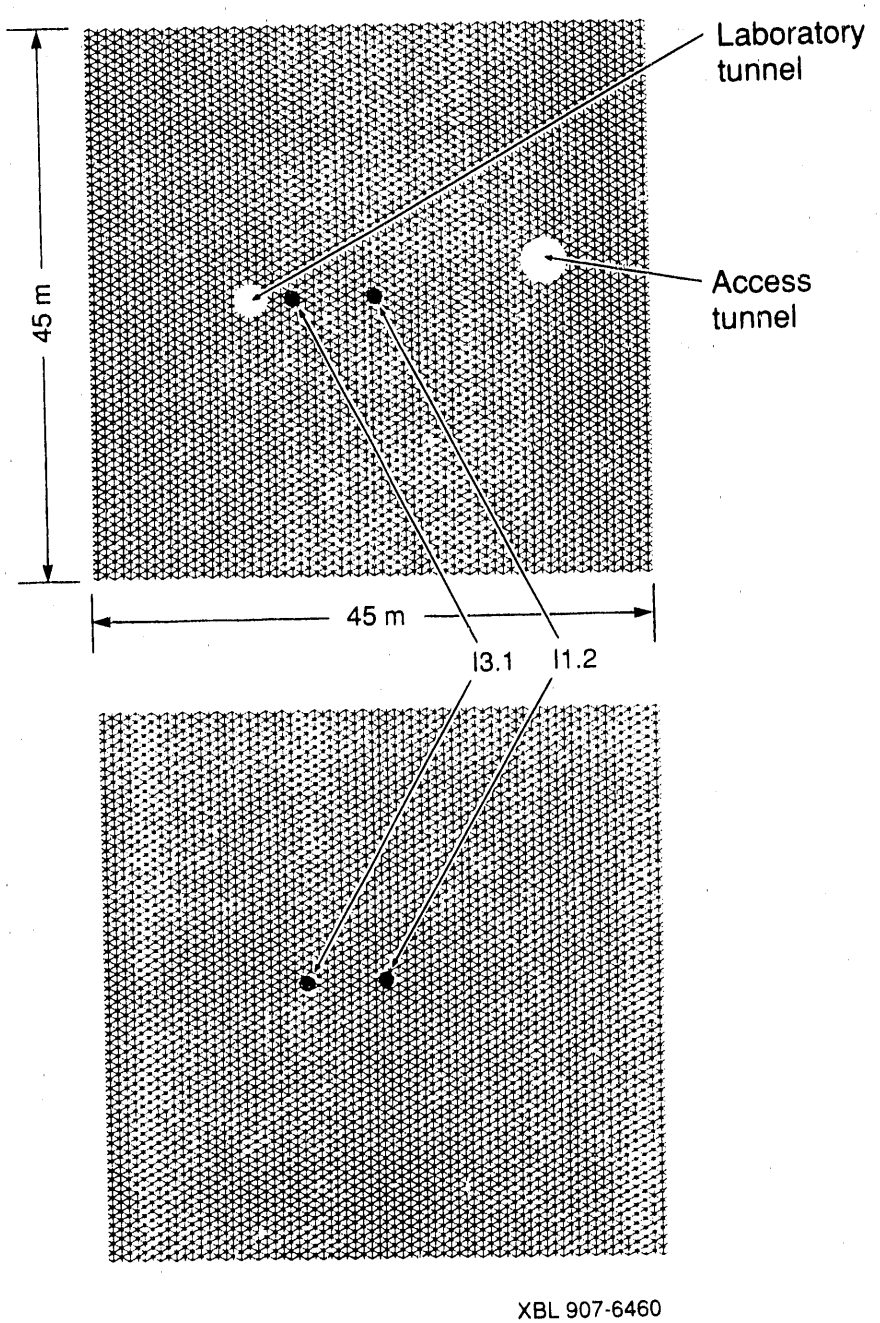

Figure 5.14. Numerical model of the FRI fracture a) with and b) without tunnels.

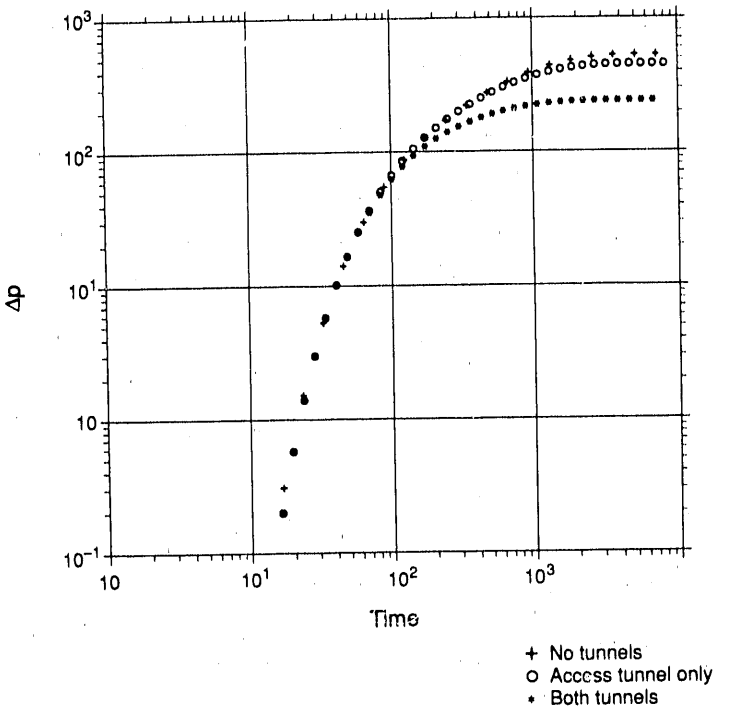

Figure 5.15. Simulated data for the pressures at I3.1.

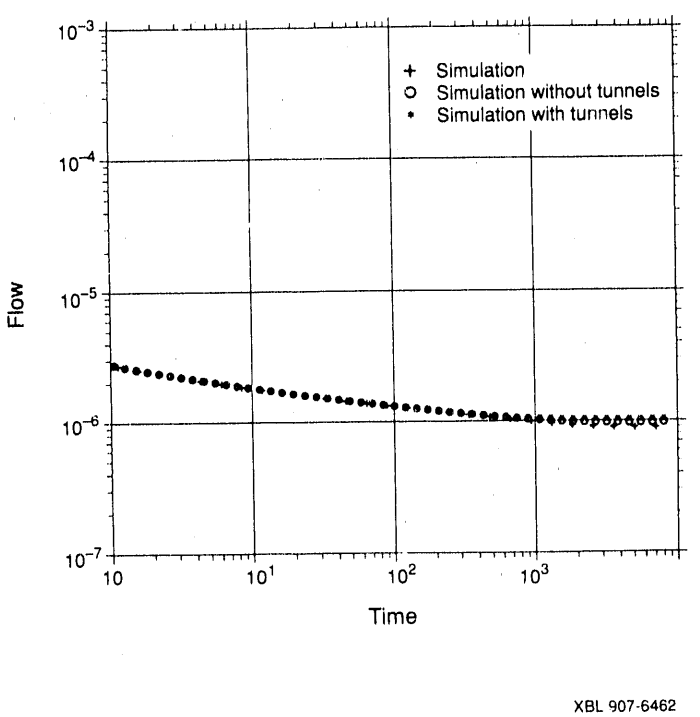

Figure 5.16. Simulated data for the flow rates at I1.2.

6.0. INFLATION TESTS

6.1. Introduction

The purpose of the inflation tests was to determine the mechanical stiffness of the kakirite fracture intersected by BOFR 87.001 and BOFR 87.003 in order to evaluate the influence of changing fluid pressure in this fracture on seismic waves propagation and hydrologic behavior. The mechanical stiffness of the kakirite fracture in the FRI was pertinent to interpretation of both the in-situ hydrologic and seismic experiments. Relative to the hydrologic measurements, storativity of a fracture is directly related to fracture stiffness. In addition, the fracture stiffness relates the applied stress to the changes in fracture aperture which significantly affects the permeability of the fractures. With respect to the seismic measurements, the objective was to obtain an in-situ measurement of fracture stiffness which could be input into the theoretical model to predict the effect of the fracture on seismic wave propagation. If changes in fluid pressure were sufficient to change the fracture stiffness, then the effects of this change would be observed in seismic measurements made during the inflation tests.

6.2. Description of the Experiment

In order to determine the stiffness of the fracture it was first necessary to measure the deformation of the fracture in response to a change in stress across the fracture plane. The change in stress was provided by pressurizing an interval between two packers. In order to perform deformation measurements while at the same time pressurizing the fracture, special equipment, the Bofex, which is schematically illustrated in Figure 6.1 was required. This figure shows that the displacement measurements were made between two anchors fixed in the borehole. The linkage between the anchors passes through the mandrel of the packers, so the anchors are independent of packer deformations caused by water pressure changes. The displacement transducer is

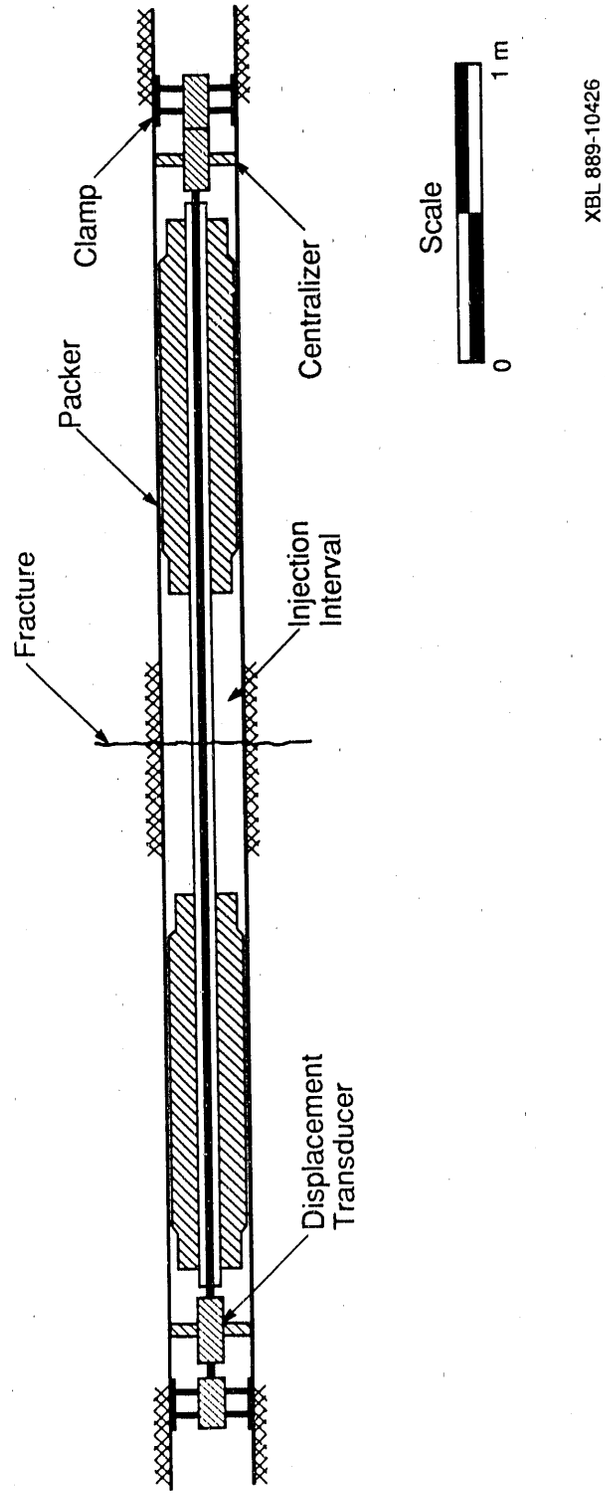

Figure 6.1. Bofex instrumentation for fracture displacement measurements.

rigidly attached to one anchor (clamp at right in Figure 6.1). A spring-loaded plunger in the transducer rests against the other anchor (at left in Figure 6.1) The output of the displacement transducer was ± 10.0 V for a total possible displacement of ±6.35 mm (0.25 in). The electronics provided a 1 mV sensitivity, so the displacement resolution was 0.64 μm.

As discussed in Chapter 5, interval I1.2, which contained the kakirite fracture was about 4 m long (Figure 5.3). This interval encompassed several fractures. Inspections of the core from BOFR 87.001 and BOFR 87.003 suggested, however, that the kakirite fracture (which actually consisted of two closely spaced fractures in the core from BOFR 87.001) was the principal conductor. For the inflation tests, interval I1.2 was therefore shorten d considerably and centered over the kakirite fractures. Packer locations are shown in Figure 6.2 and tabulated in Table 6.1. Similarly, new packer locations were determined for BOFR 87.003.

BOFR 87.001 and BOFR 87.002 were filled with water by placing packers in the end of the holes as shown in Figure 6.2. Packer P1.1 was a special design with a seal so that the push rod for the seismic transducer could pass through the packer while keeping water in the borehole.

Packers P1.2 and P1.3 were inflated simultaneously after the hole was filled with water. Packer P3.1 was inflated in BOFR 87.003 first. Then the borehole was filled with water and packer P3.2 was inflated. This procedure assured that no air was in the injection intervals I1.2 and I3.1. Packers in BOAU 83.034 and BOFR 87.004 were not disturbed. Therefore, for the inflation test, water pressures were monitored in intervals I1.2, I3.1, I34.1 and I4.1.

In order to accommodate the seismic measurements, pressure and flow tubes to interval I1.2 were routed up BOFR 87.001 to the access tunnel, back through another borehole to the laboratory tunnel and then to the monitoring apparatus, a distance of about 150 m. Packers P1.2 and P1.3 were inflated to about 50 bars and P3.1 and P3.2 were inflated to about 30 bars. When packers P1.2 and P1.3 were inflated the pressure in I1.2 increased to 15 bars and a slight reaction was noted in I3.1. The 15 bar pressure was held only momentarily. Interval pressure in I1.2 and I3.1 were left to stabilize overnight at about 1.5 bars.

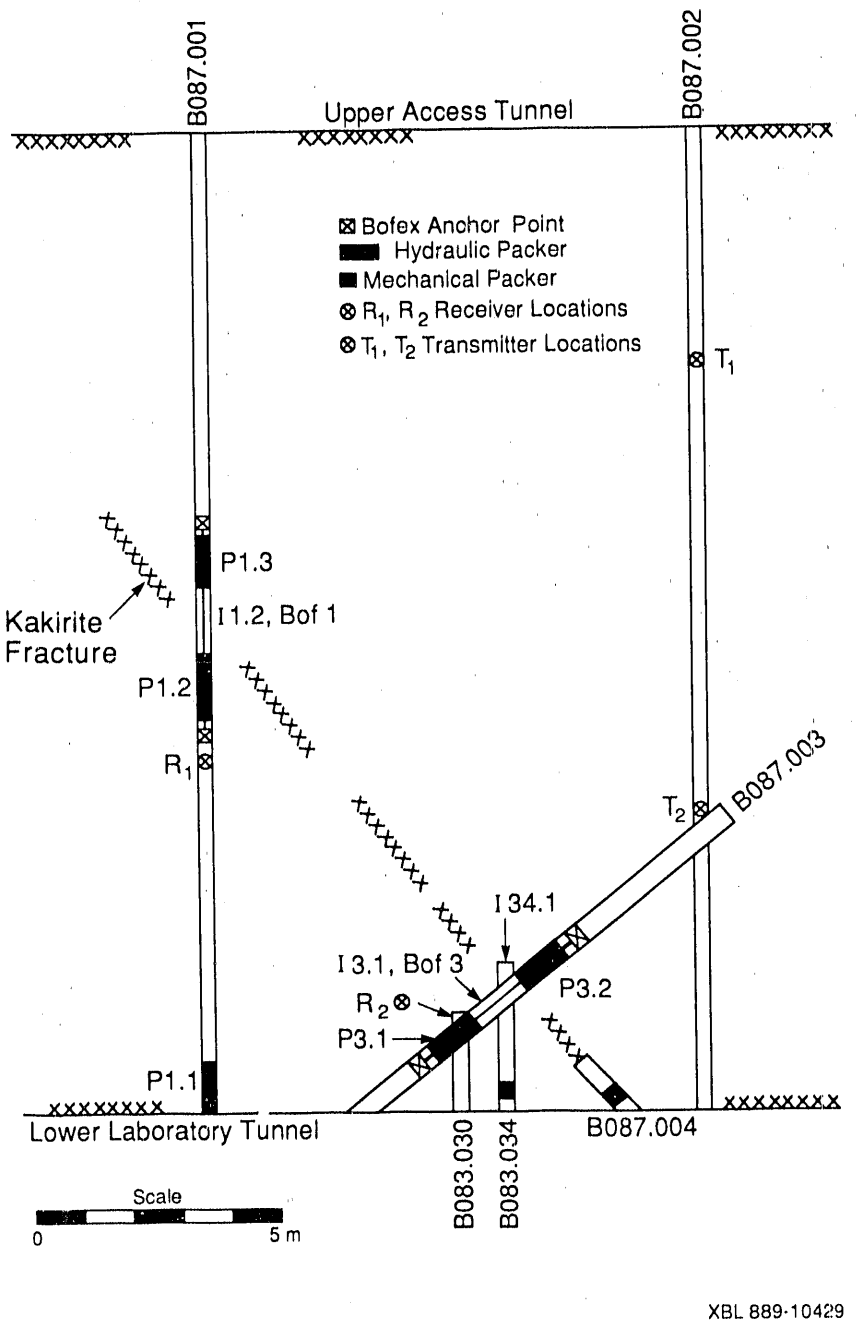

Figure 6.2. Plan view showing instrumentation locations for inflation test.

Table 6.1. Packer and interval locations for inflation tests

Hole	Packer	Interval	Location in Borehole (m)
BOFR 87.003	P1.1		0.0 - 1.0
	P1.2		8.6 - 9.6
	P1.3		11.1 - 12.1
		I1.2	9.6 - 11.1
BOFR 87.003	P3.1		1.7 - 2.7
	P3.2		4.2 - 5.2
		I3.1	2.7 - 4.2

The seismic receiver location was fixed in BOFR 87.001 at the position shown in Figure 6.2. A set of seismic measurements were obtained with the transmitter at 0.5 m intervals over the length of BOFR 87.002. The transmitter location was then fixed as shown in Figure 6.2 so that the direct ray path between receiver and transmitter was roughly normal to the fracture zone.

The Bofex 1 transducer required several hours to stabilize. It also generated a 8kHz signal which was detected by the receiver in borehole BOFR 87.001. Thus, when seismic measurements were made it was necessary to disconnect power to the transducer. Stabilization after reconnection occurred in a matter of minutes.

Measurements associated with the inflation tests took place over the course of six days. A time line of events and pressure history of I1.2 and I3.1 are shown in Figure 6.3. On the first day interval I1.2 was pressurized to 20 bars and maintained constant. Flow rates were measured as a check on hydrologic properties measured in the previous test. Seismic measurements were made periodically with the receiver and transmitter in fixed locations.

At about 17 hours into the experiment the pressure in I1.2 dropped to 6 bars for about 3 hours due to equipment problems. Additional seismic measurements were made and then the interval pressure was increased from 6 to 35 bars and held at that level for about 9 hours. Deformation and pressures were monitored and periodic seismic measurements were made during this time. Due to further equipment problems it was necessary to reduce the I1.2 pressure to 20 bars after this 9-hour duration.

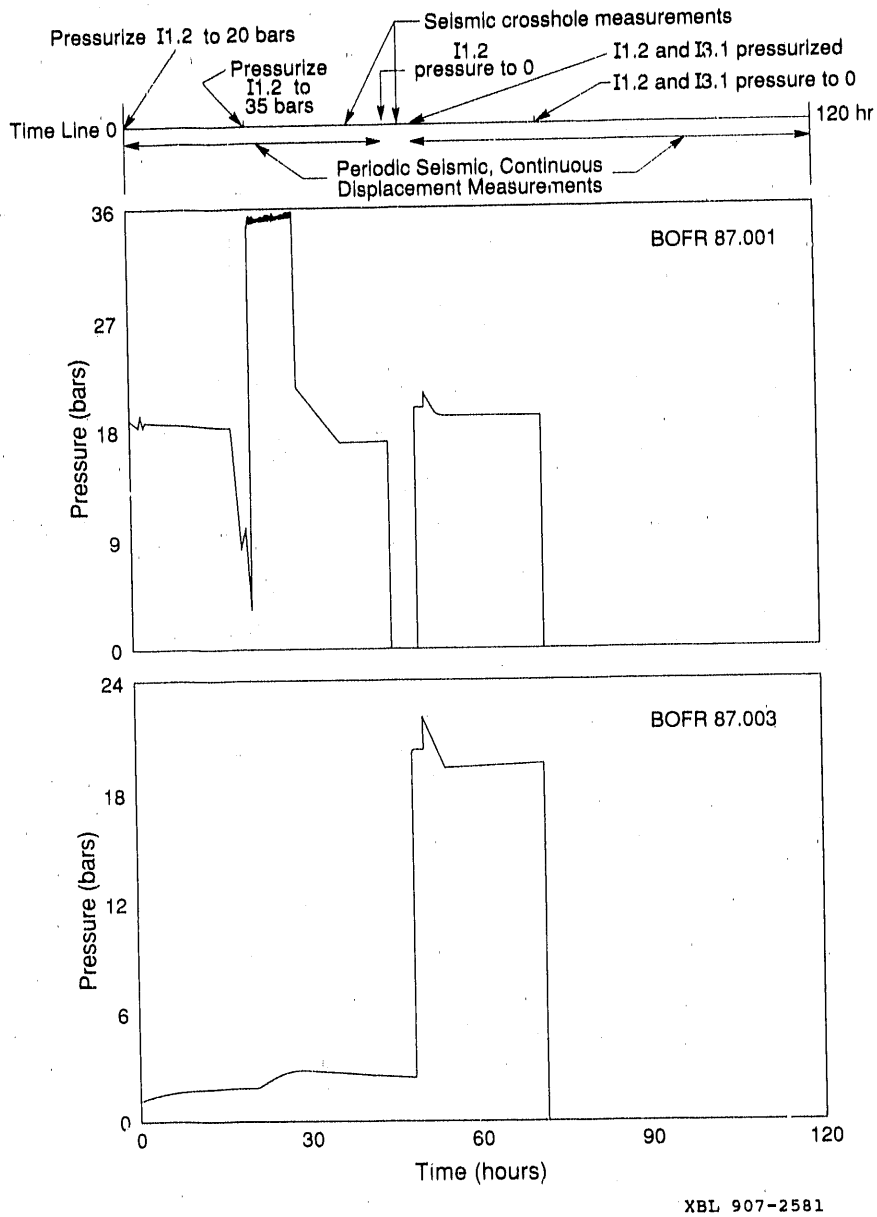

Figure 6.3. Time line of events in inflation test and pressure history in intervals I1.2 of BOFR 87.001 and I3.1 of BOFR 87.003.

At about 40 hours a set of seismic measurements were made with the transmitter at 0.5 m intervals alon$_g$ the length of BOFR 87.002. An additional set of seismic measurements were then made with the receiver moved to a distance of 4.69 m in borehole BOFR 87.001 and the transmitter at 0.5 m intervals along the length of BOFR 87.002.

At about 45 hours the experimental configuration was changed. In order to further inflate the fracture, interval I3.1 was pressurized to 20 bars while maintaining 20 bars pressure in interval I1.2. Before the next phase of the test was carried out, the seismic transducer locations were changed so that both source and receiver were in close proximity to the fracture. As shown in Figure 6.2 the receiver was placed in BOAU 83.030 at approximately 2 m in the hole while the transmitter in BOFR 87.002 was relocated so that the direct line ray path between the transducers was normal to the fracture zone.

In order to remove the receiver from BOFR 87.001 it was necessary to drain the borehole. It was then refilled, but this process caused a large perturbation in the Bofex 1 readings. Due to schedule constraints it was necessary to begin injection into interval I3.1 before Bofex 1 was restabilized.

A set of seismic measurements were made before interval I3.1 was pressured. It was then pressurized to 20 bars. Pressures and flow measurements were made at short time intervals during the initial pressurization. In order to permit independent inflation of the packers in BOFR 87.003, the pressure line was used as a packer inflation line. Thus, for the inflation test, both flow and pressure measurements were made on the same line. In addition, the flow line from I1.2 had been connected to the flow line from I3.1, so the total flow was the sum of that going to both intervals.

Seismic measurements were made just prior to releasing the pressure to zero in intervals I1.2 an I3.1 at about 62 hours. Displacements were monitored and periodic seismic measurements were made until the equipment was removed at 120 hours.

6.3. Deformation Measurements

Fluid pressure and displacement data from the inflation test are shown in Figures 6.4a and 6.4b and Figures 6.5a and 6.5b. Fluid pressures are measured relative to atmospheric. Figure 6.4a shows the pressure-time history in interval I1.2 in BOFR 87.001 while the corresponding displacements measured by Bofex 1 are shown in Figure 6.4b. Similarly, Figure 6.5a gives the pressure time history of I3.1 in BOFR 87.003 while Figure 6.5b shows the corresponding displacements of Bofex 3.

During the first 18 hours of the inflation test, while a constant pressure was maintained in interval I1.2, fracture displacements as measured by Bofex 1 gradually increased. This increase in displacement was due to the expanding pressure front in the fracture. Increasing the pressure in I1.2 to over 35 bars at about 25 hours resulted in an increased rate of deformation in Bofex 1. After the fluid pressure was again reduced, recovery i.e., fracture closure was observed. The Bofex 1 measurements were affected by draining, refilling and repressurizing interval I1.2 at about 49 hours as shown in Figure 6.4b. As seen, deformations re-stabilized at 55 hours at a level about equal to that prior to the perturbation. Instantaneous reduction of the interval pressure to zero resulted in an abrupt apparent fracture opening. It is believed this apparent deformation may be instrument-related and is therefore not "real." The abrupt change at about 20 hours, which also occurred upon depressurization may also be instrument-related. For the last portions of the test, during which the interval pressure was zero, the Bofex 1 measurements show a time dependent closure of the fracture which is consistent with a reduction in pressure in the fracture.

Figure 6.5a shows that the total fluid pressure increase in interval I3.1 during the first thirty hours of the inflation test was less than two bars. During this time Bofex 3 shows little change and then an apparent abrupt increase in fracture deformation at about 18 hours. Though it can barely be distinguished in the figure, this change occurred about 20 minutes before the pressure in I1.2 was increased to 35 bars and was coincident with turning the power on and off to the transducers to permit seismic measurements. The interpretation of the data from Bofex 3 during the first forty hours of testing is that little, if any, deformation occurred in the fracture at BOFR

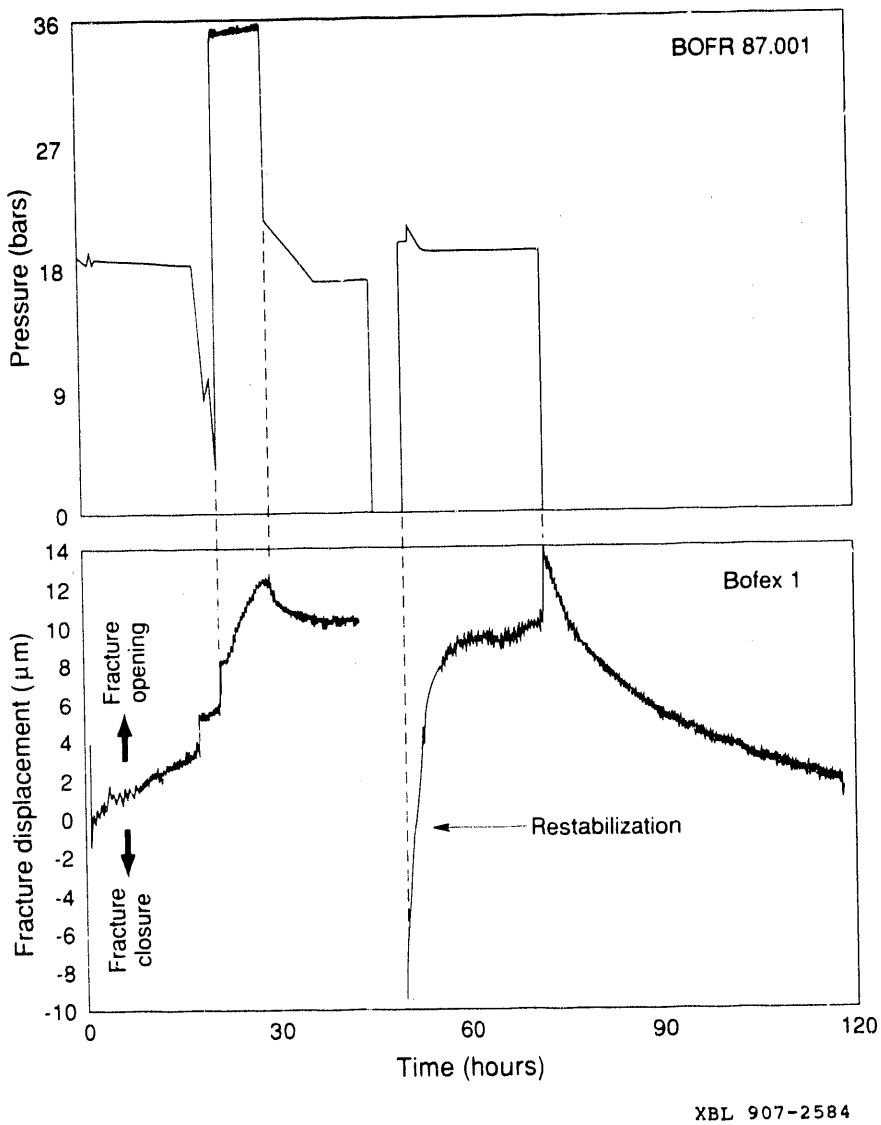

Figure 6.4. (a) Pressure history in interval I1.2, BOFR 87.001, during inflation test; (b) fracture displacements as measured by Bofex 1 in BOFR 87.001 during inflation test. Vertical dashed lines show coincidence in time of events.

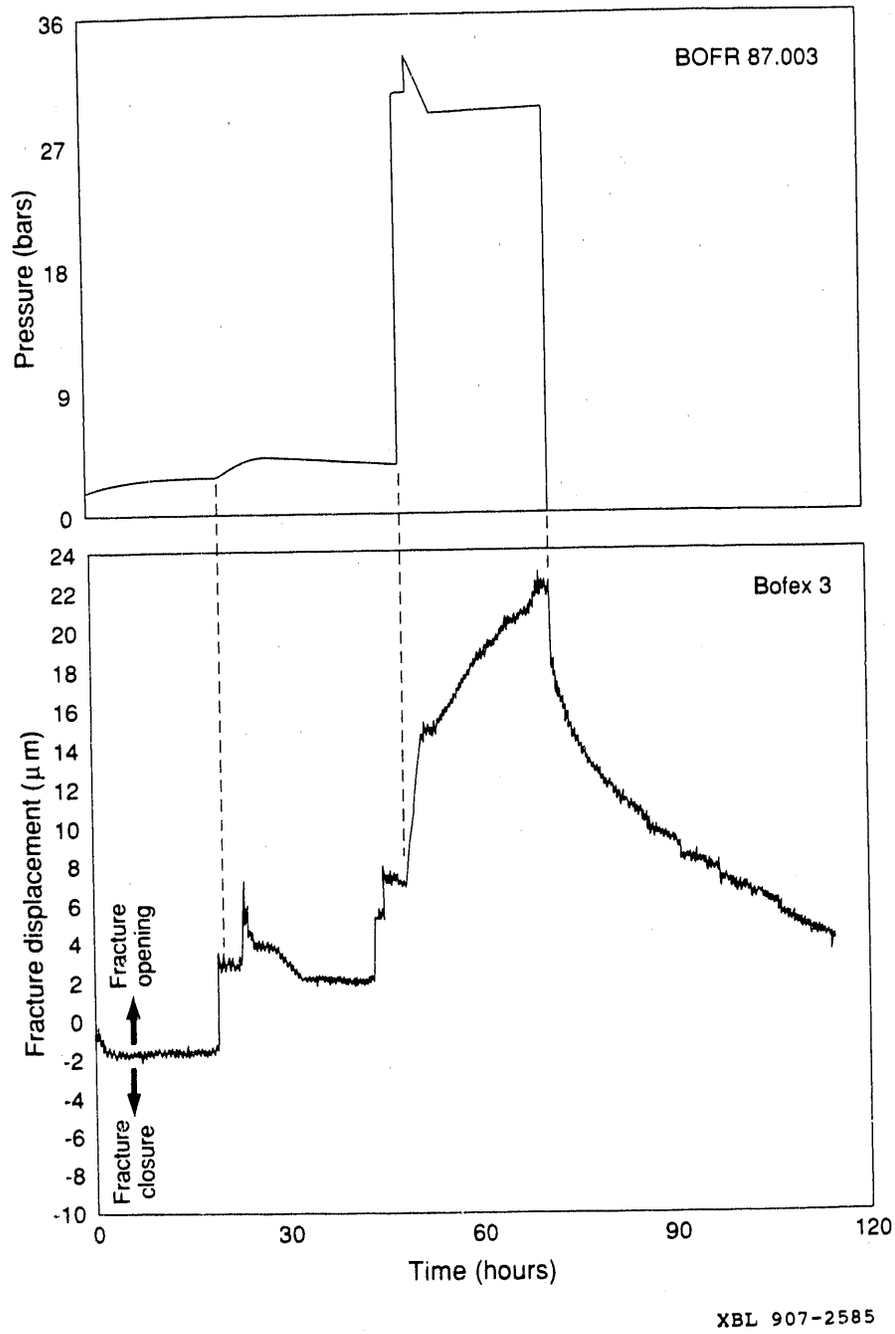

Figure 6.5. (a) Pressure history in interval I3.1, BOFR 87.003, during inflation test; (b) fracture displacements as measured by Bofex 3 in BOFR 87.003 during inflation test. Vertical dashed lines show coincidence in time of events.

87.003 in response to the pressurization of I1.2. When interval I3.1 in BOFR 87.003 was pressurized, the fracture opened rapidly in response to the pressure front moving out from the borehole. The resulting total deformation was greater than observed for Bofex 1 for a similar duration of time. This observation is consistent with the data showing flow rates to be higher at the same injection pressure in I3.1 than in I1.2. Since the fracture intersected the tunnel wall at an oblique angle, the stress normal to the fracture at locations in close proximity to the wall, such as in BOFR 87.003, was less than at other locations deeper in the rock mass. This lower normal stress could lead to higher fracture permeability. In addition the wedge of rock formed at the intersection of the fracture plane and the tunnel wall may have been deformed, resulting in further opening of the fracture.

After depressurization of I3.1, Bofex 3 showed a time dependent closure in response to pressure reduction in the fracture. This response was similar in form, though greater in magnitude than observed in Bofex 1 (Figure 6.4b).

6.4. Analysis of Deformation Measurements

The deformation measurements were made in order to evaluate the mechanical stiffness, at an in-situ scale, of the kakirite fracture. The analyses were complicated by the fact that the fluid pressure in the fracture was localized in extent. Therefore, in addition to the usual calculation of stiffness, referred to as a zero-order approximation, two additional calculations were performed to evaluate the effects of the limited areal extent of the fluid pressure. The first modelled the fracture as a single crack with stiffness. The second modelled the fracture as a co-planar array of parallel cracks.

The stiffness, κ, of a fracture is defined as the ratio of the applied stress to the deformation it produces. The units of κ are Pa/m. The deformations are those which occur in addition to the deformation of the intact rock adjacent to the fracture. As a zero-order approximation, then, the measured values of displacement of the fracture in FRI can be used directly to calculate fracture stiffness. Using the measured value of displacement from Bofex 1 after 17 hours, assuming a pressure increase of 19 bars and correcting only for the angle between the Bofex and the normal

to the fracture, κ is given by:

$$\kappa = \frac{P}{\delta} = \frac{1.9 \times 10^6 \text{ Pa}}{1.4 \times 10^{-6} \text{ m}} = 1.3 \times 10^{12} \text{ Pa/m} \tag{6.1}$$

where P is pressure and δ is displacement.

The assumption implicit in this calculation is that the pressure was everywhere equal and applied over a fracture area of very large extent. Since the fluid pressure was non-uniform and of limited extent in area, the calculation in Equation (6.1) should yield a very conservative (high) estimate of stiffness.

A more realistic model is shown in Figure 6.6, element I (top of figure). The fracture is represented as a single two-dimensional mathematical crack in plane strain, with a spatially varying pressure applied over a portion of the crack surface. The effect of the fracture stiffness is represented schematically in the figure by springs of stiffness κ connecting the surfaces of the crack. Using field data as input to the model, values of κ as a function of crack length, 2c, were determined.

The approach to solving the problem analytically involved the use of linear elastic fracture mechanics. Since elasticity was assumed, the problem in I (Figure 6.5) could be decomposed into two simpler elements designated by II and III in the figure. By superposition, then:

$$\delta^{I}_{(x)} = \delta^{II}_{(x)} + \delta^{III}_{(x)} \tag{6.2}$$

where $\delta_{(x)}$ is the displacement in the y direction. The value of $\delta^{I}_{(0)}$ was known from the Bofex 1 measurements.

The pressure distribution, P, in the crack was represented by a cubic polynomial of the form:

$$P = P_0(a_0 + a_1 x + a_2 x^2 + a_3 x^3) \tag{6.3}$$

where

$$P\Big|_{x=0} = \text{constant} = P_0$$

$$P\Big|_{x=l} = 0$$

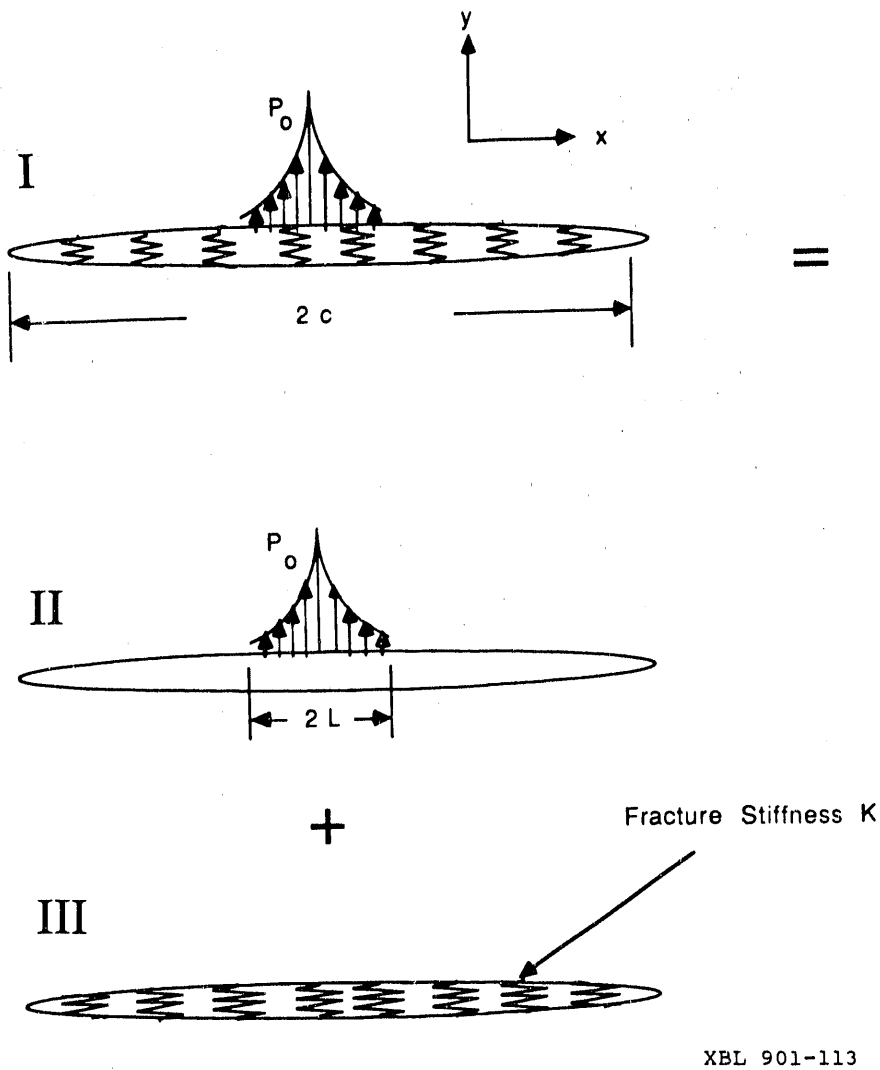

Figure 6.6. Modelling the inflation experiment by a pressurized crack with stiffness. Assuming elasticity, model I is decomposed into two simple models designated II and III.

$$\left.\frac{dP}{dx}\right|_{x=l} = 0$$

$$\left.\frac{d^2P}{dx^2}\right|_{x=0} = 0$$

For the FRI test coefficients in (6.3) were evaluated as:

$$a_0 = 1 \quad a_2 = 0$$
$$a_1 = -\frac{3}{2l} \quad a_3 = \frac{1}{2l^3} \tag{6.3a}$$

Calculations were carried out assuming pressure conditions after 17 hours were represented by P_0 = 19 bars at x = 0 and the pressure in BOFR 87.003 was 1.87 bars. Assuming the distance between pressure measurement points, as measured along the fracture, was 10 m, the value of l = 13.6 m.

To calculate displacements it was necessary to obtain expressions for the mode I stress intensity factor, K_I. For an elliptical crack of length 2c and point loads of magnitude P located at a distance x = ± b from the midpoint of the crack, K_I is given by:

$$K_I = 2P\left[\frac{c}{\pi(c^2-b^2)}\right]^{1/2} \tag{6.4}$$

The stress intensity factor for a distributed pressure is found by integration of Equation (6.4) over the length of the crack. Substitution of Equation (6.3) into (6.4) and integration yields:

$$K_I^{II} = 2\left[\frac{c}{\pi}\right]^{1/2} P_0 \left\{ \sin^{-1}\left(\frac{l}{c}\right) + \frac{3}{2l}\, c \left[1-\frac{l^2}{c^2}\right]^{1/2} - \frac{3c}{2l} + \frac{c^3}{2l^3}\left[-\left[1-\frac{l^2}{c^2}\right]^{1/2} + \frac{1}{3}\left(1-\frac{l^2}{c^2}\right)^{3/2} + \frac{2}{3}\right]\right\} \tag{6.5}$$

The displacements, $\delta_{(x)}^{II}$, corresponding to the unconstrained crack (element II in Figure 6.6) can now be found. Substitution of Equation (6.8) into the following equation yields displacements perpendicular to the crack plane as a function of position x:

$$\delta_{(x)}^{II} = \frac{2K_I}{E}\,[2(c-x)/\pi]^{1/2}\,(1-\nu^2) \tag{6.6}$$

Displacements from (6.6) with the pressure distribution given by (6.3) and (6.3a), a Young's modulus, E, of 42.7 GPa and a Poisson's ratio of ν = 0.25 are given in Figure 6.7 for a range of

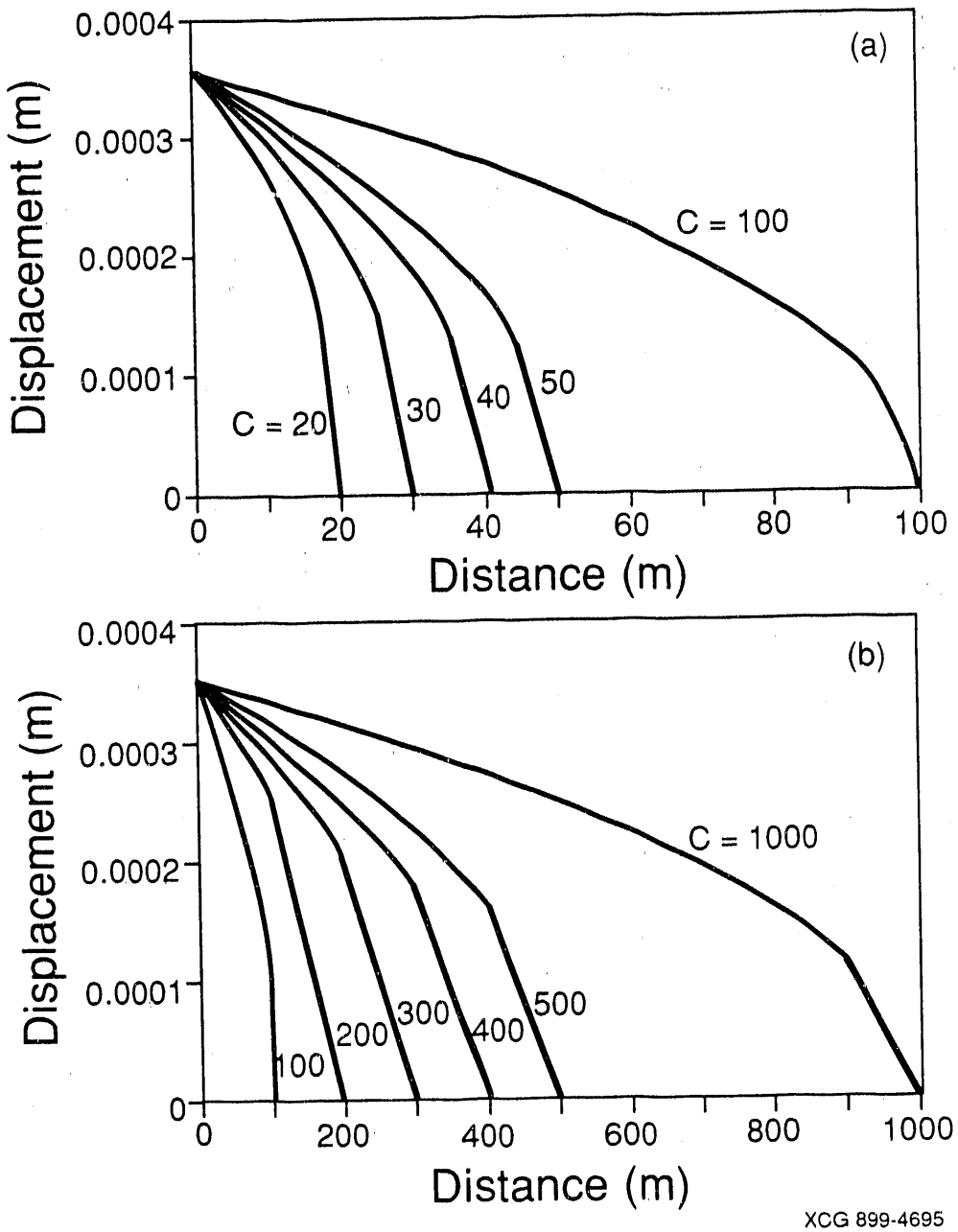

Figure 6.7. Displacement as a function of distance from the midpoint of the crack in element II, assuming l = 13.62 m and crack lengths from 20 to 1000 m.

crack lengths. These plots show that for crack lengths greater than 20 m, there is no dependence of δ^{II} on crack length.

In the model as represented in Figure 6.6 the fracture stiffness, κ, constrains the deformation. These deformations in II, δ^{II}, are greater than those of I, δ^{I}, according to the value of the stiffness. In the limit, for a stiffness of zero, $\delta^{I} = \delta^{II}$, while for $\kappa \rightarrow \infty$, $\delta^{I} \rightarrow 0$. The difference between the displacements in I and II is that due to the stiffness of the fractures and is given by $\delta^{III}_{(x)}$. The pressure, $P'(x)$, which must be applied in III to yield these displacements, $\delta^{III}_{(x)}$, must be given by:

$$P'(x) = \kappa \delta^{I}_{(x)} \tag{6.8}$$

It is also assumed that the displacements δ^{II} and δ^{I} differ only by a constant of proportionality given by $\delta^{I}_{(x)}/\delta^{II}_{(0)}$ where $\delta^{I}_{(0)}$ is given by the measured Bofex 1 value of displacement and $\delta^{II}_{(0)}$ is calculated from Equation (6.6). Thus,

$$P'(x) = \kappa \left[\frac{\delta^{I}_{(0)}}{\delta^{II}_{(0)}} \right] \delta^{II}_{(x)} \tag{6.8a}$$

and Equation (6.2) can be rewritten as:

$$\delta^{III}_{(x)} = \delta^{I}_{(x)} - \delta^{II}_{(x)} = \left[\frac{\delta^{I}_{(0)}}{\delta^{II}_{(0)}} - 1 \right] \delta^{II}_{(x)} \tag{6.9}$$

The expression for $\delta^{III}_{(x)}$ is given by

$$\delta^{III}_{(x)} = \frac{2K_I^{III}}{E} [2(c-x)/\pi]^{1/2} (1 - \nu^2) \tag{6.10}$$

and K_I^{III} is determined by substitution $P'(x)$ and integrating Equation (6.4). In this case, $P'(x)$ is applied over the whole length of the crack. Values of $P'(x)$ were expressed as a cubic polynomial, so K_I^{III} is given by

$$K_I^{III} = 2\sqrt{\frac{c}{\pi}}\, \kappa \left[a_0 \frac{\pi}{2} + a_1 c + a_2 c^2 \left(\frac{\pi}{4}\right) + \frac{2}{3} a_3 c^3 \right] \frac{\delta^{I}_{(0)}}{a_0} \tag{6.11}$$

where $a_0 = \delta^{II}_{(0)}$

For arbitrary values of c the fracture stiffness κ was then determined subject to the conditions that

$$\delta^{I}_{(0)} - \delta^{II}_{(0)} = \delta^{III}_{(0)} \tag{6.12}$$

where $\delta^{I}_{(0)}$ is, again, the measured displacement. Thus, combining Equations (6.10) and (6.11) with (6.9),

$$\delta^{I}_{(0)} - a_0 = \frac{4c}{\pi} \frac{(1-\nu)^2}{E} \sqrt{2} \left\{ \kappa \frac{\delta^{I}_{(0)}}{a_0} \left[a_o \frac{\pi}{2} + a_1 c + \right. \right.$$

$$\left. \left. + a_2 c^2 \frac{\pi}{4} + \frac{2}{3} a_3 c^3 \right] \right\} \tag{6.13}$$

For different values of crack length it is then possible to determine the corresponding stiffness. These are plotted in Figure 6.8. While the extent of the fractured zone is not known, it is expected to be in excess of ten times the pressurized region. For crack lengths of this order of magnitude Equation (6.13) yields values of κ on the order of 4×10^{10}–2×10^{11} Pa/m, or almost two orders of magnitude less than that derived for two half-spaces joined by a stiffness as in Equations (6.1).

In the approach just described the displacements along the face of the crack are given as a function of the stress intensity factor. Because of the simplifying assumptions used in deriving the stress intensity factor, there is a discrepancy between displacements predicted using it and those which would be predicted by a full elasticity solution. This discrepancy is very small close to the crack tip but increases with distance from the work tip. The result of the approximations involved in using a stress intensity factor to calculate the stiffness of a crack with springs is that the calculated stiffness is lower than would be predicted by the full elastic solution.

A second approach involving a different set of assumptions was to model the kakirite fracture as a row of two-dimensional coplanar cracks of equal crack length, 2c, and uniform spacing, 2b. In this model the ligaments of material between the cracks can be taken to represent the areas of contact between the faces of the fracture, and the cracks to represent those areas not in contact.

Simulations of the model for different crack spacings 2b and ratios of crack length to crack spacing c/b were conducted assuming the material properties already noted above in the

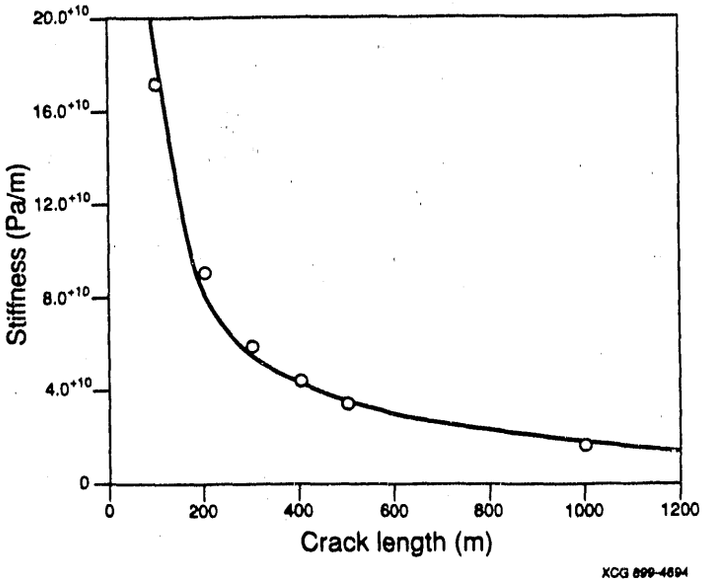

Figure 6.8. Predicted fracture stiffness as a function of crack length.

TWODD two-dimensional boundary element program developed by Crouch and Starfield (1983). Crack spacing, 2b, ranged from 50 m as upper limit to 0.10 m as the lower limit. Crack length to crack spacing ratios, c/b, ranged from 0.05 to 0.99. The range of c/b values for each b was selected to best match observed results. The deformations were calculated for a position of 0.75 m above the midpoint of the center fracture.

The number of cracks for each simulation was chosen to accommodate the extent of the pressure distribution as observed in the field so that the row of cracks extended from x = 0 m to x = ±13.6 m with the first crack centered at the origin. The pressure distribution was assumed to act only within the cracks. The effect of additional unpressurized cracks was found to be minimal. Simulations were run for a single crack of 40 m length containing the entire pressure distribution and c/b = 0.8. Additional deformation for fourteen cracks on either side of the pressurized crack increased the deformation by less than six percent. Simulations for a smaller crack spacing of 2b = 2 m and a c/b ranging from 0.95–0.99 showed an even less pronounced effect on the deformation.

Simulations were run for crack spacing values ranging from 2b = 0.1 m to 2b = 1.0 m, for a range of c/b values from 0.05–0.99. Results for the simulation are shown in Figure 6.9. All simulations show the same trend of deformation increasing exponentially with increasing c/b, or decreasing contact area. The effect of the crack spacing 2b on the deformation is significant; for a given c/b, the deformation increases exponentially with increasing b. Proportional decrease in c/b for a given deformation is less than the proportional increase in b. If Figure 6.9 is interpreted in terms of contact area, it shows that for a given contact area deformation increases with increasing b, and the contact area required to provide a given deformation increases with increasing b. This corroborates the work of Hopkins et al. (1987), who found that for a given contact area, the smaller the individual areas of contact the higher the stiffness of a fracture.

The horizontal line in Figure 6.9 represents the measured deformation *in situ* (1.42×10^{-6} m). It is seen that for a given crack size quite large spacings are required to match the observed results. Figure 6.10 is a plot of the percent contact area (1 – c/b) required to match

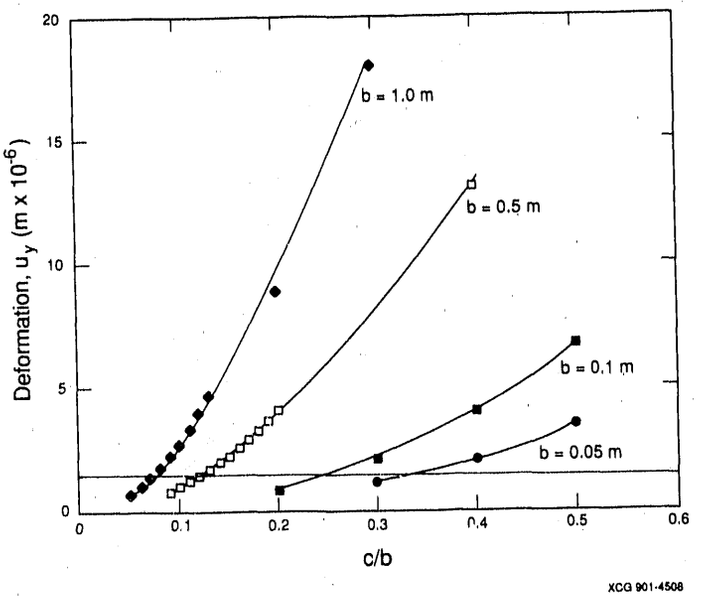

Figure 6.9. Deformation between two points located 0.75 m either side of the midpoint of the center crack of a row of pressurized coplanar cracks.

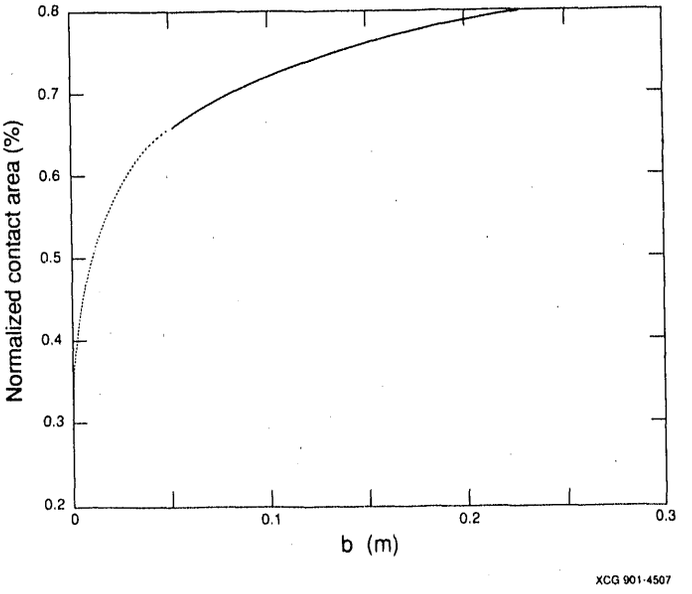

Figure 6.10. Normalized contact area of fracture faces as a function of crack half spacing b for a deformation of 1.42×10^{-6}m.

the observed information as a function of crack spacing. This shows that for spacing 2b of 0.1 m the contact area would still have to be about 66 percent. Because of limitations in computing capacity it was not possible to make calculations of deformation for b less than 0.05 m. An extrapolation of the curve in Figure 6.10 (dotted line), based on a curve fit of the values obtained at larger values of b shows that even if the crack spacing 2b were 0.05 m, the contact area would be about 59 percent.

An independent assessment of the contact area in the fracture zone could not be made. However, since the zone contained gouge material, high contact areas might be expected. Another possibility is that the fluid in the fracture was confined to channels and did not have access to all available void space.

For a row of co-planar cracks the average displacement, $\bar{\delta}$ is given by

$$\bar{\delta} = \frac{-8\sigma b(1-\nu^2)[ln\ \cos(\pi c/2b)]}{\pi E} \tag{6.14}$$

Since by definition, stiffness, κ, is related to $\bar{\delta}$ by

$$\frac{1}{\kappa} = \frac{\bar{\delta}}{\sigma} \tag{6.15}$$

hen the stiffness of a r. . of co-planar cracks is given by:

$$\frac{1}{\kappa} = \frac{-8b(1-\nu^2)[ln\ \cos(\pi c/2b)]}{\pi E} \tag{6.16}$$

Using equation 6.16 and values of c and b from Figure 6.9 corresponding to the in-situ measured deformation, values of K were calculated which ranged from 2×10^{11} Pa/m to 3×10^{11} Pa/m. As expected, these correspond to the high end of the range of stiffness values obtained from the crack-with-springs model.

The effect of a single fracture with a stiffness of 3×10^{11} Pa/m on seismic wave propagation can be evaluated using the seismic displacement discontinuity model described in the initial part of this section. Figure 6.11 is a plot of the magnitude of the transmission coefficient, |T|, and normalized group time delay, t_g/t_{go}, for a wave normally incident upon a fracture (Pyrak-Nolte et al., 1990). Values of $[\omega/(\kappa/z)]$ were calculated for $\kappa = 3 \times 10^{11}$ Pa/m, $z = 1.4 \times 10^7$ kg/m^{2}s, and ω

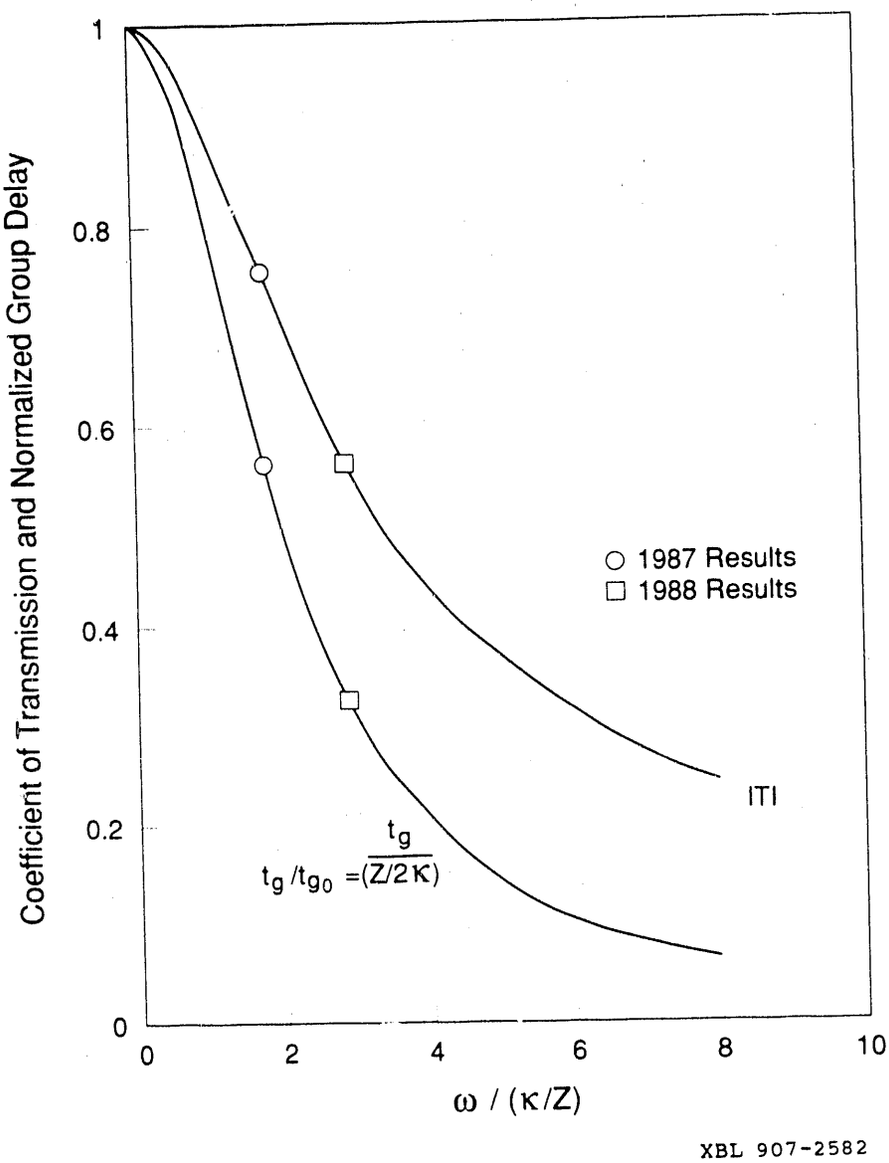

Figure 6.11. Magnitude of the transmission coefficient and normalized group delay for a seismic wave normally incident upon a displacement discontinuity as a function of normalized frequency.

corresponding to the center frequency of the P-waves in the tomographic survey. For the 1987 survey this frequency was about 6 kHz while for the 1988 survey it was about 10 kHz. In Figure 6.11 the corresponding values of |T| and t_g/t_{go} are plotted as circles for the 1987 survey and squares for the 1988 survey.

For a 6 kHz wave normally incident on a fracture with stiffness of 3×10^{11} Pa/m the value of |T| is seen to be about 0.75 while for a 10 kHz wave it is about 0.56. A value of |T| = 0.75 means that, a wave propagated across the fracture would have an amplitude about 25% lower than one propagating over the same path length of intact rock. Because of the higher frequency used in the 1988 survey, the amplitude reduction (i.e. |T| = .56) is predicted to be greater. From Figure 6.11 it is seen that the value of t_g/t_{go} for the 1987 survey was about 0.55 while for the 1988 survey it was about 0.31. Since $t_{go} = [\, 1/2\ (\kappa/z)]$, values of t_g were found to be 0.013 m sec and 0.007 m sec for the 1987 and 1988 surveys, respectively. A value of 0.013 m sec means that the measured travel time of a wave crossing the fracture would be 0.013 m sec longer than that of a wave propagated over the same distance through intact rock. These results indicate that, because of the difference in frequency of the sources used in the two surveys, the fracture zone would be less distinct in the 1988 tomogram than in the 1987 tomogram, and this was observed. If the group time delay for the 10 kHz waves is converted to an effective change in velocity, the theory predicts that the fracture zone should result in about a 1% decrease in velocity relative to "unfractured" rock. This decrease is also similar to the difference between background and fracture zone velocity in the tomogram after anisotropy was removed.

In order to complement the in-situ stiffness measurements, laboratory measurements were made on fractured specimen #2 (see Chapter 3), containing a single natural fracture. The measurements were performed in conjunction with the seismic measurements under saturated conditions. The apparatus used to jacket the specimen are described in Chapter 3.4. Additional apparatus consisted of a capillary tube, partially filled with water under 10 psi pressure, connected to the saturated specimen. As axial load on the specimen was increased water was expelled from the fracture. Upon unloading water flowed into the fracture. Assuming water

moved into or out of only the voids in the fracture, the stiffness of the fracture is given by

$$\kappa = \sigma/(\Delta v/A)$$

where σ is the normal stress on the fracture, Δv is the change in volume of water and A is the fracture area.

Five repeat measurements were made on fractured specimen #2. Typical results are shown in Figure 6.12a,b. Shown in part a of the figure is the water volume change as a function of applied stress. Arrows indicate the sequence of loading steps. As load increased the volume of water in the capillary tube increased, indicating expulsion of water from the specimen. Upon unloading water moved back into the specimen. However as can be seen, there was a large hysteresis in the measurements; more water was expelled than imbibed. It is believed that the measurements reflect the movement of water in and out of the porosity of the intact rock as well as the fracture. The highly foliated nature of the rock apparently introduces more interconnected porosity than is usually observed in granite. Loading the rock to the highest load level also may have introduced some dilation, leading to the observed decrease in water volume at the highest loading step.

Fracture stiffness values calculated from the volume change measurements are shown in Figure 6.12b. These are incremental values, calculated from the volume change at each load step. Because of the affect of the porosity of the rock adjacent to the fracture, these stiffness values are lower than the true fracture stiffness; it is thought that the error is less for the values obtained during unloading. The laboratory measured values of stiffness (during unloading) were about an order of magnitude higher than those measured in-situ. If the in-situ value of fracture stiffness was comparable to that of the laboratory measurements, the seismic displacement discontinuity theory predicts that such fractures would have little affect on wave propagation. However, a direct comparison for scale effect was not possible because the fracture in the laboratory specimen was not the kakirite fracture.

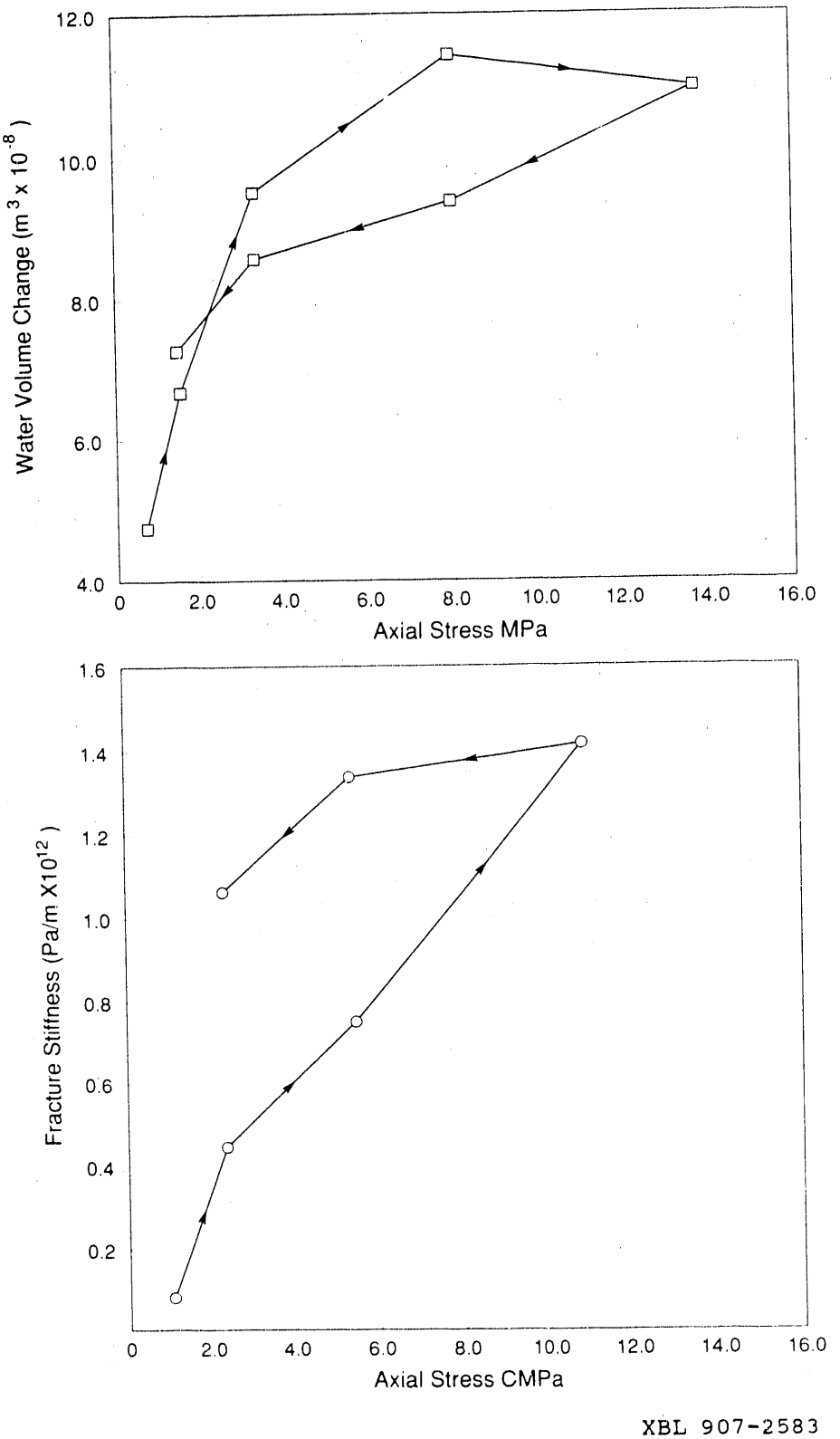

Figure 6.12. Typical results of laboratory measurement of stiffness of the fracture in fractured specimen #2; (a) change in volume of water in the fracture during loading and unloading, (b) stiffness based on volume change measurements.

6.5. Seismic Results of Inflation Tests

As part of the FRI inflation experiments we attempted to determine the effect of changing the fracture aperture on seismic properties. During the inflation tests we propagated seismic energy across the fracture. Because we were attempting to detect very small changes in the seismic wave propagation properties, it was necessary to be very careful in our measurement procedure.

The purpose of the first test, started on 24 August 1988, was to determine baseline properties. This first test was a cross-borehole sweep, taken with the receiver clamped and held stationary at 8.0 meters up borehole BOFR 87.001 from the AU tunnel, and the source being moved down BOFR 87.002 from 18.5 meters from the AU tunnel to 4.0 meters from the AU tunnel, at 0.5 meter intervals. This test is referred to as pressure test at zero pressure, (PT0). The reason we moved the source and not the receiver was that we felt that the receiver was clamped to the wall, but the transmitter relied mainly on fluid in the borehole for coupling, and had more stable coupling as it was moved. All three components of these data are shown in Figure 6.13.

After the baseline data were obtained the transmitter was left in place at 5.0 meters down BOFR 87.002 from the access tunnel. The pressure in the fracture was increased to 20 bars and seismic measurements were then repeated with the source and receiver kept stationary. The locations of the source and receiver were chosen so that the ray path crossed the fracture as close as possible to the injection point. These measurements were repeated over two days in order to detect any transient changes in seismic properties. Keeping the source and receiver stationary would hopefully reduce any error associated with coupling. This data set is referred to as PT20S. Immediately after this test but before depressurization we again took a sweep identical to PT0, with the pressure field at 20 bars. This data set is referred to as PT20D. To keep the results as clear as possible we will first compare the two borehole sweeps, i.e., PT0 and PT20D. We will then discuss the results of the transient measurement (PT20S) when the source and receiver were held stationary over two days time.

All 3 components of both sweeps before (PTO) and after (PT20D) 2 days of pressurization are shown in Figures 6.13 (PT0), and 6.14 (PT20D). Each set of data is a set of 10 stacked traces. It is immediately evident from these figures that the waveforms of the two sweeps are quite similar to each other in all three components. The traces at the top of the plots pass closest to the pressured zone. When the maximum amplitude from each trace for each component is plotted (Figures 6.15a 6.15b, and 6.15c), with the open squares corresponding to the data after two days of pressurization, (PT20D), it is seen that the amplitudes may have increased slightly for the traces close to the pressurized zone. One explanation for this could be that when the receiver is clamped for two days the coupling may have improved as the clamp seats in the hole. In any case if the fracture had opened, we would have expected a decrease in amplitude.

It is interesting to note that the amplitudes for components 2 and 3 (Figures 6.15b and 6.15c) show lobes with minima at stations 9 and 18 and maxima at 4, 13 and 22. The closest point between source and receiver is at about station 12 or 13. During calibration of the source it was seen that the radiation pattern for the source is almost exactly circular, therefore these lobes are not due to radiation pattern effects of the source. In addition these lobes are not observed on component 1 (Figure 6.15) and are even more pronounced after pressurization. A possible explanation is some sort of interference in the plane of components 2 and 3. However, though this is an interesting phenomenon, it apparently does not relate to the inflation test. In any case, it appears that from looking at the results of the before (PTO) and after (PT20D) tests, no significant changes were noted. The results of leaving the source and receiver stationary (PT20S) were somewhat more encouraging, however, also confusing.

On 24 August, before the fracture was pressured to 20 bars the source was left stationary at 5.0 meters down (from the access tunnel) borehole BOFR 87.002 and the receiver clamped in a stationary position at 8.0 meters up (from the lab tunnel) BOFR 87.001. Hourly measurements were made only during the day, because no access was allowed to the site at night. The schedule of measurements is shown in Table 6.2. The first measurement was taken immediately after the PT0 sweep, Table 6.2, measurement 1, and prior to pressurization. Note that the amplitude for

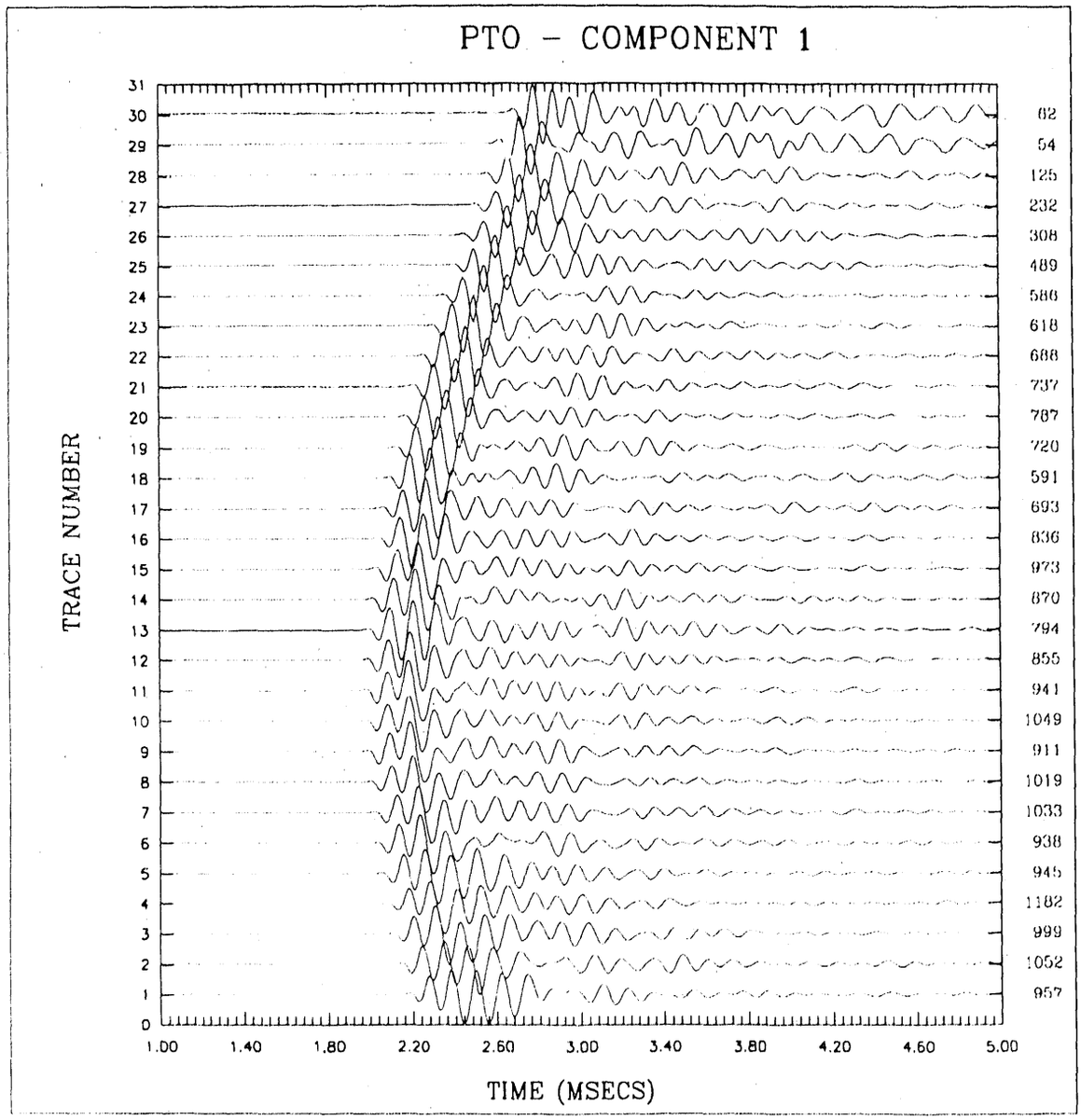

Figure 6.13a. Recorded wave form data for component 1 prior to inflation test in BOFR 87.001.

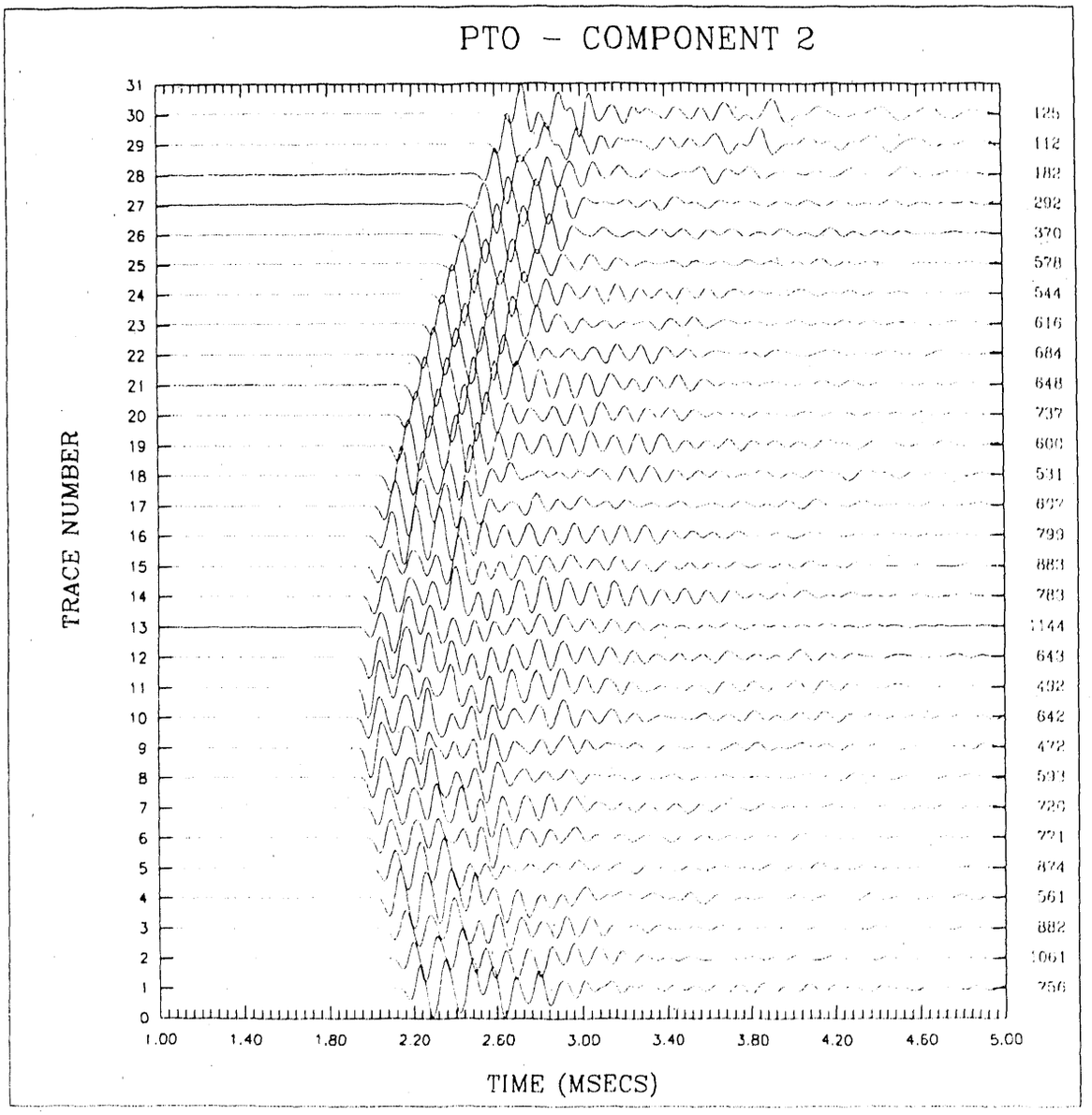

Figure 6.13b. Recorded wave form data for component 2 prior to inflation test in BOFR 87.001.

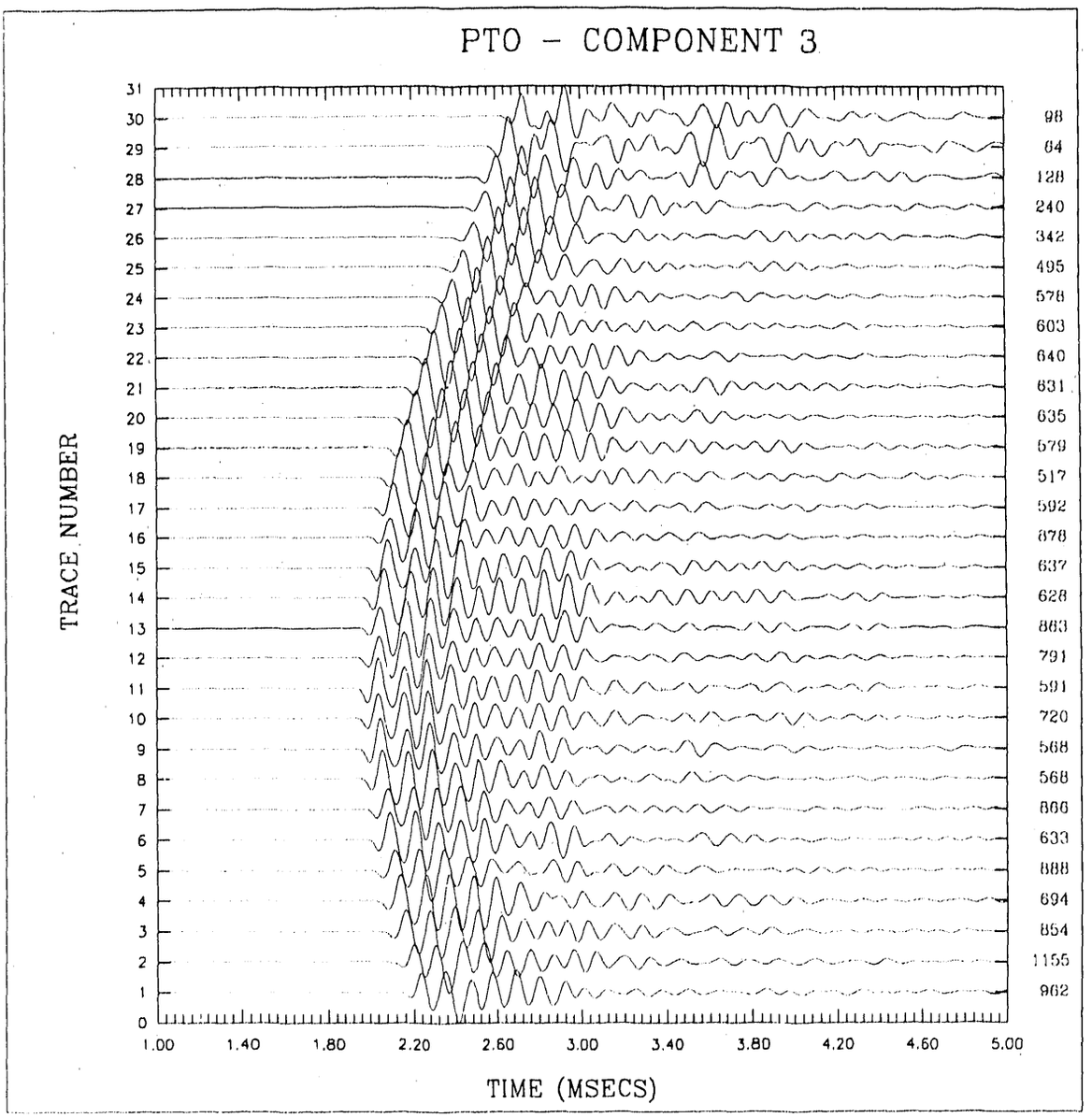

Figure 6.13c. Recorded wave form data for component 3 prior to inflation test in BOFR 87.001.

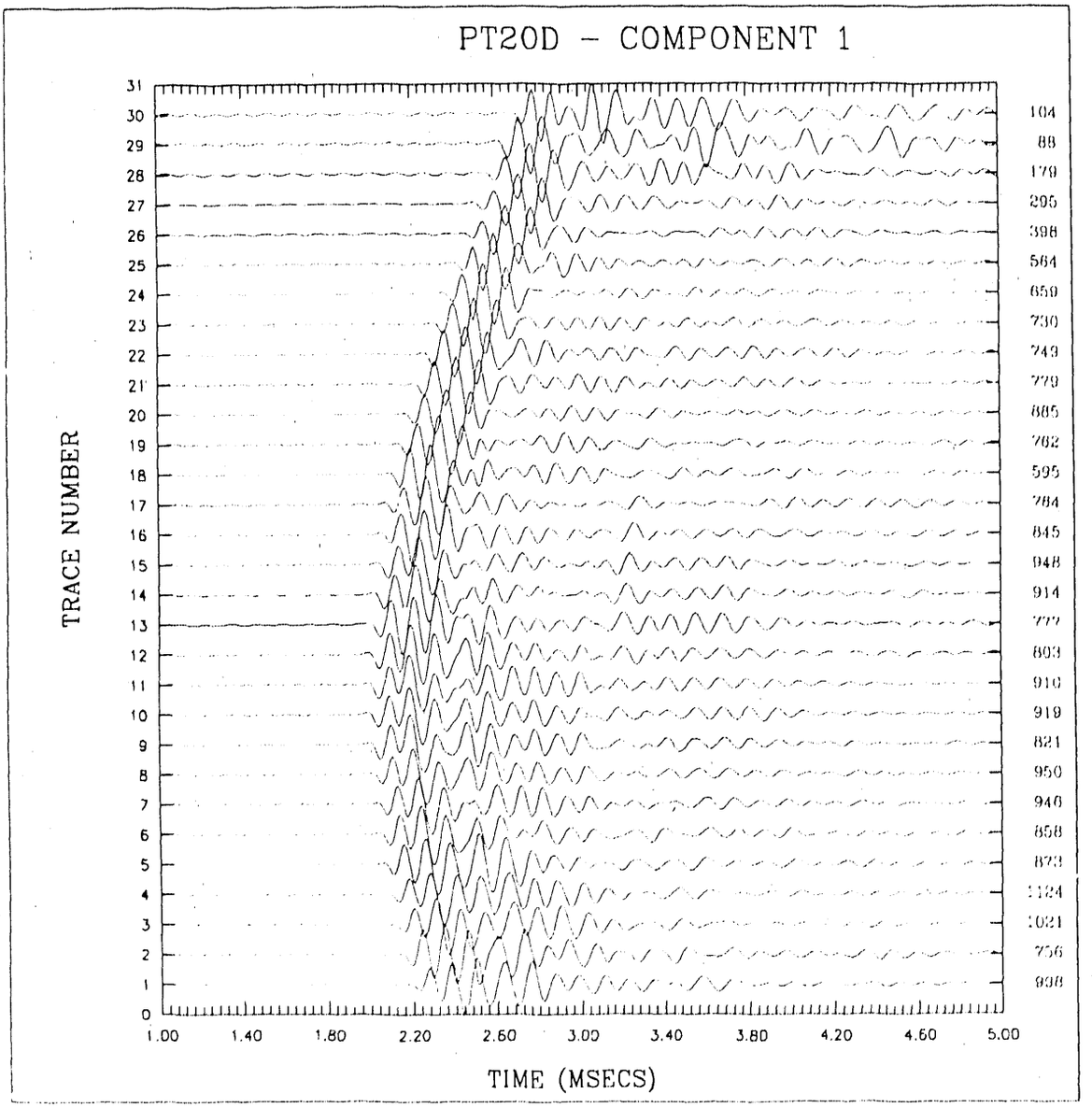

Figure 6.14a. Recorded wave form data for component 1 after fracture had been pressurized to 20 bars in BOFR 87.001 for two days.

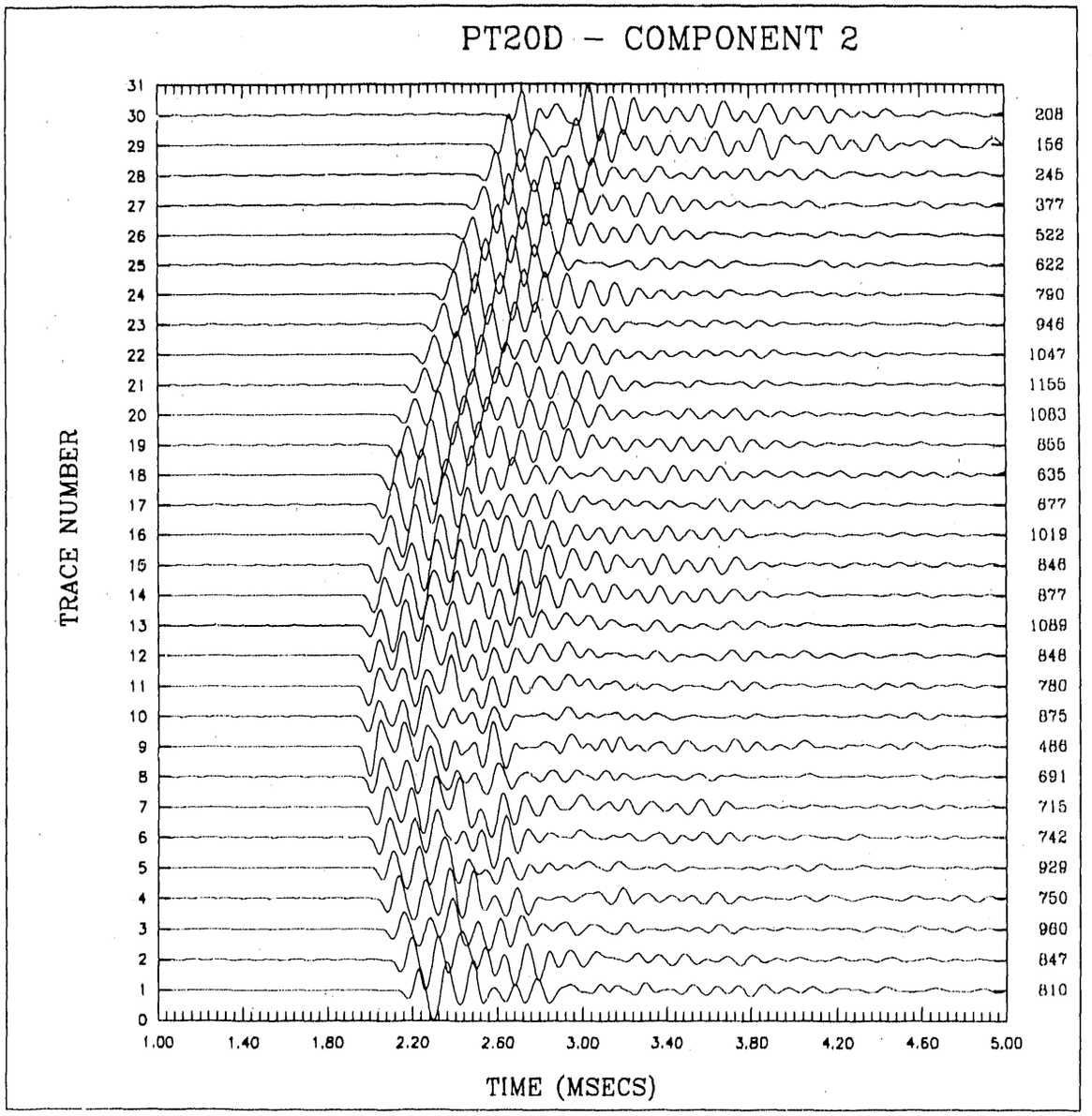

Figure 6.14b. Recorded wave form data for component 2 after fracture had been pressurized to 20 bars in BOFR 87.001 for two days.

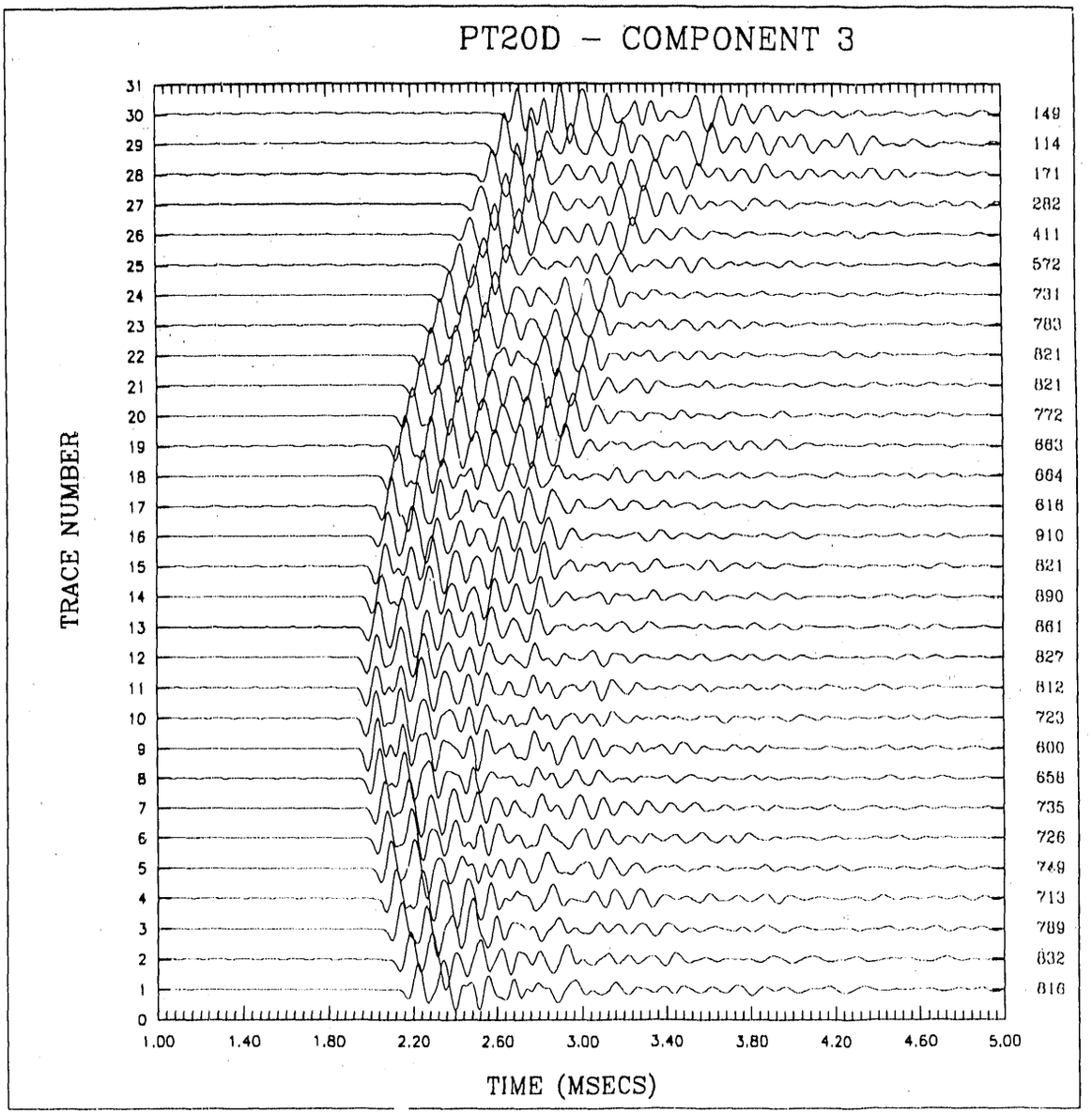

Figure 6.14c. Recorded wave form data for component 3 after fracture had been pressurized to 20 bars in BOFR 87.001 for two days.

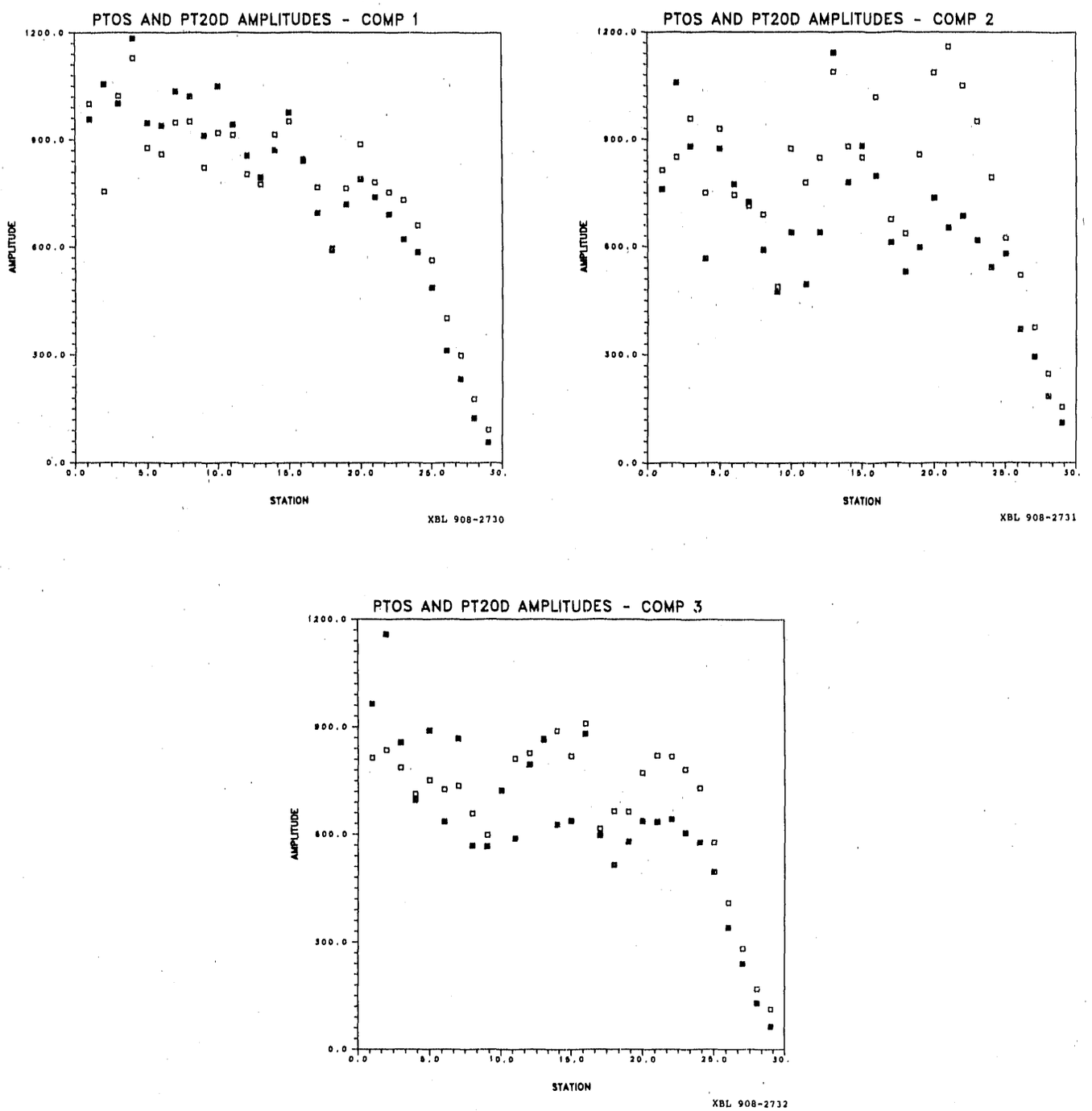

Figure 6.15. Amplitude versus station number for the unpressurized data, (dark squares), and after 2 days of pressurization, (open squares) for (a) component 1, (b) component 2, and (c) component 3.

Table 6.2. Measurement schedule for pressurization of BOFR 87.001 for test PT20S.

No.	Date	Time	P (Bars)	Maximum amplitude	No. of Stacks
1	24AUG	11.31	0	86.55469	16
2	24AUG	11:46	20	42.73584	10
3	24AUG	12:02	20	50.21338	10
4	24AUG	13:00	20	43.08276	10
5	24AUG	14:00	20	41.04785	10
6	24AUG	15:00	20	68.06396	10
7	24AUG	16:00	20	47.05322	10
8	25AUG	7:14	7	60.12549	16
9	25AUG	8:12	35	51.11719	10
10	25AUG	8:27	35	49.17871	10
11	25AUG	8:42	35	49.06128	10
12	25AUG	9:42	35	49.00537	10
13	25AUG	10:45	35	56.00000	10
14	25AUG	10:46	0	56.01074	10
15	25AUG	11:46	35	56.07202	10
16	25AUG	12:46	35	53.03198	10
17	25AUG	13:45	35	56.99194	10
18	25AUG	14:45	35	57.91748	10
19	25AUG	15:45	35	57.83203	10
20	25AUG	16:13	20	60.86938	10
21	26AUG	07:35	20	74.51733	10

Amplitudes are for component 1.

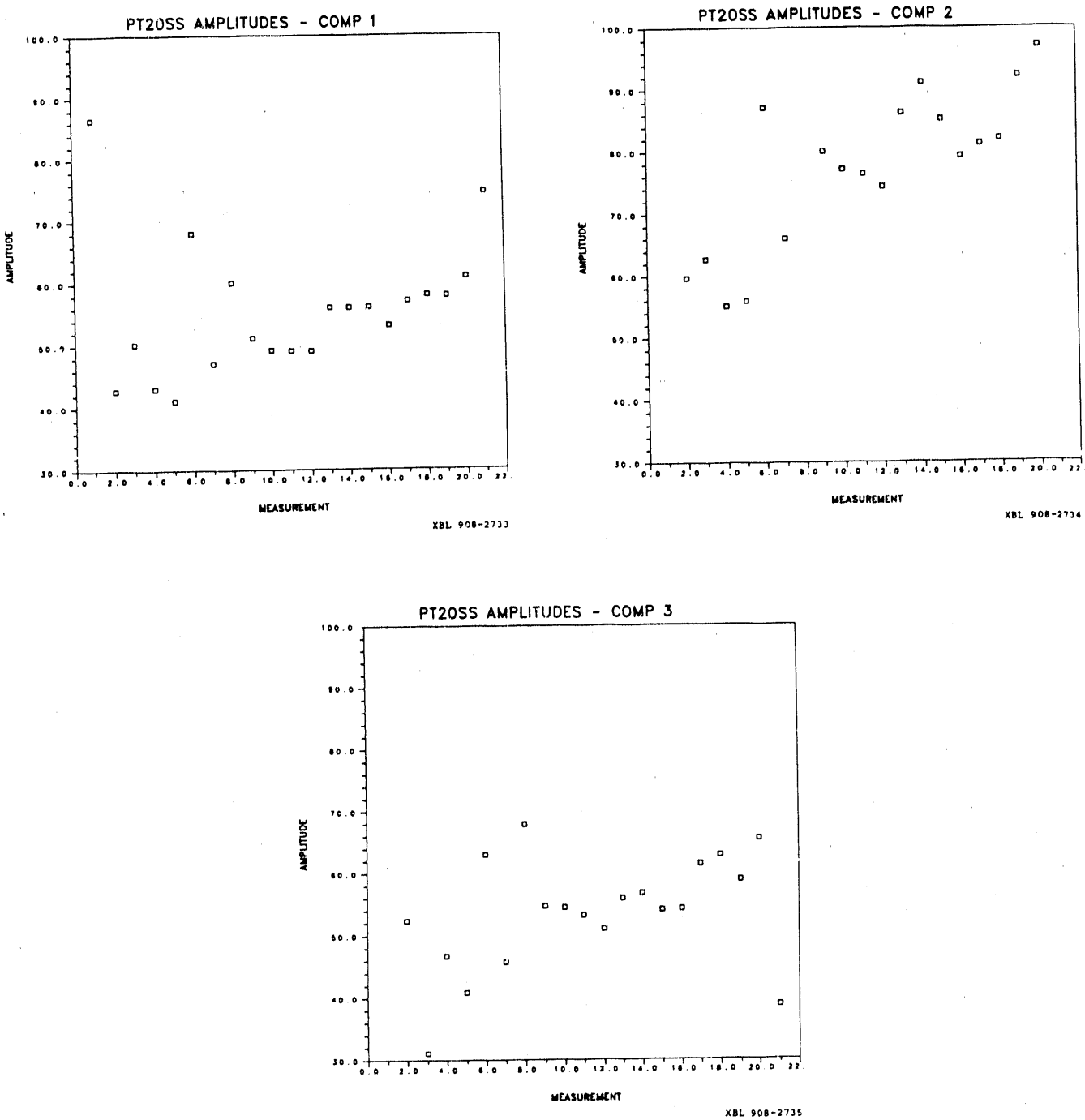

Figure 6.16. Amplitude values for data given in Table 6.2 for (a) component 1, (b) component 2, and (c) component 3.

this source-receiver pair has decreased from approximately 123 in PT0 (Figure 6.11, COMP 1, TRACE 28) to 86 Table 6.2, measurement 1. This illustrates the necessity of keeping the source and receiver clamped in the exact position through out the experiment. The second measurement was taken approximately 15 minutes after this and directly after the interval was pressurized. This measurement shows a dramatic decrease in amplitude from 86 to 42 (Table 6.2). One would like to think that the fracture immediately lost stiffness upon pressurization causing the amplitude reduction. There are two reasons why this may not be true: (1) the straight source-receiver path intersects the fracture about 5 meters from the pressurized interval, and (2) measurement 6 (Figure 6.16) taken about 3 hours later shows a large increase in amplitude, for no apparent reason. There are just not enough ray paths taken to justify the amplitude reduction, especially since there seems to be no other correlation throughout the rest of the experiment.

Measurement 8, taken the following day after 2 hours of depressurization again shows an immediate increase in amplitude in accordance with the stiffness theory. The pressure is increased to 35 bars an hour later and the amplitude again immediately decreases. The pressure remains at 35 bars throughout the day (except for measurement 14 which measured the effect of only about a minute depressurization; this does not show up on the pressure data which was taken every 5 minutes). Also, throughout the day the amplitudes seem to steadily increase, with a jump at measurement 13, which is opposite of what the stiffness theory predicts. We would expect a steady decrease in amplitude as the pressure down the length of the fracture increased, thus decreasing the stiffness by opening the fracture. By the end of the day (measurement 20) the pressure is back up to where it was in the morning (measurement 8) after it was depressurized. Therefore, we cannot say that the amplitude increased when the pressure decreased. However, by the next day (measurement 21) the amplitude has increased. These ambiguous results are supported by the sweeps PT0 and PT20D as previously discussed.

Plotting the relative attenuation may show the results more clearly (Figure 6.17). This plot shows the attenuation with respect to the first measurement which is said to have almost zero attenuation. The figure shows the large jump between measurement 1 and 2. It also shows a con-

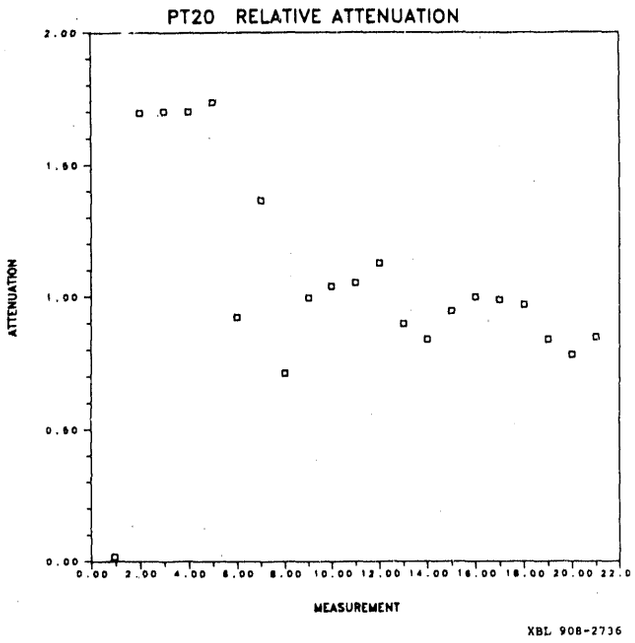

Figure 6.17. The relative attenuation between measurements for the values in Table 6.2, measurement 1 is taken as baseline. All three components have been averaged to obtain the amplitude values.

sistent attenuation for the next four measurements, then more fluctuations with a general downward trend, opposite of what is expected, unless leak off in the region of ray coverage is occurring.

After the seismic measurements were made during the inflation of borehole BOFR 87.001 we wanted to perform similar measurements while borehole BOFR 87.003 was presurized. Therefore, on 26 August the receiver was moved to 2.0 meters up the water filled borehole BOAU 83.034 to a point adjacent to the fracture and Bofex 3 in BOFR 87.003 and clamped in place. The close proximity of the receiver to the Bofex and the inflation point enabled us to measure the seismic wave directly across the maximum inflation point, unlike the case when the fracture was inflated from BOFR 87.001. Initially, a baseline sweep was taken (PT0E) down borehole BOFR 87.002 with the source at the same points as in tests PT0, and PT20D. The source was then left stationary at 15.0 meters down BOFR 87.002 and hourly measurements taken to produce data set PT2020. The measurement schedule and amplitudes while the source and receiver were fixed is shown in Table 6.3. The results of this sequence are similar to BOFR 87.001, however the variation in amplitudes between measurements is smaller. The amplitudes initially seemed to decrease as required, though not significantly (Figure 6.18).

In accordance with these tests, an attempt should be made to explain why the amplitudes varied so much between measurements. This problem is real in that each of the amplitudes in the traces which made up the stack were consistent with each other, but different from the measurements taken just a few minutes later. The explanation must be that some physical change in either the source or receiver position or the rock itself occurs in the short time span; maybe due to the shot itself. Another explanation would be some time dependent variability in the electronics of the source amplitude. To determine if the amplitude variation was due to equipment or rock condition a calibration was carried out at LBL over a two day time period. The source was placed in a water filled borehole and the receiver was clamped into a water filled borehole exactly in the same fashion as the field condition. The only difference being that the boreholes at LBL were not in a fracture zone but in a 2 m × 2 m × 2 m concrete block. Measurements were

Table 6.3. Measurement schedule for inflation of BOFR 87.003

No.	Date	Time	P (bars)	Maximum Amplitude	No. of Stacks
1	26AUG	12:15	0	604.0903	10
2	26AUG	12:30	20	596.0745	10
3	26AUG	12:45	20	595.1597	10
4	26AUG	13:00	20	581.0745	10
5	26AUG	13:45	20	557.0640	10
6	26AUG	14:30	20	566.1304	10
7	26AUG	15:05	20	573.7874	10
8	26AUG	16:00	20	576.5081	10
9	27AUG	10:21	20	670.8962	10
10	27AUG	10:39	20	683.5027	10
11	27AUG	10:46	20	690.5825	10
12	27AUG	11:00	0	686.8218	10
13	27AUG	11:20	0	700.6729	10
14	27AUG	11:40	0	698.1968	10
15	27AUG	12:02	0	698.4734	10
16	27AUG	13:00	0	705.7234	10
17	27AUG	14:00	0	682.1172	10
18	27AUG	15:00	0	657.0347	10
19	27AUG	15:30	0	655.7820	10
20	29AUG	7:15	0	670.8962	10
21	29AUG	7:20	0	719.9255	16

The amplitude values are from component 1.

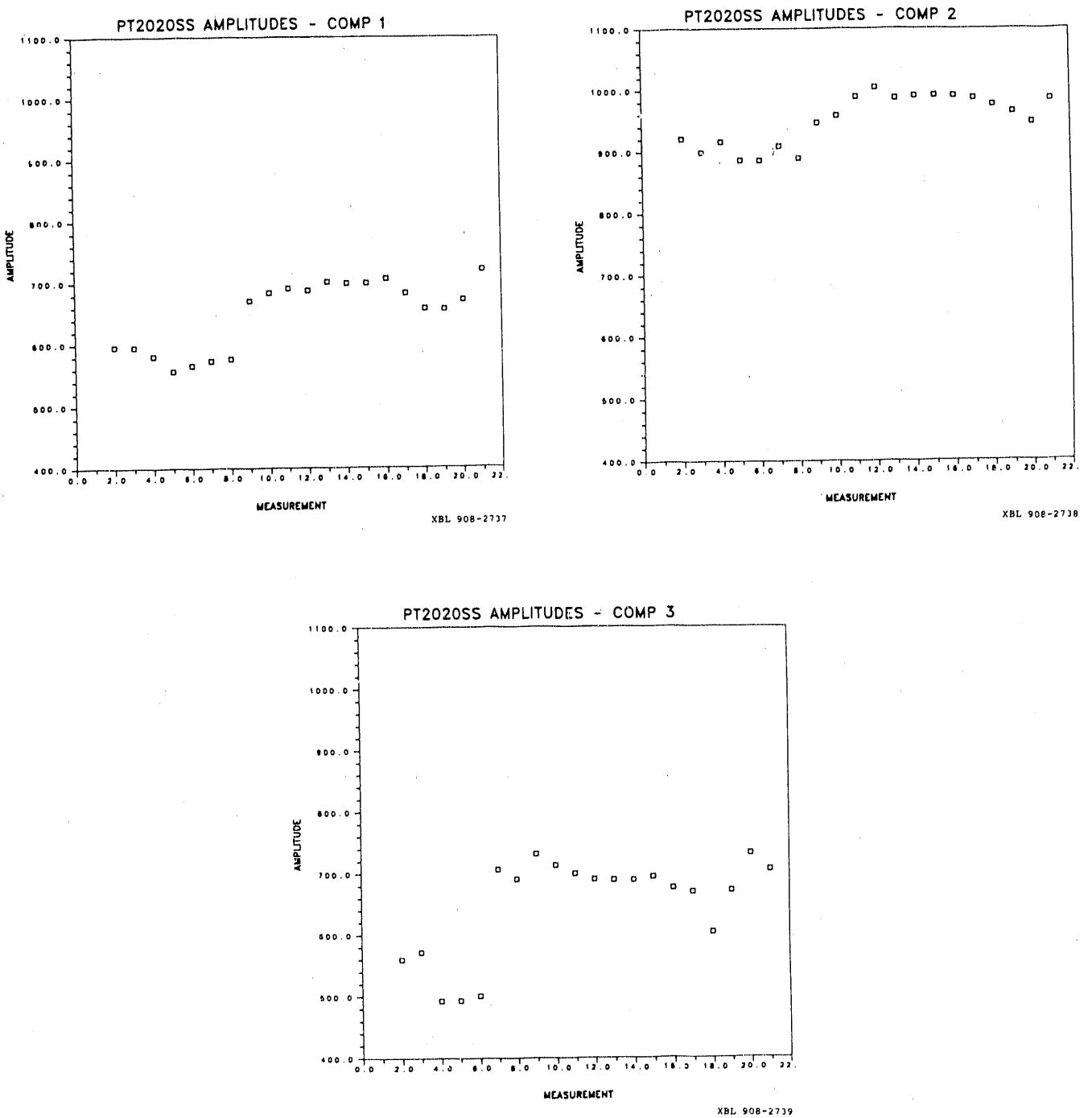

Figure 6.18. Amplitude values for a data given in Table 6.3 (a) component 1, (b) component 2, and (c) component 3.

taken at 1 hour intervals over two days. The signals were also recorded on a transducer permanently mounted on the block. This transducer would determine if any variations were due to source variation or the clamping of the receiver. The results were that there was no perceptible change in the signal over a two day period. This would indicate that the changes in amplitude at Grimsel were due to rock property changes and not clamping or electronics changes. Obviously we did not have a simple rock type in the FRI experiment. The observed changes were due to either pressurization effects, chemical changes of the rock from injected fluid or some other factors. In any case, unfortunately, the results of the inflation experiment are such that the stiffness theory could not be tested in a rigorous fashion. Improvements of the experimental procedure that may help future attempts are:

1. More measurements, both seismic and pressure/Bofex should be taken.
2. The entire experiment should remain at steady state for at least a day if possible, and
3. A reference receiver should be put in place outside of the pressure zone.

6.6. Hydrologic Analysis

The storativity of a fracture can be defined as:

$$S = S_s b = \rho g b(\phi c_w + c_f) = \rho g(b c_w + \frac{1}{\kappa}) \quad , \tag{6.14}$$

where ρ is the density of water, g is the acceleration of gravity, ϕ is the porosity, which is unity, c_w is the water compressibility, and c_f is the fracture compressibility. The fracture compressibility, c_f and the stiffness, κ, is related by:

$$c_f = \frac{1}{b\kappa} \tag{6.15}$$

In order to calculate the stiffness value and the specific storage using Equation (6.15) the fracture aperture must be known. However, the aperture value is very difficult to estimate. One way to estimate the aperture is from the transmissivity using the cubic law:

$$T = \frac{b^3 \rho g}{12\mu} \quad , \tag{5.16}$$

where b is the fracture aperture. As a first approximation the transient flow rate curve at I1.2 was best-fitted to the straightforward analytical solution and the transmissivity was estimated to be $2.3 \times 10^{-10} m^2/s$. If Equation (6.16) is used to solve for b, the aperture becomes $6.6 \times 10^{-6} m$. From Equation (6.14) and the aperture value, the fracture storativity is calculated to be 5.9×10^{-8} assuming a value of κ of 2×10^{11} Pa/m (from Section 6.4). It turns out that b is so small that the first term in Equation (6.14) is negligible.

Bofex measurements showed displacement of the fracture during the inflation tests (Figures 6.4b and 6.5b). This indicates that the fluid pressure is affecting the stress field significantly enough to displace the fracture. The stress field change in turn can cause change in the permeability field. In this section we will examine the flow rate measurements to see if the fracture permeability had changed during the inflation test.

As was briefly discussed, the injection pressure was changed three times during the inflation test in BOFR 87.001. The initial inflation pressure in interval I1.2 was at 19 bars (Stage 1) and was raised to 35 bars at about 20 hours into the test (Stage 2). Then after five hours at 35 bars it was brought back down to about 17 bars (Stage 3). At about 50 hours the pressure was set to about 19 bars again (Stage 4). This pressure time history is shown in Figure 6.4a. The flow rate into interval I1.2 during the injection is shown in Figure 6.19. During Stage 4, interval I3.1 was opened to the same pressure as interval I1.2 and therefore, the flow rate in Stage 4 is the sum of the flows into the both intervals.

If fluid pressure does not affect permeability, the flow rate (at a given time or at steady state) should be linearly proportional to the injection pressure. Change in proportionality indicates change in permeability. Therefore, one can examine injectivity, which is defined as the ratio of flow rate to injection pressure to evaluate any possible change in permeability due to pressure change. Injectivity of BOFR 87.001 during the inflation test is shown in Figure 6.20. As can be seen in the figure, the injectivity has increased by as much as 50% during Stage 2. The higher pressure seems to have increased the permeability of the fracture by displacing it. During Stage 3, the injectivity fell back to where it had been at Stage 1. This implies that the permeabil-

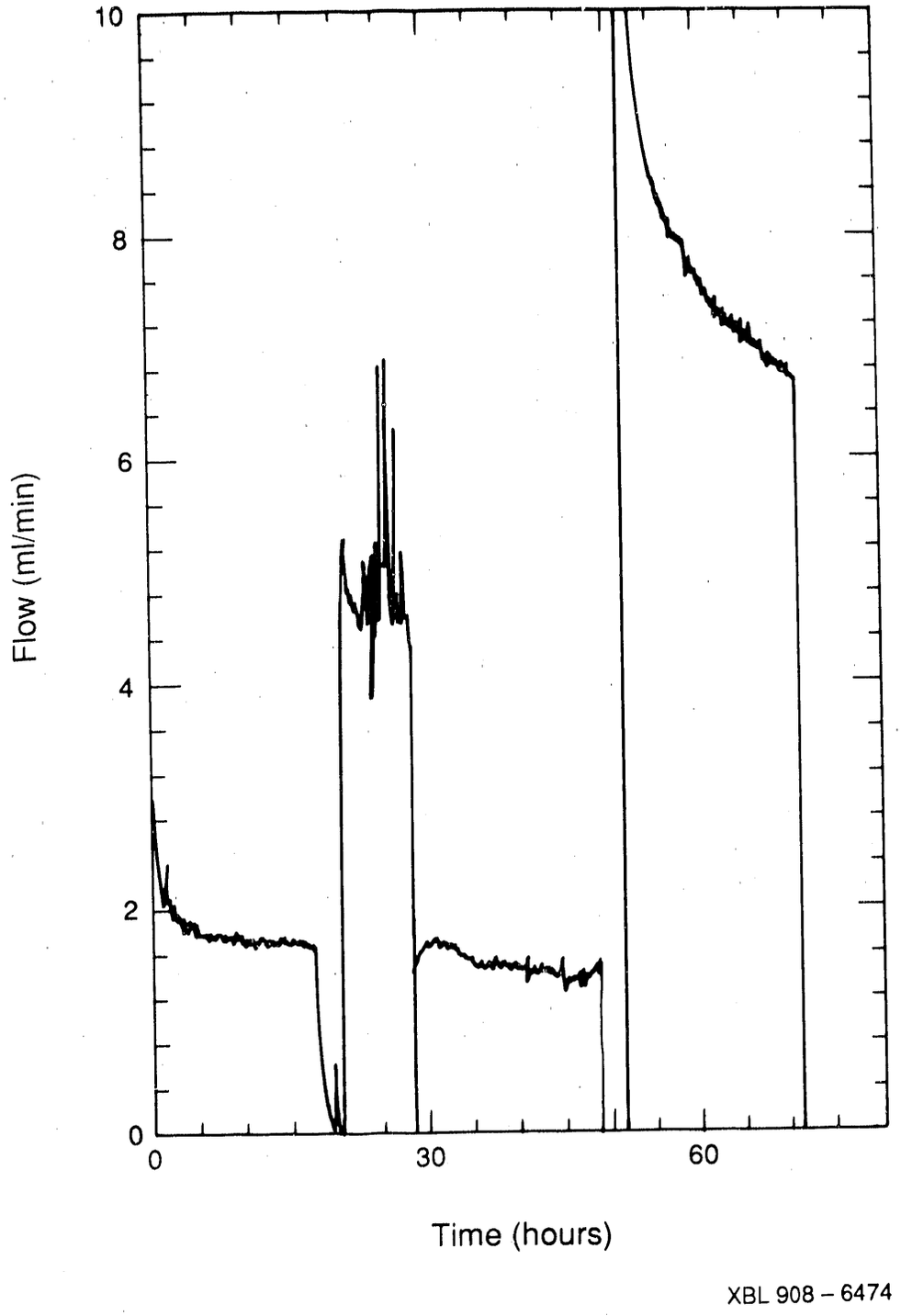

Figure 6.19. Flow rate into I1.2 during injection.

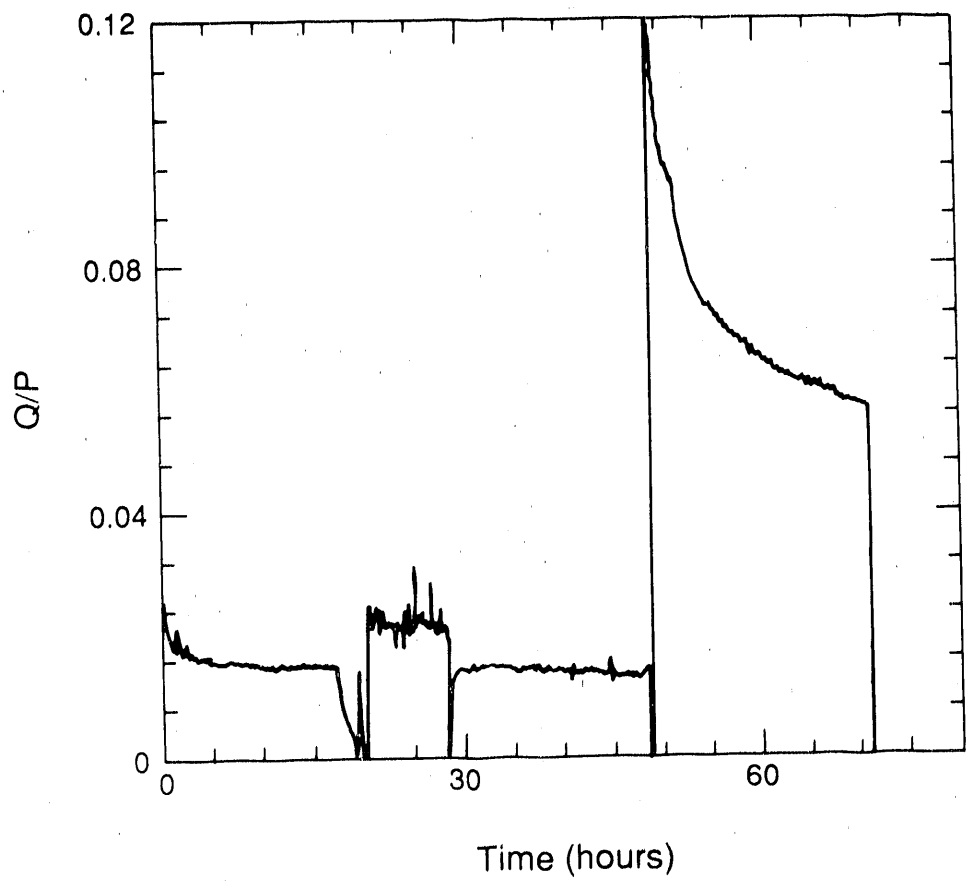

Figure 6.20. Injectivity (Q/P) of BOFR 87.001 during the inflation test.

ity had decreased back to the original value. However, the corresponding displacements measured by Bofex 1 in Figure 6.4b indicate that the fracture displacement is not back to what it was during Stage 1. This discrepancy may be due to the fact that Bofex only 'sees' displacements occurring at the wellbore whereas injectivity is the measure of the fracture transmissivity averaged over the effective flow field. In other words, the fracture could have been hydraulically back in the state it had been during Stage 1, it was mechanically still open at the wellbore.

If the injectivity of the two boreholes, BOFR 87.001 and BOFR 87.003, are the same, the injectivity during Stage 4 should be twice as large. However, as can be seen in Figure 6.20, the injectivity almost quadrupled. This indicates that the permeability of BOFR 87.003 may be as much as three times larger than that of BOFR 87.001. Larger injectivity of BOFR 87.001 may be explained by the fact that BOFR 87.003 is much closer to one of the tunnels than BOFR 87.001. It should be noted, however, that injectivity is best compared under steady-state conditions. If transient data are used, the initial conditions should be consistent, i.e., if tests are conducted one after another, enough time should be allowed for recovery between tests. In the present case, it was neither at steady-state nor the same initial conditions existed for the four stages. Therefore, the results are somewhat qualitative.

7.0. SUMMARY, CONCLUSIONS, AND RECOMMENDATIONS

The motivation for the FRI project was to improve our abilities to use seismic imaging as a tool for characterizing fractured rock, particularly for the purpose of hydrologic analysis. We chose a fracture zone which was clearly present, hydrologically conductive, and accessible so that we could test, calibrate, and improve our abilities to image and characterize such a feature with seismic tomography. Four other studies were conducted in association with the seismic experiments. A detailed geologic investigation provided the appropriate background and insight for interpretation of the tomograms. Geomechanical studies allowed controlled measurement of the rock and fracture properties and allowed us to develop hypotheses to help interpret the results from the tomographic studies. A limited number of hydrologic tests were used to check the visual observation that the fracture zone was hydrologically active and to see if other features marked by seismic anomalies might also conduct fluid. Finally, we attempted to significantly modify the fracture zone properties by inflating the kakirite fracture, measuring its stiffness and permeability change *in situ*, in order to determine if we could simultaneously detect changes in the seismic response.

The site of the FRI experiments was picked because upon initial visual inspection, it appeared structurally simple and it was accessible from four sides. However, as more detailed investigations were performed, it became clear that the site is not at all simple. The rock is heterogeneous and anisotropic. In addition to the main shear zone, there are different granitic rock types, lamprophyres interspersed in the rock, fractures or joints, and mineralized veins. The excavation of the tunnels bounding the FRI site apparently caused significant additional fracturing at the tunnel walls.

Laboratory results indicated that the level of saturation has a dominant effect on P- and S-wave velocities and amplitudes. The velocity was significantly lower and the attenuation was

greater in dry samples than in saturated samples. We could not test the effect of the kakirite fracture in the laboratory because the core containing it was reduced to rubble. The effect of smaller, but still macroscopic fractures that we could test was not found to be significant. The effect of heterogeneity in the rock was exemplified by one of the fractured specimens which had a *higher* velocity than the adjacent intact rock specimens. This highlights an important aspect of using seismic information to locate and characterize fractures: the seismic tomography is imaging mechanical properties and not all of these mechanical properties may be correlated to hydrologic properties.

The tomographic images produced in 1987 and 1988 are different. The major fractures containing kakirite were imaged clearly as Feature A in the 1987 velocity tomogram. In the 1988 tomogram, the feature is still imaged, but it is not as pronounced. The damaged zones near the tunnel walls are clearly seen in 1987 and are not obvious in 1988.

Several hypotheses to explain the differences in the two surveys were explored first, if the rock in the vicinity of Feature A and in the tunnel damage zone had been more saturated in 1988 than in 1987 due to fluid injection just prior to the 1988 seismic testing, laboratory results indicate that the fracture zone would have been characterized by a higher velocity and lower attenuation in 1988 and would have therefore produced a smaller seismic anomaly. However, there is no strong evidence to show that the rock was not saturated in 1987.

Different sources and coupling mechanisms were used in the two years, so the reason for the differences in the tomograms might be that the seismic source used in 1987 was not as powerful. Thus the first arrivals of waves which were severely attenuated as they passed through the shear zone and the damaged zones near the drifts were not detected in 1987. Having missed the first arrivals the velocity appeared to be slower. The first arrivals were seen in 1988 and the zone was a weaker velocity anomaly.

Probably the most interesting hypothesis for increased attenuation in 1987 is that frequency differences between 1987 and 1988 were the cause of the different images. The dominant frequency of the received signal used in 1987 was lower than in 1988. By calculating values of

stiffness at the 1987 and 1988 dominant frequencies, we have shown that this difference in frequency would result in significantly more delay through the fracture in 1987 than in 1988. Thus, stiffness theory alone could account for the smaller anomalies in 1988. This unintentional change in frequency may have resulted in the best evidence so far for the applicability of stiffness theory to acoustic wave propagation in fractured media. The 1987 results essentially combined attenuation and velocity tomography through serendipity, but it may be beneficial to look for frequencies which combine attenuation and velocity tomography by design.

The hydraulic tests that were conducted confirmed the hydrologic significance of the kakirite-bearing fractures in the FRI zone identified by the seismic tomography. Conduction along the zone was observed, but the hydraulic response curves did not indicate flow in an infinite plane. Several scenarios which could effectively cause leakage were examined to see if they could explain the deviations. The boundary effect caused by drainage into the tunnels seems to be very small. It is possible that the leakage from the FRI fracture may occur locally though another feature that intersects it. There is evidence from the hydrologic tests for some permeability perpendicular to the fracture which may correspond to features identified through tomography in the FRI site. If the FRI work continues, we recommend that holes be drilled into these other features to validate the tomographic results. Further hydrologic testing should also be conducted to determine the behavior of these features. Tracer tests may also help us further characterize the hydrology of FRI fractures. In any case, the interaction between the seismic and well test results showed how the seismic results could be used to guide the well test design and the well test interpretation could be used to develop hypotheses for further seismic and hydrologic testing.

A method for in-situ determination of mechanical stiffness of a fracture was successfully demonstrated. In this regard it was shown that corrections for the limited areal extent of the inflation pressure in a fracture can significantly affect how such measurements should be interpreted. The lack of any consistent observable change in the associated seismic measurements was also most likely due to the limited extent of fracture inflation. Furthermore, it is clear that a future test should be carried out under more controlled conditions being sure that more measure-

ments are taken and a reference path is used. As a result of these short comings, the joint geomechanical and seismic measurements were inconclusive in confirming the fracture stiffness theory.

Hydraulic storativity, which is notoriously hard to estimate, was independently estimated for the FRI fracture using the geomechanics measurements. This work represents new possibilities for joint mechanical and hydrologic well test interpretation. Further independent mechanical measurement might provide a new way to explain the apparently non-linear flow behavior often observed in well tests in fractured rock.

An interesting sidelight of the seismic work was that the damage zones caused by mining are significant seismic anomalies that can be defined by tomography. This information might be very useful in a mine-by experiment designed to evaluate the effect of excavation. Some of the seismic perturbation might be due to desaturation, and it would be very elucidating to repeat such measurements over time following excavation.

The seismic work points to several other promising areas for new work. The greatest potential use for the seismic methods lie in the combined use of P- and S-wave analyses, although to date there are no adequate high frequency S-wave sources available. None of the sources tried at the FRI site produced good S-waves. Also, large amounts of data are necessary for tomographic imaging. Hundreds of thousands of traces may be collected. These must be taken back to the office and the first arrivals picked by hand in order to prepare the data for tomographic inversion. Many problems with the field data may not show up for months after the data are collected. If in-field, real-time data processing were developed, experimenters could see the results of the data processing as the data were collected. This would speed up the analysis and allow problems with the data to be identified and corrected in the field.

The FRI site is not as simple as we had originally envisioned, and consequently the results of the individual testing programs are not unequivocal. However, the combined results clearly show how seismic methods can be more effectively applied to image fractured rock. In addition, we have gained a better understanding of the relative significance of the physical properties

affecting the propagation of seismic energy and the importance of the seismic results relative to the hydrologic properties of fractured rock. Although the work was primarily carried out in saturated, fractured granite, the results are focused on the physics of the processes and thus applicable to almost any rock that is dominated by fracture permeability.

8.0. REFERENCES

Carslaw, H. S. and J. C. Jaeger, 1946. *In Conduction of Heat in Solids*, Clarendon Press, Oxford.

Crampin, S., 1978. Seismic-wave propagation through a cracked solid: Polarization as a possible dilatancy diagnostic, *Geophys. J. Roy. Astron. Soc., 53*, 467-496.

Crampin, S., 1981. A review of wave motion in anisotropic and cracked elastic-media, *Wave Motion, 3*, 343-391.

Crampin, S., 1984a. Effective anisotropic propagation through a cracked solid, In Crampin, S., Hipkin, R. G., and Chesnokov, E. M., eds., Proc. of the First International Workshop on Seismic Anisotropy, *Geophys. J. Roy. Astron. Soc., 76*, 135-145.

Crampin, S., 1984b. Anisotropy in exploration seismics, *First Break, 2*, 19-21.

Crampin, S., 1985. Evaluation of anisotropy by shear wave splitting, *Geophysics, 50*, (1) 142-152.

Crouch, S. L. and A. M. Starfield, 1983. *Boundary Element Methods in Solid Mechanics: With Applications in Rock Mechanics and Geological Engineering*, Allen and Unwin, London, Boston.

Da Prat, G., H. Cinco-Ley, and H. J. Ramey, Jr., 1981. Decline curve analysis using type curves for two-porosity systems, *Society of Petroleum Engineers Journal*, Society of Petroleum Engineers of AIME, 354-362.

Ehlig-Economides, C. A., 1979. Well test analysis for wells produced at a constant pressure, Ph.D. Thesis, Stanford University, Stanford, California.

Geotest, 1988. Felslabor Grimsel Fracture Zone Investigation, 3052 Zollikofen/Bern, Switzerland.

Hopkins, D. L., N. G. W. Cook, and L. R. Myer, 1987. Fracture stiffness and aperture as a function of applied stress and contact geometry, *Proc. 28th U.S. Symp. Rock Mech.*, Univ. of Arizona, Tucson, Arizona, June 29-July 1, 1987.

Johnson, L. R. and J. E. Peterson, 1986. Analysis of ultrasonic velocities in Kouros, LBL Report LBID-1175.

Kucuk, F. and Brigham, W. E., 1979. Transient flow in elliptical systems, *Soc. Pet. Eng. J.*, 401-410.

Nagra Technical Report 85-46, 1985. Grimsel Test Site - Overview and test programs, Baden, Switzerland, 118 pp.

Pyrak-Nolte, L. J., L. R. Myer and N. G. W. Cook, 1990. Anisotropy in seismic velocities and amplitudes from multiple parallel fractures, *J. Geophys. Res.*, (in press).

Pyrak-Nolte, L. J., L. R. Myer and N. G. W. Cook, 1989. Transmission of seismic waves across single fractures *J. Geophys. Res.*, (in press).

Schoenberg, M., 1980. Elastic wave behavior across linear slip interfaces, *J. Acoust. Soc. Am., 68*, (5) 1516-1521.

Schoenberg, M., 1983. Reflection of elastic waves from periodically stratified media with interfacial slip, *Geophys. Prosp., 31*, 265-292.

Van Everdingen, A. F., W. Hurst, 1949. The application of the Laplace Transformation to flow problems in reservers, *Trans., AIME, 186*, 305-324.

Wyss, E., 1988. Kurzbericht Zu Den Ersten Hydrogelogischen Untersuchungen Im Rahmen Des Versuches FRI, 616, NAGRA, Internal Data Report.

Appendix A

A.1. Description of Data Acquisition System

An important aspect of this project was to test and evaluate equipment for the collection of tomographic data. The initial system was a modification of a system LBL used at the Spent Fuel Test Experiment in the Climax Stock at the Nevada Test site. This system was a high voltage source connected to a piezoelectric cylinder. This was used to produce kilohertz signals in a simple and rapid means. In 1987 this system was used to produce the signals. The data were recorded on an IBM PC/AT system that had a special data acquisition board installed. This board was manufactured by RC Electronics Corporation in Santa Barbara, California. This board was used with the RC Scopedriver Software. This software allowed rapid and easy collection of multiple waveforms. In 1988 and 1989 a larger piezoelectric source was used with completely newly designed pulse electronics. The "pulser" of high voltage is outlined in Figure A-1. This pulser allowed for up to 4.5 kilovolts to be transmitted to the piezoelectric source. As described in Section 4.0 the improvement in data quality was dramatic from 1987 to 1988. Specifications of the equipment are given in Table A-1.

Although this has been an extremely useful system it is still a research system and not a commercial system. Improvements are needed in the piezoelectric source, for more power output, and in the collection system. Future work should focus on an infield system with processing capabilities to "first look" the data. Multiple station recording, and stronger sources for greater areas of imaging are also needed. The S-wave generation problem seems to be the most difficult. We see a means for solving most of the problems associated with high resolution imaging, but how to generate strong, SH and SV polarized waves in a controlled fashion seems to be a most difficult task.

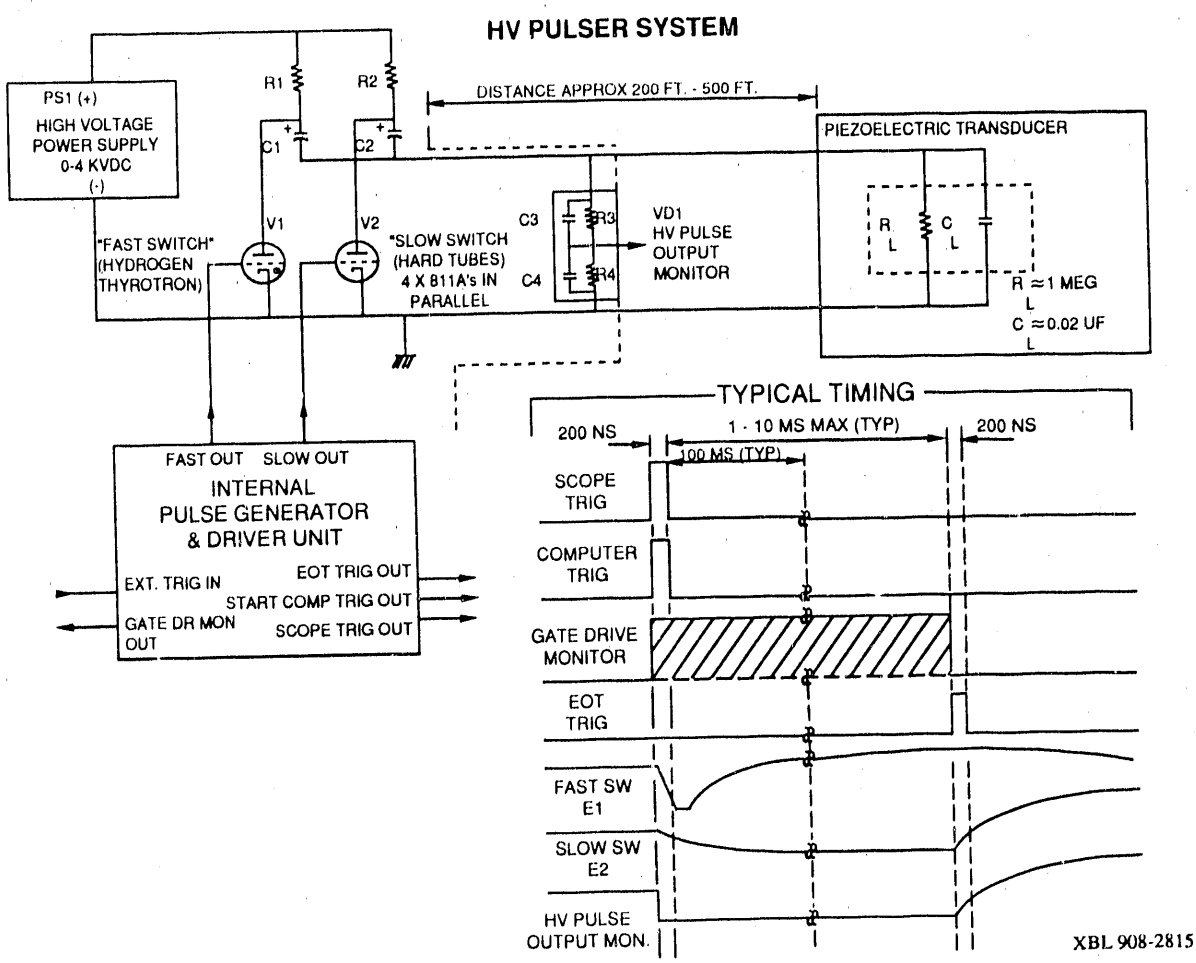

Figure A-1. HV pulser system.

Table A.1. Specifications of data acquisition system

Piezoelectric Source

Stack of 4 cylindrical Navy 5500 piezoelectric material. Each element in stack is 3 inches in diameter, 2 inches high and 1/4 inch wall thickness.

High Voltage Pulser

The "high voltage pulser" provides the necessary voltage to excite a piezoelectric transducer. The pulser unit consists of the following: (see Figure A.1)

(1) A variable high voltage power supply, 0 to 4.5 kVdc, HVPS.

(2) An energy storage and electronic switching system.

(3) An internal pulse generator and driver unit.

(4) A precision high voltage pulse output monitor, VD1.

The high voltage power supply (HVPS):

The HVPS provides a variable dc source of high voltage (0 to 4.5 kVdc) necessary to charge the energy storage system capacitors, C1 and C2. The maximum current available from the HVPS is 50 mAdc.

The energy storage and electronic switching system:

The purpose of this section of the HV pulser is to provide the piezoelectric transducer with a very short rise time, long duration, negative high voltage pulse with adjustable amplitude.

This pulse is generated by using two independent capacitors: switching circuits, namely the fast switch and the slow switch.

The fast capacitor switch circuit consists of R1, C1 and V1. The slow circuit consists of R2, C2 and V2.

Please refer to Figure A-1 for circuit and timing details.

The internal pulse generator and driver unit

The pulse generator and drive units provides the necessary gates and triggers required for proper operation of the high voltage pulser.

Output triggers are provided to the computer indicating the start of the output pulse and end of the pulse.

Please refer to Figure A-1 for "typical timing."

The precision high voltage pulse output monitor.

The output HV pulse monitor provides an output of 1000v/v, into 50 ohms. The pulse rise and fall time of this circuit is good enough to observe the main hv pulse with reasonable fidelity.

Data Storage

IBM PC/AT with 2 Mb of RAM. RC Electronics, Inc. "scope driver" system. Data throughput of 1 million samples/sec over 16 channels maximum. 64,000 data points collected, per "shot." Capability to stack in real time up to 10,000 shots. Various off line analysis software.

END

DATE FILMED

01 / 29 / 91